Vibro-Acoustic behaviour of Flexible Rectangular Ducts

A Dissertation Submitted

In Partial Fulfillment of the Requirements for Degree of

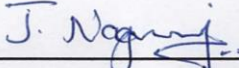## *Doctor of Philosophy*

By

Nagaraja Jade

भारतीय प्रौद्योगिकी संस्थान हैदराबाद

Indian Institute of Technology Hyderabad

Department of Mechanical and Aerospace Engineering

Indian Institute of Technology Hyderabad

Hyderabad-502285, India

July 2018

Declaration

I declare that this written submission represents my ideas in my own words, and where others' ideas or words have been included, I have adequately cited and referenced the original sources. I also declare that I have adhered to all principles of academic honesty and integrity and have not misrepresented or fabricated or falsified any idea/data/fact/source in my submission. I understand that any violation of the above will be a cause for disciplinary action by the Institute and can also evoke penal action from the sources that have thus not been properly cited, or from whom proper permission has not been taken when needed.
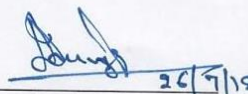
Nagaraja Jade
(ME12P1002)

Approval Sheet

This thesis entitled **Vibro-Acoustic behaviour of Flexible Rectangular Ducts** by **Nagaraja Jade** is approved for the degree of *Doctor of Philosophy* from IIT Hyderabad.

Prof. M. L. Munjal
Department of Mechanical Engineering
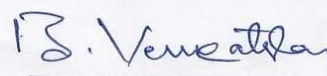Indian Institute of Science Bengaluru
External Examiner-1

Prof. A. R Mohanty
Department of Mechanical Engineering
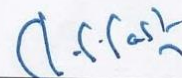Indian Institute of Technology Khargapur
External Examiner-2

Dr. C. P. Vyasarayani
Department of Mechanical & Aerospace Engineering
Indian Institute of Technology Hyderabad
Internal Examiner

Dr. B. Venkatesham
Department of Mechanical & Aerospace Engineering
Indian Institute of Technology Hyderabad
Adviser/ Guide

Dr. C. S. Sastry
Department of Mathematics
Indian Institute of Technology Hyderabad
Chairman

Acknowledgments

Dedicated to

Gurus of my Life

My mother Mallamma and father Shivarudra Gowda, my primary school
teachers Chennamma H. and Sudha S., high school teacher Chandbasha
for inspiring me to learn new things and lead fruitful life

Abstract

Ducts are extensively used in Heating, Ventilation and Air Conditioning (HVAC) applications and gas industries for transmission of substance, especially liquid or gas. These ducts carry the noise generated by Air-Handling Units (AHU) in axial and transverse directions. Sound radiated in the transverse direction due to acoustic excitation of duct walls is known as '*Breakout noise*'. Sound radiation from duct depends on its structural properties as well as the medium's acoustic properties. The present research interest is to study sound radiation and vibration characteristics of rectangular ducts using direct and inverse techniques.

First part of the work describes analytical, experimental and numerical models to understand sound radiation characteristics of a flexible rectangular duct. Firstly, an analytical model is developed based on an *'equivalent plate model'* of the rectangular duct. This model has considered the coupled and uncoupled behaviour of both, acoustic and structural subsystems. Modal radiation efficiencies of a rectangular duct are estimated and compared to those of simple rectangular plate. This comparison shows a similarity between duct sound radiation behaviours in terms of plate modes. The analytical model results are validated using Finite Element-Boundary Element Method (FEM-BEM) numerical results. As a part of the study, sound radiation behaviour of a duct is studied to understand its equivalence with monopole and dipole sources. As second step, an experimental setup is developed to measure the breakout noise in terms of Transverse Transmission Loss (TTL) and radiation efficiency, by providing a plane-wave excitation. A methodology is developed to calculate input sound power from measured pressure signals inside the cylindrical tube using an autospectrum of a progressive wave. Radiated sound power is measured using two different methods, namely- intensity probe method (P-P method) and Microflown technique (P-U method). Using the measured input and radiated sound power, TTL and radiation efficiency are calculated. These results have been corroborated with analytical results of *'equivalent plate model'* and FEM-BEM numerical results.

Second part of the current study is to understand the effect of duct joints on modal parameters. In this study, three different rectangular ducts with two types of joints

(welded and adhesive joints) are considered. Pre-test analysis is performed to know the number of measuring points and their locations. Then, Experimental Modal Analysis (EMA) is performed on these three ducts to identify natural frequencies and mode shapes. These EMA (measured) results are compared to Numerical Modal Analysis (NMA) results (predicted). It has been observed from all cases that natural frequencies are in good agreement. Mode shapes of measured and predicted results are compared in terms of Modal Assurance Criteria (MAC) plot, mode pair table and visual inspection. Low MAC values are observed for the duct with welded joints. However, a duct with an adhesive joint similar to the ideal shape has good MAC value. Detailed section analysis is performed on a duct with a two-welded joint configuration to understand mode shape deviation. It is observed from experimental and numerical results that joints play a critical role in deviation of mode shapes for thin flexible structures. Hence, as next part of the study, an analytical model is developed to incorporate joint effects in estimating the modal parameters. Here, the joint condition is represented using linear and rotational spring's stiffness. Natural frequencies and mode shapes of a rectangular duct are found analytically by Rayleigh-Ritz method using an *'equivalent plate model'*. These results are validated with experimental results for a rectangular duct with Pittsburgh lock joint. Natural frequencies of the duct in both cases are in good agreement. Mode shapes of symmetric modes remained same for both ducts, whereas antisymmetric modes deviated from each other. This deviation is observed only in duct walls next to the joint.

Third part of the study focuses on sound source reconstruction using two inverse techniques such as Inverse Numerical Acoustics (INA) and Near-field Acoustic Holography (NAH) methods. Here, INA is used to reconstruct the vibration velocity on a flexible duct surface in structural-acoustic coupled system. Effect of measurement locations, measurement points and mesh density on reconstruction results is discussed at both coupled and uncoupled frequencies. L-curve regularization parameter selection method is used to overcome the ill-posed problem. It is verified from reconstruction results that vibration velocity can be obtained accurately with less than 10% error.

Four different NAH techniques are used in the present investigation to identify distribution of fan noise source strength and radiation pattern. Firstly, number of reference microphones needed to find the incoherent sources by Singular Value Decomposition (SVD) is evaluated. Later, sound source is reconstructed with measured sound pressure using different NAH techniques. The reconstructed results showed that ESM method is best to reconstruct fan noise sources with minimal error. The behaviour of a fan at blade passing frequency (BPF) is akin to a dipole sound source. A comparison of reconstructed pressures with measured values indicates that reconstructed pressure correlates very well with measured pressure. As part of study, ESM is used to reconstruct sound source at uncoupled and coupled frequencies for a rectangular box with a single compliant wall. Sound pressure data for reconstruction is generated from numerical simulations instead of actual measurements. Reconstructed results are compared to actual results at both frequencies. Effect of noise on accuracy of the reconstruction is studied for different signal to noise ratio (SNR) values. Higher SNR values led to good accuracy in reconstruction. Based on the regularization studies, it can be concluded that L-curve method is better compared to GCV method for reconstruction at uncoupled and coupled frequencies.

Finally, from the present research work it is concluded that vibro-acoustic behaviour of the flexible rectangular ducts is studied effectively using direct (sound intensity method, Microflown technique) and inverse techniques (INA and NAH).

Contents

Nomenclature

Abbreviations

AHU	Air-Handling Units
AS-AS	Antisymmetry-Antisymmetry
AS-S	Antisymmetry-Symmetry
ATM	Acoustic Transfer Matrix
ATV	Acoustic Transfer Vector
BC	Boundary condition.
BEM	Boundary Element Method
DAQ	Data Acquisition System
DFT	Discrete Fourier Transform
DOF	Degree of Freedom
DPR	Drive Point Residue.
EMA	Experimental Modal Analysis
ESM	Equivalent Source Method
EWM	Elementary Wave Model
FEA	Finite Element Analysis
FEM	Finite-Element Method
F-F	Free-Free
FFT	Fast Fourier Transforms
FNAH	Fourier NAH
FRF	Frequency Response Functions
FT	Fourier Transform
GCV	Generalized Cross Validation
GI	Galvanized Iron
HELS	Helmholtz's Equation Least-Squares
HVAC	Heating, Ventilation and Air Conditioning
IBEM	Inverse Boundary Element Method
IFT	Inverse Fourier Transform
IMCM	Impedance-Mobility Compact Matrix
INA	Inverse Numerical Acoustics
KH	Kirchhoff–Helmholtz
LN-EWM	Least-Norm Elementary Wave Model

LS-EWM	Least-Square Elementary Wave Model
MAC	Modal Assurance Criteria
MDOF	Multi Degree of Freedom
MP	Measurement plane
MPC	Modal Phase Collinearity
MvMIF	Multivariate Mode Indicator Function
NAH	Near-field Acoustic Holography
NMA	Numerical Modal Analysis
S-AS	Symmetry-Antisymmetry
SD	Stand-off distance
SNR	Signal-to-Noise ratio
SONAH	Statistically Optimized Near-field Acoustic Holography
SS	Simply supported
S-S	Symmetry-Symmetry
SVD	Singular Value Decomposition
TF	Transfer factor
TM	Transfer Matrix
TTL	Transverse Transmission Loss

Latin letters

A_s	Cross-sectional area of a cylinder
A_d	Duct surface area
$A(f)$	Amplitude of progressive wave as function of frequency
a	Modal acoustic pressure vector
$a_n(\omega)$	Complex amplitude of the nth acoustic pressure mode
$\boldsymbol{B}$	Matrix of wave function values at measurement positions
$B(f)$	Amplitude of reflective wave as function of frequency
$b_m(\omega)$	Complex amplitude of the mth vibration velocity mode
b	Modal structural vibration velocity vector
C	Coupling coefficient matrix
C_{bc}	Stiffness induced by boundary conditions
$C_{n,m}$	Coupling coefficient between n^{th} acoustic mode and m^{th} structural mode
C_{plate}	Rectangular plate stiffness

C_{rs}	Stiffness induced by rotational springs
C_{ts}	Stiffness induced by translational spring
$\mathbf{C}_{pp}$	Auto-spectral matrix of holographic signal
$\mathbf{C}_{rp}$	Cross-spectral matrix between reference and holographic signal
$\mathbf{C}_{rr}$	Auto-spectral matrix of references signal
$\mathbf{C}_{vv}$	Cross-spectral matrix between the virtual references
$\mathbf{c}\,(\mathbf{r})$	Complex estimation weights of sound pressure
D	Flexure rigidity
d	Microphone separation distance (spacer length)
E	Elastic (young's) modulus
$f(\mathbf{z},\omega)$	Force distribution on the surface of the duct wall
f_a	Analytical natural frequencies
f_e	Experimental natural frequencies
f_n	Numerical natural frequencies
G	Free space Green's function
G_{hv}	Free-space Green's function associated with source point 'v' and field point 'h'
$\mathbf{g}$	Generalized modal force vector
H	Hermitian transpose
H_{AA}	Autospectrum of progressive wave
$H_{AA}(f)$	Autospectral density of $A(f)$
$H_{BB}(f)$	Autospectral densities of $B(f)$
$H_{AB}(f)$	Cross-spectral density between $A(f)$ and $B(f)$.
$\mathbf{H}_{rp}$	Transfer matrix which relates measured and reference signals
$\mathbf{H}_{vp}$	Transfer matrix which relates virtual reference data with measured data
h	Thickness of, duct wall or equivalent rectangular plate
I	Sound intensity
I_a	Active intensity
I_0	True intensity
I_r	Reactive intensity
$\hat{I}_r$	Measured intensity
J_0	True reactive intensity

K_{window}	2D Harris cosine window
k	Wave number
k_c	Cut-off wavenumber
k_r	Rotational spring stiffness
k_x, k_y, k_z	Wavenumbers along x, y and z-directions, respectively
$\mathbf{k}_n$	Sampling points in the wavenumber domain
L_1	Length of the rectangular duct along x-direction
L_2	Length of the rectangular duct along y-direction
L_3	Length of the rectangular duct along z-direction
L_a	Length of equivalent(rectangular) plate along axial direction
L_c	Length of equivalent(rectangular) plate along circumferential direction
L_x	Length of measurement plane along x-direction
L_y	Length of measurement plane along y-direction
m_m	Modal mass
$P_h, P_s, P_v,$	Holographic, Actual, Virtual source surfaces
$\widehat{\mathbf{P}}$	Decomposed partial fields of the sound
p_h / p_F	Sound pressure measured in holographic/ field plane
p_s	Sound pressure on source plane
p-RI	Pressure-residual intensity index
p_{rms}	RMS value of sound pressure
$\mathbf{Q}_v$	Virtual source strength vector
$q(\boldsymbol{x}, \omega)$	Acoustic density function
$\mathbf{q}$	Modal source strength vector
q_v	Virtual source strength of distributed point sources
$\boldsymbol{r}$	Position of measurement point
Re	Real value
S	Sound radiating surface
s	Distance between two microphones in cylindrical tube
S_f	Flexible surface area of structure
S_s	Scanning surface area
T	Kinetic energy of an elastic, thin, isotropic plate
t	Time
$T_{n,m}$	Transfer factor for n^{th} acoustic mode coupled to m^{th} structural mode
U	Strain energy of an elastic, thin, isotropic plate

U_{rs}	Strain energy due to rotational springs
$[U]$	Unitary / orthogonal matrix (left)
u	Particle velocity
V	Duct volume
V_i	Net volume displacement
V_i^{EMA}	Modal vector of the ith mode obtained from experimental modal analysis
V_j^{FEM}	Modal vector of the jth mode obtained from the numerical modal analysis
$[V]$	Unitary / orthogonal matrix (right)
v_n	Normal vibration velocity
Δv_m	Volume displacement associated with amplitude displacement of mth element in n^{th} plate.
$\langle v \rangle^2$	Mean square surface velocity of the duct structure
W_i	Input sound power given to the duct
W_P	Sound power radiated from the piston source
W_r	Sound power radiated from the duct wall surface
W_{rad}	Sound power radiated from an unbaffled rectangular plate
$\langle w \rangle$	Root mean square vibration velocity of the piston source
$w(z, \omega)$	Normal velocity of a flexible structure surface
w	Flexural deflection of the plate
x_w	Width of Tukey window
$\mathbf{x_m}$	Position vectors of field point (measurement)
$\mathbf{y_n}$	Position vectors of source point
$\mathbf{Y_s}$	Uncoupled structural mobility matrix
$\mathbf{y_m(\alpha)}$	m^{th} static beam functions along circumferential direction of the plate
$\mathbf{y_n(\beta)}$	n^{th} static beam functions along axial direction of the plate
$\mathbf{Z}$	Radiation impedance matrix
$\mathbf{Z_a}$	Uncoupled acoustic modal impedance matrix

Greek letters

$\psi_n(\mathbf{x})$	Uncoupled acoustic mode shape function of the duct
$\Phi_m(\mathbf{z})$	Uncoupled vibration(structural) mode shape function of the duct
Θ	Elementary wave function
Ω	Radiated sound field

α	Positive constant
β_e	Phase calibration error
β_f	Phase between acoustic pressure and particle velocity in the sound field
$\boldsymbol{\varepsilon}$	Regularization parameter
ρ_s	Structural density
ρ_0	Air density
c_0	Speed of sound in air
κ	Scaling factor
ϱ_n	Complex expansion coefficients
φ_e	Phase error between the microphones in intensity measurements
ω_c	Critical frequency for a simply supported rectangular plate
ω	Circular natural frequency (angular frequency)
γ	Virtual coherence
μ	Poisson's ratio
σ_e	Sound radiation efficiency calculated experimentally
σ_a	Sound radiation efficiency calculated analytically
$[\Sigma]$	Diagonal matrix of the singular values
$\Phi_m(\alpha)$	Admissible functions in circumferential direction
$\Psi_n(\beta)$	Admissible functions in axial direction

List of Figures

xxiii

List of Tables

Chapter 1

Introduction

1.1 General introduction

Heating, Ventilation, and Air-conditioning (HVAC) system is used to transport the conditioned air from generating point to the occupants. HVAC system includes Air-Handling Units (AHU), ducts and plenums for transferring conditioned air. Fig.1.1 shows different parts of a typical HVAC system with an indication of air flow and noise transmission. Common sources of noise generation in these systems are: i) Air-Handling Units (AHU) such as fan, blower and compressors, ii) transmission of noise generated by AHU through ducts, iii) velocity of the airflow, and iv) turbulence generated in the complex and narrow shaped ducts etc.
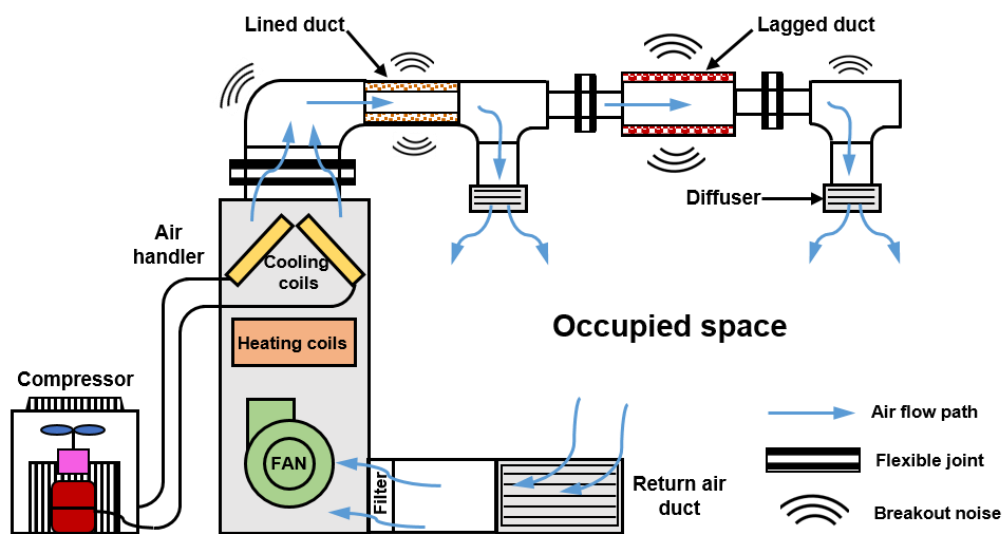
Figure 1.1: Schematic diagram of a typical HVAC system with an indication of air flow and noise transmission through the ducts.

Duct is an enclosed passage for transmission of substance, especially liquid or gas with extensive usage in HVAC applications, gas industries, aircraft industry and gas turbine power generation applications. These ducts carry the noise generated by Air-Handling Units (AHU) such as fan, blower and compressors along with conditioned air in axial and transverse directions. The most commonly used duct cross sections are rectangular, circular and flat oval.

Of all the geometries, rectangular ducts had maximum breakout noise at lower frequencies, which means minimum wall transmission loss [1]. Figure 1.1 shows a schematic diagram of sound propagation in a flexible rectangular duct for the given input acoustic source. Sound radiated in the transverse direction due to acoustic excitation of duct wall is known as 'Breakout noise'. Similarly, sound transmitting into the duct from surrounding environment is called 'Breakin noise' [1].
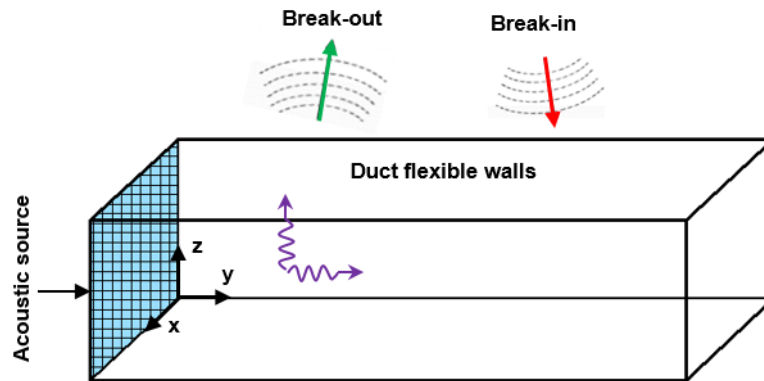
Figure 1.2: Schematic diagram of the sound propagation in a rectangular duct

Generally, noise generated by AHU is at low frequency where structural-acoustic coupling is dominant. Study of interaction between the structural and acoustical subsystem is important to understand breakout noise phenomena in HVAC systems. Airborne and structure-borne sounds contribute to duct breakout noise, which is more dominant at lower frequencies [1]. Hydrodynamic force and acoustic pressure waves excite the duct wall and cause structure-borne noise. These forces and pressure waves are associated with flow and propagation of sound through the duct, respectively. The excitation due to hydrodynamic force generates lower frequency vibration, which can be a focus for fatigue analysis. Noise generation due to turbulence occurs at a high flow velocity of the fluid and dominates at low frequency range. As the fluid flow velocity is less than 10 m/s in HVAC systems (lower Mach numbers), noise generated due to fluid flow is negligible and hence, it is not considered in the present study.

Figure 1.3 shows the schematic of source characterization by direct and inverse techniques. In case of direct method (forward progression), sound sources are characterized by measuring radiated sound pressure, intensity or sound power. However, in case of inverse techniques, sound sources are reconstructed using measured sound pressures near the source surface. These methods are also called as array techniques as they are based on measurement of sound field using an array of microphones. Examples of direct measurement methods for noise

source identification are: Sound intensity method, Microflown technique. Examples of vibration measurements are: Mounting accelerometers, laser vibro meter, etc. Examples for inverse methods are: Near-field Acoustic Holography (NAH), Beamforming and Inverse Numerical Acoustics (INA). Fig. 1.4 shows direct and inverse measurement techniques used for noise source identification.
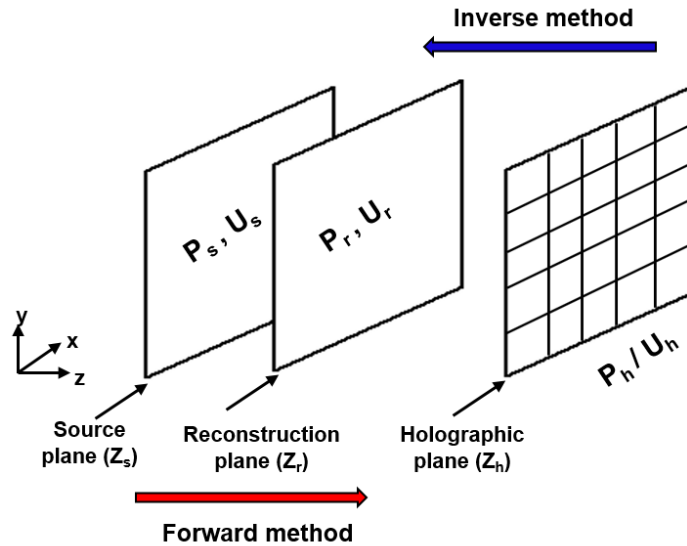
Figure 1.3: Sound source characterization by direct and inverse techniques.

Sound intensity probe technique is used to measure radiated sound power and locate the noise sources. Scanning of the sound source with this probe provides information on flow of acoustic energy from the noise source. This method is more suitable for stationary sound fields since measurements can be made at one single point at a time. The main limitation of this method is particle velocity calculation on basis of measured sound pressures separated by a known length of spacer. Another drawback is, measurement of sound intensity closer to surface is not possible due to presence of the probe.

Microflown technique is an advanced tool to measure and visualize the sound fields in broader frequency range. As this technique is not affected by reflections or background noise, it is more suitable in conditions where sound pressures are high compared to sound intensity ratio. The major advantage of this method is that sound pressures, particle velocity, sound power and acoustic impedances are measured directly. In this method, a reference sensor can also be used to obtain relative phase information of the surface velocities.

(a)
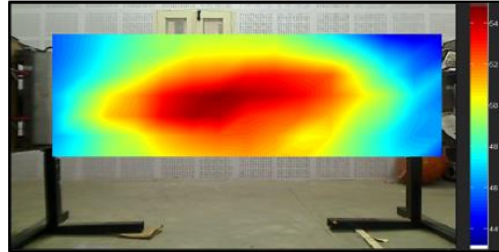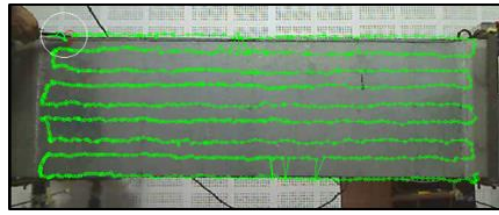
Intensity probe   Scan and Paint system (Microflown)

(b)

Near-field Acoustical Holography   Beamforming*

Figure 1.4: Noise source identification methods: (a) Direct and (b) Inverse techniques.

[*Reference: Karl B et al., Correlating noise sources identified by beamforming]

NAH is a good inverse technique to identify sound sources in low frequency applications. In this method, a sound field map is reconstructed on source surfaces using measured sound pressures in near-field of the source. The advantage of this method is, sound pressure, particle velocity and sound intensity or sound power can be obtained on the source plane. The major drawback of this method is requirement of more number of microphones and large measurement plane to cover the entire source making it cumbersome and economically costly.

Beamforming is an efficient method to identify noise sources for high frequency applications. This technique provides the detailed contour plots of sources with single set of measurement data. This method is limited to far-field measurements only and not suitable to identify acoustic parameters near the source. Further, it is difficult to distinguish between the closely spaced sources [72].

Generally, ducts are fabricated by bending thin metal sheets into suitable shapes with edges being joined with different joints in axial and transverse directions using seams and connectors. Most common types of joints (connectors and seams) used for fabricating the ducts are shown in Fig. 1.5. Seams are: Pittsburgh lock, standing seam, button punch snap lock, single corner seam, lap seam and corner weld. Connectors are: drive slip, weld flange, T-6 hemmed "S" slip, etc.

(a)

(b)
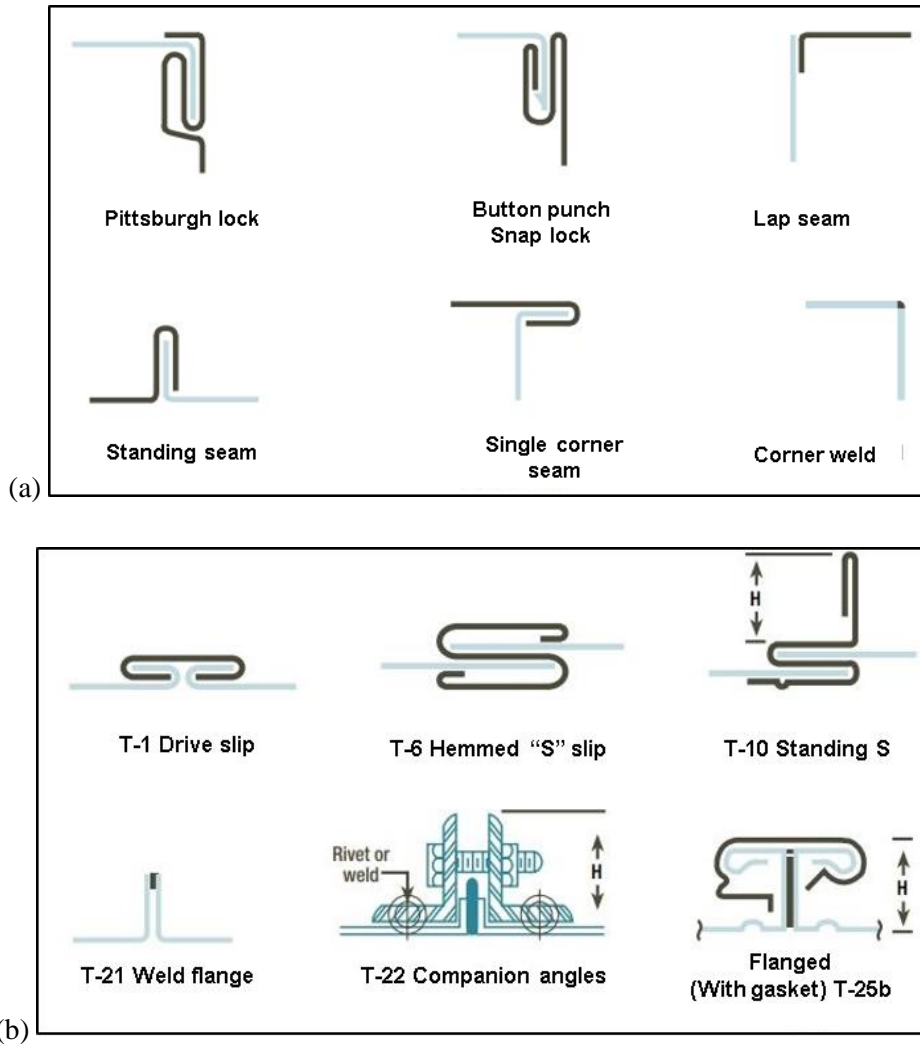
Figure 1.5: Joints used in the fabrication of rectangular ducts: (a) Seams and (b) Connectors.

[*Reference*: tambemetal.com/pdfs/Rectangular.pdf]

1.2 Literature study

1.2.1   Breakout noise characterization

Sound transmissions through duct walls are characterized in terms of transverse transmission loss (TTL) and sound radiation efficiency. Typical TTL curve with respect to frequency is shown in Fig. 1.6 where analytical and numerical results are presented. The troughs of TTL curve indicate most efficient radiating modes which are a major contributor to breakout noise. These frequencies are represented in Fig. 1.6 such as: f_{s1} which is an uncoupled structural natural frequency and f_{c1} and f_{c2} are the first and second coupled natural frequencies, respectively.
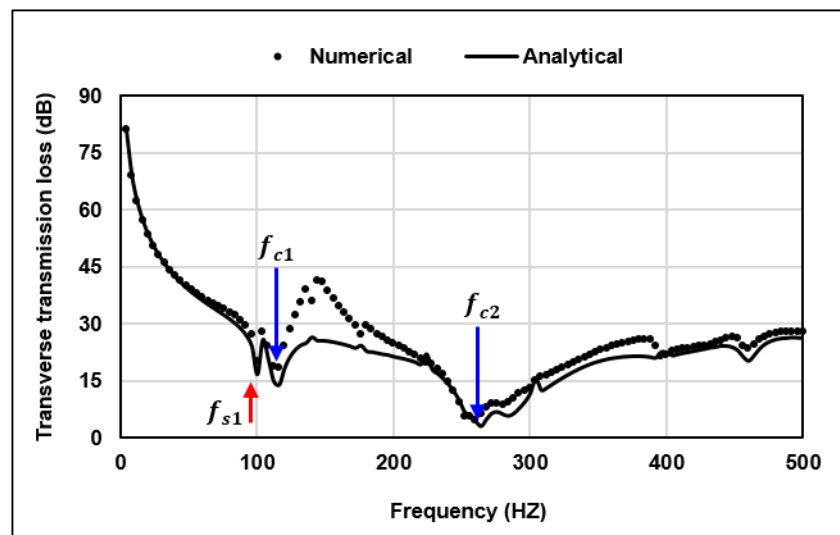
Figure 1.6: Transverse transmission loss of a rectangular duct as a function of frequency [14].

Cummings, Astley, Kirby et al. [1-5] studied extensively to calculate sound transmission from flexible duct walls for different geometrical cross-sections such as cylindrical, rectangular and flat oval shape. Cummings [1] discussed the role of various duct cross-section geometries on breakout and break-in noise. Further, he provided research review progress for past two decades on "duct breakout noise" and explained vibro-acoustic coupling phenomena and described the possible methods to reduce breakout noise.

Breakout noise is an important issue in HVAC ducts applications and gas flow pipes used in large scale industries [6]. There are different analytical models developed to characterize sound radiation from duct walls namely: finite-length line source model [7-9], equivalent cylindrical model [10, 11], and equivalent plate model [5, 12-14]. Subsequently, few researchers used Finite Element Method (FEM) to analyse transmission loss and sound

6

radiated from duct walls [3, 4, 15, 16]. In most of the cases, it is assumed that sound field inside the ducts is composed of propagating modes of either uncoupled acoustic duct modes or vibro-acoustic coupled modes [17].

In the study of sound radiation from ducts, it is sufficient to consider force wave excitation in the transverse direction only, since structural or acoustical resonant modes in axial directions do not play a major role in the breakout noise. To understand this phenomenon, the coupling concept is useful [1]. An acoustic wave excites the duct walls strongly and causes structural vibrations. These vibrations induce acoustic pressure inside the duct. This phenomenon continues under coupling and is efficient at strongly coupled modes. Coupling depends on acoustic, structural natural frequencies and spatial distribution of mode shapes. Transfer factor identifies the strongly coupled structural and acoustical modes [18].

Coupling of structural duct modes with acoustic cavity modes is studied in the literature to understand breakout noise phenomena [19]. An analytical model is developed by Dowell et al. [20] for predicting the coupled response of structural-acoustic coupled system. Kim and Brennan [21] rearranged the same formulation in terms of impedance-mobility compact matrix. Later, Lin and Pan [22] analysed sound radiation characteristics for a box type structure with flexible walls using a boundary element method. Venkatesham et al. [12-14] developed analytical models for prediction of breakout noise for different configurations. They assumed strong coupling between structure walls and interior volume while weak coupling between structure walls and surrounding environment. Sound pressure inside the cavity was calculated by impedance-mobility compact matrix (IMCM) approach. Radiated sound power was calculated using "Kirchhoff–Helmholtz (KH)" integral formulation for plenum [13] and an "equivalent unfolded plate model" for rectangular duct [14].

Duct cross-sectional geometry has a significant effect on the characteristics of breakout and also break-in noise. Ideal circular cross-section ducts have the highest TTL compared to other shapes at lower frequencies. However, distorted duct circular duct causes "mode coupling" effect, thereby plane acoustic modes excite the higher order structural modes, which enhance sound power radiation and lowering TTL [23-26]. In case of rectangular shaped ducts, breakout noise is predominant and leads to lower TTL at low frequencies due to strong structural-acoustic coupling [7, 8, 27]. Flat-oval shaped ducts have characteristics of rectangular shape ducts at a lower frequency and are akin to that of a circular duct at resonance mode of circular duct of dimensions (diameter) similar to circularly curved sides of flat-oval

ducts. Chang and Cummings described a simplified analytical model to predict transmission loss and compared it to numerical and experimental results of flat-oval ducts [2, 28, 29].

Breakout noise can be minimized by treating duct walls with acoustic absorptive material either inside and/or outside of the ducts which are named as lining and lagging, respectively. Astley et al. [15] studied the effect of bulk reacting liner on the sound transmission of flexible ducts by finite element analysis (FEA) and compared to experimental results. Cummings and Astley [30] investigated the flanking mechanism in lined ducts by modelling wall flexibility effect. A simple analytical model was proposed by Cummings [31] to understand effects of lagging on the ducts and compared these results with measured ones. It was noticed from the comparison study that overall response for lagged ducts was captured nicely. Later, breakout noise from lagged pipes and rectangular ducts was discussed by Munjal et al. using a transfer matrix approach [32, 33]. The important benefit of this method is that of combining different layers of lagging in a simple way by modelling inner duct walls as lumped impedance. Another possible method for reduction of breakout noise in rectangular ducts is stiffening the duct walls so that fundamental structural resonance frequency of duct walls is increased [34].

Acoustic breakout noise radiated from duct walls can also be studied in terms of modal radiation efficiencies. This calculation helps in finding efficient sound radiation modes in total sound power radiated from a duct. Wallace [35] discussed an analytical formula for calculating radiation efficiencies at low frequencies from a baffled rectangular plate. Lin and Pan [22] studied the vibration and sound radiation characteristics of box structures. It provides a basis for understanding vibration energy flows between panels of the box, grouping of various modes, radiation efficiencies and various kinds of sound sources.

Measurement of transverse transmission loss (TTL) helps in the understanding of efficient sound radiating modes and dominant vibration pattern. This can be performed by measuring input sound power supplied to the duct and radiated sound power. In literature, methods available to measure the duct's TTL are pressure based which require standard environments such as reverberation or anechoic chambers [1].

As HVAC ducts are fabricated using thin metal sheets with different types of joints, it is essential to study the effect of duct joints and any geometrical deviation on breakout noise. In majority of literature study, breakout noise prediction models are assuming ideal duct cross-sectional shapes but experimental models consider joints. Modeling of duct joints is quite challenging in analytical method and is computationally expensive for numerical methods. So, it is preferred to consider ideal duct in numerical modeling. Limited research is available

to understand the joint effect on breakout noise. Cummings [34] attempted to reduce the breakout noise from rectangular duct by changing stiffness of duct joint condition. Cummings et al. [23] and Yoursi and Fahy [24] investigated the effect of distortion (geometric distortion and deviation due to structural joint condition) on transmission loss of circular ducts. These studies show that the presence of distortion leads to "mode coupling" effect, which in turn enhances radiated sound power from duct walls and further leads to lower transmission loss.

1.2.2 Modal parameter estimation

Sound radiated from ducts depends on the structural properties as well as medium's acoustic properties. It is important to study modal parameters of the ducts to understand sound radiation mechanism which can be obtained by its free vibration analysis. Different analytical, numerical and experimental methods are available in the literature to estimate natural frequencies and mode shapes of rectangular ducts [36].

Finite Element Analysis (FEA) is a quick and easy way to know dynamic characteristics of any structure but determining its damping parameters is difficult. Another method is to use analytical technique for solving mathematical models which represent actual structure. Experimental Modal Analysis (EMA) is the most common and effective method to determine, improve and optimize dynamic characteristics of an engineering structure [36]. The analytical and FEA models can be verified using EMA. Kennedy and Pancu [37], first proposed a most significant method of EMA before Fast Fourier Transforms (FFT) was invented. Fu and He [38], provided a detailed theory of analytical and experimental modal analysis to characterize dynamic behavior of any structure. Significant advances in experimental techniques enhanced modeling of a structure and determining its dynamic properties. Experimental results can be used as a reference (i) to modify existing structure and to optimize structure design by an iteration process (ii) to validate analytical models for refining future designs [39].

Prior to the actual modal test, it is essential to identify optimal number, locations of excitation and response measurement point to acquire all the modes excited within the interested frequency range. In the literature, a few researchers proposed techniques for calculating optimum number and position of measurements for modal test based on frequency response functions (FRF) [40] and finite element analysis [41]. Similarly, it is important to choose an apt excitation method, as the influence of each mode on overall response of the structure depends on the type of excitation. Shaker and impact hammer are the most common types of excitations.

Dynamic characteristics are extracted from measured FRF's using curve fitting methods. Selection of curve fitting techniques is important in extracting dynamic characteristics from measured time domain or frequency domain data [42-44]. In this regard, different algorithms are developed based on Single Degree of Freedom (SDOF) and Multi Degree of Freedom (MDOF) methods [45-48]. The modal vectors obtained from experimental measurements are compared using numerical modal vectors by correlation analysis, in terms of Modal Assurance Criteria (MAC) plot. Allemang [49] and Ewins [50], discussed various existing methods to perform a systematic comparison and correlation between two sets of vibration data, namely numerical and experimental data. Figure 1.7 shows the methodology involved in numerical and experimental modal analysis and corresponding correlation analysis between these results.
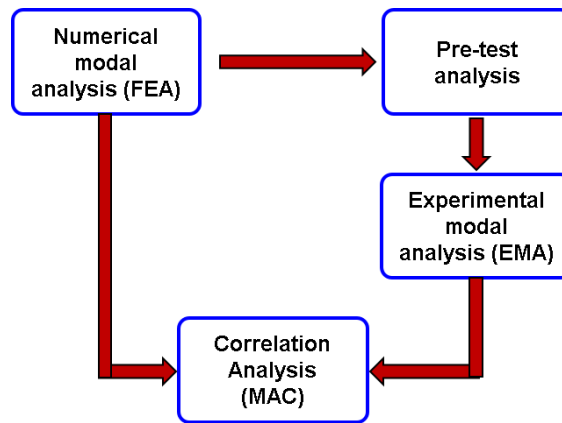
Figure 1.7: Correlation analysis for comparison of experimental and numerical modal analysis results.

Different analytical methods are proposed in the literature for calculating natural frequencies and mode shapes of rectangular and circular ducts with different axial boundary conditions [51]. Soedel and Azmi et al. used line receptance approach to calculate natural frequencies and mode shapes of polygonal cylindrical ducts [52, 53]. Later, a transfer matrix approach is developed by Yamada and Kobayashi [54] to calculate modal parameters of a folded plate. Lee [5] and Venkatesham et al. [13, 14, 55] developed an equivalent plate model using Rayleigh-Ritz method. Here, selection of admissible functions for the folded plate is simplified by equivalent unfolded plate model. Here, creases (joints) between the plates are modelled with linear springs and folded boundaries are modelled with rotational spring. They calculated the free vibration response for square and rectangular ducts, respectively. FEM methods are also available in literature to obtain free vibration response of polygonal ducts [56].

10

Majorly in the literature, an ideal rectangular duct geometry is considered in analytical and numerical studies. However, practical ducts are fabricated with different joint conditions. Therefore, it is necessary to study the effect of joint conditions on modal parameters namely; natural frequencies and mode shape of rectangular ducts using analytical and experimental techniques. Limited literature is available for considering the effect of joints on modal parameters.

Xiao et al. [57] studied the effect of variation in geometry, boundary conditions and material properties on vibration characteristics of a cylinder. Gorrepati and Rao [58] estimated modal parameters for beams with adhesively bonded double strap joints and proved that natural frequencies obtained analytically are inconsistent with experimental results. Xu and Deng [59] discussed modeling of simplified spot welded joint, majorly used in automobile structures, for dynamic analysis. Tian et al. [60] presented a method for dynamic modeling of a bolted joint to calculate modal parameters. Based on experimental and analytical results, they verified and deduced that both natural frequencies and mode shapes are in good agreement. Zaman et al. [61] studied the effect of bolted joints on dynamic properties of beam and frame structures and indicated that natural frequencies decrease due to presence of joints. Modeling of joints in numerical analysis is important since it directly influences the simulation results. Alexandre et al. [62] studied modeling of welded joint by different element types and proved that shell element with increased thickness is better to model the welded connections.

1.2.3 Near-field Acoustic Holography techniques

NAH is an inverse array technique used to reconstruct acoustic parameters by measuring sound pressure with an array of microphones, in a parallel and near to the sound source. Basic principle of NAH methods is described as a flow chart and shown in Fig. 1.8. The current research provides study of four most popular methods of NAH technique and same methods are employed in the reconstruction of sound sources. Four NAH techniques considered in the present study are:

> ➢ Fourier NAH (FNAH)
> ➢ Statistically Optimized NAH (SONAH)
> ➢ Equivalent Source Model (ESM)
> ➢ Inverse Boundary Element Method (IBEM)

Sound radiated from the noise source can be measured in terms of sound pressure on a plane near to source surfaces with a set of microphones arranged in a suitable pattern. These measured pressures are related to unknown source strength by transfer matrix. Calculation of the elements of Transfer Matrix (TM) varies for different NAH methods. In Statistically Optimized NAH (SONAH) method, TM can be formulated using elementary wave functions. For Equivalent Source Method (ESM), TM can be calculated using free space Green's function and for Inverse Boundary Element Method (IBEM), TM can be obtained using Helmholtz integral equation. As all these NAH methods are ill-posed problems, regularization is necessary to overcome the same and for reconstructing accurate results.
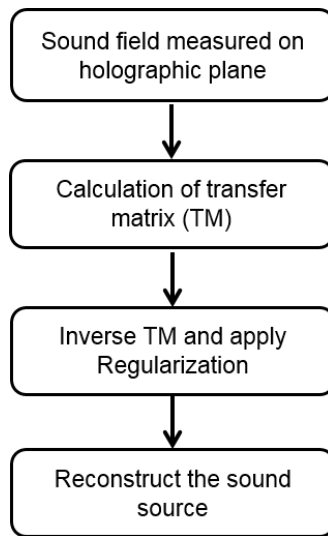
Figure 1.8: Flowchart of the procedure involved in NAH reconstruction techniques.

NAH method was first proposed by Maynard and Williams in the 1980's based on discrete Fourier transform [63]. Primary objective of using this method is to reconstruct sound pressure, particle velocity on / near to the actual source surface. By using these two quantities, active intensity can be calculated and thus total radiated sound power can be obtained. A good overview of the development of NAH techniques is described by Bai et al. [64], Magalhaes and Tenenbaum [65] and Chelliah et al. [66]. Methods based on measurement of particle velocity to reconstruct the sound field were also developed and were found to be more beneficial, if the particle velocity is reconstructed [67, 68]. Main drawback of this method is difficult to practically match the velocity sensors, unlike pressure sensors. Different NAH methods vary with the model used to correlate sound pressure measured at different microphones to acoustic quantities on the source surface.

12

Fourier NAH (FNAH) method uses Discrete Fourier Transform (DFT) in Cartesian coordinates to reconstruct sound field on the surface parallel to measurement plane [63, 69, 70]. This DFT transforms the sound pressure from spatial to wavenumber domain (k-space). Here, the sound field is expressed as propagating and evanescent waves. Multiplying this wave component with inverse propagator function yields sound field in wave number domain on the required plane. Inverse Fourier Transformation (IFT) is applied to obtain reconstructed acoustic quantities in spatial domain. FNAH method can also be implemented in cylindrical and spherical coordinates [70]. It is efficient and more suitable for planar sources, but main drawback is the size of measurement surface, which needs to be at least two times larger than source leading to tedious measurement process. To overcome these limitations, a patch holography technique such as Statistically Optimized NAH method [71] is proposed.

In SONAH method, acoustic quantities are reconstructed on the mapping surfaces near the source. These quantities are calculated using the transfer matrix comprising set of propagating and evanescent waves with appropriate weightage. J. Hald [71], described detailed mathematical formulation for reconstruction of sound pressure and particle velocity. Gomes [72] and Hald et al. [73, 74] investigated applicability of SONAH method on different cases such as non-planar surfaces and cabin environment using two-layer array. Similar to SONAH, another method called HELS (Helmholtz Equation Least Squares) is developed which uses spherical wave functions instead of plane wave functions (used in SONAH method) [75-77]. In this method, a number of elementary waves are always less than or equal to number of microphones.

IBEM has been developed to obtain accurate reconstructions in NAH for arbitrarily shaped vibrating surfaces. Firstly, this method is developed based on the Helmholtz integral equation, which relates sound pressure in field plane (exterior to the source) to sound pressure and velocity on the source surface [78, 79]. Later, IBEM is formulated based on use of continuous distribution of virtual sources on the boundary to represent radiated sound field [80, 81]. If partial measurements are available, then conventional IBEM can't be used. However, an approximation method, called as patch IBEM, has been developed. The advantage of this method is, it can be implemented on large source [82] while major drawback being the chances of reconstruction errors to be high, due to ignoring of partial source region in the measurements.

Equivalent source method is also treated as an alternative method to BEM since BEM requires large computational resources for complex structures [83]. This method uses a set of virtual

sources such as monopole, dipole or combinations to represent sound radiation from source and are placed inside the vibrating body. Actually, this method is developed for the forward progression problem to predict the radiated sound field [84, 85]. Later on, this method was used to solve inverse problems also [86, 87]. The basic idea of this method is to estimate the source strengths of distributed simple sources by mapping the model with measured sound pressure. Using these source strengths, sound field on the source can be estimated. Main advantage of ESM is, the computational time required is much lesser than other NAH methods. Essential benefits of ESM and patch NAH methods are combined and developed new near-field acoustic holography surface decomposition method by Valdivia et al. [88]. Selection of appropriate stand-off distance (SD, distance between actual source plane to virtual plane) is important to obtain accurate reconstruction results. M.R. Bai et al. [89] described the selection of optimal SD and suggested that optimum distance varies from 0.4-0.5 of microphone spacing for planar sources and for spherical sources it may vary from 0.8-1.7 times of average spacing.

Inverse techniques are also implemented on aero-acoustic sources to visualize sound field. Lee et al. used NAH technique based on virtual coherence method for reconstruction of sound field for small ducted fan assembly [90]. Kim and Nelson [91] described estimation of acoustic source strengths using measured radiated sound field within the cylindrical duct. They proved that accuracy of estimating source strength and spatial resolutions can be achieved by improving conditioning of the transfer matrix (frequency response function matrix). Lowis and Joseph [92] proposed a new method, based on modified Green's function, for estimating broadband source strength over the ducted rotor using sound pressure measured at duct walls. Zhang et al. [93] developed a generalized NAH method based on boundary element method to reconstruct the noise source inside a ducted fan. In this method, aero-acoustic sources are represented as point sources such as monopole and dipoles. Sound field on the duct surface was measured and utilized to reconstruct noise sources.

As these NAH techniques are inverse methods, reconstructed results are ill-posed due to presence of evanescent waves. Regularization methods are used to overcome ill-posedness of the problem [94]. Main purpose is to avoid amplification of the noise while solving inverse problem. Tikhonov regularization is the most commonly used technique for NAH methods [95, 96]. Conjugate gradient approach is another method used in inversion [97, 98]. The choice of proper regularization parameter is most important to obtain better inversion results. Different methods available to select regularization parameters are: L-curve method [99, 100], Generalized Cross Validation (GCV) method [101] and Morozov discrepancy principle [102].

14

1.2.4 Inverse Numerical Acoustics (INA)

INA is developed to overcome difficulties faced in conventional methods to measure normal vibration velocities. INA is a reconstruction technique in which surface vibration velocities can be reconstructed using measured sound pressure in the near-field [103]. It can be implemented using both direct and indirect boundary elements methods [104-106]. In this technique, generally, number of sound measurement points are less than the number of nodes on which vibration velocities are to be reconstructed. Hence, INA is the ill-posed problem and is very sensitive to experimental errors and signal noise. Regularization technique can be used to overcome this problem [94].

1.3 Motivation and research objectives

Studying sound radiation characteristics of ducts at a lower frequency is of great interest to reduce breakout noise level at the design stage itself. It is of significant practical interest to predict the noise that transmits through a ducted system from source to a receiver space to achieve the desired noise goal. Reducing the noise at the planning stage is fairly economical and cost-effective. Basic step when treating noise problem is to identify the sources locations and their characteristics. There are several methods (direct and inverse) to visualize the sound field and to find noise source characteristics such as sound pressure, particle velocity, sound intensity and sound power. In the current research work, rectangular cross-section ducts are considered (since breakout noise is dominant due to less stiffness of duct walls) for understanding the sound radiation characteristics.

In the literature study, breakout noise is studied in terms of transverse transmission loss and vibration behaviour of duct structure. However, it can also be studied in terms of modal radiation efficiencies which is described in the present study. According to the author's knowledge, there is no attempt of breakout noise measurement using sound intensity technique. Hence, one of the main motivations of present research work is to measure the breakout noise of a flexible rectangular duct by sound intensity techniques. Based on the literature study, it is noticed that there is scope to study the effect of duct joint conditions on modal parameters as well as breakout noise. Inverse techniques can also be used to reconstruct acoustic quantities on duct surfaces.

1.3.1 Research objectives

Major objective of the current research work is to study vibro-acoustic behaviour of flexible rectangular ducts using direct and inverse techniques. However, detailed objectives are given below:

➢ Understand the physics of sound radiation mechanism at structural and acoustic coupling frequencies and at the uncoupled structural frequency.

➢ Develop a methodology for measurement of breakout noise using two different sound intensity methods.

➢ Investigate the effect of duct joint conditions on the breakout noise and modal parameters of the rectangular ducts.

➢ Develop analytical models to incorporate the duct joint in predicting modal parameters.

➢ Investigate applicability of the inverse technique to reconstruct sound source at structural-acoustic coupled frequencies.

1.4 Structure of the Thesis

The present research interest is to study sound radiation and vibration characteristics of rectangular ducts by analytical, experimental and numerical techniques. Current work is broadly divided in to three stages: (i) studying of sound radiation characteristics of the rectangular duct by analytical, experimental and numerical methods (Chapters-2 and 3), (ii) studying modal parameters of the rectangular ducts by experimental, numerical modal analysis (Chapter-4) and effect of joints on these parameters using analytical, experimental methods (Chapter-5) (iii) sound source reconstruction using inverse techniques such as NAH and Inverse Numerical Acoustics (INA) (Chapters- 6-8).

Chapter-2 discusses an analytical model, to predict sound radiation characteristics like total radiated sound power level, modal radiation efficiency, and directivity of the radiated sound from duct walls. The proposed analytical model results are validated with numerical results obtained using Finite-Element Method (FEM) and Boundary Element Method (BEM). Duct acoustic and structural modes are analysed to understand the sound radiation behaviour of a duct and its equivalence with monopole and dipole sources. The most efficient radiating modes are identified by vibration displacement of duct walls and for these, the radiation

efficiencies have been calculated. The calculated modal radiation efficiencies of a duct were compared to a simple rectangular plate.

Chapter-3 discusses methodology for calculating transverse transmission loss and radiation efficiency through experimental, analytical and numerical methods. The experimental setup to measure input sound power, directivity of input excitation and radiated sound power are described. The P-P and P-U based intensity techniques are used for measuring breakout noise of rectangular duct. It also describes numerical model to predict transverse transmission loss, radiation efficiency and these results are compared to experimental and analytical results.

Chapter-4 discusses an experimental and numerical modal analysis carried out on three different rectangular ducts having different joints and materials. It describes the procedure of pre-test analysis and experimental modal analysis. It also discusses the methods used to find a correlation between experimental and numerical results such as: Modal Assurance Criteria (MAC), frequency comparison and auto-MAC plots.

Chapter-5 discusses the influence of duct joint on structural dynamic characteristics (modal parameters) of a rectangular duct. An analytical model is developed to consider effect of duct joint on modal parameters. The joint condition is modelled as a combination of linear and torsional spring's stiffness. The developed analytical model is then validated with experimental results for a rectangular duct with Pittsburgh lock joint. For further understanding the influence of duct joint on modal parameters, current analytical model results are compared to duct without joint results.

Chapter-6 discusses Inverse Numerical Acoustic technique to reconstruct normal vibration velocity on the duct surface at coupled and uncoupled frequencies. It describes finite element and boundary element (FEM-BEM) based numerical models to calculate sound pressure in near-field of the duct surfaces. It also discusses the effect of pressure measurement points, measurement location and mesh density on the vibration velocity reconstruction at both coupled and uncoupled frequencies.

Chapeter-7 discusses four NAH methods namely: Fourier NAH, SONAH, ESM and IBEM to reconstruct sound pressure field near the fan source. Firstly, number of reference microphones needed to find the incoherent sources is evaluated using Singular Value Decomposition (SVD). Next, using measured sound pressure the sound source is reconstructed by different array techniques.

Chapter-8 discusses the reconstruction of sound source at uncoupled and coupled frequencies using equivalent source method for a rectangular box with the single compliant wall. Data for reconstruction is generated from numerical simulations instead of actual measurements. Effect of regularization and Signal-to-Noise Ratio (SNR) on the accuracy of reconstruction is discussed. The numerical model is developed to understand coupling phenomena between structural and acoustic subsystem.

Chapter 9 discusses the main conclusions of the present research work and points out potential areas for future work.

1.4.1   Research plan of investigation

Research work described in the present thesis is outlined and shown in Fig. 1.9
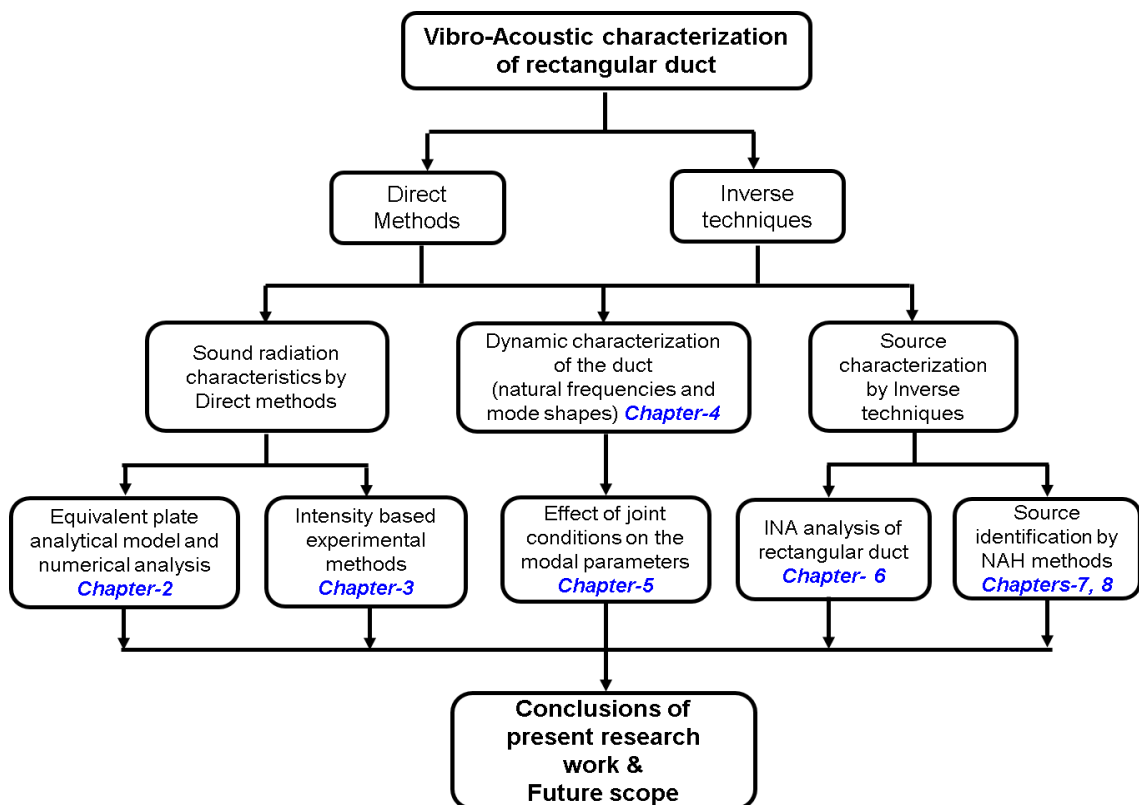
Figure 1.9: Thesis structure of the present research work.

Chapter 2

Sound Radiation Characteristics of a Flexible Rectangular Duct

2.1   Introduction

The study of sound radiated from thin flexible rectangular duct walls helps in understanding breakout noise. It may be noted from literature study that sound radiation from the ducts is studied in terms of radiated sound power and transverse transmission loss (TTL) [14]. However, present work describes the sound radiation characteristics like total radiated sound power, modal radiation efficiency, and directivity of radiated sound from duct walls. A detailed numerical and experimental studies have been done to validate the existing prediction models of breakout noise described in the Ref. [14]. Modal radiation efficiency calculation helps in finding efficient sound radiation modes in total sound power radiated from a duct.

Uncoupled structural modes of rectangular duct and acoustical cavity modes are calculated using analytical method and validated with numerical results. These rectangular duct modes are classified into four different groups and are similar to box structures as discussed in Ref. [22]. In these four groups, most efficient radiating modes are estimated based on the symmetries between panel pairs and net volume displacements in a particular mode. Modal radiation efficiencies of different groups of a rectangular duct are estimated analytically and compared to numerical results. These modal radiation efficiencies of the rectangular duct of four groups are compared to those of simple rectangular plate. This comparison shows a similarity between duct sound radiation behaviour in terms of plate modes. As a part of the study, total sound power radiated from duct walls is estimated using the Finite-Element Method (FEM) and Boundary Element Method (BEM). Sound radiation behaviour of a duct is also studied to understand its equivalence with standard sound sources such as monopole and dipole sources. Total radiation efficiencies of coupled acoustic and structural modes are also calculated and are used for validation of the proposed analytical model.

19

2.2   Theoretical formulation

The outline of an analytical model of sound radiation from the rectangular duct is shown in Fig. 2.1. The main objective here is to calculate total sound power radiation and radiation efficiency from flexible duct walls. Assumptions made in this model are (i) strong coupling amongst inside duct volume and flexible duct wall area. (ii) weak coupling between flexible wall area and outside environment. (iii) coupled behaviour can be expressed in terms of a finite number of uncoupled acoustic and structural modes.

The proposed model has two stages as discussed in Ref [14]. In first stage, inside duct pressure and wall vibration velocity, due to an acoustic excitation are calculated by considering structural-acoustical coupling and Impedance-Mobility approach. In this approach, coupled response between structural and acoustical domains is represented in the form of uncoupled acoustic and structural subsystems natural frequencies and mode shapes. In second stage, an equivalent plate model with duct wall vibrations as boundary condition is developed to predict the characteristics of sound radiation. Further details are discussed in the subsequent sections.
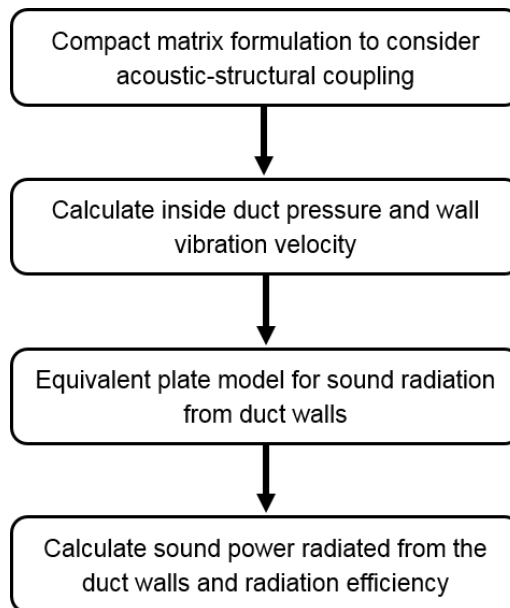
Figure 2.1: Flowchart of analytical formulation for sound power radiation from duct walls.

2.2.1 Pressure field inside the duct and wall vibration velocity

Pressure field inside the duct in terms of uncoupled acoustic mode shapes is given as,

$$p(\mathbf{x}, \omega) = \sum_n \psi_n(\mathbf{x}) a_n(\omega) = \boldsymbol{\psi}^T \mathbf{a} \tag{2.1}$$

Compliant duct wall vibration velocity in terms of uncoupled structural mode shapes is given as,

$$w(\mathbf{z}, \omega) = \sum_m \Phi_m(\mathbf{z}) b_m(\omega) = \boldsymbol{\phi}^T \mathbf{b} \tag{2.2}$$

where, $\psi_n(\mathbf{x})$ is an uncoupled acoustic mode shape function of duct, $a_n(\omega)$ is complex amplitude of nth acoustic pressure mode, $\Phi_m(\mathbf{z})$ is an uncoupled vibration mode shape function of duct, and $b_m(\omega)$ is complex amplitude of mth vibration velocity mode.

Complex amplitude of the nth acoustic mode under structural and acoustic excitation is given as [21],

$$a_n(\omega) = \frac{\rho_0 c_0^2}{V} A_n(\omega) \left(\int_V \psi_n(\mathbf{x}) \, q(\mathbf{x}, \omega) dV + \int_{S_f} \psi_n(\mathbf{y}) w(\mathbf{z}, \omega) dS \right) \tag{2.3}$$

where ρ_0 and c_0 denote density and speed of sound in air, respectively. Function $q(\mathbf{x}, \omega)$ denotes acoustic source strength density function (volume velocity per unit volume) in duct volume V and $w(\mathbf{z}, \omega)$ denotes normal velocity of a surrounding flexible structure for surface area S_f.

Complex vibration velocity amplitude of mth structural mode can be expressed as [21],

$$b_m(\omega) = \frac{1}{\rho_s h S_f} B_m(\omega) \left(\int_{S_f} \Phi_m(\mathbf{z}) f(\mathbf{z}, \omega) dS - \int_{S_f} \Phi_m(\mathbf{z}) p(\mathbf{z}, \omega) dS \right) \tag{2.4}$$

where, ρ_s and h denote density of material and thickness of duct wall, respectively. $f(\mathbf{z}, \omega)$ is force distribution on the surface of duct wall. $p(\mathbf{z}, \omega)$ is inside acoustic pressure distribution on the surface of duct wall. Uncoupled acoustical mode shapes and natural frequencies of a rectangular duct is calculated by using the formula given in Ref. [21]. Similarly, an equivalent plate model is used to calculate the uncoupled structural natural frequencies and mode shapes of rectangular duct.

Modal acoustic pressure vector **a** given in Eqs. (2.1) and (2.3) have expressed in terms of impedance and mobility as,

$$\mathbf{a} = \mathbf{Z_a}(\mathbf{q} + \mathbf{q_s}) \tag{2.5}$$

$\mathbf{Z_a} = \frac{\mathbf{A}\,\rho_0 c_0^2}{V}$ is uncoupled acoustic modal impedance matrix and $\mathbf{q}$ is modal source strength vector and $\mathbf{q_s} = \mathbf{Cb}$. Where, C is matrix representing coupling coefficient $C_{n,m}$ between n^{th} acoustic mode and m^{th} structural mode. Coupling represents the spatial distribution of an acoustic mode on flexible surface.

Modal structural vibration velocity vector $\mathbf{b}$ given Eqs. (2.2) and (2.4) can be expressed in matrix form as,

$$\mathbf{b} = \mathbf{Y_s}(\mathbf{g} - \mathbf{g_a}) \tag{2.6}$$

$\mathbf{Y_s} = \frac{\mathbf{B}}{\rho_s h S_f}$, represents uncoupled structural mobility matrix and $\mathbf{g}$ is generalized modal force vector and $\mathbf{g_a} = \mathbf{C^T a}$. Using Eqs. (2.5) and (2.6), complex amplitude of acoustic and structural modes are given as,

$$\mathbf{a} = \left(\mathbf{I} + \mathbf{Z_a C Y_s C^T}\right)^{-1} \mathbf{Z_a}\left(\mathbf{q} + \mathbf{C Y_s g}\right) \tag{2.7}$$

$$\mathbf{b} = \left(\mathbf{I} + \mathbf{Y_s C^T Z_a C}\right)^{-1} \mathbf{Y_s}\left(\mathbf{g} - \mathbf{C^T Z_a q}\right) \tag{2.8}$$

When $\left(\mathbf{I} + \mathbf{Z_a C Y_s C^T}\right)^{-1} \sim \mathbf{I}$ or $\left(\mathbf{I} + \mathbf{Y_s C^T Z_a C}\right)^{-1} \sim \mathbf{I}$ or coupling matrix is zero matrix then Eqs. (2.7) and (2.8) calculates uncoupled system responses. Selection of strongly coupled acoustic and structural modes is done based on a transfer factor [18] which is given as,

$$T_{n,m} = \left(1 + \frac{(\omega_n^2 - \omega_m^2)\rho_s h S_f V}{4\rho_0 c_0^2 C_{n,m}^2}\right)^{-1} \tag{2.9}$$

$T_{n,m}$ can be interpreted as a transfer factor for n^{th} acoustic mode coupled to m^{th} structural mode.

2.2.2 Calculation of Sound power and Radiation efficiency

In this method, an unfolded equivalent plate representation is used to model the rectangular duct. Fig. 2.2 shows rectangular duct and its equivalent plate representation of dimensions L_c x L_a. Where, L_c is duct perimeter and L_a is duct length. The folded joint is modelled as a rotational spring (K_r) and creases of two adjacent plate panels are modelled as linear springs (K_t). Simply supported (SS) boundary condition is applied to equivalent plate boundaries along axial direction (i.e along y-axis at y=0 and L_a). Rayleigh–Ritz method is used to

calculate duct's uncoupled structural natural frequencies and mode shapes. The description of Rayleigh-Ritz model of an equivalent plate to calculate the uncoupled natural frequency of various axial boundary conditions is given in Ref. [5].
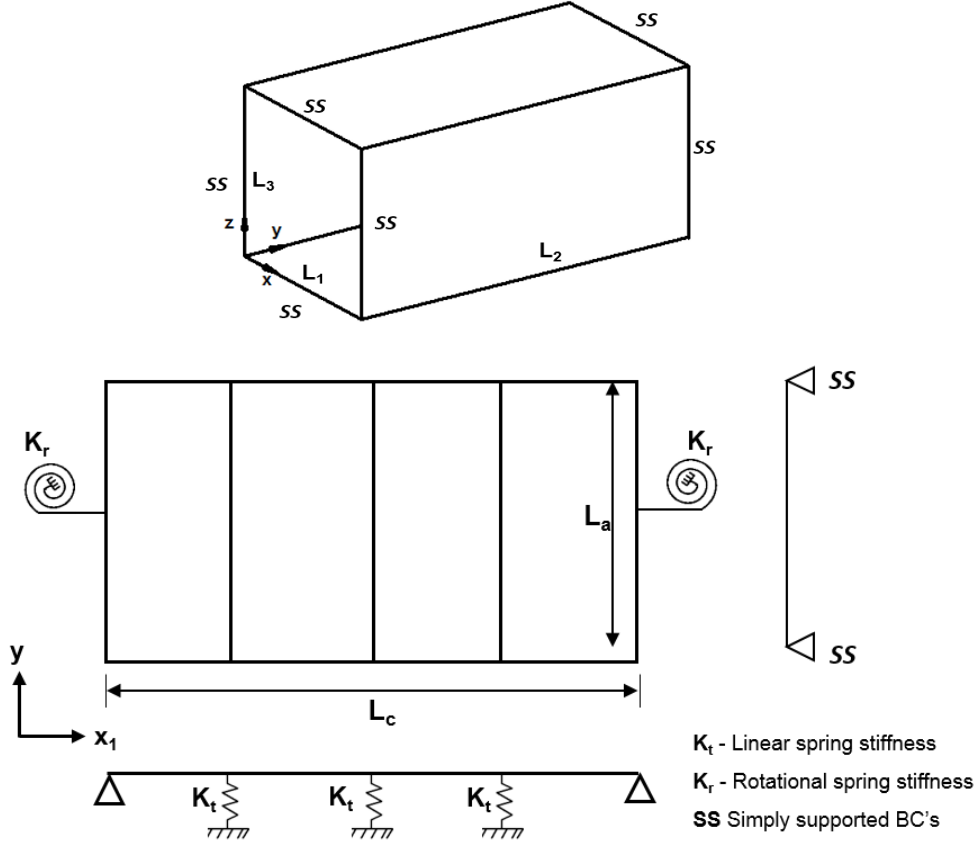
Figure 2.2: Equivalent plate representation of a rectangular duct with simply supported boundary condition.

Sound power radiated from duct walls is expressed in terms of modal amplitudes of vibration velocity **(b)** and radiation impedance matrix **[Z]**. It is given as follows,

$$W_{\text{rad}} = \frac{1}{2}\mathbf{b}^H Re[\mathbf{Z}]\,\mathbf{b} \tag{2.10}$$

Here, superscript 'H' is Hermitian transpose and *Re* indicate real value. Radiation impedance can be expressed in terms of Rayleigh integral as,

$$Re[Z_{m_1 m_2 m_1' m_2'}] = \frac{k}{2\pi} \int_0^{L_c} \int_0^{L_a} \int_0^{L_c} \int_0^{L_a} \sum_{m_1} \sum_{m_2} A_{m_1 m_2} \sin\left(\frac{m_1 \pi y}{L_a}\right) \sin\left(\frac{m_2 \pi x_1}{L_c}\right) * \ldots$$

$$\sum_{m_1'} \sum_{m_2'} A_{m_1' m_2'} \sin\left(\frac{m_1' \pi y'}{L_a}\right) \sin\left(\frac{m_2' \pi x_1'}{L_c}\right) \frac{\sin(kR)}{R} dx_1' \, dy' \, dx_1 \, dy \tag{2.11}$$

where, $R = \sqrt{(y - y')^2 + (x_1 - x_1')^2}$, $m_1', m_2', m_l,$ and m_2 are modal indices

(2.12)

The Eqn. (2.11) can be rewritten as

$$Re\big[Z_{m_1 m_2 m_1' m_2'}\big] = \frac{k}{2\pi} \sum_{m_1} \sum_{m_2} \sum_{m_1'} \sum_{m_2'} A_{m_1 m_2} A_{m_1' m_2'} I_{m_1 m_2 m_1' m_2'} \; , \quad (2.13)$$

Expression of integral I in Eq. (2.13) can be written as,

$$I_{m_1 m_2 m_1' m_2'} = \int_0^{L_c} \int_0^{L_a} \int_0^{L_c} \int_0^{L_a} \left(\sin\left(\frac{m_1 \pi y}{L_a}\right) \sin\left(\frac{m_2 \pi x_1}{L_c}\right) \sin\left(\frac{m_1' \pi y'}{L_a}\right) \sin\left(\frac{m_2' \pi x_1'}{L_c}\right) \frac{sin(kR)}{R} \right) dx_1' \, dy' \, dx_1 \, dy$$

(2.14)

Simplification of the quadruple integral of Eq. (2.14) is given in *Appendix-A*.

An analytical equation to calculate the modal radiation efficiency as a function of frequency for a given input sound source is given as [22],

$$\sigma_a = \frac{W_{rad}}{W_P} \tag{2.15}$$

$$W_P = \rho_0 c_0 S_f \langle \, \boldsymbol{w} \, \rangle^2 \tag{2.16}$$

where, W_{rad} is radiated sound power and W_P is plane wave sound radiation power by a piston source having same surface area of duct structure and vibrating with same root mean square velocity as the structure [22]. S_f is flexible duct wall area and is given by $L_a \, x \, L_c$, and vibration velocity of structure is given by $\langle \boldsymbol{w} \rangle^2$.

2.3   Numerical modelling

Numerical models based on FEM are developed to calculate uncoupled structural and acoustic natural frequencies. Both of these models are linked for coupled analysis. Fig. 2.3 shows the flowchart of the numerical modelling procedure to calculate sound power radiation, modal radiation efficiency, and quadratic velocity.
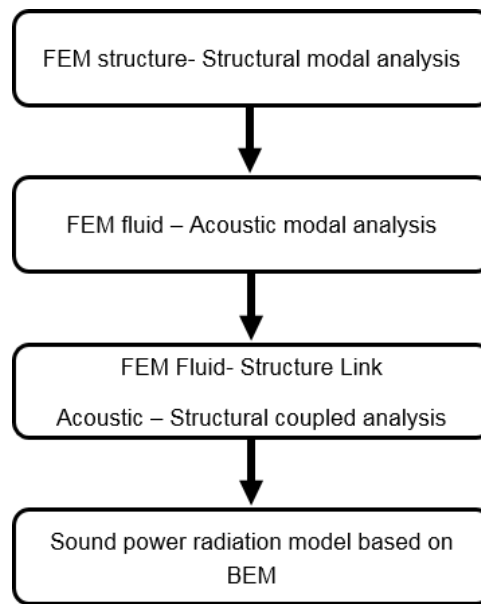
Figure 2.3: Flowchart of numerical model to estimate sound power radiation.

2.3.1   Uncoupled Structural Model

Figure 2.4 (a) shows a numerical model of a duct structure. A rectangular duct of dimensions 0.3 m x 0.4 m x 1.5 m (L_1=0.3, L_2=1.5, L_3=0.4) with duct wall thickness of 5 mm is modelled and meshed using SHELL-63 elements. Simply supported (SS) boundary condition are applied at both ends of the duct as shown in Fig. 2.4 (a). Aluminium material properties are applied to structure such as: density is 2770 kg/m^3, Young's modulus is 71 GPa, Poisson's ratio is 0.33 and structural damping ratio is 0.01.

2.3.2   Uncoupled Acoustical Model

An enclosed duct volume of dimensions 0.3 m x 0.4 m x 1.5 m is modelled and meshed using SOLID-185 elements as shown in Fig. 2.4(b). Acoustic medium (air) properties such as: speed of sound as 340 m/s, density as 1.225 kg/m^3, acoustic damping ratio of 0.01 are applied to acoustic volume. The boundaries of acoustic cavity are assumed to be rigid.
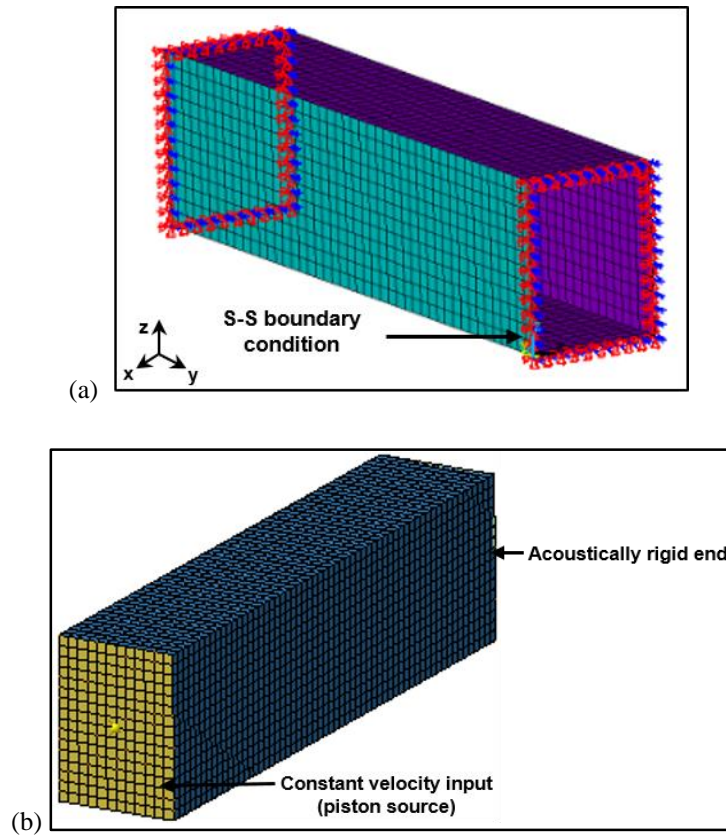
Figure 2.4: Numerical models to calculate the radiated sound power and radiation efficiency, (a) Structural model, (b) Acoustic model.

2.3.3   Acoustic-Structural Coupled Model

Coupled model considers structural (duct) and acoustic (cavity) domains and these are solved in FEM acoustic module of LMS virtual lab-13. A constant velocity piston source excitation is applied to the inlet face of an acoustic mesh, which as shown in Fig. 2.4(b). The coupled system of equations helps in determining structural displacements on flexible circumferential duct walls and its pressure inside the duct.

2.3.4   Calculation of Sound power radiation

A numerical model to calculate sound radiated from the flexible duct walls is shown in the Fig. 2.5. Total sound power radiated from duct walls is estimated using BEM acoustics exterior method. In first step of BEM, acoustic potentials such as pressure and particle velocity are solved on the boundary mesh. In order to determine sound radiated to the exterior of duct, acoustic potentials are solved on the field point mesh which is a virtual surface surrounding the BE mesh. It is assumed that, field point mesh is a non-reflecting surface where

wave just propagates and doesn't reflect. Fig. 2.5 shows boundary element mesh and field point mesh. Dimensions of field point mesh are 0.4 m x 0.5 m x 1.5 m.
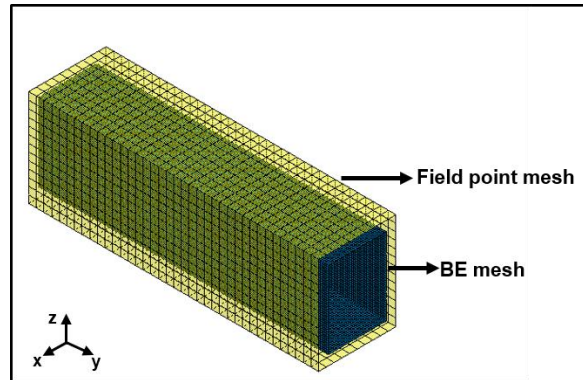
Figure 2.5: A numerical model to calculate the sound radiated from the flexible duct walls.

Modal radiation efficiency is calculated numerically by activating selected structural or acoustic modes. A theoretical study is performed to estimate radiation efficiency by choosing a different combination of structural and acoustic modes participation in sound radiation. However, two cases are discussed such as (i) a single acoustic mode can be coupled to multiple structural modes and (ii) single structural mode can be coupled to the multiple acoustic modes.

2.4   Results and discussion

Uncoupled structural modes of duct structure are calculated using the proposed equivalent plate model and compared to numerical results as discussed in Sec. 2.4.1. These uncoupled modes are classified into four groups based on net volume displacement and symmetry behaviour at a particular mode which is described in Sec. 2.4.2. The uncoupled acoustic modes are calculated using analytical model and compared to numerical results as shown in Sec. 2.4.3. Calculation of coupled modes and identification of strong coupling modes based on transfer factor are discussed in Sec. 2.4.4.

As next step, modal radiation efficiencies are calculated by an equivalent plate model for all four groups and validated with numerical results using a rectangular duct model. Sec 2.4.5 shows comparisons of radiation efficiency for strongly coupled modes. In Sec 2.4.6, duct modal radiation efficiencies calculated using the proposed method are compared to a simple rectangular plate available in the literature. Behaviour of radiation efficiency when single

acoustic mode coupled with multiple structural modes are studied and results are shown in Sec. 2.4.7. Sound radiation behaviour is also studied and shown in Sec. 2.4.8.

2.4.1 Uncoupled structural modes

Table 2.1 shows a comparison of analytical and numerical results of the first ten uncoupled structural natural frequencies of a simply supported rectangular duct. It is observed that analytical and numerical results are in a good agreement. An equivalent plate model is appropriate to explain the free vibration behaviour of a rectangular duct for further studies.

Table 2.1: First ten uncoupled structural modes of a rectangular duct with a simply supported boundary condition calculated with the proposed analytical and numerical model.

Mode	Analytical (Hz)	Numerical (Hz)
1	99.26	99.22
2	114.65	114.59
3	130.95	127.08
4	140.59	140.51
5	142.72	141.94
6	163.98	163.47
7	177.29	177.17
8	195.67	189.68
9	196.05	195.60
10	209.76	208.72

Structural modal analysis helps in understanding the displacement pattern of a structure subjected to a given boundary condition. Displacement pattern is expressed in terms of mode shape. Figures 2.6 (b) and (d) shows developed surface of rectangular duct and its mode shape. The perimeter of chosen duct dimensions is 1.4 m and length of 1.5 m. Figures 2.6 (a) and (b) shows a comparison of analytical and numerical model results of fundamental duct mode shape. Similarly, Figs. 2.6 (c) and (d) shows the 10th mode shape. Analytical mode shapes shown in Figs. 2.6 (b) and (d) are equivalent plate model results. It is observed from the Fig. 2.6 that both analytical and numerical model results have the same behaviour.
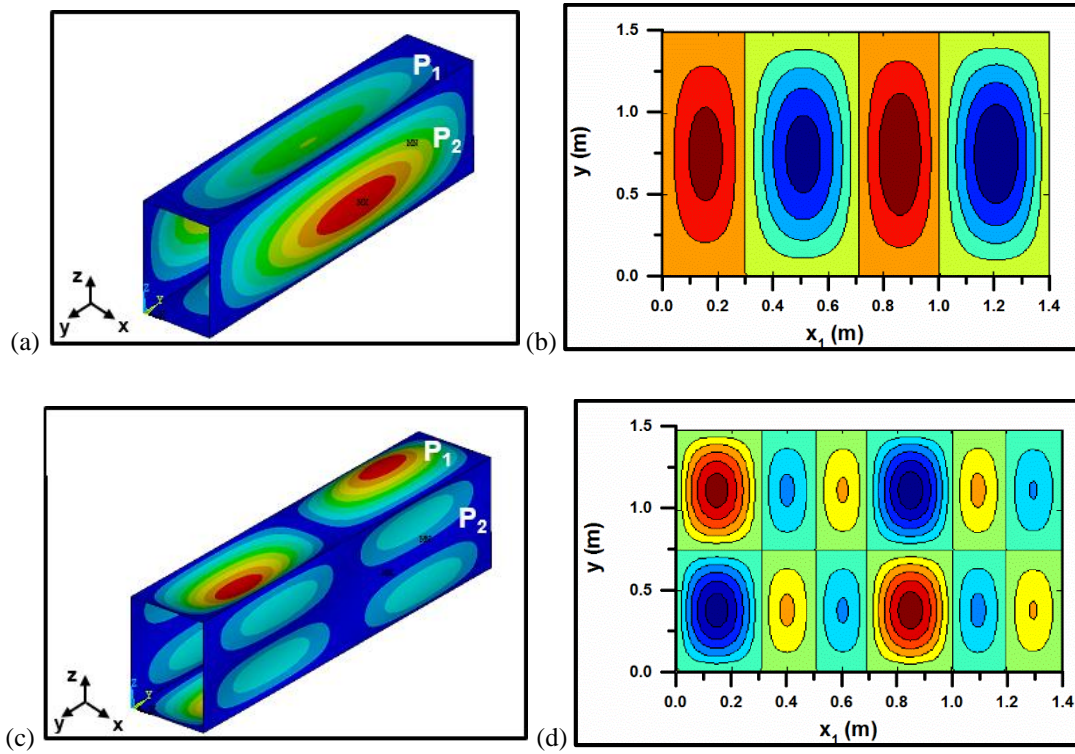
Figure 2.6: (a) Fundamental structural duct mode shape at 99.22 Hz-Numerical (b) Fundamental structural duct mode shape at 99.26 Hz-Analytical (c) Tenth duct mode shape at 208.72 Hz-Numerical (d) Tenth duct mode shape at 209.76 Hz-Analytical.

2.4.2 Mode shapes representation, grouping and calculating net volume displacement

Structural mode shapes of duct are analysed to understand the free vibration behaviour of rectangular duct, symmetry behaviour, and relative change of phase between panel pairs.

A particular notation has been followed to describe each mode shape in terms of natural frequency, number of anti-nodes on panel pairs and symmetry behaviour. Fundamental structural mode shape as shown in Fig. 2.6 (a) can be represented according to proposed notation as $[D\_S\,(1,\,1),\,S\,(1,\,1)]_{99.2}$ Hz. It can be described as follows: first term in the bracket indicates number of anti-nodes on x-panel pairs that is at $x=L_1$ (plate P_2) and $x=0$ (plate P_4) along y and z-directions and for given example, it is (1, 1) means one antinode in y and z directions. Second term indicates number of anti-nodes on z-panel pairs, that is, at $z=L_3$ (plate P1) and z=0 (plate P3) along x and y-directions and modal indices description is same as previously. Letter 'D' indicates dominating pair which can be identified by comparing modal

29

displacement amplitude between a pair of plate panels. Letter 'S' denotes symmetry of mode shape behaviour of duct walls and end number is modal frequency.

Similarly, 10th mode shape can be represented as [S (2, 2), D_AS (1, 2)] $_{209.72}$ Hz. Here, number of anti-nodes on x-panel pairs (that is on P_2 and P_4) are (2, 2) and number of anti-nodes on z-panel pairs (that is on P_1 and P_3) are (1, 2). Dominant amplitude (D) is on z-panel pair. Letter 'AS' denotes anti-symmetry mode shape behaviour of duct walls. So based on this proposed notation, modes are categorized into four groups based on mode symmetry and anti-symmetry behaviour. Group-1 represents Symmetry (S)-Symmetry (S) behaviour of x-axis pair and z-axis pair. Similarly, the other three groups are S-AS, AS-S, and AS-AS.

Net volume displacement for each uncoupled structural mode is calculated with Eq. (2.17). It helps to understand efficiently radiating sound modes and types of sound source.

$$V_i = \sum_{n=1}^{4}(\sum_m \Delta v_m)_n \tag{2.17}$$

Here, i represents mode number, n represents panel number varying from 1 to 4 which are considered as four walls of duct. Δv_m is volume displacement associated with amplitude displacement of mth element in n^{th} plate, i.e. each duct walls [22].

First, thirty modes of a simply supported rectangular duct are classified into four groups and net volume displacement of each mode is calculated according to Eq. (2.17). These results are given in Table 2.2. It is observed that modes in groups 2, 3 and 4 have zero net volume displacement. Modes with odd modal index in group-1 (odd, odd) have higher net volume displacement values than remaining modes in the group. Modes which have symmetrical panel pairs, and largest net volume displacement in group-1, are efficient sound radiators and also identified as monopole type of sound source. Modes having (odd, even) or (even, odd) mode shapes in group-1 behave as a dipole sound source and are less efficient sound radiators. It is observed by calculating radiation efficiency and their slope.

Table 2.2: Duct mode group classification and net volume displacements for each mode.

Groups	Mode No.	Mode description	Net volume displacement
Group-1	1	[D_S(1,1),S(1,1)]$_{99.2}$ Hz	0.1182
	2	[D_S(1,2),S(1,2)]$_{114.59}$ Hz	0
	4	[D_S(1,3),S(1,3)]$_{140.5}$ Hz	0.0421
	7	[D_S(1,4),S(1,4)]$_{177.17}$ Hz	0
	11	[D_S(1,5),S(1,5)]$_{224.69}$ Hz	0.0277
	14	[S(1,1)*,D_S(1,1)]$_{248.96}$ Hz	0.2630
	16	[S(1,2)*,D_S(1,2)]$_{259.43}$ Hz	0
	18	[S(1,3)*,D_S(1,3)]$_{278.08}$ Hz	0.0868
	19	[D_S(1,6),S(1,6)]$_{283.08}$ Hz	0
	21	[S(1,4)*,D_S(1,4)]$_{306.25}$ Hz	0
	23	[S(1,5)*,D_S(1,5)]$_{345.11}$ Hz	0.0512
	24	[D_S(1,7),S(1,7)]$_{352.37}$ Hz	0.0216
	29	[S(1,6)*,D_S(1,6)]$_{395.46}$ Hz	0
Group-2	3	[D_AS(1,1),S(2,1)]$_{127.08}$ Hz	0
	5	[D_AS(1,2),S(2,2)]$_{141.94}$ Hz	0
	6	[D_AS(1,3),S(2,3)]$_{163.47}$ Hz	0
	9	[D_AS(1,4),S(2,4)]$_{195.60}$ Hz	0
	13	[D_AS(1,5),S(2,5)]$_{239.22}$ Hz	0
	20	[D_AS(1,6),S(2,6)]$_{294.53}$ Hz	0
	25	[D_S(1,7),S(2,7)]$_{361.47}$ Hz	0
Group-3	8	[S(2,1),D_AS(1,1)]$_{189.68}$ Hz	0
	10	[S(2,2),D_AS(1,2)]$_{208.72}$ Hz	0
	12	[S(2,3),D_AS(1,3)]$_{233.06}$ Hz	0
	17	[S(2,4),D_AS(1,4)]$_{267.39}$ Hz	0
	22	[S(2,5),D_AS(1,5)]$_{312.34}$ Hz	0
	26	[S(2,6),D_AS(1,6)]$_{368.20}$ Hz	0
Group-4	27	[D_AS(2,2),AS(2,2)]$_{375.41}$ Hz	0
	30	[D_AS(2,3),AS(2,3)]$_{403.43}$ Hz	0

2.4.3 Uncoupled Acoustic modes

Uncoupled acoustical modes for the duct volume subjected to rigid termination boundary conditions are calculated analytically and numerically. Table 2.3 shows a comparison of first ten uncoupled acoustical modes of duct. First acoustical mode occurs when a wavelength matches with two times of largest dimension. In this case, it is 113.3 Hz in the longitudinal direction. It is observed that uncoupled acoustic modes estimated analytically and numerically are in a good agreement.

Table 2.3: First ten uncoupled acoustic modes of a rectangular duct volume with rigid end condition.

Mode No.	Analytical (Hz)	Numerical (Hz)
1	113.3	113.3
2	226.7	226.6
3	340	340
4	425	425
5	439.9	439.8
6	453.3	453.3
7	481.7	481.6
8	544.3	544.2
9	566.7	566.6
10	566.7	566.6

2.4.4 Comparison of coupled and uncoupled response

Sound pressure inside the duct is calculated both by an analytical and numerical method for coupled and uncoupled cases. Variation of sound pressure inside the duct at a location ($0.5 \times L_1$, $0.4 \times L_2$, $0.5 \times L_3$) with respect to frequency for coupled and uncoupled analysis are shown in Figs 2.7 (a) and (b), respectively. A good agreement between both analytical and numerical results is observed. It is observed from Fig. 2.7(b) that first peak in a pressure spectrum, based on an uncoupled model occurring at 113.3 Hz, corresponds to uncoupled acoustic mode. Similarly, two pressure peaks in the coupled model are observed at 105 Hz and 122 Hz. Energy exchange between acoustic and structural subsystems at coupling frequency converts to a multi-degree freedom system. Similarly, at 226 Hz it is divided into two coupled frequencies, each at 220 Hz and 228 Hz.
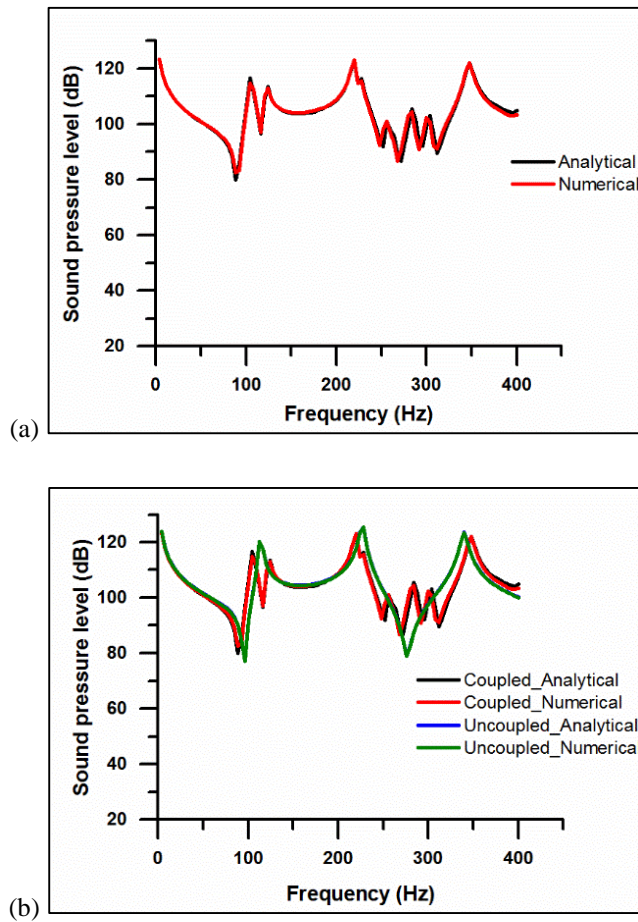
Figure 2.7: (a) Variation of inside duct pressure with respect to frequency for coupled analysis. (b) Comparison of uncoupled and coupled pressure inside the duct.

Table 2.4 gives first thirty coupled modes which are estimated numerically by coupled modal analysis. These coupled modes contain both acoustical and structural modes. It can be observed that coupling occurs close to acoustical modes.

Table 2.5 shows a comparison of uncoupled and coupled modes of a rectangular duct. It shows that an acoustic mode at 113.3 Hz and a structural mode at 114.59 Hz are strongly coupled, and a shift in a natural frequency leads to coupled modes at 105.36 Hz and 121.47 Hz. Similarly, acoustic mode at 226.6 Hz is coupled with structural mode at 224.69 Hz and leads to 219.39 and 226.30 Hz coupled modes. There also exists, a strong coupling of a structural mode at 345.1 Hz and an acoustical mode at 345 Hz which results in coupled modes at 343.82 Hz and 347.07 Hz

Table 2.4: Coupled modes of a rectangular duct.

Mode No	Frequency (Hz)	Mode No	Frequency (Hz)	Mode No	Frequency (Hz)
1	100.48	11	208.23	21	282.82
2	105.36	12	219.39	22	294.39
3	121.47	13	226.30	23	301.62
4	126.61	14	232.59	24	311.92
5	140.08	15	238.81	25	343.82
6	141.47	16	254.16	26	347.07
7	162.99	17	258.02	27	352.22
8	177.12	18	260.92	28	361.28
9	189.14	19	266.91	29	367.71
10	195.22	20	282.74	30	374.89

Table 2.5: Comparison of Uncoupled and Coupled modes of a rectangular duct.

Uncoupled Mode Frequency (Hz)	Mode type	Coupled mode Frequency(Hz)
99.22	structural	100.48
113.3	acoustic	105.36
114.59	structural	121.47
127.08	structural	126.61
140.51	structural	140.08
141.94	structural	141.47
163.47	structural	162.99
177.17	structural	177.12
189.68	structural	189.14
195.60	structural	195.22
208.72	structural	208.23
224.69	structural	219.39
226.6	acoustic	226.30
345.1	structural	343.82
345	acoustic	347.07

Table 2.6 shows transfer factor values for strongly coupled acoustic modes. Transfer factor values are close to one representing a strong coupling. It is observed from the table that a strong coupling exists between fundamental acoustic mode at 113.3 Hz and second structural mode at 114.59 Hz. Second acoustic mode (226.6 Hz) is strongly coupled to 11th, 14th, 18th (224.69 Hz, 248.96 Hz, 278.08 Hz) structural modes. Third acoustic mode is strongly coupled to 21st structural mode at 306.25 Hz. Generally, lesser difference in uncoupled acoustic and structural natural frequencies and good spatial matching of the mode shapes provide higher transfer factor values.

Table 2.6: Transfer factor values of strongly coupled acoustic modes.

Acoustic Mode (Hz)	Structural Mode (Hz)	Transfer Factor $T_{n,m}$
113.3	114.59	0.99
226.6	224.69	0.98
	248.96	0.66
	278.08	0.57
340	306.25	0.79

2.4.5 Calculation of radiation efficiency for strongly coupled structural modes

Based on transfer factor values, structural mode frequencies with highest transfer factor are identified and these coupled modes are considering for sound power radiation calculation and then radiation efficiency. Figure 2.8 shows radiation efficiencies of one structural mode coupled to multiple acoustic modes calculated both analytically and numerically. It shows that both analytical and numerical results are in good agreement. It is clear that the equivalent plate model can be used effectively to calculate modal radiation efficiency.

It observed from Fig. 2.8 that mode-14 (248.96 Hz) is the most efficient radiating mode followed by mode-1 (99.26 Hz). It also observed that the net volume displacement of mode-14 is large when compared to other modes (Table 2.2). This is due to substantial net volume displacement and symmetry between the panel pairs of mode-14 at 248.96 Hz. Similarly, structural modes (1, 11, 14, and 18) at 99.2 Hz, 224.69 Hz, 248.96 Hz and 278.08 Hz have the same kind of slopes, which is a characteristic observed in (odd, odd) mode. A slope of 20dB/ decade is observed in (odd, odd) modes. Individual groups such as S-S (group-1) with (odd-odd) indices are the effective sound radiators. Structural modes (2, 21) at 114.59 Hz and

306.25 Hz are (odd, even) modes, have a slope of 40 dB/decade. Table 2.7 shows slopes of strongly coupled structural modes and comparison of slopes for analytical and numerical models. It shows that both results are in good agreement.
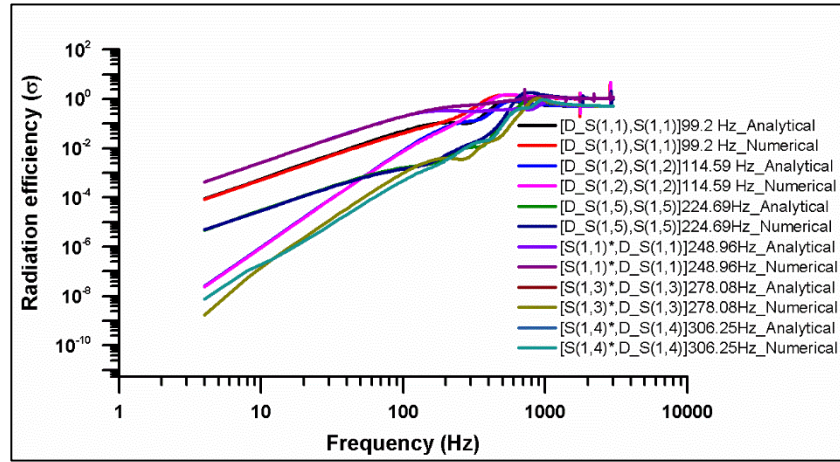
Figure 2.8: Modal radiation efficiency of the strongly coupled structural modes.

Table 2.7: Radiation efficiency slopes of a strongly coupled structural modes.

Mode	Frequency(Hz)	Analytical (dB/decade)	Numerical (dB/decade)
1	99.26	19.42	18.90
2	114.59	39.25	39.00
11	224.69	17.27	16.96
14	248.96	18.72	18.74
18	278.08	16.75	16.90
21	306.25	38.05	38.69

2.4.6 Comparison of duct radiation efficiencies with a plate

Radiation efficiency of a duct is compared to a plate radiation efficiency so as to understand the correlation and approximate duct sound radiation behaviour. A simply supported plate with equivalent dimensions of duct's perimeter and length is considered for comparison. Modal radiation efficiency for a simply supported rectangular plate can be calculated using analytical equations given in Ref. [35]. The critical frequency for a simply supported rectangular plate can be calculated using Eq. (2.18) as given in Ref. [35].

36

$$\omega_c = c_0^2 \left(\frac{\rho_s h}{D}\right)^{\frac{1}{2}} \qquad (2.18)$$

where, c_o is speed of sound, $\rho_s h$ is surface density and D is flexure rigidity.

Modal radiation efficiencies for duct are calculated for one structural mode coupled to multiple acoustic modes which exist within the critical frequency of equivalent plate. However, this frequency range is high as compared to the interested frequency range for breakout noise studies. These calculated radiation efficiencies are compared to radiation efficiency of a simply supported plate with dimensions of (1.4 m x 1.5 m). Figures 2.9 to 2.12 shows comparison of duct modal radiation efficiencies with plate modal radiation efficiency for four different groups.

Figure 2.9 shows the modal radiation efficiency comparison of (1, 1) plate with [D_S, S] group modes. All the modes in group-1 with (odd, odd) modal indices exhibit same slope of 20 dB/decade to that of a simply supported plate (1.4 m x 1.5 m) until the critical frequency. After that, the curve becomes asymptotic and radiation efficiency curve approaches unity.
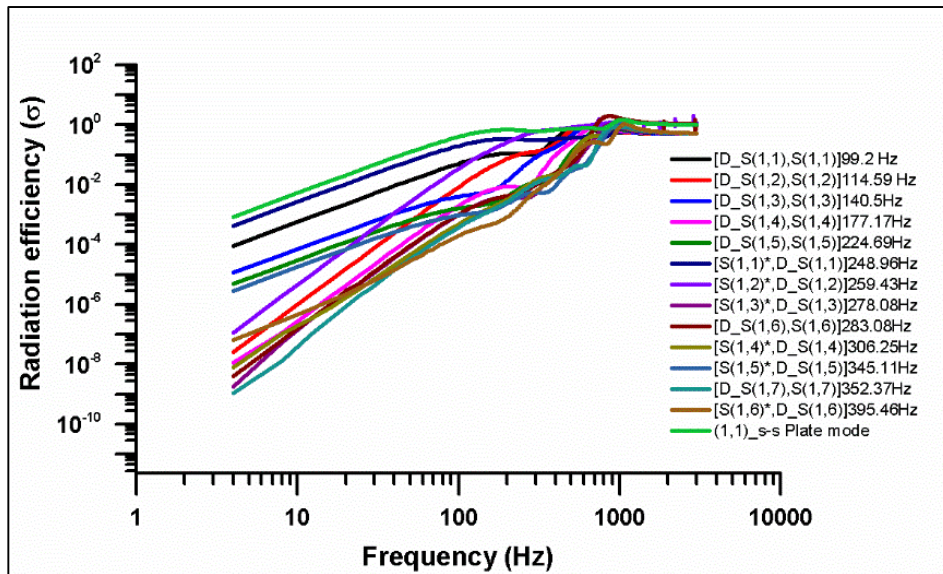
Figure 2.9: Calculation of duct modal radiation efficiency with respect to frequency for [(D_S, S)] group and plate mode (1, 1).

Figure 2.10(a) shows a variation of modal radiation efficiencies corresponding to [D_AS, S] group. It is observed that analytical and numerical results are in good agreement. It is consistent with the observation made based on volume displacement. However, the small peaks are observed at higher frequencies in duct radiation efficiencies due to numerical errors. Fig. 2.10 (b) shows a variation of modal radiation efficiencies corresponding to [D_AS, S]

group and comparison with that of a simply supported plate of (2, 1) mode. Slope of radiation efficiency in group-2 is high when compared to group-1. Similarly, volume displacement in group-2 is less compared to group-1. A plate with equivalent dimensions has the same slope as a duct with group-2 mode shapes, but it has a higher slope when compared to the lower mode in the same group. Slope behaviour of 40 dB/decade is observed until critical frequency, after that values approach unity and curve becomes asymptotic. It is also observed that radiation efficiency values are lower for higher modes when compared to the fundamental mode.

(a)

(b)
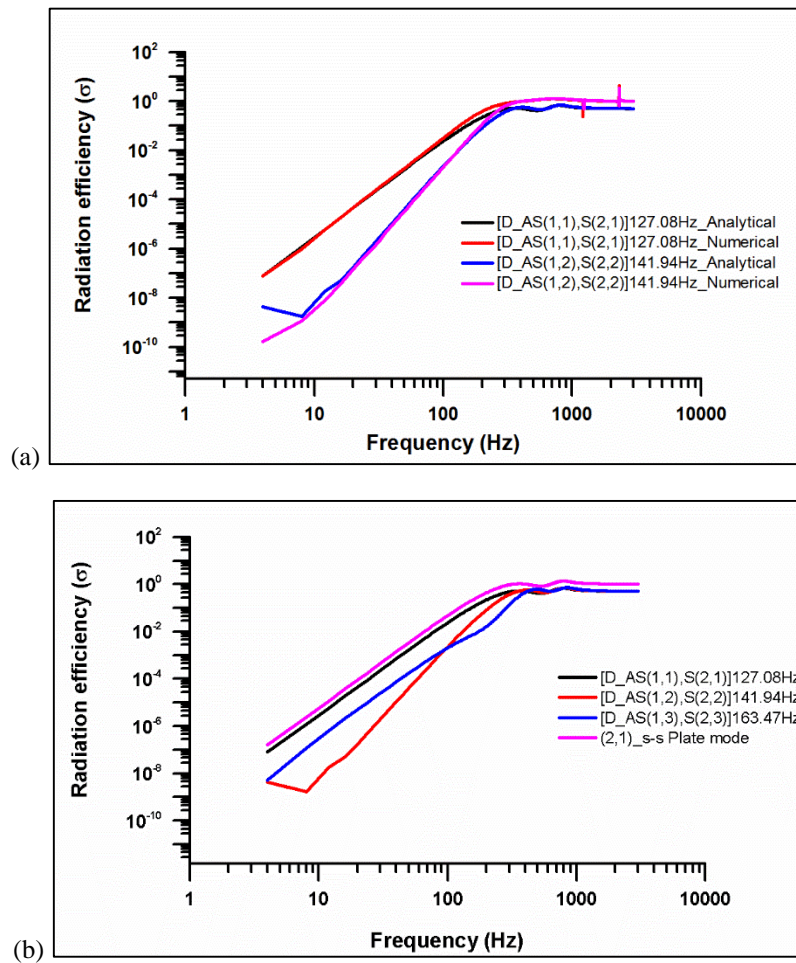
Figure 2.10: (a) Comparison of analytical and numerical model results for a duct Modal Radiation efficiency for [D_AS, S] group. (b) Calculation of duct modal radiation efficiency with respect to frequency for [D_AS, S] group and plate mode (2, 1).

Figure 2.11(a) shows a variation of modal radiation efficiencies corresponding to [S, D_AS]; Slope value of this group of modes is the same as [D_AS, S] group. It can be observed that analytical and numerical results are in good agreement. Fig. 2.11(b) shows a variation of

38

modal radiation efficiencies corresponding to [S, D_AS] and comparison with that of a simply supported plate of (1, 2) mode. Slope values of this group is the same as [D_AS, S] group. It exhibits that both groups have similar radiation curves. These groups have slope behaviour same as a simply supported plate (1, 2) mode with a value of 40 dB/decade until critical frequency.

(a)

(b)
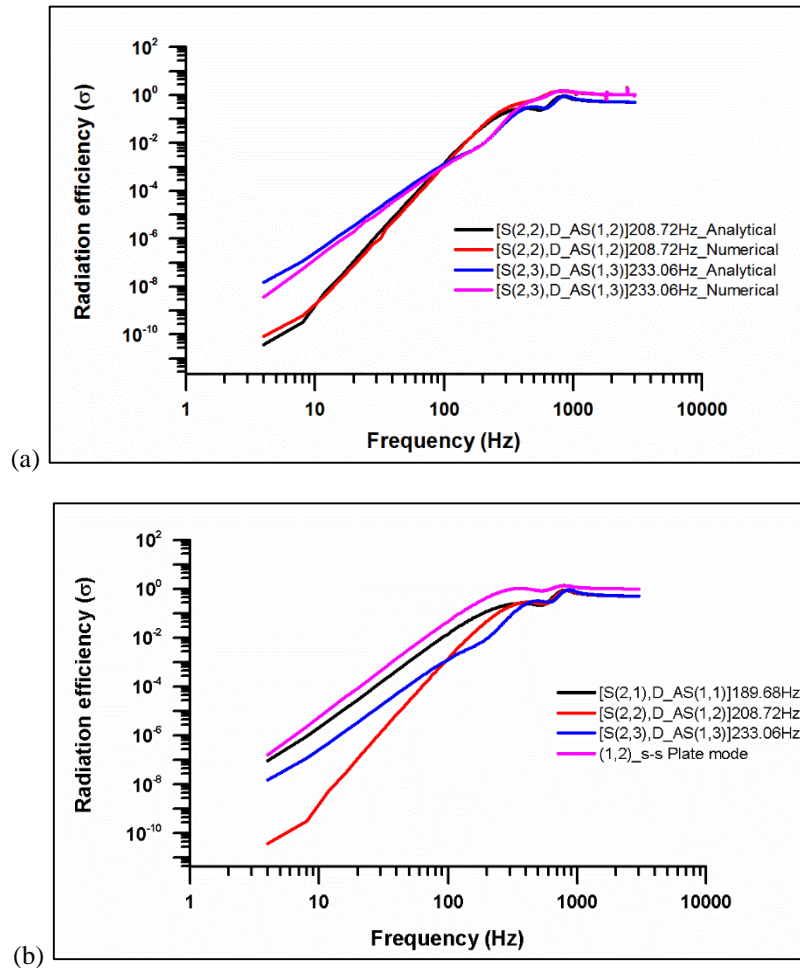
Figure 2.11: (a) Analytical and Numerical comparison of Modal Radiation efficiency for [S, D_AS] group. (b) Calculation of duct modal radiation efficiency with respect to frequency for [S, D_AS] group and (1, 2) plate mode.

Figure 2.12(a) shows a comparison of numerical and analytical modal radiation efficiencies corresponding to [D_AS, AS]. Fig. 2.12(b) shows a comparison of modal radiation efficiency of [D_AS, AS] group with simply supported plate mode of (2, 2). All the modes in this group have (even, even) modal indices and exhibit similar slope to that of a simply supported plate

(1.4 m x 1.5 m) with 60 dB/decade for the group (even, even) modal indices. Slopes of these curves are highest when compared to any other group.

(a)

(b)
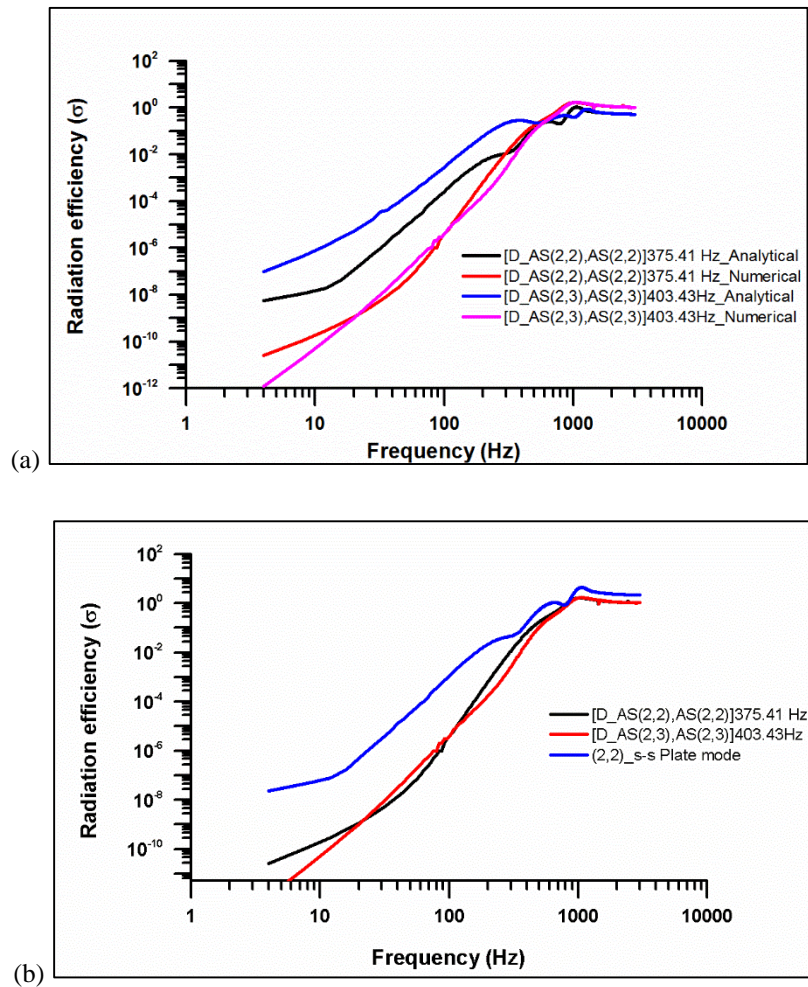
Figure 2.12: (a) Comparison of analytical and numerical model results for a duct Modal Radiation efficiency for [D_AS, AS] group. (b) Calculation of duct modal radiation efficiency with respect to frequency for ([D_AS, AS]) and (2, 2) plate mode.

Table 2.8 shows a comparison of slope values of all the four groups for a few selected duct modes and simply supported plate modes. Duct radiation efficiency slope values of all groups are the same as an equivalent plate. It can be observed from Figs 2.9 to 2.12, that radiation efficiency curves for single structural mode coupled to multiple acoustic modes and plate mode behaviour are found to be similar. Therefore, it can be concluded that duct radiation efficiencies of different groups can be calculated based on an equivalent plate model with minimum error. Equivalent plate model for a rectangular duct proposed in this research work

is an appropriate way to predict the free vibration behaviour and sound radiation characteristic of a duct.

Table 2.8: Comparison of the radiation efficiency slopes for duct modes and simply supported plate modes.

Group	Duct Mode	Duct mode Analytical (dB/decade)	Duct mode Numerical (dB/decade)	S-S Plate mode (dB/decade)
1	[D_S(1,1),S(1,1)]99.2 Hz	19	19	19
2	[D_AS(1,1),S(2,1)]127.08Hz	41	41	39
3	[S(2,3),D_AS(1,3)]233.06Hz	37	39	39
4	[D_AS(2,2),AS(2,2)]375.41Hz	57	58	54

2.4.7 Calculation of radiation efficiency for one acoustic mode coupled to multiple structural modes

In order to understand the effect of coupling closer to an acoustic mode, case of one acoustic mode is coupled to multiple structural modes has been studied. Figure 2.13 shows radiation efficiency of three acoustic modes such as 113, 226 and 339 Hz frequencies that are individually coupled to all structural modes with respect to frequency. It can be observed that both analytical and numerical results are in good agreement.
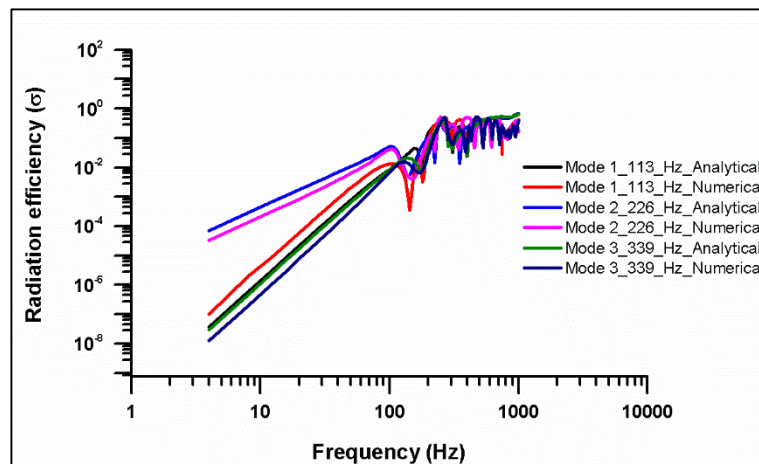
Figure 2.13: Radiation efficiency of the first three acoustic modes coupled with multiple structural modes (Numerical v/s Analytical).

2.4.8 Total radiation efficiency and Radiated sound power

Figures 2.14 and 2.15 shows total radiation efficiency and sound power radiated from multiple acoustic modes when coupled with multiple structural modes. All peaks in sound power curve are associated with coupled modes. First peak in the total sound power curve occurs at fundamental acoustic mode 113.3 Hz. Second prominent peak in curve occurs close to second acoustic mode at 226.6 Hz where acoustic energy is exchanged between three structural modes. Third prominent peak occurs close to third acoustic mode at 340 Hz. It is observed that second acoustic mode is more efficient in radiating sound due to strong coupling amongst three structural modes as compared to other two acoustical modes.
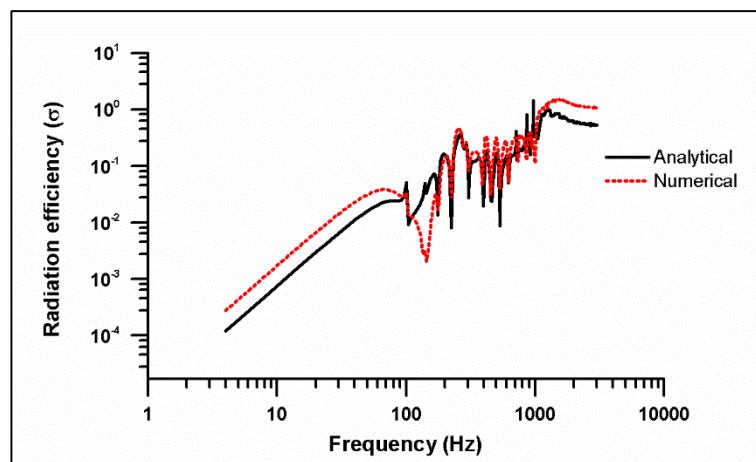
Figure 2.14: Total radiation efficiency of the rectangular duct (Numerical v/s Analytical).
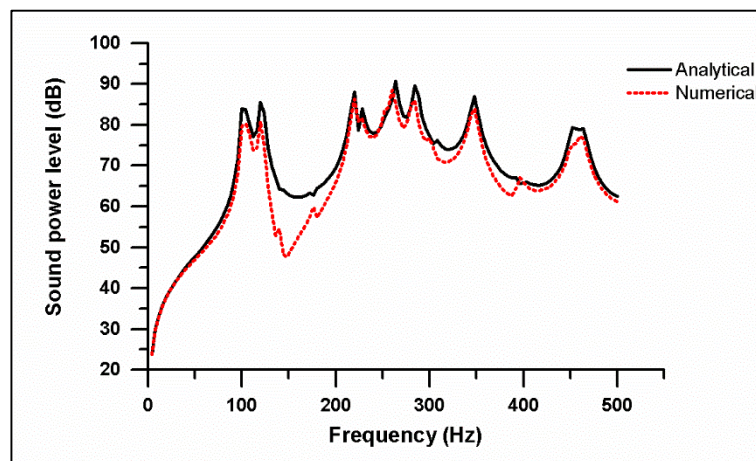
Figure 2.15: Total sound power radiated from the rectangular duct.

Figure 2.16 represents pressure distribution at a point on x-panel (x=0.35m, y=0.75m, z=0.25m) and z-panel (x=0.15m, y=0.75m, z=0.45m), respectively. All the peaks correspond to coupled frequencies. Figure 2.17 represents numerical results of the sound radiation pattern

of first three coupled acoustic modes at 113 Hz, 226 Hz, and 340Hz. For third acoustic mode, radiation pattern is similar to structural mode shape (306 Hz), where a strong coupling is observed and has a dipole behaviour.
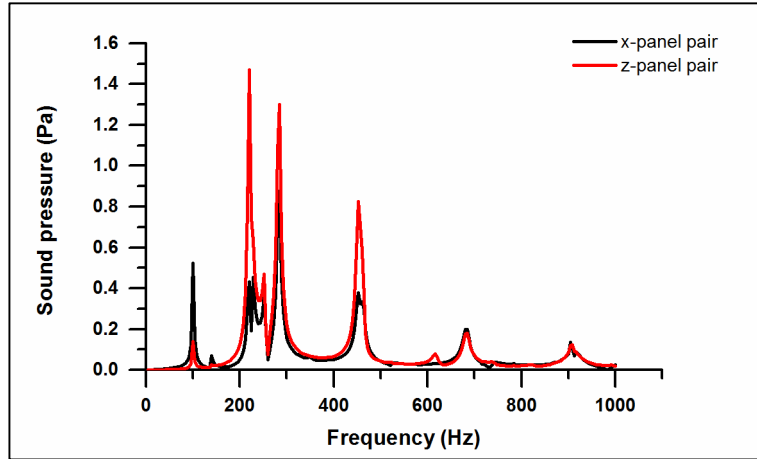
Figure 2.16: Sound pressure at field point on x-panel pair (0.35m, 0.75m, 0.25m) and z-panel pair (0.15m, 0.75m, 0.45m).

(a)   (b)

(c)
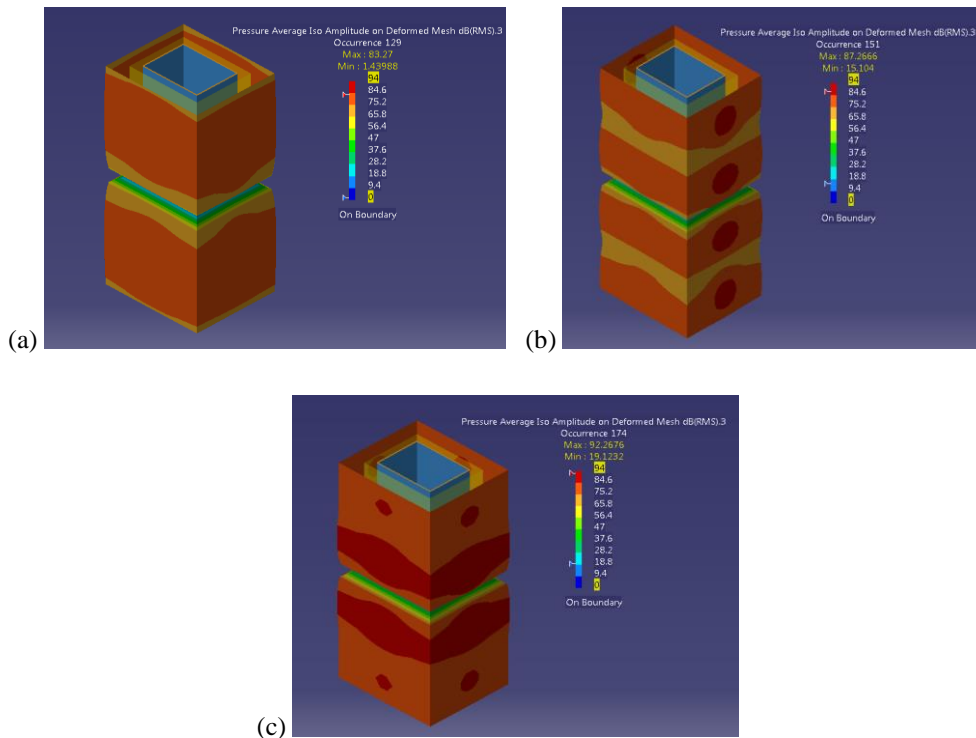
Figure 2.17: Sound radiation pattern of the first three coupled acoustic modes at 113 Hz, 226 Hz, and 340Hz.

43

It is observed from previous results that both analytical and numerical results are in good agreement to capture the acoustic and structural behaviour of both coupled and uncoupled sub-systems. Modal grouping based on free-vibration study shows that group-1 (Symmetry-Symmetry) modes with (odd-odd) indices are more effective sound radiators and thus justified based on radiation efficiency results. The proposed equivalent plate model for rectangular duct can be effectively used to predict the free vibration behavior and sound radiation characteristics.

2.5 Summary

Analytical and numerical models for calculating sound radiation characteristics of a rectangular duct have been discussed. Predicted results from the two models are in good agreement. It has been verified that rectangular duct can be modelled as an equivalent plate for free vibration analysis. Uncoupled structural duct modes have been categorized into four different groups and it was found that Symmetry-Symmetry mode group with (odd, odd) modal indices behave as efficient sound radiators. These were determined from higher net volume displacement of (odd, odd) modes when compared to others.

Effect of acoustic and structural mode coupling on radiation efficiency has been studied and compared to a simply supported plate behaviour. The slope of radiation efficiency curves for four duct mode groups has been compared to simply supported plate curves. It has been shown that sound radiation efficiency of the rectangular duct is similar to a plate of equivalent dimensions. There is a scope to relate duct radiation characteristics to simple rectangular plate characteristics. The plate formulation simplifies to estimate the breakout noise prediction in early design stage with less computational time.

An analytical model of the total sound power radiated from duct walls has been validated with numerical results. Duct radiation pattern is also calculated and observed that which are similar to standard sound sources such as monopole and dipole.

Chapter 3

Measurement of Breakout Noise Characteristics

3.1   Introduction

Measurement of transverse transmission loss (TTL) helps in understanding of efficient sound radiating modes and dominant vibration pattern. In the literature, methods available to measure duct's TTL are pressure based which require standard environments such as reverberation or anechoic chambers. However, in the present work, sound intensity techniques are implemented to measure the breakout noise of a flexible rectangular duct, which can be performed in a normal environment. The measured transverse transmission loss results are used to validate the "equivalent unfolded plate" analytical model. These results are also compared with numerical results obtained by Finite Element Method (FEM) and Boundary Element Method (BEM).

An experimental test setup is developed to measure input and radiated sound power along with vibration displacement and particle velocity. Using the obtained input and radiated sound power, transverse transmission loss (TTL) and radiation efficiency are calculated. Input sound power is calculated by using an autospectrum of a progressive pressure wave. Radiated sound power is measured using two different methods, namely- intensity probe method (P-P method) and Microflown technique (P-U method).

3.2 Calculation of TTL

Transverse transmission loss (TTL) is defined as a ratio of input power (W_i) to radiated power (W_r), and is given as [1],

$$TTL = 10 \log_{10} \left({W_i}/{W_r} \right) \tag{3.1}$$

3.2.1 Determination of input sound power

Input sound power given to the duct can be determined by calculating an autospectrum of forward progressive plane wave and is given by the following equation,

$$W_i = \frac{H_{AA}}{2\rho_0 c_0} A_s \qquad (3.2)$$

where, H_{AA} is an autospectral density of progressive wave, A_s is cross-sectional area of a cylinder, ρ_0 is air density and c_0 is speed of sound. An autospectrum of input power signal can be calculated by measuring sound pressure signal inside the cylinder at two microphone locations separated by a fixed known distance.

The sound pressure $p(z, t)$ at any location inside the cylinder is given by following Eq. (3.3) [107],

$$p(z, t) = A(f)e^{j(\omega t - kz)} + B(f)e^{j(\omega t + kz)} \qquad (3.3)$$

where, k is wave number, z is axial direction co-ordinate, between two microphones, ω is angular frequency, t is time and $A(f)$, $B(f)$ are amplitudes of progressive wave and reflective wave as a function of frequency, respectively. Applying the Fourier transform to pressure equation as given in Eq. (3.3) at two microphone positions over time T gives P_1 and P_2 as,

$$P_1(f, T) = A(f, T)e^{-jkz_1} + B(f, T)e^{jkz_1} \qquad (3.4)$$

$$P_2(f, T) = A(f, T)e^{-jkz_2} + B(f, T)e^{jkz_2} \qquad (3.5)$$

An autospectrum and crosspectrum of pressure signals at microphone positions 1 and 2 can be calculated by using Eqs. (3.4) and (3.5), which are given as follows,

$$H_{11}(f) = H_{AA}(f) + H_{BB}(f) + 2\{M_{AB}(f)\cos(2kz_1) + N_{AB}(f)\sin(2kz_1)\} \qquad (3.6)$$

$$H_{22}(f) = H_{AA}(f) + H_{BB}(f) + 2\{M_{AB}(f)\cos(2kz_2) + N_{AB}(f)\sin(2kz_2)\} \qquad (3.7)$$

$$Re\{H_{12}(f)\} = M_{12}(f) = H_{AA}(f)\cos\big(k(z_1 - z_2)\big) + H_{BB}(f)\cos\big(k(z_1 - z_2)\big) +$$
$$M_{AB}(f)\big[2\cos\big(k(z_1 + z_2)\big)\big] + N_{AB}(f)\big[2\sin\big(k(z_1 + z_2)\big)\big] \qquad (3.8)$$

$$Imag\{H_{12}(f)\}N_{12}(f) = -H_{AA}(f)\sin\big(k(z_1 - z_2)\big) + H_{BB}(f)\sin\big(k(z_1 - z_2)\big) \qquad (3.9)$$

$H_{AA}(f)$ and $H_{BB}(f)$ are the autospectral densities of $A(f)$ and $B(f)$, respectively. $H_{AB}(f)$ is the cross-spectral density between $A(f)$ and $B(f)$. Its real and imaginary values are represented as M_{AB} and N_{AB}. By solving Eqs. (3.6) to (3.9), the expression for autospectrum of forward progressive (H_{AA}) can be written as,

$$H_{AA} = \frac{1}{4}\text{cosec}(ks)[-2M_{12}\text{cot}(ks) + \text{cosec}(ks)\, 2N_{12}\text{sin}(ks) + H_{11} + H_{22}] \qquad (3.10)$$

Once autospectrum of forward progressive is calculated, then by using Eq. (3.2), input sound power can be calculated. Here, s is distance between two microphones in cylindrical tube.

3.2.2   Determination of radiated sound power

Sound power radiated from the duct wall surface is determined by using, measured intensity over the virtual surface area and can be written as [108],

$$W_r = I\, A_d \qquad (3.11)$$

where, A_d is duct surface area and I is sound intensity measured by two different methods such as the intensity probe method and the Microflown technique. The details of the measurement setup and procedure are given in section 3.4.

3.2.3   Radiation efficiency

Sound radiation efficiency (σ_e) of duct walls can be calculated using the radiated sound power and experimentally measured surface velocity and is given as [108],

$$\sigma_e = \frac{2W_r}{S_s\, \langle v \rangle^2\, \rho_0 c_0} \qquad (3.12)$$

where, W_r is radiated sound power, S_S is scanning surface area, $\langle v \rangle^2$ is mean square surface velocity on the structure, ρ_0 is air density, c_0 is velocity of sound.

3.2.4   Analytical method

An analytical model discussed in Chapter-2 for a rectangular duct with flexible walls is considered for the comparative study. In this model, sound pressure field inside the duct and normal vibration on the duct surface are calculated using impedance-mobility compact matrix

approach. The sound power radiated from a flexible duct wall is calculated using an "equivalent unfolded plate" model. Figure 3.1 shows the schematic diagram of a rectangular duct with four walls flexible. L_1, L_2, and L_3 are the dimensions of the duct along x, y and z co-ordinate system, respectively. An acoustic input source is given at inlet of the duct (i.e. at y=0) and another end is acoustical rigid termination (i.e. at y= L_2). A constant velocity excitation is applied at an inlet side of a duct.
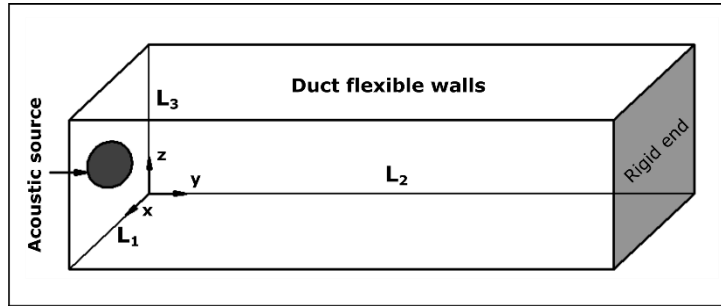
Figure 3.1: Schematic diagram of a flexible rectangular duct with one end acoustic excitation and another end rigid termination.

Sound power radiated from the piston source having same surface area of the duct structure and vibrating with same root mean square velocity as the structure $\langle w \rangle$ is given as [22],

$$W_\mathrm{P} = \frac{1}{2}\rho_0 c_0 S_f \langle w \rangle^2 \tag{3.13}$$

Sound power radiated from an unbaffled rectangular plate in terms of the complex phasor of vibration velocity vector (**b**) and radiation impedance matrix [**Z**] can be expressed as [14],

$$W_\mathrm{rad} = \frac{1}{2}\mathbf{b}^\mathrm{H} Re[\mathbf{Z}]\,\mathbf{b} \tag{3.14}$$

3.3 Numerical model

Finite-Element Method (FEM) and Boundary Element Method (BEM) are used to calculate the input sound power, radiated sound power and transverse transmission loss. Fig. 3.2 shows the numerical models developed for coupled analysis and radiated sound power calculations.

Coupled analysis considers structural (duct) and acoustic (cavity) models as shown in the Fig. 3.2(a). To create the structural model, an ideal rectangular duct of dimensions 0.3 m x 0.4 m x 1.2 m with wall thickness of 1.01 mm without any joints is modelled and meshed using 2D shell elements. Galvanized iron (GI) material properties such as: density as 7800 kg/m³,

48

Young's modulus as 210 GPa, Poisson's ratio of 0.3 and structural damping ratio of 0.01 are applied to the structure. A simply supported boundary condition is applied at both ends of the duct. An acoustic cavity of dimensions 0.3m x 0.4m x 1.2m is modelled and meshed with 3D solid elements. Air properties such as: speed of sound as 340 m/s, density as 1.225 kg/m^3, acoustic damping ratio of 0.01 are applied. A constant velocity piston source excitation is used as input sound source. Coupling is created between the flexible duct wall structure and acoustic cavity surfaces and solved by using coupled FEM module of LMS virtual lab-13. This analysis predicts the sound pressure inside the duct and structural displacements on the four flexible duct walls. Here, modal analysis is also performed for calculating the coupled and uncoupled modal parameters.
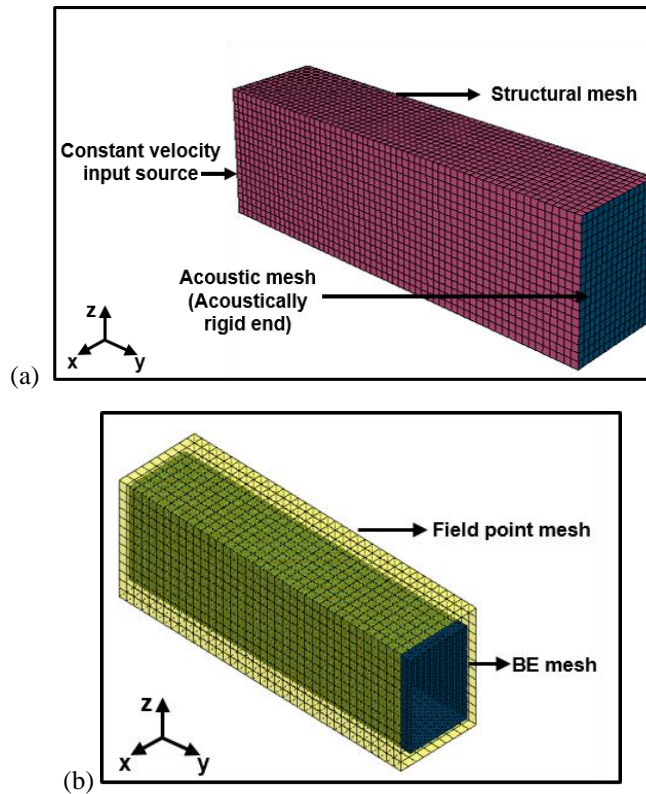
Figure 3.2: Numerical models for coupled analysis and sound radiation prediction (a) Acoustic and structural mesh for coupled analysis, (b) Field point mesh and boundary element mesh to calculate the radiated sound power.

Sound power radiated from four flexible walls of the duct is calculated using BEM acoustics exterior method. Structural displacement obtained from the coupled analysis is used as an acoustic boundary condition to estimate sound power radiated from the duct. Sound power is calculated on the virtual surface surrounding the BE mesh with an assumption that it is a non-

reflecting surface and as shown in the Fig. 3.2(b). Dimensions of field point mesh are 0.4 m x 0.5 m x 1.2 m.

Once the input and radiated sound power are estimated by FEM-BEM analysis, the transverse transmission loss is calculated by using the Eq. (3.1). Radiation efficiency is also calculated numerically using Eq. (2.15).

3.4 Experimental set-up and measurement procedure

3.4.1   Input and radiated sound power measurement

Experimental setup to measure input and radiated sound power is shown in Fig. 3.3. A speaker is attached to a cylindrical tube (with dimension of 0.1m diameter) to generate plane wave excitation as an input source to the duct. The specifications of the speaker are: 0.102m diameter, 20W power, 8Ω impedance with the working frequency range of 20-8000 Hz. A rectangular duct made up of galvanized iron (GI) sheet (with dimensions 0.3 m x 0.4 m x 1.2 m and 20 gauge (1.01 mm) thickness) is considered in the present study. Duct is fabricated by bending a rectangular sheet at three corners and edges joined with Pittsburgh locking mechanism. Simply supported (SS) boundary condition is applied at both ends of the duct and is established by making a point contact with the steel balls in a rectangular frame as shown in the Fig. 3.3(b).

The cut-off frequencies for plane wave propagation in the chosen cylindrical and rectangular ducts are 1991.4 Hz and 425 Hz, respectively. Since, breakout noise is predominant at lower frequencies, up to 400 Hz is considered for analysis in the present study.

Figure 3.4 shows the schematic diagram to measure the input sound power provided to a rectangular duct with speaker excitation. Progressive and reflecting pressure waves in the cylindrical tube are represented as "*A* and *B*". Two different microphones (of IEPE type) are used to measure the sound pressure at two positions (1 and 2 as shown in Fig. 3.4) which are separated by a distance of 0.3 m.

(a)

(b)
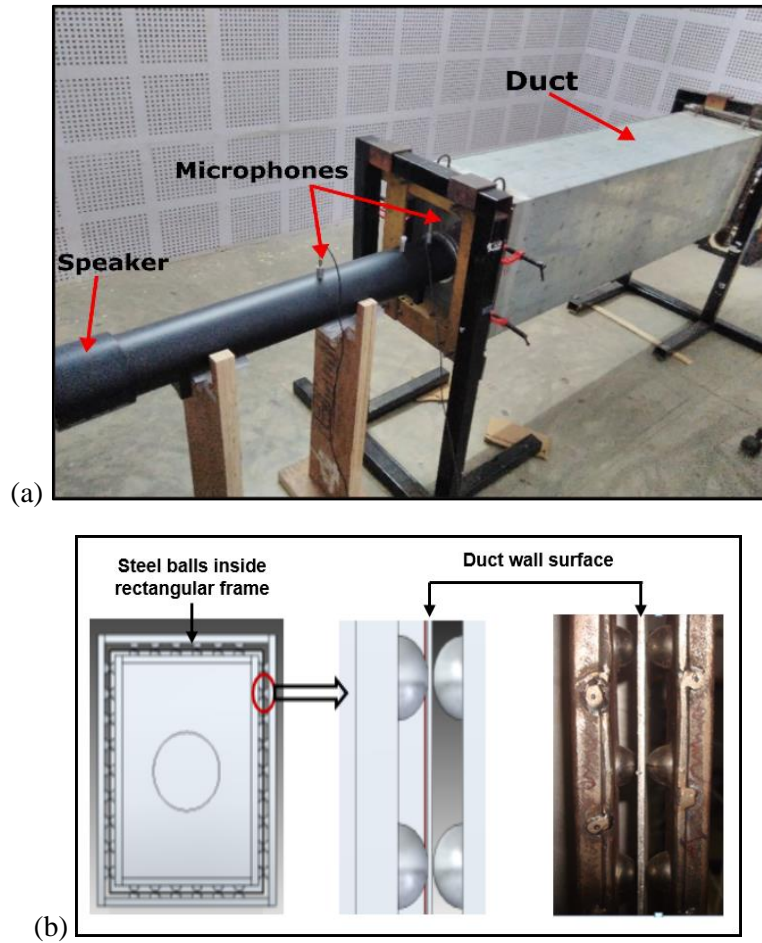
Figure 3.3: (a) Experimental setup for measuring input and radiated sound power measurement, (b) Simply supported boundary condition.
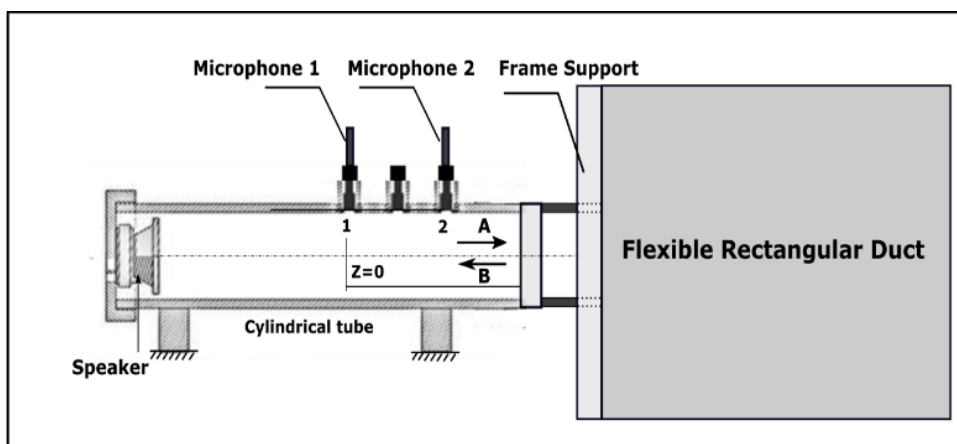
Figure 3.4: Schematic diagram of input sound power measurement setup.

Radiated sound power from all four flexible surfaces of a duct is measured by two different methods such as P-P (pressure–pressure) and P-U (pressure-velocity). The experimental arrangements for both methods are shown in Figs. 3.5 and 3.6. In both the cases, measurement was done with different scanning pattern and it is verified that the repeatability is good.

The intensity probe method (P-P) measures radiated sound pressure with two matched microphones separated by a spacer, over a virtual surface as shown in Fig. 3.5. In the present study spacer with 50mm length and ½ inch diameter is used to measure up to 1.25 kHz frequency. Intensity probe (Brüel & Kjær (B&K) of type 2270) is calibrated using sound intensity calibrator type B&K 4297 for amplitude of the sound pressure and phase difference between the microphones. Error in sound power, due to phase mismatch, is expressed in terms of pressure-residual intensity (p-RI) index. According to international standard IEC 1043, the p-RI index should be as high as possible. It should be at least 17 dB above 125 Hz for the microphone separation distance of 50mm [109]. So in present case p-RI index is 23.5 dB above 125 Hz after calibration of the intensity probe.
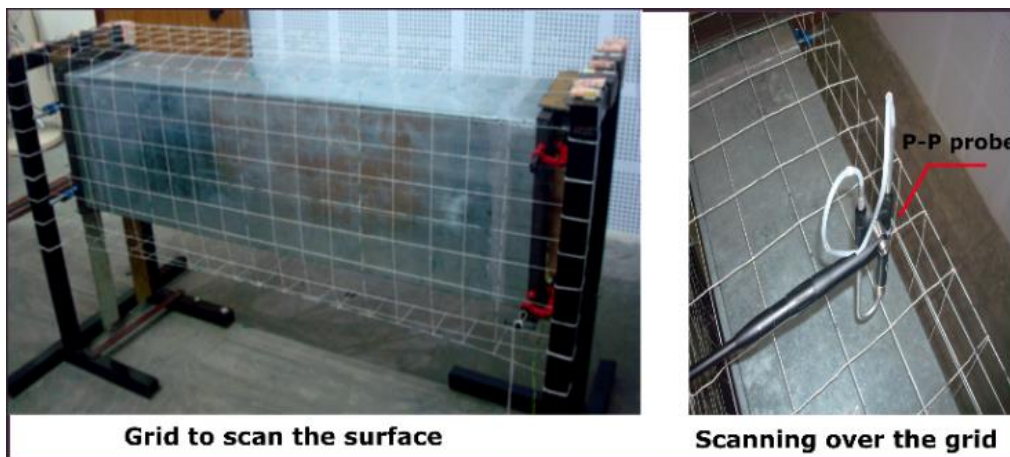
Figure 3.5: Experimental setup for sound power measurement by intensity probe method (P-P method).

Microflown technique (P-U) measures both sound pressure and particle velocity near the duct surface as shown in Fig. 3.6. A high sensitivity Microflown probe containing both pressure and velocity sensors is used for scanning the duct surface. The distance from the duct surface for scanning is chosen based on reactivity (ratio of reactive intensity to active intensity), which should be less than 7 dB to obtain good measurements [110]. Based on different measurements, a distance of 0.08m from the duct surface is used in the present study. The radiated sound power from all four flexible surfaces of a duct is obtained by using sound intensity over the measured surface area.
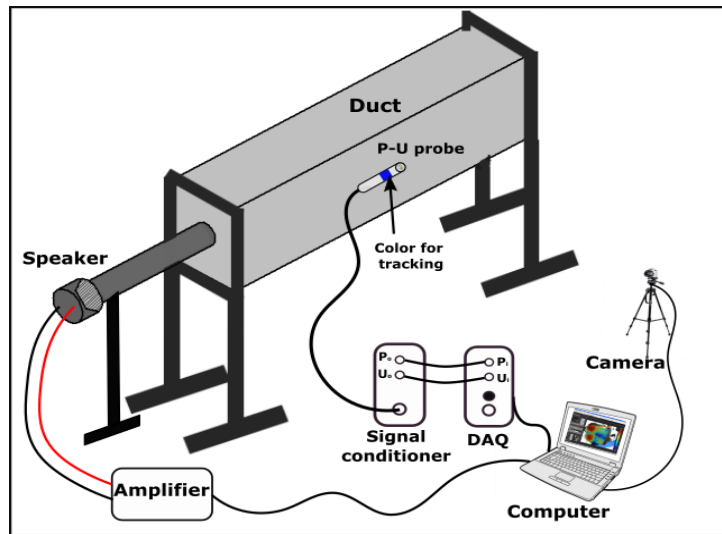
Figure 3.6: Experimental setup for sound power measurement by Microflown technique (P-U method).

3.4.2 Directivity measurement

Plane-wave excitation given to the duct is verified for two different cases using measurements and numerical simulations. In the first case, directivity measured in a plane parallel to the cross-section of cylindrical tube without test duct attachment. Sound pressure distribution inside the test configuration as shown in Fig. 3.3(a) is simulated using numerical models as a second case.

The schematic diagram of an experimental setup for directivity measurement is shown in Fig. 3.7. The measurement plane has a dimension of 0.5 m radius at a distance of 0.6 m from the cylindrical tube end. Sound pressure levels were measured with a sound level meter at 12 locations in the plane at an equal angle interval of 30^0. Two tonal sounds at 141 Hz, 220 Hz, and one random signal are used as input sound signals for the directivity test.
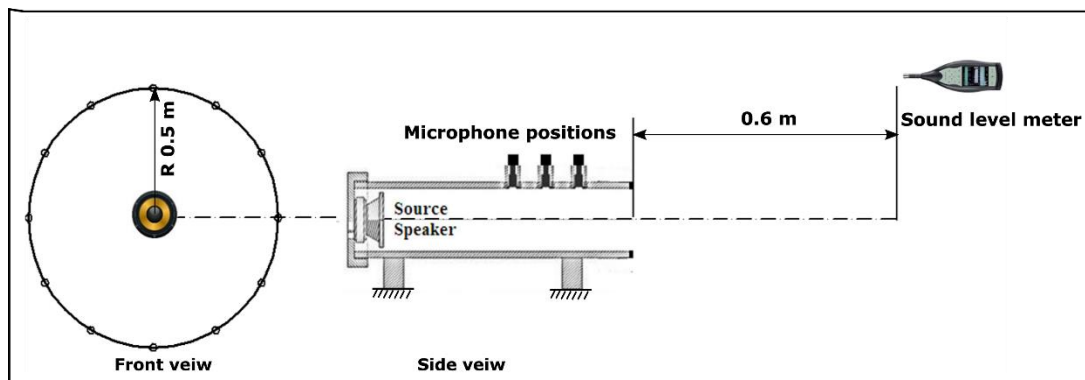
Figure 3.7: Schematic diagram of input source directivity measurement setup without test duct attachment.

3.4.3   Vibrations measurement

Vibrations on the duct walls surface are measured with an accelerometer and using measured acceleration data, vibration velocity and displacement are calculated. High sensitivity and low weight sensors are used for acquiring the vibration data. Measurements are taken at the mid-section of a duct ($0.5L_2$). Five measuring points are considered on each duct surface. The schematic diagram of test setup used for vibration measurement is shown in Fig. 3.8. A speaker attached to the cylindrical tube is used as a source for excitation of the duct and simultaneously vibration generated on flexible walls of the duct is measured from 10-400 Hz (frequency range) by accelerometers mounted on the duct wall.
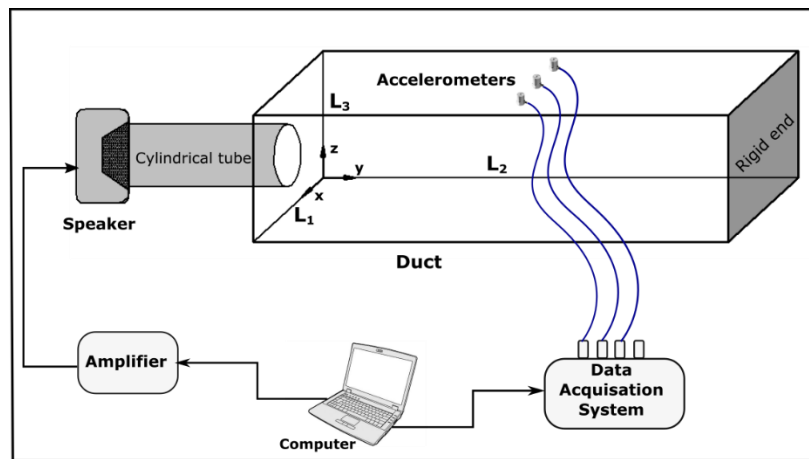
Figure 3.8: Schematic diagram of vibrations measurement with accelerometers at duct mid-section along the perimeter.

3.5 Results and discussion

Modal parameters calculated by numerical analysis have been discussed in Sec. 3.5.1. The measurement of input sound power and plane wave excitation conditions given to the duct is discussed in Sec.3.5.2. Radiated sound power measured by two different intensity methods, reactivity and pressure-residual intensity (p-RI) index are given in Sec.3.5.3. The transverse transmission loss calculation by experimental, analytical and numerical analysis is discussed in Sec.3.5.4. In the Sec.3.5.5, the vibration displacement and particle velocity results obtained by experimental and numerical analysis are discussed. In the last section, radiation efficiency calculated by experimental, analytical and numerical analysis is discussed.

3.5.1 Modal Parameters

Natural frequencies and mode shapes of both uncoupled structural and acoustic subsystems and coupled systems are calculated by numerical modal analysis. For chosen test duct configuration, there exist two uncoupled acoustic modes within the interested maximum frequency. These acoustic natural frequency values are 141.67 Hz and 283.33 Hz. However, there are 165 number of structural modes that exist in the interested range due to thin rectangular walls. So, only the first twenty natural frequency values are given in Table 3.1. Transfer factor helps to find the coupling between acoustic and structural modes [13]. It varies from zero to one. Zero means uncoupled and one means strongly coupled. From transfer factor values, it is observed that the first uncoupled acoustic mode 141.67 Hz is strongly coupled with structural mode frequency at 146.46 Hz with transfer factor of 0.922. Similarly, the second uncoupled acoustic mode 283.33 Hz is coupled with structural modes at 283.94 Hz and 292.69 Hz with transfer factor of 0.97 and 0.71, respectively.

Table 3.1: Rectangular duct natural frequencies obtained by numerical analysis.

Mode Number	Frequencies (Hz)	Mode Number	Frequencies (Hz)
1	20.64	11	50.77
2	25.52	12	52.19
3	26.85	13	54.17
4	30.70	14	60.36
5	33.77	15	60.54
6	37.75	16	62.73
7	40.03	17	63.20
8	44.53	18	69.83
9	45.44	19	74.14
10	48.39	20	77.66

3.5.2 Input sound power

Sound pressure should be uniform in a plane parallel to the cross-sectioned section of the duct for given plane wave excitation. It is verified by measuring directivity of the input sound source without test rectangular duct. The measurement plane is parallel to the cylinder cross-section. Directivity plots of the given input sound source are shown in Figs. 3.9(a) to (c) for two sinusoidal signals at frequency 141 Hz, 220 Hz and a random signal. It is a polar plot with a step size of 5 dB sound pressure level change. It is observed from Fig. 3.9 that the

directivity of the sound is varying from 0.8 to 1.01 for both sine-wave excitation signals. However, it varies from 0.7 to 1.1 for a random signal with frequency range of up to 400 Hz.

Objective in the current experimental setup is to generate plane wave excitation at the inlet of the test duct but verifying the same with test duct attachment is quite challenging. So, a numerical model is developed to understand the pressure distribution inside the duct. Geometry considered for simulation is similar to the experimental setup as shown in Fig. 3.3(a) but the speaker excitation is modelled as constant velocity source. Acoustic response analysis is done for the frequency range of 10-400 Hz in steps of 1 Hz. Sound pressure distribution at a frequency of 141 Hz is shown in Fig. 3.10(a) along the duct and cylindrical tube. It is observed that sound pressure distribution is uniform at the inlet cross-section as shown in Fig. 3.10(b). Similar behaviour is observed for other frequencies also. Hence, it validates that the given input sound source is a plane wave excitation.
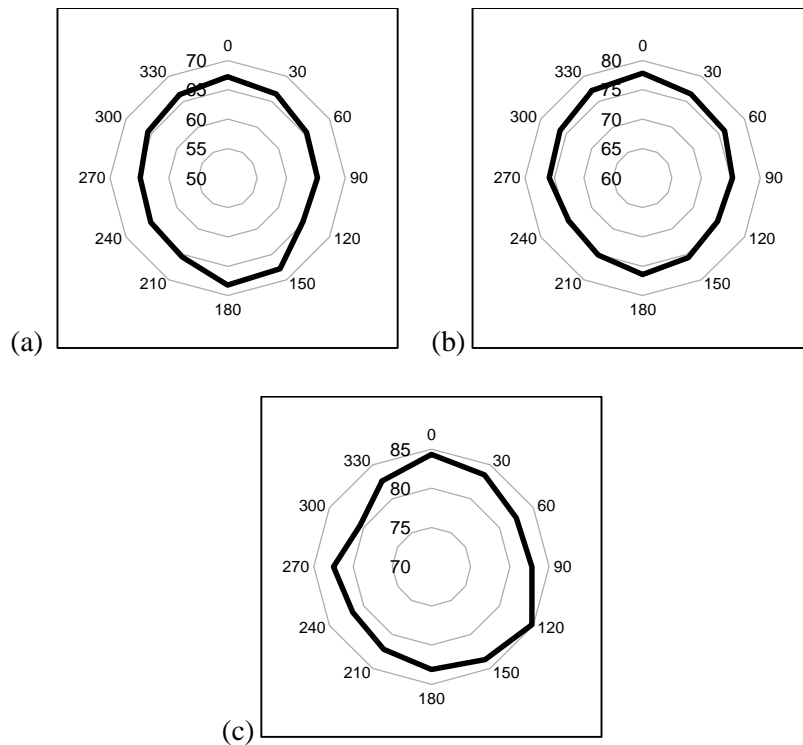
Figure 3.9: Sound source directivity for different excitation signals represented in terms of sound pressure level, dB (a) Sine wave 141 Hz, (b) Sine wave 220 Hz and (c) Random signal (up to 400 Hz).
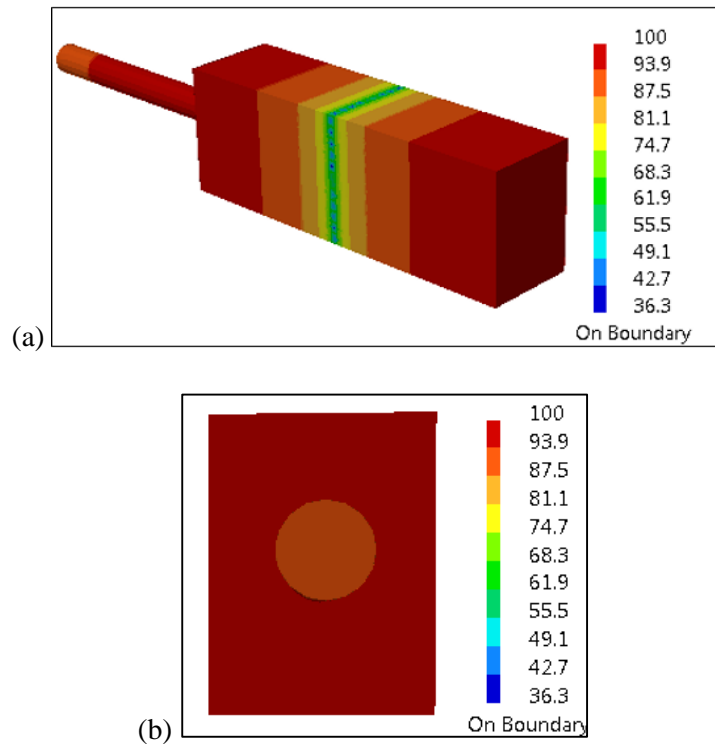
Figure 3.10: (a) Sound pressure distribution inside the duct and cylindrical tube, (b) Pressure distribution at inlet cross-section of rectangular duct.

A random signal as an input excitation source is used for breakout noise measurements. Autospectrum of the forward wave is calculated by measuring sound pressure signals at microphone position 1 and 2. The distance between microphones is 0.3 m. Input sound power is calculated using Eq. (3.2). Experimentally measured input sound power in one-third octave band frequencies is shown in Fig. 3.11.
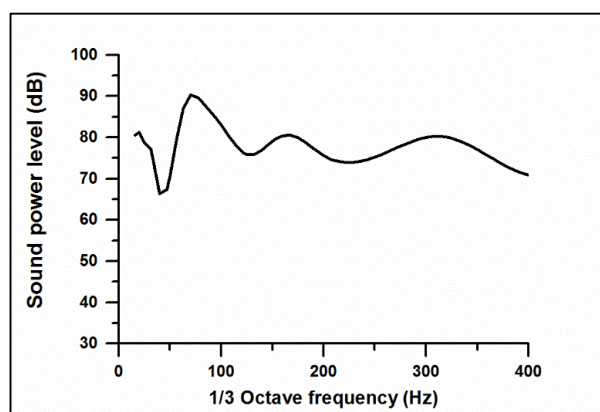
Figure 3.11: One-third spectrum of measured input sound power level.

57

3.5.3 Radiated sound power

Experimentally, radiated sound power from the duct wall surface is measured by using sound intensity (using P-P and P-U methods) over the duct surface. The results from both these methods are compared as shown in Fig. 3.12. It shows that the radiated sound power trend is similar in both methods, but there is a small deviation between P-P method and P-U method at a lower frequency. This discrepancy is due to the measurement error.
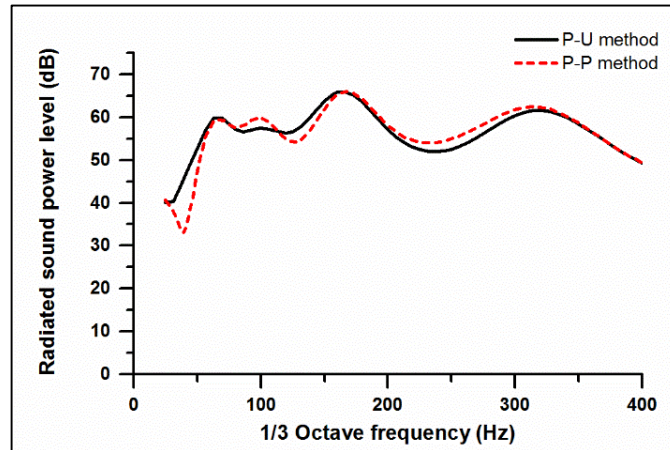
Figure 3.12: Measured radiated sound power spectrum from duct wall surfaces using P-U and P-P method.

Generally, the measurement errors are broadly categorized as random errors and bias errors. Random errors occur as a result of poor repeatability and reproducibility. In the present study, it is verified that the sound power measurements are repeatable with good accuracy. However, the discrepancy in the results between the two methods is because of the bias errors. These errors occur due to the influence of phase mismatch between the pressure sensors in P-P method and pressure and velocity sensors in the P-U method. The error in the sound intensity measurements due to phase mismatch is expressed in terms of pressure-residual intensity index (p-RI) for P-P method and in terms of reactivity for P-U method. The detailed analysis of reactivity and p-RI index are given in the following sections.

3.5.3.1 Reactivity

In P-U method, the phase mismatch error between pressure and velocity sensor is more sensitive in reactive fields. Higher phase mismatch error leads to bias errors. These errors are described in terms of reactivity and reactivity error. The measured sound intensity in terms of phase error is given by [109],

$$\hat{I}_r \approx I_0 \left(1 - \varphi_e \frac{J_0}{I_0} \right) \tag{3.15}$$

where, $\hat{I}_r$ is measured intensity, I_0 is the 'true' intensity, J_0 is the 'true' reactive intensity and φ_e phase error.

It can be observed from Eq. (3.15) that error in the measured sound intensity is directly proportional to the phase error, and it is sensitive when J_0 is high compared to I_0. The uncertainty which is induced by reactivity index and phase mismatch can be estimated in terms of reactivity error, and it can be expressed as [110],

$$\text{Error (dB)} = 10\log_{10}\left(1 + \beta_e \tan\beta_f\right) \tag{3.16}$$

where, β_e phase calibration error and β_f is the phase between acoustic pressure and particle velocity in the sound field.

Reactivity which was calculated using the measured active and reactive intensities by P-U probe near the duct walls is shown in Fig. 3.13(a). It shows that the maximum reactivity is 3.7 dB at 31.5 Hz, and it is within the acceptable standard values. It can be observed from Fig. 3.13(b) that maximum reactivity error is 2 dB at most of the measured position within the frequency range of 25 to 500 Hz. So, it can be concluded that sound power radiated from the duct wall surface measured by P-U method is accurate.
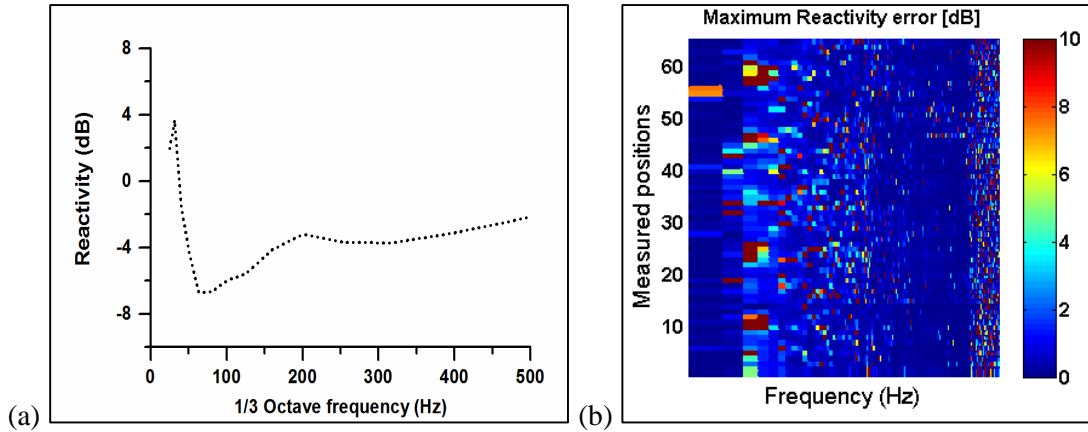
Figure 3.13: (a) Reactivity with respect to 1/3 octave frequency (b) Reactivity error with respect to frequency from 25Hz to 500 Hz.

3.5.3.2 Pressure-residual intensity index

In P-P method, a small error in phase mismatch leads to bias error in the sound intensity measurement, which can be approximated by [111],

$$\hat{I}_r \approx I_0 - \frac{\varphi_e}{kd} \frac{p_{rms}^2}{\rho_0 c_0} \tag{3.17}$$

where, $\hat{I}_r$ is biased intensity (measured), I_0 is the 'actual' intensity (unaffected by phase mismatch), φ_e phase error, p_{rms} is rms value of sound pressure, k is the wave number, d is microphone separation distance (spacer length). Here, pressure-residual intensity index can be calculated by measuring the ratio of phase error to the product of wave number and separation distance. It is observed from Eq. (3.17) that the bias error which is resulting in the measurement of sound intensity is directly proportional to the phase error and the mean square pressure. Inversely proportional to the microphone separation distance and wave number (i.e. frequency). It is observed that any error in the measured sound power in P-P method is due to background noise (sound pressure), selecting the inappropriate length of the spacer or due to phase error between microphones.

The p-RI index values in the P-P intensity measurement method after the phase calibration is shown in Fig. 3.14. It can be observed that below 63Hz frequency, the p-RI index is low and varying. So, which results the discrepancy in intensity measurements and hence in sound power. However, from 80 Hz onwards it is an almost constant value of approximately 23.5 dB and which is higher than the recommended minimum IEC standard p-RI index value.
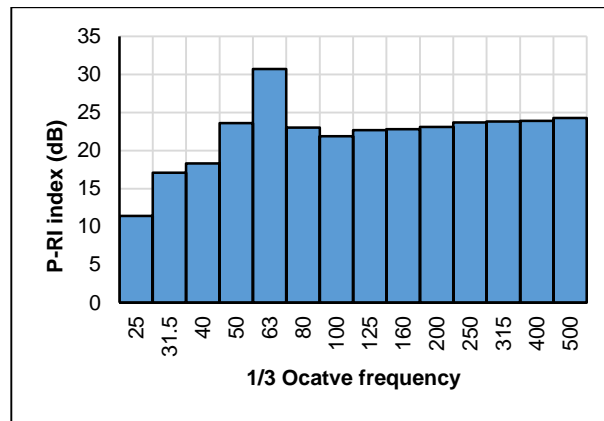
Figure 3.14: Pressure-residual intensity index in P-P measurement method.

3.5.4 Transverse Transmission loss (TTL)

The comparison of experimental, analytical and numerical results of TTL is shown in Fig. 3.15. It is observed that there is a reasonable agreement between the experimentally measured and prediction results from analytical and numerical models. It is noticed from Fig. 3.15, that there is a small discrepancy in P-P method at a lower frequency. However, above 125 Hz

frequency both intensity methods are in good agreement. The main reason for the discrepancy is only because of the phase mismatch between the pressure microphones which led to bias error as mentioned in the previous section. Since, in the present study the spacer of 50 mm length is used for the sound power measurements, which is more appropriate for low frequency and also the measurement has been done in the semi-anechoic room, so the background noise is not affecting.

Major limitation of P-P measurement method is in obtaining particle velocity based on the finite difference approximation. Hence, any error in phase-mismatch of the probe will lead to low p-RI index values and results in estimation errors of the particle velocity and overall radiated sound power calculations. So, obtaining reliable sound intensity measurements below 80 Hz in P-P method is quite challenging if there is a phase mismatch between the pressure microphones [111]. This error can be minimized by improving the p-RI index which in turn can be done by repeating the phase calibration by a number of times.
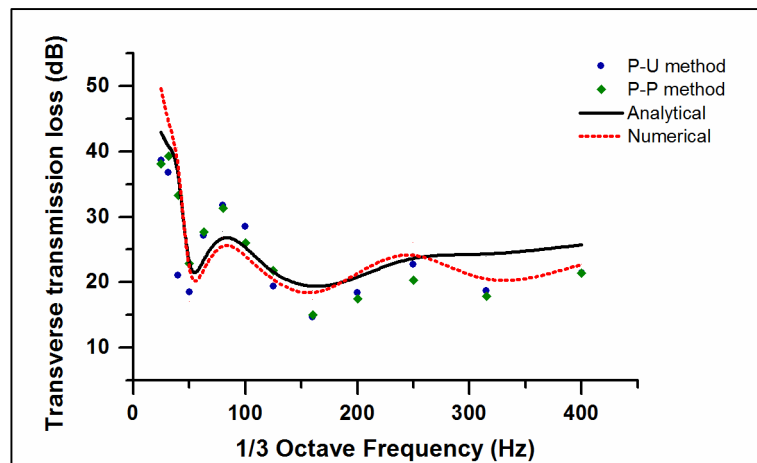
Figure 3.15: Comparison of experimental, analytical and numerical results for TTL of a rectangular duct.

In Fig. 3.15, the first dip is observed at 50 Hz centre frequency, which is due to structural mode at 54 Hz. The second dip is at the one-third octave band of 160 Hz centre frequency, and the third dip is at 315 Hz centre frequency band, which are due to strong acoustic-structural coupling at 146.46 Hz, 283.94 and 292.69 Hz. These trough frequency bands are the peaks of the radiated sound power spectrum as shown in Fig. 3.12.

3.5.5   Vibration displacement and velocity

Displacement distribution on the duct surface varies as a function of frequencies. Figure 3.16 shows displacement along the circumference of a rectangular duct measured at the mid-length for different frequencies. Here, the perimeter length from 0 to 0.3 represents the top surface, 0.3 to 0.7 represents right surface, 0.7 to 1.0 represents bottom surface, 1.0 to 1.4 represents left surface and these are indicated as 1, 2, 3 and, 4 respectively in Fig. 3.16. The frequencies 54, 87, 152 and 319 Hz are chosen based on troughs in TTL curve, maximum amplitude of vibration and odd-odd modal indices within the interested frequency range. Odd-odd modal indices of the flexible rectangular ducts are efficient sound radiating modes as discussed in Chapter-2. Displacement distribution at interested frequencies is similar to breathing mode of a duct. It is observed that sound radiates efficiently at 54 Hz and 152 Hz due to the uncoupled structural mode and structure-acoustic coupling mode. It is further noticed that the amplitude of vibration displacement is not symmetric in parallel wall surfaces (i.e., top and bottom, right and left). This is due to the existence of joint between the top (1) and left (4) plate of the duct and it makes stiffer walls. Hence, the amplitude of vibration is less in these two walls compared to other walls.
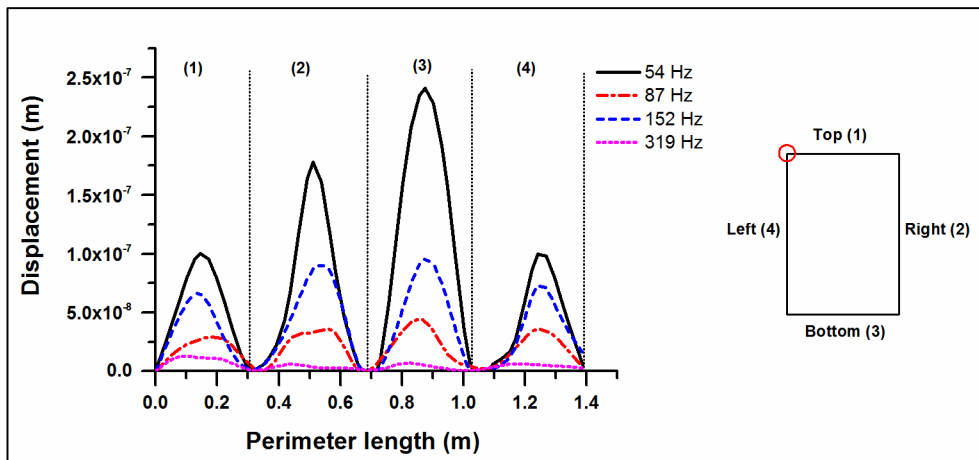
Figure 3.16: Vibration displacement at different frequencies along the perimeter of a duct measured at mid-length (left). A cross-sectional view of the rectangular duct (right).

Figure 3.17 shows the comparison of normalized vibration velocity of experimental and numerical results along the perimeter of a duct at mid-section for 54Hz frequency. Symmetry behaviour is observed in amplitude of the vibration velocity on top (1) and bottom (3) surfaces in numerical results unlike the experimental. Similar symmetric behaviour is also observed for the right (2) and left (4) surfaces. Further analysis is done to understand the relationship

between acoustic and structural response by choosing a particular frequency of 54 Hz. Nevertheless, the same approach can be followed for other frequencies.
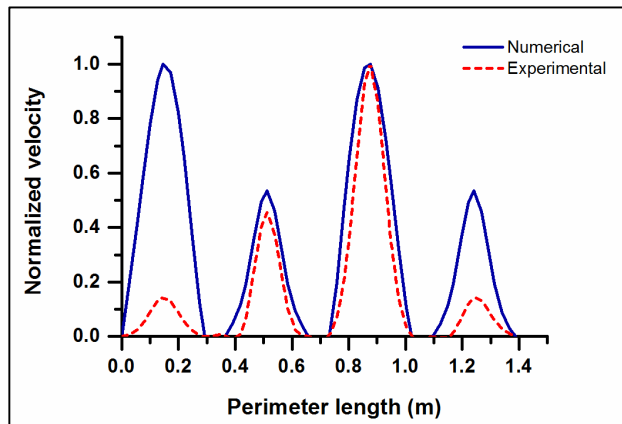
Figure 3.17: Comparison of normalized vibration velocity of experimental and numerical results along the perimeter of a duct at mid-section for 54Hz.

Acoustic particle velocity is measured directly by using P-U probe and vibration velocity is calculated using the measured acceleration. The velocity normalization has been done with reference to maximum amplitude observed within the measured points at a given frequency. Figure 3.18 shows a comparison of both normalized velocities along the perimeter at mid-section of a duct for 54 Hz, where structural resonance occurs. Normalized particle velocity and vibration velocity are in good agreement, but discrepancy exists in the top (1) and left (4) plate of a duct. The difference between these two results is due to the presence of a joint along the length of a duct.
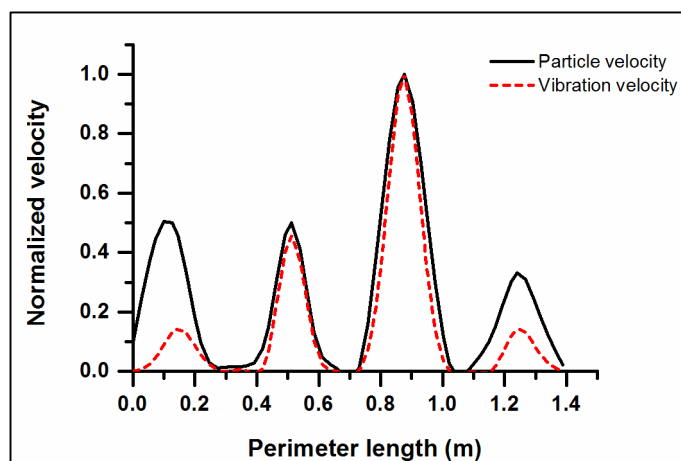
Figure 3.18: Comparison of normalized vibration velocity and acoustic particle velocity along the perimeter of a duct at mid-section for 54Hz.

Figure 3.19 (a) shows a comparison of sound pressure radiation pattern measured near the right side of a duct wall surface at 54 Hz with structural vibration displacement response using Finite Element Analysis (FEA). Similar comparisons were done for all other surfaces. These distribution patterns are the same and in the form of duct breathing mode. In other words, the sound radiation pattern from duct walls due to plane wave excitation is in the form of breathing mode, and it is dominant at the structural mode. The similar behaviour was also observed in the literature [1, 5]. Similarly, Fig. 3.19 (b) shows a comparison of sound pressure radiation pattern with structural vibration displacement at 87 Hz frequency.
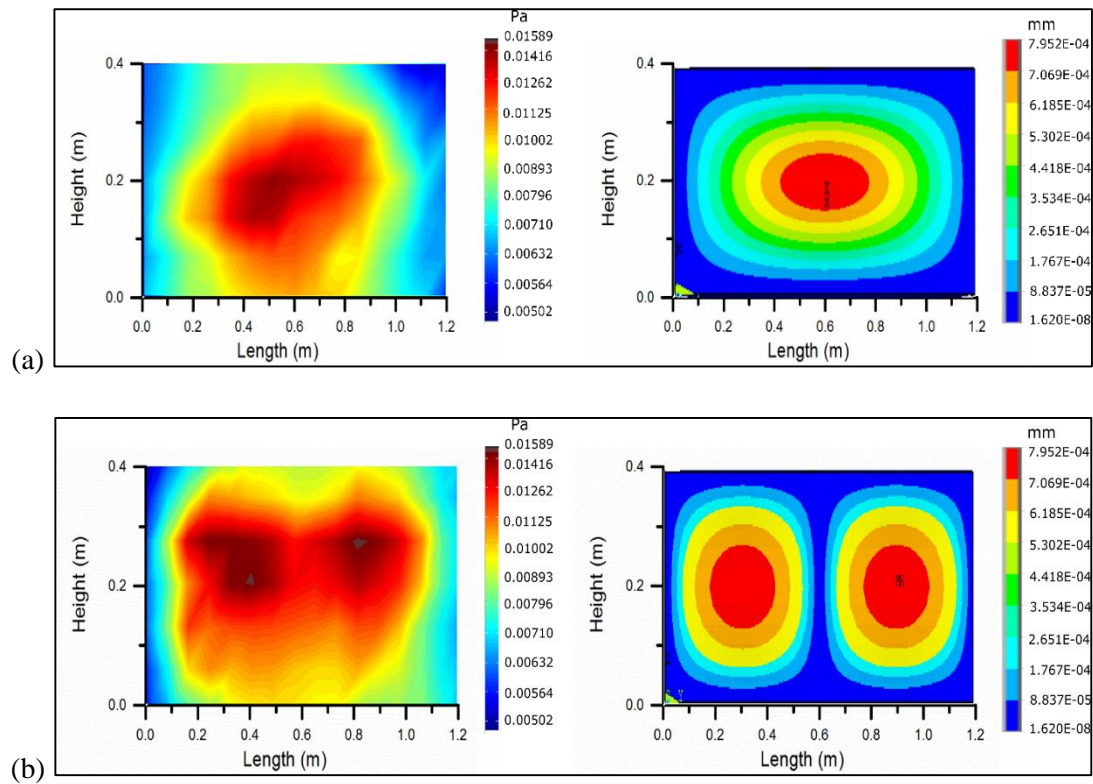
Figure 3.19: Comparison of sound pressure radiation pattern (left) with vibration displacement pattern (right) on the side wall of the rectangular duct: (a) 54 Hz, (b) 87 Hz.

3.5.6 Sound radiation efficiency

Sound radiation efficiency of the duct walls is calculated experimentally and analytically using Eqs. (3.12) and (2.15), respectively. It is also calculated from numerical simulations. Fig. 3.20 shows the comparison of experimental, analytical and numerical results of radiation efficiency as a function of one-third octave frequencies. It is observed that both analytical and

numerical results in good agreement. It is further noticed that experimental results obtained by P-U method are in closer agreement with numerical and analytical results, whereas there is a small deviation for results obtained by P-P method. This deviation is because of the discrepancy in the radiated sound power measurement which is resulted by phase mismatch error. However, the measured radiation efficiency curve is similar to analytical and numerical results and approaches to unity at higher frequencies.
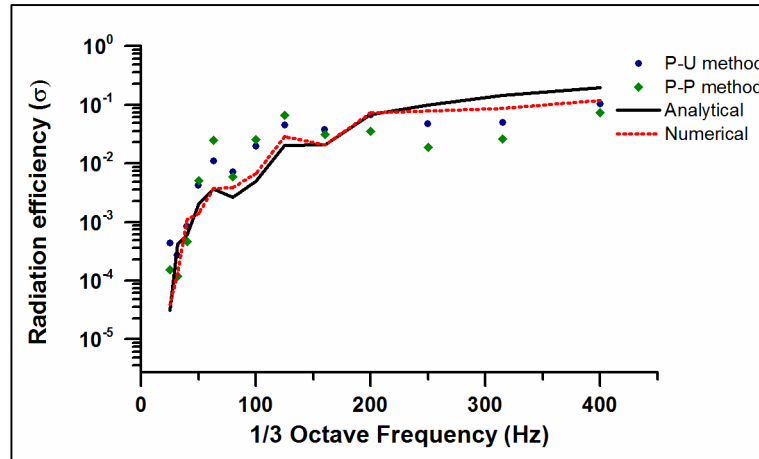
Figure 3.20: Comparison of experimental, analytical and numerical results of rectangular duct sound radiation efficiency.

3.6 Summary

The present chapter discusses the measurement of breakout noise characteristics for a flexible rectangular duct with simply supported boundary conditions. An experimental setup has been developed to measure the breakout noise in terms of TTL and radiation efficiency by providing a plane-wave excitation as an input sound source to a rectangular duct. A methodology is developed to calculate the input sound power from measured pressure signals inside the cylindrical tube. Radiated sound power from a flexible rectangular duct is measured by using intensity-based methods such as P-P and P-U methods.

Sound radiated from the duct wall dominates at uncoupled structural and coupled acoustic-structural resonance frequencies. Efficient vibration radiating modes are identified by measuring vibration displacement along the perimeter at the mid-section of a duct at different frequencies. Normalized vibration velocity and particle velocity near the duct wall surface are compared and they are in good agreement away from the joint but discrepancy is observed near the duct joint. Similar behaviour is also observed in the comparison of experimental and

numerical results. Vibration displacement pattern at the structural resonance frequency is similar to sound pressure radiation pattern.

Transverse transmission loss and radiation efficiencies measured by two different experimental intensity methods are in good agreement with analytical and numerical results. However, the small discrepancy in P-P method at a lower frequency is because of the phase error, which can be minimized by matching the phase of sound pressure microphones. Further studies have been done to understand the effect of different joints, used in duct fabrication, on modal parameters, vibration behaviour and which are discussed in the next chapter.

Chapter 4

Experimental Modal Analysis of Rectangular Ducts

4.1 Introduction

The previous chapter discussed the sound radiation characteristics of duct and vibration distribution on flexible rectangular duct walls. It was observed that deviation between predicted and experimental results near the joint. So, the present chapter discusses the effect of joints on modal parameters. Flexible rectangular ducts are made from thin sheet metal with connecting joints. Practically, duct shapes have deviations from ideal geometric shapes, predominantly in thin-walled structures due to joint conditions. To understand the effect of joints on modal parameters, the present study considers three different ducts and two types of joints (welded and adhesive joints). Pre-test analysis is performed to know the number of measuring points and their locations. Auto-MAC analysis is performed to verify if a sufficient number of degrees of freedom are considered in the modal test. Numerical Modal Analysis (NMA) is then performed on these ducts by modeling the corresponding joints. The Modal Assurance Criteria (MAC), frequency comparison and auto-MAC plots are used to check the correlation between the experimental and numerical results.

4.2 Pre-test Analysis

Three different rectangular ducts of dimensions of 0.3m x 0.4m x 1.2m with different thickness are considered for analysis, as shown in Fig. 4.1. Ducts-1 and 2 are fabricated with mild steel plates of 11 gauge (~3mm) thickness along with two and four welded joints, respectively. The material properties are: Elastic modulus is 210 GPa, density is 7850 kg/m^3 and Poisson's ratio is 0.3. Duct-1 is fabricated by bending plate as a "C" section and the top plate is welded at its two corners. In Duct-2 configuration, four individual plates are welded at four right angle corners. Duct-3 is fabricated using four individual smooth and plain acrylic sheets of 9 gauge (~4mm) thickness and joined using cyanoacrylate adhesive which

establishes a strong bond and smooth connectivity between them. The fabricated duct is closer to an ideal rectangular shape. The material properties are: Elastic modulus is 3.2 GPa, density is 1100 kg/m^3 and Poisson's ratio is 0.4.
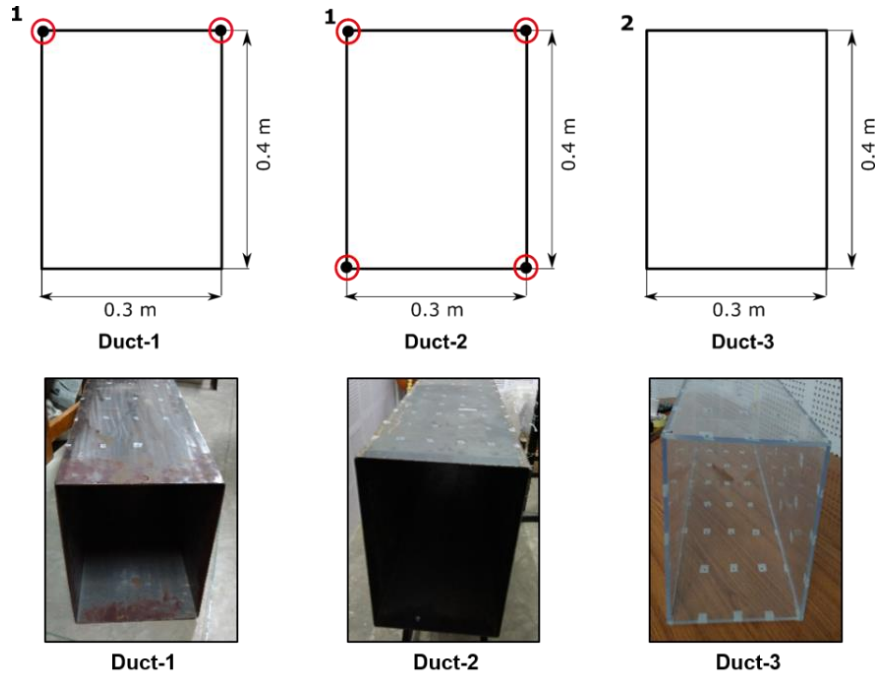
Figure 4.1: Cross-sectional view of three different duct configurations used in the experimental modal analysis (schematic and actual ducts).

Prior to conducting EMA, selection of excitation, response location and a number of measurement points are important to obtain accurate modal parameters from measured FRF's. Pre-test analysis is performed based on NMA solution to find a reference point and response locations to mount accelerometers. The modes existing within the frequency range of 10-200 Hz are considered in the present study. The pre-test analysis result is shown in Fig. 4.2, which indicates the positions and number of measurement points. Since the modes are closely spaced, 144 measurement points are considered (for all three duct cases) to differentiate each mode shape at higher frequencies.

Drive Point Residue (DPR) can be stated as equivalent to mode participation factor. DPR measures how well each mode is excited or participated in overall response of the structure at the driving point. Definition of the DPR, for mode 'i' and node 'j' is given by [41],

$$DPR_i(j) = \frac{\phi_{ji}^2}{2m_{m_i}\omega_i} \tag{4.1}$$

68

where, ϕ is the mode shape (modal vector), ω is the circular natural frequency, m_m is the modal mass. The degrees of freedom (DOF) with maximum average DPR for overall mode shapes are considered to be the best excitation DOF's for a particular set of target modes. Fig. 4.2(b) shows three drive points which are best suited for excitation in modal the test. The positions of these points are [x=0, y=0, z=0.3], [x=0.3, y=1.2, z=0.3] and [x=0, y=1.2, z=0.3] for chosen duct dimensions.
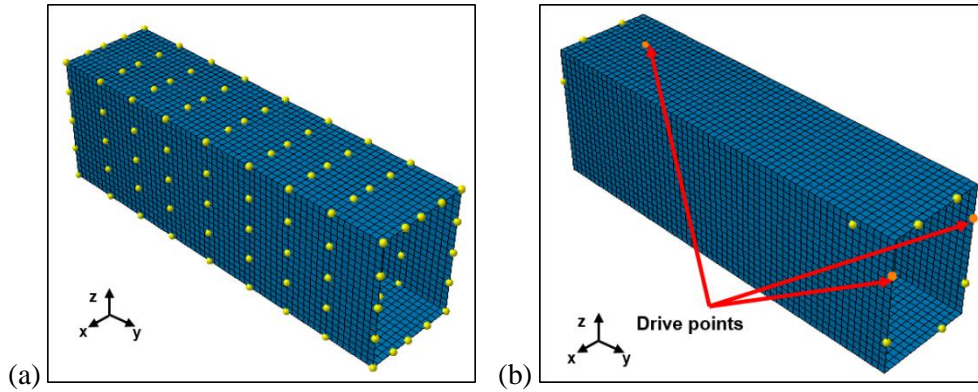
Figure 4.2: Pre-test analysis results: (a) Response measurement points highlighted with dots (b) Drive points chosen based on DPR value.

4.3 Experimental test setup

There are mainly three important steps involved in EMA, namely; establishing measurement set-up, acquiring data and extracting modal parameters. Preparation of measurement set-up involves preparation of boundary conditions (BC), selection of excitation method, type of transducers and measurement locations. Once measurement set-up is established, FRF's are measured with appropriate settings such as sampling frequency, bandwidth, number of samples and windowing function. It is important to verify the quality of acquiring data to ensure that measurements errors are minimal. This verification is done by observing input excitation, coherence and FRF's which are shown in Fig. 4.3. It can be observed that input excitation given to the duct is impulse and measured response is appropriate since the coherence values are approximately one almost at all the frequencies. As the last step, modal parameters are extracted from measured FRF data using curve fitting methods.

Modal analysis experiment is conducted on ducts with free-free (F-F) BC, the test setup is shown in Fig. 4.4. This BC is achieved by suspending the duct with flexible bungee ropes near the nodal points of the duct (these nodal positions are obtained from NMA). A reciprocity

test has been performed for the chosen duct configuration by interchanging the input and response measurement positions and which is shown in Fig. 4.5. It is clearly noticed that FRF functions for both cases are matching exactly and it can be stated that the reciprocity principle holds good for the considered duct. Hence, EMA is conducted by roving hammer method i.e. response measurement locations are fixed and excitation is given at different locations of the duct. High sensitivity light-weight tri-axial and uni-axial accelerometers are used to capture the vibration response. Two Uni-axial sensors (Dytran model-3055B1) with sensitivities of 10.17mV/g and 10.06 mV/g, respectively are used. A tri-axial sensor (Dytran model-3023A2) with a sensitivity of 10.11 mV/g, 9.98 mV/g, 9.96 mV/g along x, y and z directions, respectively is used. A Dytran impact hammer (Model-5800B3) with a sensitivity of 11.50 mV/N is used for excitation in order to induce vibrations in the structure. The weight of uni and tri-axial accelerometers is 10 and 3 grams, respectively and weight of impact hammer is 100 grams. As the weight of these sensors is much lesser than the duct weight, mass loading effect is neglected.
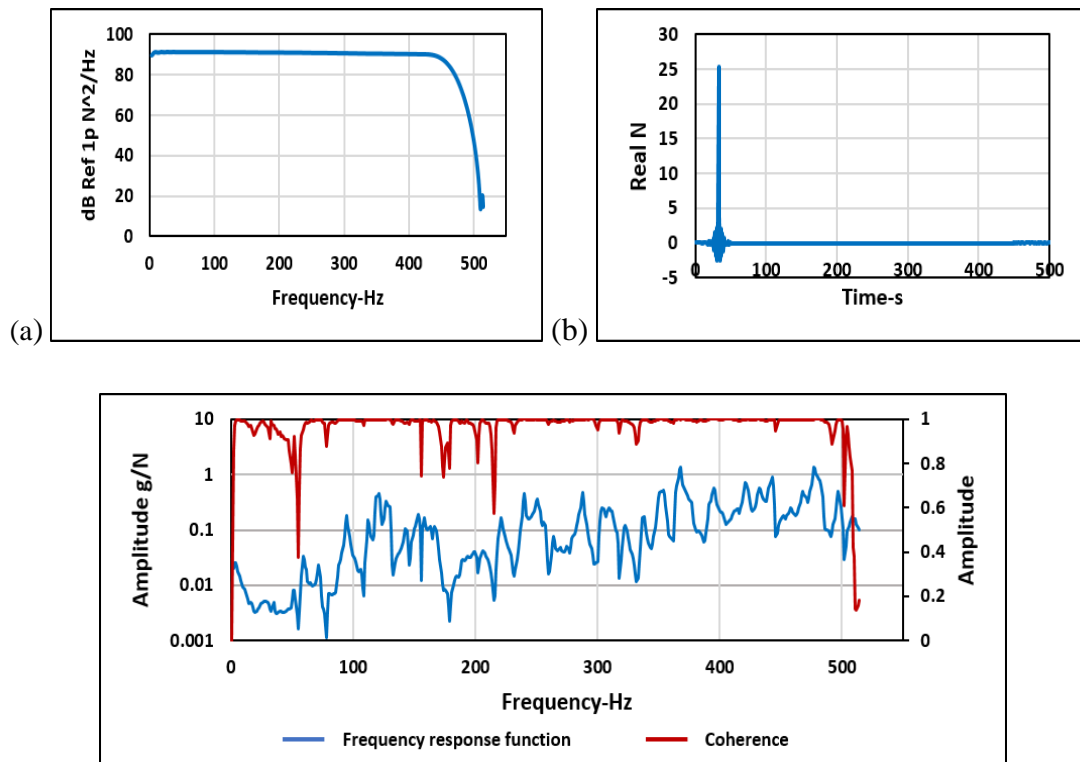
Figure 4.3: Data acquisition plots: (a) power spectral density, (b) impact pulse signal, and (c) frequency response function and coherence.

In the current study, m+p VibPilot Data Acquisition System (DAQ) with m+p international analyser is used for acquiring and post-processing. The vibration response data is acquired with a useful bandwidth of 400 Hz frequency at a sampling rate of 1024 Hz and frequency resolution of 1 Hz. For acquiring the data, force/exponential windowing with force width of 10% and exponential end of 1% is taken. Four readings are considered at each measurement location and these are linearly averaged.
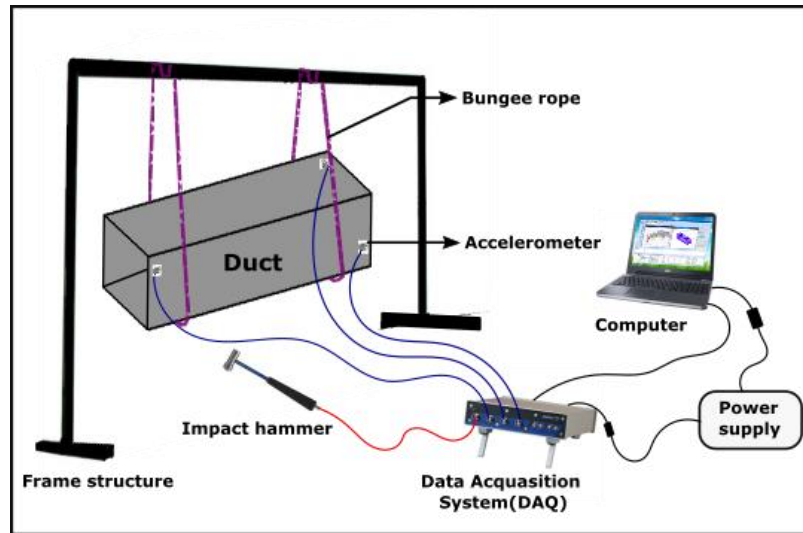
Figure 4.4: Experimental modal analysis test setup of the rectangular duct with roving hammer method.
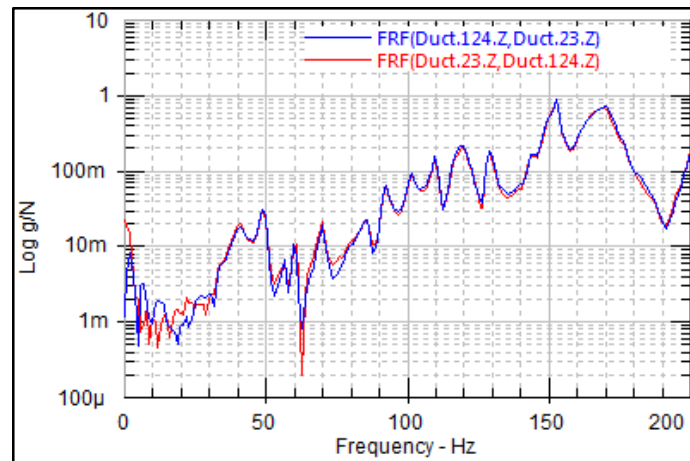
Figure 4.5: Frequency response functions of the reciprocity test.

Figure 4.6 shows a stability diagram for a multi-degree of freedom (MDOF) analysis of the duct to select the poles. Multivariate Mode Indicator Function (MvMIF) is used for extracting the modal parameters. The pole's selections have verified by comparing the measured drive

71

point FRF and the synthesized MvMIF curve. The selected poles have indicated by solid squares.
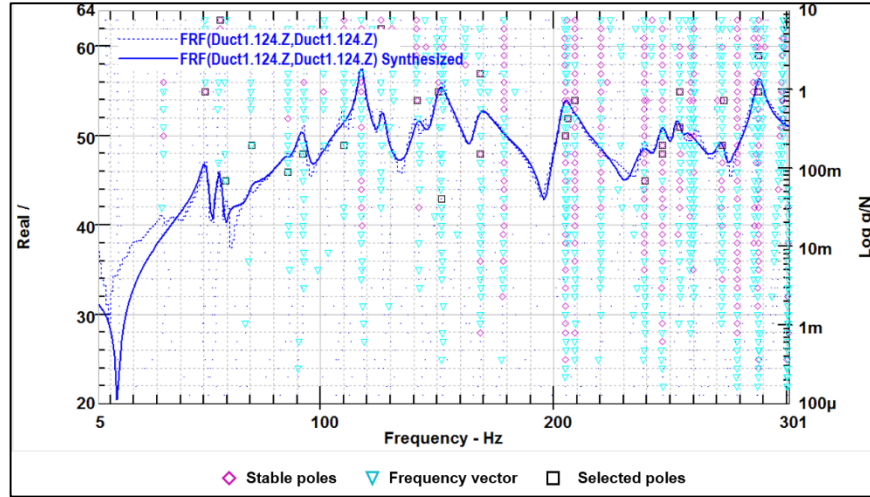
Figure 4.6: Stability diagram for MDOF analysis of the duct as a function of frequency

4.4 Numerical Modal Analysis

Finite Element Analysis (FEA) is used to calculate natural frequencies and mode shapes of all ducts using commercial software (ANSYS). The flexibility of duct joints can be incorporated either in terms of material properties or stiffness of the joint. From literature study, it is noticed that the material properties of welded joints do not significantly differ from the base material. Hence, in the present study, welded joints are modelled and meshed with different thickness elements to incorporate stiffness of the joint conditions. The plate thickness of 5 mm is chosen at joints (by measuring weld bead) and duct wall thickness (3 mm) is considered at other locations. However, if joints are modelled with 3mm thickness elements then the duct becomes an ideal duct.

A rectangular duct, Duct-1, of dimension 0.3 m x 0.4 m x 1.5 m is modelled and meshed using SHELL-63 elements as shown in Fig. 4.7(a). Based on the convergence study, an element size of 0.005 m is chosen for meshing. Mild steel properties such as: Elastic modulus is 210 GPa, density is 7850 kg/m^3, Poisson's ratio of 0.3 are applied for both joint and base material of a duct. NMA is performed to calculate the modal parameters by applying F-F boundary conditions at both ends of the duct. Similarly, for Duct-2, welded joints are modelled at its four corners as shown in Fig. 4.7(b). and corresponding material properties are applied thereupon NMA is performed. In a similar way, Duct-3 is modelled as an ideal duct shape i.e.

72

full duct is meshed with the same thickness elements since joints are glued with adhesive. NMA is performed for Duct-3 considering appropriate acrylic material properties. NMA results can be referred as predicted results in the present study.
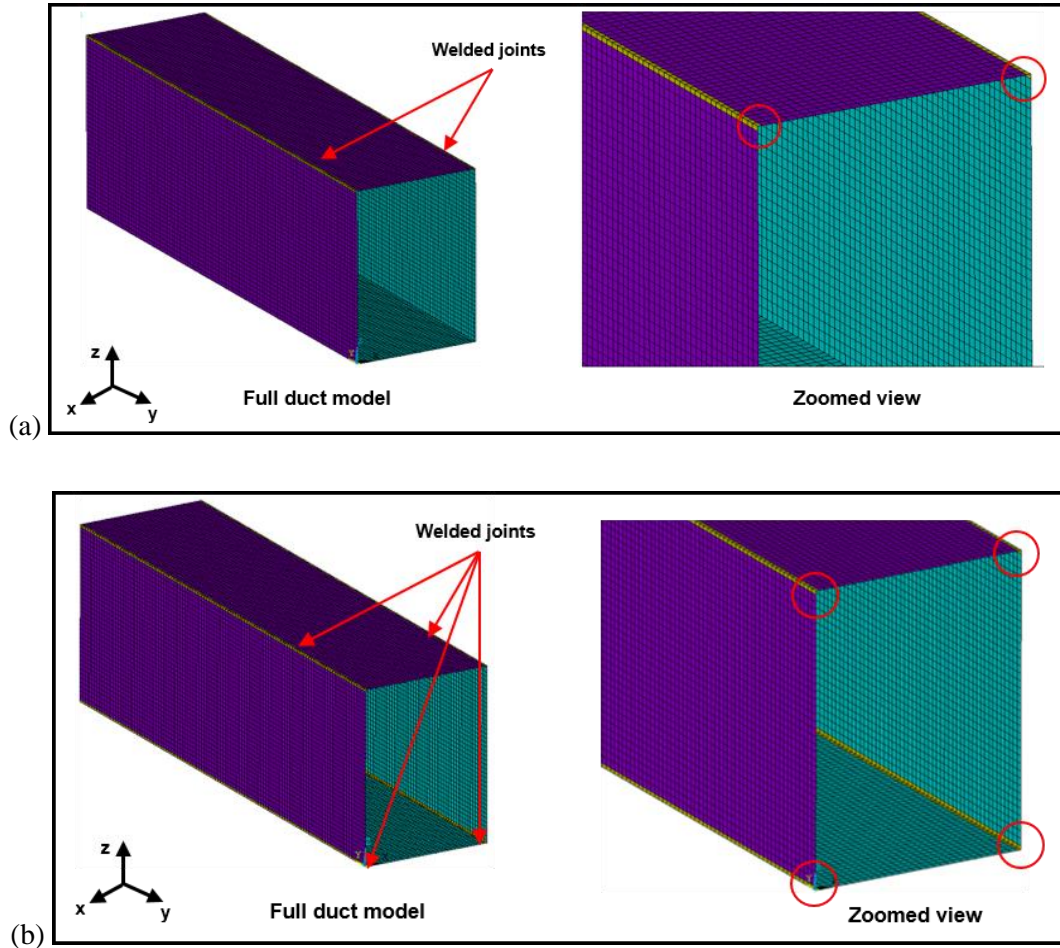
Figure 4.7: Finite element model for numerical modal analysis with F-F BC's. (a) Duct-1 with two welded joint conditions, and (2) Duct-2 with four welded joints

Once modal parameters are estimated by NMA, these results are used for correlation analysis to compare with EMA results. There are different methods available for performing the model correlation using modal parameters [49]. Modal Assurance Criterion (MAC) is most commonly used to check the correlation between numerical and experimental mode shapes. The expression for MAC is shown in Eq. (4.2). MAC is a scalar quantity, which ranges between 0 and 1. If two mode shapes are same, then MAC value is 1. If V_i^{EMA} is modal vector from EMA and V_j^{FEM} is from FEA, then MAC is given as,

$$MAC_{ij} = \frac{\left|\{V_i^{EMA}\}\{V_j^{FEA}\}^T\right|^2}{\left\{\{V_i^{EMA}\}\{V_i^{EMA}\}^T\right\}\left\{\{V_j^{FEA}\}\{V_j^{FEA}\}^T\right\}} \tag{4.2}$$

where, 'V' is the modal vector, 'i' and 'j' are the mode number of the experimental and numerical results, respectively.

4.5 Results and discussion

Experimental and numerical modal analysis results of ducts corresponding to all three cases are discussed here. First, Auto-MAC analysis is done for modes obtained from the modal test, to verify if enough number of nodes or DOF are considered in EMA test. Next, natural frequencies measured from EMA are compared to NMA results. The measured and predicted mode shapes are compared by visual inspection and correlation analysis in terms of MAC values.

4.5.1   Auto-MAC

Auto-correlation analysis helps to verify a number of measurement points selected in a modal test for capturing mode shapes. It is also used to check how well a particular mode is correlated with other modes within the interested frequency range [50]. Auto-MAC values are varying from 0 to 1. A well planned modal test results in high diagonal auto-MAC ($\approx$1) and very low off-diagonal auto-MAC ($\approx$0) values. Presence of any higher off-diagonal values is an indication of spatial aliasing or presence of closed modes.

Auto-correlation is performed for all ducts and corresponding auto-MAC plots are shown in Fig. 4.8. Here, experimental mode shapes are denoted as reference mode set. It is observed that auto-MAC matrix is almost diagonal since each individual modal vector is orthogonal to other modal vectors. Hence, it confirms that chosen measurement points in the present test are sufficient. However, it is observed from Fig. 4.8 that Duct-1 and 2 have some individual modes correlated with multiple modes as they are closely spaced. These modes indicate that they are not representing the independent mode shapes which leads to higher off-diagonal auto-MAC values. Especially, this can be observed in modes 6, 7 (MAC=0.45, between 87.31 Hz and 95.90 Hz) and 16, 17 (MAC=0.78, between 154.60 Hz and 156.43 Hz) for Duct-1 and modes 7, 8 (MAC=0.9, between 84.46 Hz and 95.68 Hz) and 13, 14 (MAC=0.7, between 151.44 Hz and 154.90 Hz) for Duct-2. However, the auto-MAC plot for Duct-3 is perfectly diagonal.

74
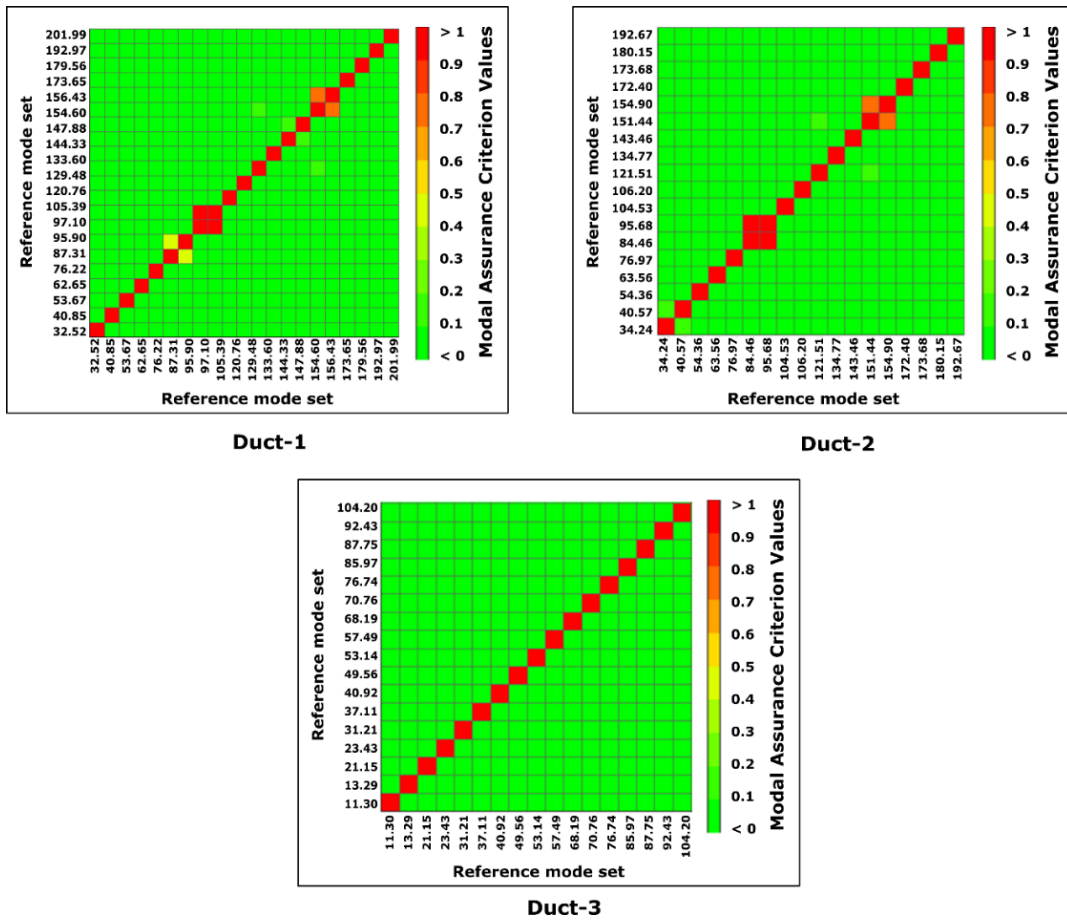
Figure 4.8: Auto-MAC plots of experimental results (reference modes) for all three ducts with different joint conditions.

4.5.2 Natural frequencies

Table 4.1 shows a comparison of natural frequencies obtained from experimental and numerical modal analysis for all three ducts. Here, f_e are experimental natural frequencies, f_n are numerical natural frequencies. It is observed that experimental and numerical results are in good agreement with less than 10% error. However, some modes are not captured in EMA such as the 9th mode for Duct-1, the 8th mode for Duct-2 and 6th mode for Duct-3. This is due to higher modal density, the existence of repeated roots (modes) and deviation of duct geometry from the symmetric condition (due to the presence of joint conditions).

75
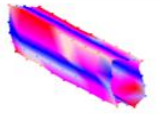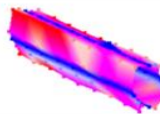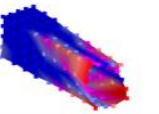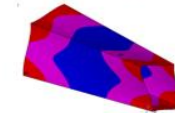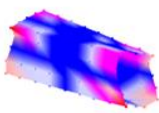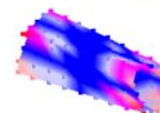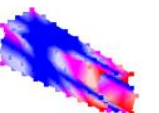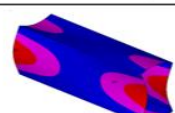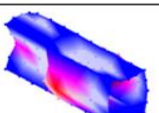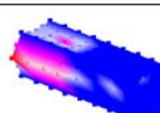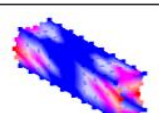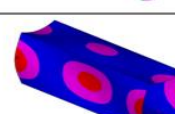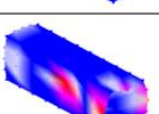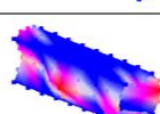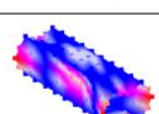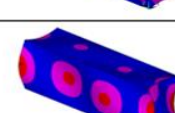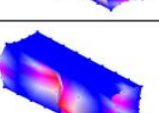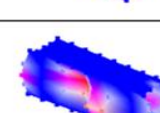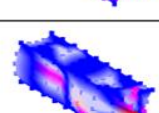
Table 4.1: Comparison between experimental and numerical natural frequencies results for all three ducts.

Mode number	Duct-1		Duct-2		Duct-3	
	f_e (Hz)	f_n (Hz)	f_e (Hz)	f_n (Hz)	f_e (Hz)	f_n (Hz)
1	32.52	35.55	34.24	35.86	11.30	12.08
2	40.85	35.96	40.57	36.20	13.29	12.10
3	53.67	56.76	54.36	56.88	21.15	19.27
4	62.65	61.01	63.56	61.43	21.15	20.44
5	76.22	74.63	76.97	75.71	23.43	24.82
6	87.31	90.74	84.46	92.18	-	30.16
7	95.90	96.75	95.68	98.47	31.21	32.11
8	97.10	101.75	-	102.82	32.73	34.23
9	-	102.5	104.53	103.41	37.11	36.46
10	105.39	109.52	106.20	111.26	40.92	42.52

4.5.3 Mode shapes

Figure 4.9 shows a comparison of the first five mode shapes obtained from EMA and NMA for all ducts. For ease visual comparison of mode shapes, notation of same color bar is maintained in both experimental and numerical results. It can be observed from Fig. 4.9 that for all three ducts, experimental mode shapes resemble equitably with numerical mode shapes based on visual inspection. However, in the Duct-1 case for 4th and 5th modes, modal displacement on the top plate is less compared to side plates. This is due to the presence of welded joints at the top edges which cause high local stiffness and geometric irregularity. It may be inferred that modal strain energy is not transferring from side plates to the top plate as observed in Ref. [112]. Similar behavior is also observed for Duct-2 but there is a higher discrepancy in mode shapes as compared to Duct-1. Modal displacement is not significant in the top plate for modes 3 to 5 and in the side plates for modes 3 and 5 due to the joint between top and side plates. In Duct-3, it is noticed that experimental and numerical mode shapes are matched very well except for the first mode. Amount of correlation between these mode pairs for all ducts can be calculated in terms of MAC values.

Figure 4.9: Comparison of experimental and numerical mode shape results for first five modes of three duct configurations.

4.5.4 Modal Assurance Criteria (MAC) plot

MAC plots for Ducts-1 to 3 are shown in Fig. 4.10 and corresponding mode pair table is presented. In MAC plot, experimental mode shapes are denoted as reference mode set and numerical mode shapes as verification mode set.

In Duct-1 case, it can be observed that experimental and numerical mode shapes are matching well at higher frequencies than at lower frequencies. Mode pair table which has MAC value greater than or equal to 0.4 is shown in Table 4.2. It is observed that the highest MAC value is 0.74 for mode pairs of experimental mode-18 (173.65 Hz) and FEA mode-23 (184.68 Hz). The main reason for low MAC value is due to welded joints on the duct's top plate surface, which makes it stiffer leading to lower modal displacement.
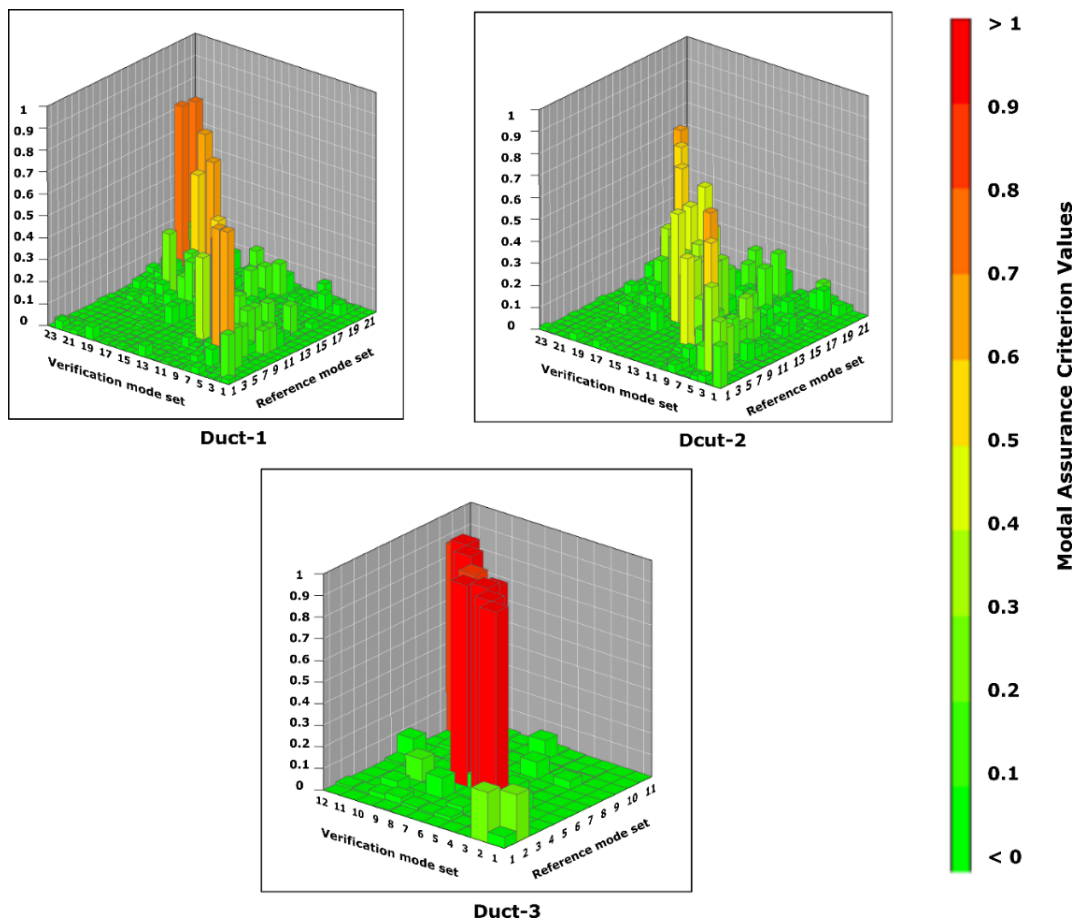
Figure 4.10: Comparison of experimental and numerical mode shapes in terms of Modal Assurance Criteria for all three duct cases-1 to 3.

In Duct-2 case, it is observed that the maximum MAC value is 0.68 between the experimental mode of 76.97 Hz and numerical mode of 92.18 Hz frequency. It is also noticed that few off-diagonal mode pairs show MAC values are approximately equal to 0.4. It indicates that one numerical mode has a correlation with multiple experimental modes, for example, Mode-11 (129.79 Hz) of numerical is correlated with Mode-9 (104.53 Hz) and Mode-10 (106.20 Hz) of experimental results. This is due to welded joints, which makes the structure stiffer at edges and each duct wall surface behaves as an individual plate.

In Duct-3 case, it is observed that predicted and measured mode shapes are correlated very well with MAC value of greater than 0.8 except at two fundamental modes. It is also clear from the MAC plot that mode pairs which are correlated are almost diagonal. Mode pair table for MAC values greater than or equal to 0.8 is shown in Table 4.2.

Table 4.2: Modal assurance criteria values for all the three ducts.

Duct-1			Duct-2			Duct-3		
f_e (Hz)	f_n (Hz)	MAC Value	f_e (Hz)	f_n (Hz)	MAC Value	f_e (Hz)	f_n (Hz)	MAC Value
53.67	56.76	0.66	54.36	61.43	0.40	21.15	19.27	0.99
62.65	61.01	0.61	63.56	75.71	0.57	23.43	20.44	0.98
76.22	74.63	0.54	76.97	92.18	0.68	31.21	30.20	0.99
95.90	96.75	0.60	84.46	103.41	0.41	37.11	36.50	0.93
129.48	132.18	0.40	132.54	137.19	0.49	40.92	42.52	0.91
147.88	151.54	0.62	151.44	154.50	0.50	49.56	46.66	0.90
156.4	163.70	0.68	154.90	166.85	0.52	53.14	54.61	0.93
173.65	184.68	0.74	172.40	176.84	0.59	68.19	68.71	0.93
206.34	201.99	0.69	173.68	184.01	0.64	70.76	73.40	0.87
						76.74	74.84	0.87
						85.97	80.58	0.81

Effect of joint condition on mode shapes can be clearly observed from above MAC results. It is noticed that MAC values are lower and more off-diagonal mode pairs exist when the number of welded joints at edges increases. The presence of welded joints in a duct leads to deviation from an ideal rectangular shape and causes lower MAC values. It also indicates that the numerical model considered in the present study for welded joint conditions is needed to be improved to incorporate joint flexibilities in its truer perspective. Duct-3 configuration is close to an ideal rectangular duct shape and has MAC values of greater than 0.8 at all modes.

It can be noticed, from all three MAC plots as shown in Fig. 4.10, that MAC value for the first two modes is very low (less than 0.25) even though mode shapes appear similar by visual inspection as shown in Fig. 4.9. Therefore, it is necessary to study the reasons for low MAC values. The complexity of modal vectors is one of the reasons. Hence, in the present work, it is calculated for measured mode shapes. Vacher et al. showed that MAC is good, only for monophase vectors [113].

4.5.4.1 Complexity of modal vector

There are different methods available in the literature to indicate the complexity of modal vectors [114]. The present study considers two approaches namely; graphical approach and Modal Phase Collinearity (MPC). The graphical approach is a simple method for analyzing the complexity of modal vector and can be obtained by plotting modal vectors in the polar plane. One can visually observe the dispersion of these vectors indicating the complexity of modal vectors. Figure 4.11 shows complexity plots of first four mode shapes for the measured data. It is observed that first mode is highly complex and second one is rather less complex. Mode-3 and -4 are almost aligned along a particular direction and this indicates that they are close to monophase vectors. Corresponding MAC values are 0.6 and 0.64, respectively.
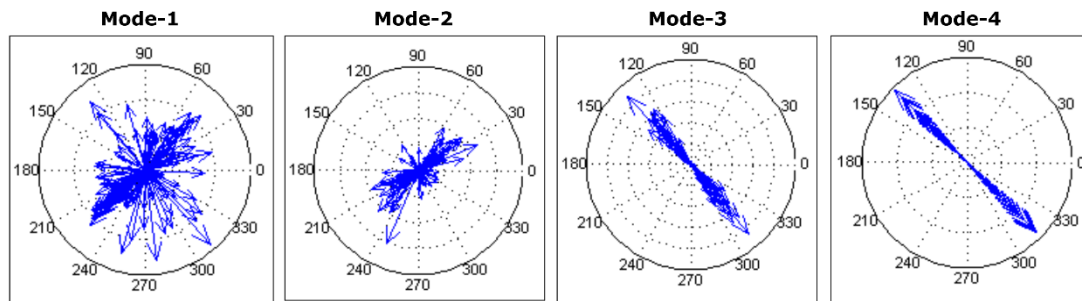
Figure 4.11: Complexity plots for the first four measured mode shapes of Duct-1.

Modal Phase Collinearity (MPC) is a criterion in order to quantify the complexity of modal vectors. MPC values vary from 0 to 1. Value '1' indicates monophase vector and value '0' indicates that the modal vector is very complex in nature. MPC values for the first ten modes of Duct-1 are shown in Table 4.3. It shows that for first mode MPC value is 0.2 which is very complex, second is moderately complex and from third mode onwards all are monophase vectors. The similar behaviour is also observed in the graphical approach of complexity plots. Therefore, it is clear that MAC correlation analysis is not appropriate for comparing the first two mode shapes of all three ducts.

Table 4.3: Modal phase collinearity values for the measured mode shapes of Duct-1.

Modes	MPC	Modes	MPC
1	0.20	6	0.92
2	0.54	7	0.97
3	0.82	8	0.99
4	0.96	9	0.97
5	0.96	10	0.99

4.5.5   Effect of joint on mode shape

A detailed study is done to understand deviation of measured mode shapes in Duct-1 in presence of a joint. For this study, as shown in Fig. 4.12, the duct is divided into four quarter sections and two C-shape section along an x-x axis and z-z axis, based on the location of welded joints represented by black dots. Figure 4.12(a) shows a cross-sectional view of the rectangular duct, Fig. 4.12(b) shows a quarter section with and without joint, and similarly, Fig. 4.12(c) shows a C-shape section with and without welded joints. Three different approaches are chosen for the study of mode shape deviation along circumferential and axial direction in presence of welded joints such as: (i) MAC analysis for quarter sections with joint and without joint, (ii) MAC analysis for C-section with and without joint conditions and (iii) Mode shape plot at different duct cross-section.

(a) Cross-section of the rectangular duct   (b) Quarter section of the duct without joint   (c) C-section of the duct without joint
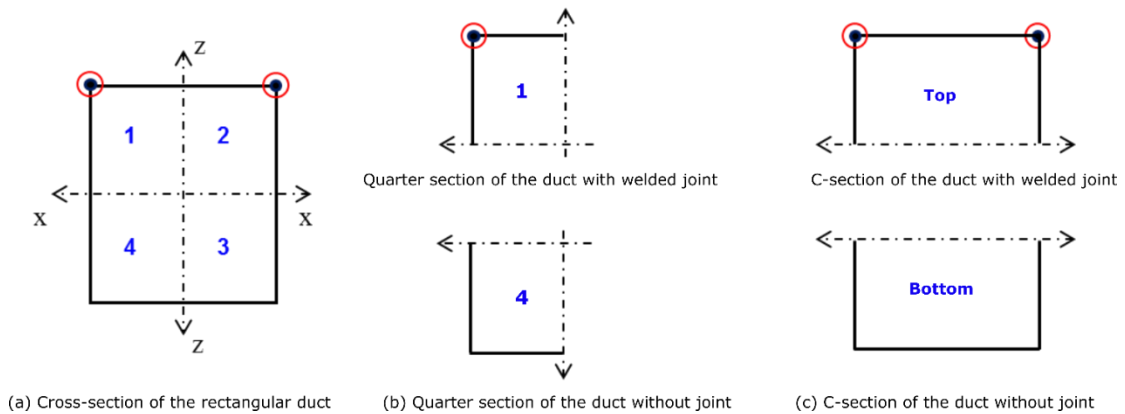
Figure 4.12: Rectangular duct with two welded joints (Duct-1) for the mode shape analysis, (a) Duct cross-section discretized into four quarter sections, (b) Two quarter sections with and without joint condition, and (c) C-section with and without joint conditions.

4.5.5.1 MAC analysis for quarter section of the duct

The duct is divided into four quarter sections along x-x and z-z axis, which are named as 1, 2, 3 and 4 as indicated in Fig. 4.12 (a). Among these, two sections are in joint condition and other two without joint condition. In the present study, two-quarter sections are considered for analysis, as other two-quarter sections replicate the same behavior. One with a welded joint (section-1) and another without joint (section-4) are considered to understand the effect of the single joint on the MAC values. As the duct is axi-symmetric in nature along the central axis of the structure, symmetric boundary conditions can be applied in numerical simulations of a quarter section. In the NMA, four different boundary conditions are applied at x- and z-

cross sectional axes along the y-direction for each quarter section. The conditions are: symmetry-symmetry (S-S), symmetry-antisymmetry (S-AS), antisymmetry-symmetry (AS-S), and antisymmetry-antisymmetry (AS-AS). Here, experimental natural frequencies are extracted by considering measured FRF's included in that particular quarter section.

MAC analysis is done for two-quarter sections of the duct, which are considered in the present study, as shown in Fig. 4.12 (b). MAC plots are presented only for three condition groups such as S-S, S-AS and AS-S, and not for AS-AS modes. Since these modes are complex modes, MAC correlation is not suitable and results in poor values (as discussed in Sec.4.5.4). MAC plot for both quarter sections of the duct i.e. without and with a joint is shown in Fig. 4.13. It is observed that MAC values are higher for duct without joint condition than later case. Another observation was that S-S modes are having good correlation compared to other groups.
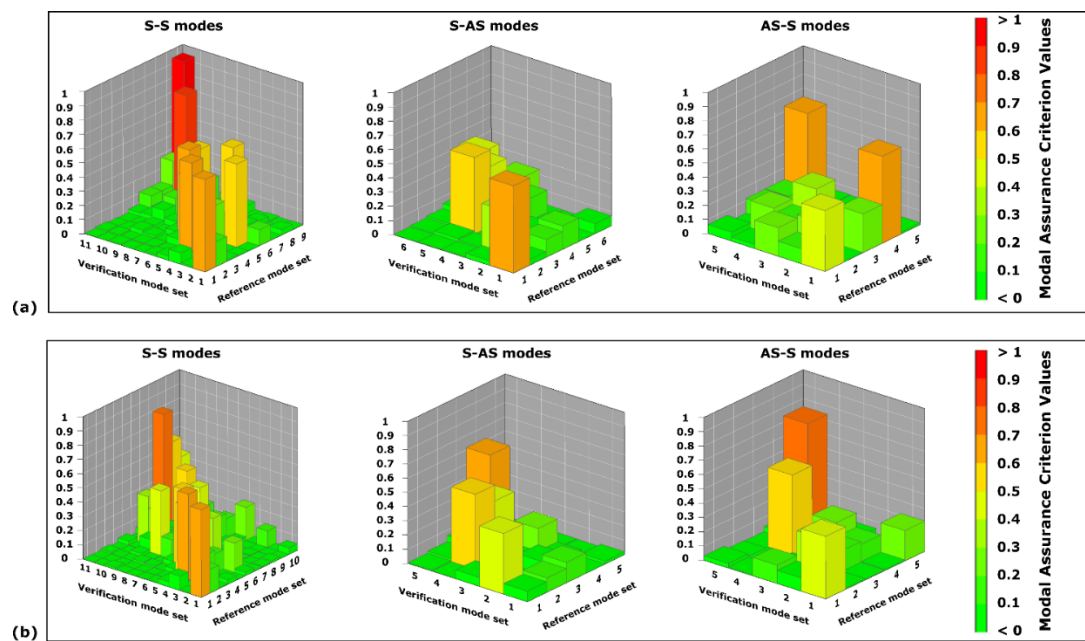
Figure 4.13: MAC plot for the quarter section of Duct-1: (a) without joint, (b) with joint.

4.5.5.2 MAC analysis for C-section of the duct

The duct is divided into two sections along x-x co-ordinate axis, namely; top C-section and bottom C-section. Here, the top section includes two welded joints and the bottom section has no joints. They are considered to understand the effect of two joints on MAC values. Figure 4.14 shows MAC plot for both the cases and MAC value greater than or equal to 0.4 are shown in Table 4.4. It is observed from MAC plot that mode shapes are well correlated in

bottom C-section compared to top C-section, which in turn clearly indicates that the presence of joints affects mode shape of ducts. Sections with joints have lower MAC values and influence full duct MAC values.
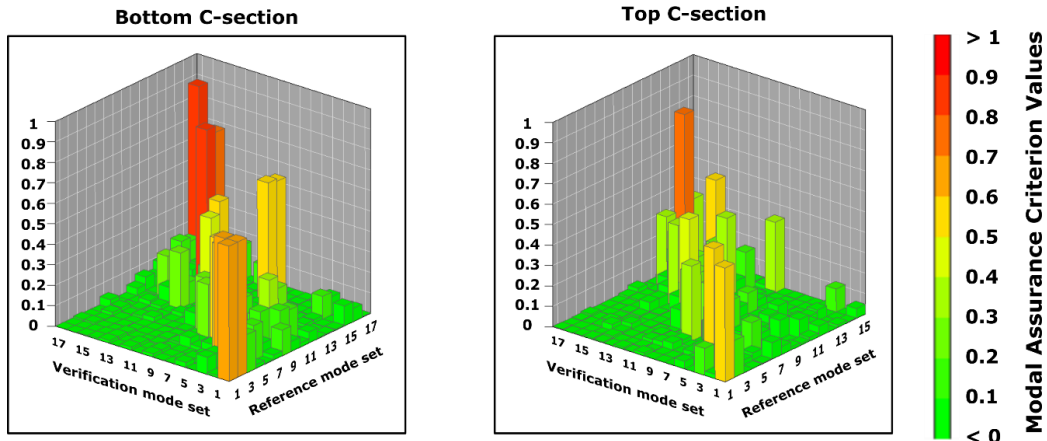
Figure 4.14: MAC plot for the bottom and top C-sections of the Duct-1.

Table 4.4: MAC values for C-section of the Duct-1

f_e (Hz)	f_n (Hz)	MAC Value	
		Without joint	With joint
53.67	56.76	0.66	0.56
76.22	74.63	0.62	0.60
87.31	90.74	0.55	0.37
154.60	151.54	0.52	0.48
156.43	163.68	0.81	0.40
173.65	163.68	0.78	0.53
192.97	127.62	0.57	0.34
201.99	206.34	0.88	0.33

4.5.5.3 Duct mode shape variation in axial direction

Duct mode shape variation at a particular cross-section along axial (y-axis) direction is also studied. The chosen axial positions along the length are 0.25L, 0.5L, 0.75L and L. Five measurement points are considered on each surface of the duct, thus total twenty points are considered at each cross-section. Two different modal frequencies are chosen based on MAC values for comparison study. However, the same exercise can be done for other modes. The chosen modes are mode-3 (53.67 Hz) and mode-8 (97.10 Hz) with a MAC value of 0.66 and 0.38, respectively.

Figures 4.15(a) and (b) shows a comparison of normalized modal displacement of experimental and numerical modal analysis results for mode-3 and mode-8, respectively. Figure 4.15(a) clearly shows that experimental mode shape is in good agreement with numerical results at three different cross-section positions. A small deviation is observed in experimental results at end cross-section (1.2 m) which leads to reduced overall MAC value at this modal frequency. For mode-8, it is observed that modal displacement for side plates of the duct is similar. However, for the top and bottom plates of ducts, there is a large deviation between experimental and numerical results. By observing the Fig. 4.15, it can be concluded that for mode-3, experimental mode shape is in good agreement with numerical mode shape. However, the correlation is poor for mode-8. A similar observation is also made in MAC plot.
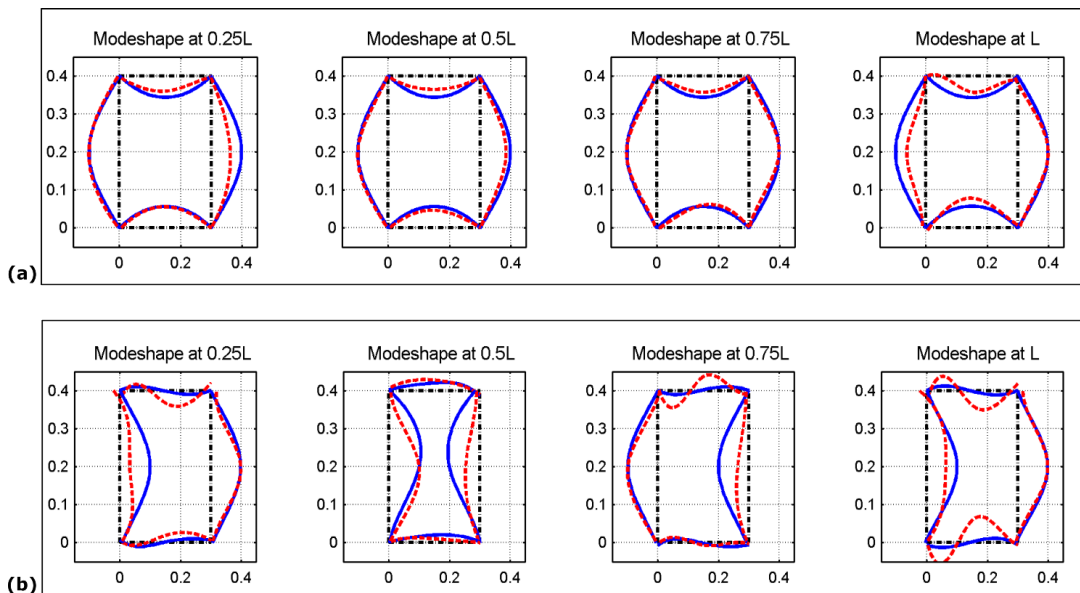
Figure 4.15: Comparison of experimental and numerical mode shapes at different cross-sections: (a) Mode-3, (b) Mode-8. (—Numerical, ⋯ Experimental).

4.6 Summary

Experimental and numerical modal analysis is performed for three different rectangular ducts to study the effect of duct joints on modal parameters. Welded joint conditions in the rectangular duct are modelled with different thickness elements for numerical calculation. Natural frequencies obtained from the experimental modal analysis (measured) are compared with numerical results (predicted). It has been observed from all cases that experimental modal frequencies are in good agreement with numerical modal frequencies, with less than 10% error. Mode shapes of measured and predicted results are compared in terms of MAC

plot, mode pair table and visual inspection. Low MAC values are observed for the duct with welded joints. However, for a duct with adhesive joint similar to the ideal shape, has good MAC value. Modal vector complexity analysis for all three ducts is performed to understand the reason for low MAC values for the first two modes. Detailed section analysis is done on a duct with a two-welded joint configuration to understand mode shape deviation. It is observed that joints play a critical role in deviation of mode shapes for thin flexible structures. It is thus concluded that duct joints have a strong influence on mode shapes compared to natural frequencies. Further studies have been done to incorporate joint conditions in analytical modelling for modal parameter predictions which are discussed in the next chapter.

Chapter 5

Influence of Duct Joint Condition on Modal Parameters of a Rectangular Duct

5.1 Introduction

Ducts are fabricated using thin sheets of metal with different joint conditions. These have deviations from ideal geometric shapes due to joint conditions. Effect of these joints on modal parameters obtained by experimental and numerical modal analysis was discussed in the previous chapter. In this chapter, an analytical model for a rectangular duct with a joint is developed to incorporate joint effects in estimating the modal parameters. In the analytical study, duct with and without joint condition is considered for the analysis. Modal parameters such as natural frequencies and mode shapes are studied in both cases to assess the effect of joint condition. Developed analytical model is validated by comparing modal parameters obtained from experiments for a duct with Pittsburgh lock joint. Effect of joint on modal parameters of the duct system is discussed based on the new analytical model.

5.2 Theoretical formulation

5.2.1 Rayleigh-Ritz approach

Natural frequencies and mode shapes of a rectangular duct can be found analytically by the Rayleigh-Ritz method using an equivalent plate model [55]. The unfolded plate model of a duct with a joint is shown in Fig. 5.1, with dimensions of circumferential length (L_c) and axial length (L_a) and assumed simply supported boundary conditions in axial directions. Here, the joint condition is represented using linear and rotational springs, whereas, in an ideal duct model simply supported boundary condition is used [55, 115].
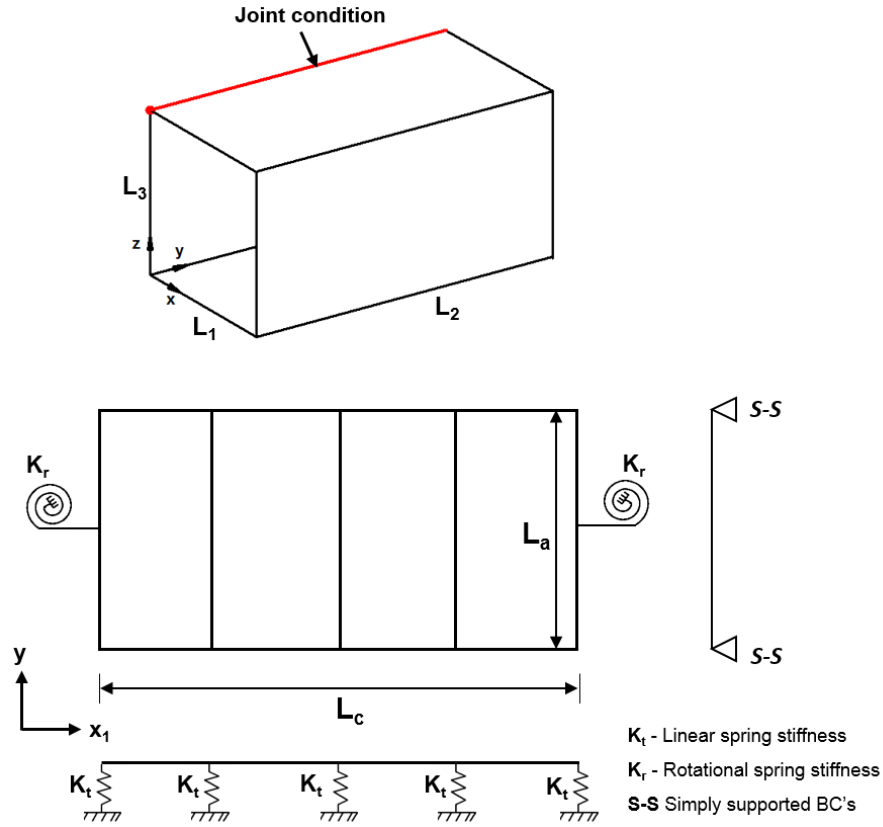
Figure 5.1: Equivalent plate model of a rectangular duct with joint condition.

Admissible basis functions along the circumference direction is a static solution of a beam with three intermediate line supports. Similarly, admissible basis function in the axial direction is static deflection solution of simply supported beam.

The strain energy (U) and kinetic energy (T) of an elastic, thin, isotropic plate can be given (from vibration theory of thin plates) as follows [55],

$$U = \frac{1}{2} \int_0^{L_c} \int_0^{L_a} \left\{ D \left(\frac{\partial^2 w}{\partial x_1^2} \right)^2 + 2D \left(\frac{\partial^2 w}{\partial x_1^2} \right) \left(\frac{\partial^2 w}{\partial y^2} \right) + D \left(\frac{\partial^2 w}{\partial y^2} \right)^2 - 4D_{xy} \left[\left(\frac{\partial^2 w}{\partial x_1^2} \right) \left(\frac{\partial^2 w}{\partial y^2} \right) - \right. \right.$$

$$\left. \left. \left(\frac{\partial^2 w}{\partial x_1 \partial y} \right)^2 \right] \right\} \, dy \, dx_1 \tag{5.1}$$

$$T = \frac{1}{2} \int_0^{L_c} \int_0^{L_a} \rho_s h \left(\frac{\partial w}{\partial t} \right)^2 \, dy \, dx_1 \tag{5.2}$$

Here, w is a flexural deflection of the plate, ρ_s is material density, h is plate thickness, D is flexural rigidity of the plate and $D_{xy} = (1 - \mu) D/2$, where μ is Poisson's ratio. The strain energy due to rotational springs (U_{rs}) is given by,

$$U_{rs} = \frac{1}{2} k_r \int_0^{L_a} \left(\left(\frac{\partial w}{\partial x_1} \right)_{x_1=0,y} - \left(\frac{\partial w}{\partial x_1} \right)_{x=L_c,y} \right)^2 dy \tag{5.3}$$

where, k_r is rotational spring stiffness and deflection w of the plate can be expressed as,

$$w(x_1, y, t) = W(x_1, y) e^{i\omega t} \tag{5.4}$$

In Eq. (5.4), ω is angular frequency and $W(x_1, y)$ is the mode shape function. Let α and β be non-dimensional lengths of the plate along circumferential and axial directions, respectively,

$$\text{i.e.,} \quad \alpha = \frac{x_1}{L_c} \quad \text{and} \quad \beta = \frac{y}{L_a} \tag{5.5}$$

The mode shape function in terms of non-dimensional parameters, i.e. $W(\alpha, \beta)$ can be expressed as,

$$W(\alpha, \beta) = \sum_{m=1}^{\infty} \sum_{n=1}^{\infty} A_{mn} \Phi_m(\alpha) \Psi_n(\beta) \tag{5.6}$$

Here, $\Phi_m(\alpha)$ and $\Psi_n(\beta)$ are admissible functions in circumferential and axial directions, respectively and A_{mn} are unknown coefficients. Displacement function in terms of admissible functions can be expressed as,

$$w(\alpha, \beta, t) = e^{i\omega t} \sum_{m=1}^{\infty} \sum_{n=1}^{\infty} A_{mn} \Phi_m(\alpha) \Psi_n(\beta) \tag{5.7}$$

After making proper substitutions of Eq. (5.7) into Eqs. (5.1) and (5.2) then minimizing the total energy (kinetic and strain) leads to eigen-frequency equation, as follows,

$$\frac{\partial}{\partial A_{mn}} (U_{max} - T_{max}) = 0$$

$$\sum_{m=1}^{\infty} \sum_{n=1}^{\infty} \left[C_{mnij} - \lambda^2 E_{mi}^{(0,0)} F_{nj}^{(0,0)} \right] A_{mn} = 0 \tag{5.8}$$

Here, $\lambda^2 = \frac{\rho h \, \omega^2 b^4}{D}$, where λ are eigen values of the structure and can be obtained by solving Eq. (5.8). The detailed derivation for the eigen-frequency equation is given in *Appendix-B*. Stiffness matrix C_{mnij} is given by,

$$C_{mnij} = C_{plate} + C_{bc} + C_{ts} + C_{rs} \tag{5.9}$$

where, C_{plate} is rectangular plate stiffness, C_{bc} is stiffness induced by boundary conditions, C_{ts} is stiffness induced by translational spring at duct edges and C_{rs} is stiffness induced by rotational springs. Integral functions are given by,

$$E_{mi}^{(r,s)} = \int_0^1 \left(\frac{d^r \Phi_m}{d\alpha^r}\right)\left(\frac{d^s \Phi_i}{d\alpha^s}\right) d\alpha \tag{5.10}$$

$$F_{nj}^{(r,s)} = \int_0^1 \left(\frac{d^r \Psi_n}{d\beta^r}\right)\left(\frac{d^s \Psi_j}{d\beta^s}\right) d\beta \tag{5.11}$$

Admissible functions are kind of functions which are continuous and satisfies all the geometric boundary conditions. These functions are generally selected to have a nominal smoothness and in which integration over the problem domain is compatible. Validity and accuracy of the solution depends entirely on the choice of admissible functions $\Phi_m(\alpha)$ and $\Psi_n(\beta)$. Here, a set of static beam functions are used as admissible functions for line supported rectangular plates.

$$\Phi_m(\alpha) = \boldsymbol{y_m(\alpha)} \quad \text{and} \quad \Psi_n(\beta) = \boldsymbol{y_n(\beta)} \tag{5.12}$$

$\boldsymbol{y_m(\alpha)}$ and $\boldsymbol{y_n(\beta)}$ are the mth and n^{th} static beam functions along circumferential (L_c) and axial (L_a) direction, respectively.

5.2.2 Solution of static beam functions

Static beam functions for equivalent rectangular plate along the circumferential direction with three intermediate supports are given in Ref. [115]. In a similar way, static beam functions along axial direction can be given by the deflection of a beam with end conditions [116]. These functions are shown in Eqs. (5.13) and (5.14) for axial and circumferential direction, respectively.

$$y_n(\beta) = \sum_{k=0}^3 C_k^n \beta^k + \sin(n\pi\beta) \tag{5.13}$$

$$y_m(\alpha) = \sum_{k=0}^3 C_k^m \alpha^k + \sum_{j=1}^3 P_j^m \frac{(\alpha-\alpha_j)^3}{6} U(\alpha - \alpha_j) + \sin(m\pi\alpha) \tag{5.14}$$

where, C_k^n and P_j^m are unknown co-efficient and $U(\alpha - \alpha_j)$ is a Heaviside function. It can be observed from Eqs. (5.13) and (5.14) that second term is added in Eq. (5.13), as there are intermediate supports along the circumferential direction. By using the suitable boundary conditions, unknowns can be determined and which can be written in matrix form as,

$$\begin{bmatrix} A & D \\ T & G \end{bmatrix}\begin{bmatrix} C^m \\ P^m \end{bmatrix} = \begin{bmatrix} R^m \\ S^m \end{bmatrix} \tag{5.15}$$

In Eq. (5.15), $\mathbf{A}$ is $J \times 4$ matrix, $\mathbf{T}$ is 4×4 matrix, and these are first series terms. $\mathbf{D}$ is $J \times J$ matrix, $\mathbf{G}$ is $4 \times J$ matrix, and these are second series terms. $\mathbf{R^m}$ is a $J \times 1$ matrix, $\mathbf{S^m}$ is a 4×1 matrix, and these are the third term of the Eqs. (5.13) and (5.14) for BC of the beam. C^m and P^m are unknowns and are represented as follows,

$$\boldsymbol{C^m} = \begin{bmatrix} C_0^m \\ C_1^m \\ C_2^m \\ C_3^m \end{bmatrix} \qquad \boldsymbol{P^m} = \begin{bmatrix} P_1^m \\ P_2^m \\ P_3^m \end{bmatrix} \tag{5.16}$$

Static beam functions have four unknowns along the axial direction and seven unknowns in the circumferential direction. Boundary conditions used for solving static beam functions are mentioned in next sections.

5.2.3   Boundary conditions along axial direction

Static beam function along the axial direction and its first two derivatives are respectively, given as,

$$y_n(\beta) = C_0^n + C_1^n \beta + C_2^n \beta^2 + C_3^n \beta^3 + \sin(n\pi\beta) \tag{5.17}$$

$$y'_n(\beta) = C_1^n + 2\,C_2^n \beta + 3\,C_3^n \beta^2 + n\pi\,\cos(n\pi\beta) \tag{5.18}$$

$$y''_n(\beta) = 2\,C_2^n + 6\,C_3^n \beta - (n\pi)^2\,\sin(n\pi\beta) \tag{5.19}$$

There are four unknown values in Eq. (5.17) which can be determined by applying simply supported boundary conditions along the axial direction and are given as,

- $y_n(0) = 0$ $i.e.$ $C_0^n = 0$
- $y_n''(0) = 0$ $i.e.$ $2\,C_2^n = 0$
- $y_n(1) = 0$ $i.e.$ $C_0^n + C_1^n + C_2^n + C_3^n = 0$
- $y_n''(1) = 0$ $i.e.$ $2\,C_2^n + 6\,C_3^n = 0$ (5.20) - (5.23)

The Eqs. (5.20) - (5.23) can be written in matrix form as follows,

$$\begin{bmatrix} 1 & 0 & 0 & 0 \\ 0 & 0 & 2 & 0 \\ 1 & 1 & 1 & 1 \\ 0 & 0 & 2 & 6 \end{bmatrix} \begin{bmatrix} C_0^n \\ C_1^n \\ C_2^n \\ C_3^n \end{bmatrix} = \begin{bmatrix} 0 \\ 0 \\ 0 \\ 0 \end{bmatrix} \tag{5.24}$$

5.2.4 Boundary conditions along circumferential direction

Static beam function along the circumferential direction and its first three derivatives are given as follows,

$$y_m(\alpha) = C_0^m + C_1^m \alpha + C_2^m \alpha^2 + C_3^m \alpha^3 + P_1^m \frac{(\alpha-\alpha_1)^3}{6} U(\alpha - \alpha_1) +$$
$$P_2^m \frac{(\alpha-\alpha_2)^3}{6} U(\alpha - \alpha_2) + P_3^m \frac{(\alpha-\alpha_3)^3}{6} U(\alpha - \alpha_3) + sin(m\pi\alpha) \qquad (5.25)$$

$$y_m'(\alpha) = C_1^m + 2 C_2^m \alpha + 3 C_3^m \alpha^2 + P_1^m \frac{(\alpha-\alpha_1)^2}{2} U(\alpha - \alpha_1) +$$
$$P_2^m \frac{(\alpha-\alpha_2)^2}{2} U(\alpha - \alpha_2) + P_3^m \frac{(\alpha-\alpha_3)^2}{2} U(\alpha - \alpha_3) + m\pi \cos(m\pi\alpha) \qquad (5.26)$$

$$y_m''(\alpha) = 2 C_2^m + 6 C_3^m \alpha + P_1^m(\alpha - \alpha_1)U(\alpha - \alpha_1) + P_2^m(\alpha -$$
$$\alpha_2)U(\alpha - \alpha_2) + P_3^m(\alpha - \alpha_3)U(\alpha - \alpha_3) - (m\pi)^2 \sin(m\pi\alpha) \qquad (5.27)$$

$$y_m'''(\alpha) = 6 C_3^m + P_1^m U(\alpha - \alpha_1) + P_2^m U(\alpha - \alpha_2) + P_3^m U(\alpha -$$
$$\alpha_3) - (m\pi)^3 \cos(m\pi\alpha) \qquad (5.28)$$

There are seven unknown values in Eq. (5.25) which can be determined by applying boundary conditions such as zero displacements at the end supports and intermediate line supports. Apart from these, moment continuity and shear force continuity are also maintained at end supports. These are given as follows,

- $y_m(\alpha_1) = 0 \qquad C_0^m + C_1^m \alpha_1 + C_2^m {\alpha_1}^2 + C_3^m {\alpha_1}^3 = -\sin(m\pi\alpha_1) \qquad (5.29)$

- $y_m(\alpha_2) = 0 \qquad C_0^m + C_1^m \alpha_2 + C_2^m {\alpha_2}^2 + C_3^m {\alpha_2}^3 + P_1 \frac{(\alpha_2 - \alpha_1)^3}{6}$
$$= -\sin(m\pi\alpha_2) \qquad (5.30)$$

- $y_m(\alpha_3) = 0$

$$C_0^m + C_1^m \alpha_3 + C_2^m {\alpha_3}^2 + C_3^m {\alpha_3}^3 + P_1 \frac{(\alpha_3-\alpha_1)^3}{6} + P_2 \frac{(\alpha_3-\alpha_2)^3}{6} =$$
$$-\sin(m\pi\alpha_3) \qquad (5.31)$$

- $y_m(0) = 0 \qquad C_0^m = 0 \qquad (5.32)$

- $y_m(1) = 0$

$$C_0^m + C_1^m + C_2^m + C_3^m + P_1^m \frac{(1-\alpha_1)^3}{6} + P_2^m \frac{(1-\alpha_2)^3}{6} \\ + P_3^m \frac{(1-\alpha_3)^3}{6} = 0 \tag{5.33}$$

- $y_m''(0) = y_m''(1)$

$$6\,C_3^m + P_1^m(1-\alpha_1) + P_2^m(1-\alpha_2) + P_3^m(1-\alpha_3) = 0 \tag{5.34}$$

- $EI\,y_m'''(0) + k_t\,y_m(0) = EI\,y_m'''(1)$

$$k_t\,C_0^m - EI(P_1^m + P_2^m + P_3^m) = EI(m\pi)^3\,(1-(-1)^m) \tag{5.35}$$

The Eqs. (5.29) – (5.35) can be written in matrix form as follows,

$$\begin{bmatrix} 1 & \alpha_1 & \alpha_1^2 & \alpha_1^3 & 0 & 0 & 0 \\ 1 & \alpha_2 & \alpha_2^2 & \alpha_2^3 & \frac{(\alpha_2-\alpha_1)^3}{6} & 0 & 0 \\ 1 & \alpha_3 & \alpha_3^2 & \alpha_3^3 & \frac{(\alpha_3-\alpha_1)^3}{6} & \frac{(\alpha_3-\alpha_2)^3}{6} & 0 \\ 1 & 0 & 0 & 0 & 0 & 0 & 0 \\ 1 & 1 & 1 & 1 & \frac{(1-\alpha_1)^3}{6} & \frac{(1-\alpha_2)^3}{6} & \frac{(1-\alpha_3)^3}{6} \\ 0 & 0 & 0 & 6 & 1-\alpha_1 & 1-\alpha_2 & 1-\alpha_3 \\ k_t & 0 & 0 & 0 & -EI & -EI & -EI \end{bmatrix} \begin{Bmatrix} C_0^m \\ C_1^m \\ C_2^m \\ C_3^m \\ P_1^m \\ P_2^m \\ P_3^m \end{Bmatrix} = \begin{Bmatrix} -\sin(m\pi\alpha_1) \\ -\sin(m\pi\alpha_2) \\ -\sin(m\pi\alpha_3) \\ 0 \\ 0 \\ 0 \\ EI(m\pi)^3\,(1-(-1)^m) \end{Bmatrix}$$

$$\tag{5.36}$$

5.3 Experimental modal analysis test setup

An experimental setup for performing the modal test is described in this section. EMA test is conducted on a rectangular duct with simply supported (SS) boundary conditions. A rectangular duct, of dimension 0.3m x 0.4m x 1.2m, is fabricated by bending a galvanized iron (GI) sheet, of thickness 20 gauge (~1mm), at three corners and the edges are connected using Pittsburgh lock joint. Material properties of the duct are, Elastic modulus is (E) is 210 GPa, density (ρ_s) is 7850 kg/m³ and Poisson's ratio (μ) is 0.3. SS condition is attained by inserting steel balls inside rectangular frames for making point contact with duct walls at the front and end portion of the duct as shown in Fig. 5.2.
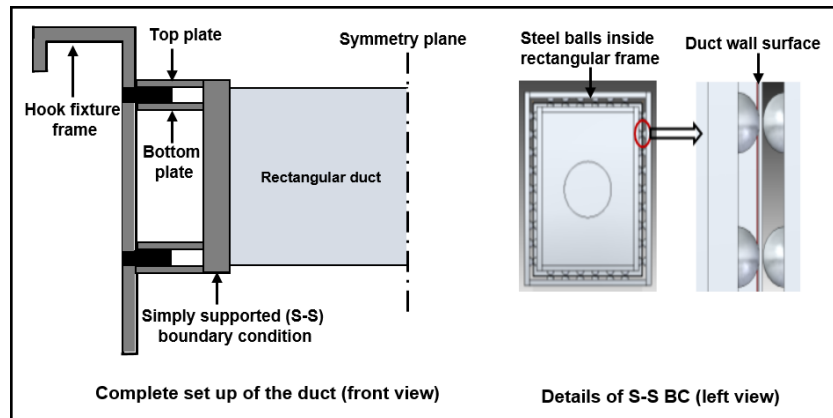
Figure 5.2: Simply-supported boundary condition setup.

EMA setup is shown in Fig. 5.3 and is performed by a roving hammer method. A high sensitivity lightweight tri-axial accelerometer with a sensitivity of 10.11 mV/g, 9.98 mV/g, 9.96 mV/g along x, y and z-directions, respectively and uni-axial accelerometer with 9.62 mV/g sensitivity are used to capture vibration responses of the structure. An impact hammer with a sensitivity of 11.50 mV/N is used for excitation in order to induce vibrations in the structure. Pre-test analysis is done based on numerical modal analysis solution to find a reference point and response locations to mount the accelerometers.

Once the measurement set-up is established, FRFs are then measured with appropriate settings such as sampling frequency, bandwidth, number of samples and windowing function. It is important to verify the quality of acquiring data to ensure measurements are consistent. This is verified by observing input excitation, coherence, and FRFs. Multivariate Mode Indicator Function (MvMIF) is used for extracting modal parameters from the Measured FRFs.
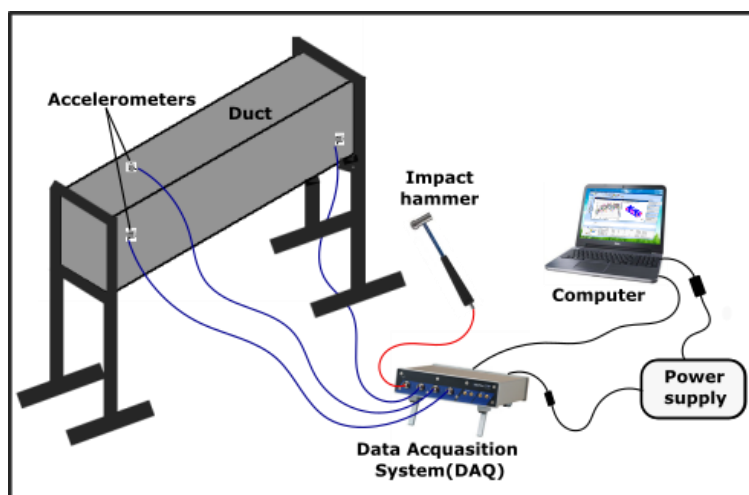
Figure 5.3: Experimental modal analysis test setup

93

5.4 Results and discussion

5.4.1   Modal parameters for duct with joint - Analytical and Experimental

Natural frequencies calculated using current analytical model are compared to experimental results as shown in Table 5.1 for the first ten modes. The rotational spring and translational spring stiffness of 10^{10} are chosen for analytical calculations. Here, f_a represents analytical natural frequencies and f_e represents experimental natural frequencies. It is observed that analytical results are in good agreement with experimental results (with less than 10% error). However, the modes 5, 8 and 10 are not captured in the experimental modal analysis due to higher modal density and geometric symmetry is lost due to the presence of joint condition.

Table 5.1: Comparison of analytical and experimental natural frequencies

Mode Number	f_a (Hz)	f_e (Hz)	% Error
1	20.08	19.82	1.31
2	24.83	22.67	9.53
3	26.16	25.63	2.07
4	29.90	31.65	5.53
5	32.86	-	-
6	36.77	37.6	2.21
7	38.99	41.12	5.18
8	43.36	-	-
9	44.22	46.83	5.57
10	47.14	-	-
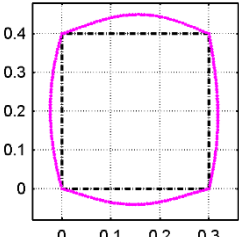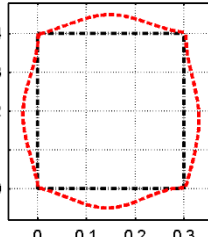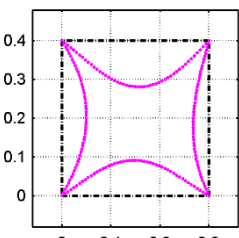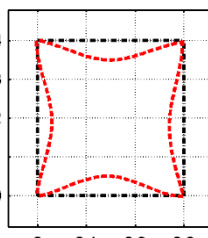
Mode shapes are categorized into two groups namely, symmetric and antisymmetric, based on the distribution of modal displacement on duct surfaces. In the present case, the duct is described by two-panel pairs, i.e. a panel pair along *x*-direction (which includes duct surfaces at *x=0, x=L₁*) and other along *z*- direction (which includes duct surfaces at *z=0, z=L₃*) as shown in Fig. 5.1. Here, for a better understanding of the influence of joint, symmetric and antisymmetric mode shapes are studied separately. In case of the duct with joint condition, joint is located at the top left corner as shown in Fig. 5.1.

5.4.1.1 Comparison of symmetric modes

In case of symmetric modes, modal displacement distribution on a pair of panels have the same amplitude and phase. In other words, the two measuring points on parallel duct surfaces move simultaneously either outward or inward at the same time with respect to the

undeformed duct. Table 5.2 shows a comparison of symmetric mode shapes, calculated analytically and measured experimentally for the duct with a joint condition. From the comparison, it can be observed that mode shapes calculated by the current analytical model are matched well with experimental mode shapes.

Table 5.2: Comparison of analytical and experimental mode shapes for symmetric modes of a duct with a joint
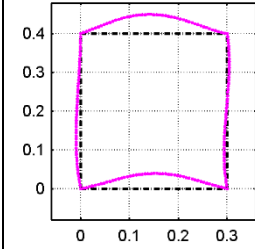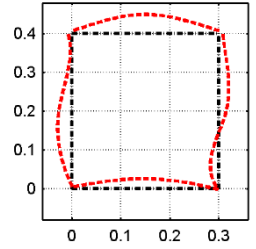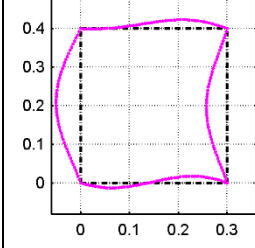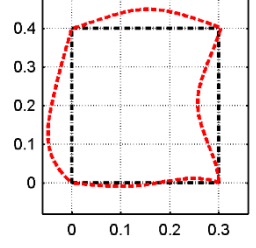
Symmetrical modes	Analytical	Experimental
1	20.08 Hz	19.82 Hz
2	24.83 Hz	22.67 Hz

5.4.1.2 Comparison of antisymmetric modes

Similar to symmetric modes, in case of antisymmetric modes, two measuring points on the parallel surface of the duct walls move with the same amplitude but are out-of-phase (one point moves outward and other inward at the same time with respect to un-deformed duct). Antisymmetric modes of the duct with a joint obtained analytically and experimentally are compared and only two modes are shown in Table 5.3. It is observed that the new analytical model is able to capture the experimental mode shapes very well. In case of mode-3, modal displacement on top and bottom surfaces of the duct is similar but left side surface is not symmetric with the right side surface. This because of joint condition located at the left corner of the duct. Similarly, for mode-7, the modal displacement on top surface is not uniform with the bottom surface. It can be noticed that deviation in the mode shapes (for antisymmetric modes) due to the presence of the joint condition is captured nicely in both experimental and

analytical results. The deviation in the mode shapes observed clearly in the neighbouring duct surfaces of the joint condition.

Table 5.3: Comparison of analytical and experimental mode shapes for antisymmetric modes of a duct with a joint

Asymmetrical modes	Analytical	Experimental
3	26.16 Hz	25.63 Hz
7	38.99 Hz	41.12 Hz

5.4.2 Modal parameters for duct with and without joint – Analytical

Natural frequencies of the duct (with and without joint condition) are compared in order to identify a shift in frequencies due to the presence of joint. Natural frequencies of the modified model (duct with joints) are compared to ideal duct model for fixed rotational spring stiffness (k_r) with varying translational spring stiffness (k_t) and vice-versa. Corresponding results are shown in Tables 5.4 to 5.6. Here, mode numbers indicated with 'S' represents symmetric modes and 'AS' represents antisymmetric modes.

It is observed from Table 5.4 that natural frequencies of the duct with a joint are not affected by the change in translational spring stiffness value (k_t). Further, natural frequencies of the ducts with and without joints are found to be in good agreement. However, it is noticed from Table 5.5 and 5.6 that, as rotational spring stiffness value (k_r) increases, natural frequencies of the duct with joints are an approach to that of the ideal duct. It can also be observed that the rotational spring stiffness value of 10^5 is sufficient to obtain natural frequencies closer to ideal duct case.

Table 5.4: Comparison of duct natural frequencies for fixed k_r and varying k_t in the analytical model.

Mode Number	Frequency (Hz) (Ideal case)	Frequency (Hz) (Duct with joint)			
	$k_r=10^{10}$ $k_t=0$	$k_r=10^{10}$ $k_t=10^{10}$	$k_r=10^{10}$ $k_t=10^{5}$	$k_r=10^{10}$ $k_t=10$	$k_r=10^{10}$ $k_t=0$
S	20.13	20.08	20.08	20.08	20.08
S	24.89	24.83	24.83	24.83	24.83
AS	26.65	26.16	26.16	26.16	26.16
AS	30.38	29.90	29.90	29.90	29.90
S	32.93	32.86	32.86	32.86	32.86
AS	37.22	36.77	36.77	36.77	36.77
AS	39.35	38.99	38.99	38.99	38.99
AS	43.73	43.36	43.36	43.36	43.36
S	44.29	44.22	44.22	44.22	44.22
AS	47.56	47.14	47.14	47.14	47.14

Table 5.5: Comparison of duct natural frequencies for varying k_r and fixed k_t in the analytical model.

Mode Number	Frequency (Hz) (Ideal case)	Frequency (Hz) (Duct with joint)			
	$k_r=10^{10}$ $k_t=0$	$k_r=0$ $k_t=0$	$k_r=10$ $k_t=0$	$k_r=10^{5}$ $k_t=0$	$k_r=10^{10}$ $k_t=0$
S	20.13	19.23	19.84	20.08	20.08
S	24.89	22.64	24.45	24.83	24.83
AS	26.65	23.95	24.57	26.16	26.16
AS	30.38	26.98	28.36	29.90	29.90
S	32.93	31.96	32.55	32.86	32.86
AS	37.22	34.53	35.47	36.77	36.77
AS	39.35	36.12	37.61	38.99	38.99
AS	43.73	40.41	41.91	43.36	43.36
S	44.29	43.31	43.87	44.22	44.22
AS	47.56	44.24	46.03	47.14	47.14

Mode shapes calculated analytically for the duct with and without joints are compared. As mentioned in the earlier Sec.5.4.1 for a better understanding of the joint effects, symmetric and antisymmetric mode shapes are studied separately. Table 5.7 shows a comparison of the first three symmetric modes and antisymmetric modes of the rectangular duct with a joint and without joint condition. In the case of symmetric modes, it is noticed that there is a good correlation between the two cases compared and it can be observed that symmetric modes are

not affected due to the presence of joints. These modes are observed to be breathing modes and have a maximum modal displacement [As discussed in Chapter-2].

Table 5.6: Comparison of duct natural frequencies for varying k_r and fixed k_t in the analytical model.

Mode Number	Frequency (Hz) (Ideal case)	Frequency (Hz) (Duct with joint)			
	$k_r =10^{10}$ $k_t =0$	$k_r =0$ $k_t =10^{10}$	$k_r =10$ $k_t =10^{10}$	$k_r =10^5$ $k_t =10^{10}$	$k_r =10^{10}$ $k_t =10^{10}$
S	20.13	19.23	19.85	20.09	20.09
S	24.89	22.65	24.45	24.84	24.84
AS	26.65	23.96	24.57	26.17	26.17
AS	30.38	26.98	28.37	29.91	29.91
S	32.93	31.96	32.56	32.87	32.87
AS	37.22	34.54	35.48	36.78	36.78
AS	39.35	36.12	37.61	39.00	39.00
AS	43.73	40.42	41.92	43.36	43.36
S	44.29	43.32	43.87	44.23	44.23
AS	47.56	44.25	46.04	47.15	47.15
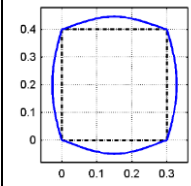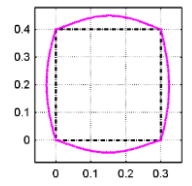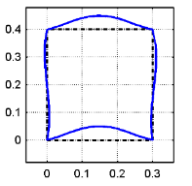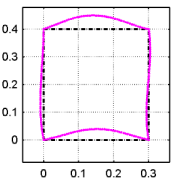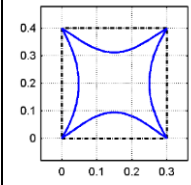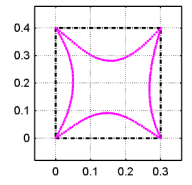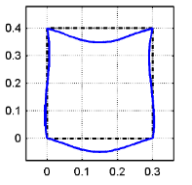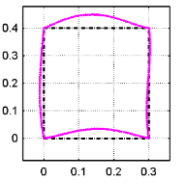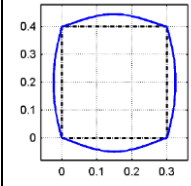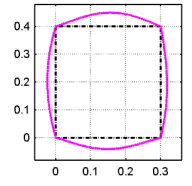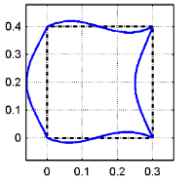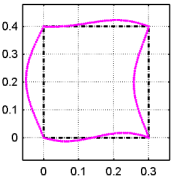
In case of antisymmetric modes, it is observed that mode shapes of the duct with joint showed deviation from ideal duct mode shapes. The antisymmetric behaviour doesn't appear on top and left plates of the duct with the joint. It is observed that vibration modes for a duct with joint condition deviate from that of ideal duct for antisymmetric modes only. The deviation from ideal duct behaviour is observed adjacent to the joint condition.

Effect on joint condition observed only in mode shape, not for natural frequencies. It clear that the joint condition affects only local behaviour (of mode shapes) not the global behaviour of the duct (natural frequencies).

5.5 Summary

An analytical model has been developed to predict the modal parameters of the rectangular duct with a joint condition. Here, the joint condition is modelled using linear and rotational springs. Analytical model results are validated with experimental results of a rectangular duct with Pittsburgh lock joint. Both natural frequencies and mode shapes calculated from the current analytical model are in good agreement with the experimental results.

Table 5.7: Comparison of symmetric and antisymmetric modes for a duct with and without joint

Symmetrical modes			Asymmetrical modes		
Mode No.	Ideal duct	Duct with joint	Mode No.	Ideal duct	Duct with joint
1			3		
2			4		
5			7		

To understand the influence of duct joint on modal parameters, a comparison study has been performed between the duct with and without joint condition (ideal duct). Natural frequencies of the duct in both cases are found to be in good agreement. Mode shapes for symmetric modes remained the same for the duct with and without joint, whereas antisymmetric modes deviate from each other.

It is clearly noticed from the current study that the presence of duct joint has a negligible effect on duct natural frequencies. However, mode shapes (only antisymmetric modes) of the duct with a joint deviate from that of an ideal duct. This deviation is observed only in duct walls next to the joints. So, it can be concluded that duct joint condition can affect mode shapes of the structure, but may not necessarily change natural frequencies.

Chapter 6

Inverse Numerical Acoustic Analysis of a Flexible Rectangular Duct

6.1 Introduction

Noise radiates efficiently from the duct at uncoupled structural natural frequencies and at coupled frequencies due to structural-acoustic coupling. It is important to know the vibration velocity on flexible duct surface to understand dominant vibration modes in noise radiation. Thin duct wall vibrations can be measured by either direct method such as non-contact laser vibrometer or in-direct method like Inverse Numerical Acoustics (INA) technique. INA is the reconstruction technique in which surface vibration velocities can be reconstructed using measured sound pressure in the near-field. INA can be implemented using both direct and indirect boundary element methods.

Main interest of the present study is to reconstruct normal vibration velocity on duct surface by INA technique at coupled and uncoupled frequencies with measured sound pressure at field points. A rectangular duct with constant velocity piston excitation source is used for the sound radiation analysis in Finite-Element Analysis (FEA). A simply supported boundary condition is applied at both ends of the duct. In the first step, sound pressure in near-field is calculated using numerical simulation methods (FEM-BEM coupled analysis). The radiated sound power is also calculated. Sound pressure obtained by numerical simulations is assumed as measured data in the present study. In second step, simulated pressure is used for INA demonstration to understand critical parameters to be considered for the actual test. Effect of pressure measurement points, measurement location and mesh density on the vibration velocity reconstruction is studied at both coupled and uncoupled frequencies. Regularization with L-curve parameter selection method is used to solve the ill-posed inverse problem. The reconstructed results are compared to actual vibration velocity obtained from coupled analysis.

6.2 Theoretical formulation

Sound radiated from the source due to vibration is calculated using Helmholtz integral equation. Sound pressure measured in the field plane is given by [117,103],

$$p_F = -\int_S \left(i\rho\omega G v_n + p_S \frac{\partial G}{\partial n}\right) dS \tag{6.1}$$

where, p_F is sound pressure measured in the field plane, p_S is sound pressure on the source plane, G is free space Green's function, v_n is normal vibration velocity on the source and n is unit normal on sound radiating surface S directed away from the sound source. Eq. (6.1) can be written in the matrix form as follows,

$$\{p_F\} = [H_F]\{p_S\} + [G_F]\{v_n\} \tag{6.2}$$

Sound pressure on the source surface are related to the surface vibrations is given by [103],

$$[H_S]\{p_S\} = [G_S]\{v_n\} \tag{6.3}$$

$$\{p_S\} = [H_S]^{-1}[G_S]\{v_n\} \tag{6.4}$$

Here, $[H_S]$, $[G_S]$ are N x N matrices and N is the number of nodes on source surface. Upon substituting Eq. (6.4) in Eq. (6.2), the relation between field point sound pressure and vibration velocity on the source can be written as,

$$\{p_F\} = ([H_F][H_S]^{-1}[G_S] + [G_F])\{v_n\}$$

$$\{p_F\} = [ATM]\{v_n\} \tag{6.5}$$

In Eq. (6.5), $[ATM] = [H_F][H_S]^{-1}[G_S] + [G_F]$ is the Acoustic Transfer Matrix which relates field point pressure to vibration velocity on the source surface.

In INA technique, normal vibration velocity (v_n) has to be calculated using the measured field pressure (p_F). Generally, number of pressure measuring points is less than reconstruction points. Hence, *ATM* matrix is not a square matrix and therefore the vibration velocity (v_n) can be obtained by applying the Singular Value Decomposition (SVD) algorithm to Eq. (6.5) and is given by,

$$[ATM]_{MXN}^T = [A]_{NXM} = [U]_{NXM}[\Sigma]_{MXM}[V]_{MXM}^T \tag{6.6}$$

Here, $[\Sigma]$ is diagonal matrix of the singular values (σ_i) of A. $[U]$ and $[V]$ are orthogonal matrices, which satisfy $[U]^T[U] = [V][V]^T = [I]$ condition.

Further, Eq. (6.5) can be rewritten as,

$$\{p_F\} = [ATM]\{v_n\} = [V][\Sigma][U]^T\{v_n\}$$

$$\{v_n\} = [ATM]^+\{p_F\} \tag{6.7}$$

Equation (6.7) shows the reconstructed vibration velocity, where $[ATM]^+$ is called Moore-Penrose pseudo inverse of the acoustic transfer matrix.

6.2.1 Methodology

The procedure involved in reconstruction of vibration velocity by INA technique is illustrated in Fig. 6.1. In the first step, boundary mesh model is prepared where the vibration velocity has to be reconstructed by including necessary boundary conditions like defining the rigid surfaces and acoustic treatments such as absorption. In the second step, first part is to create a field point mesh where sound pressures to be measured. Then, Acoustic Transfer Vector (ATV) between duct wall surface and field point is calculated using Boundary Element Method (BEM). These ATVs constitute the transfer matrix between source and receiver, and may lead to the ill-posed problem while applying matrix inversion. In the third step, the vibration velocity can be determined by inverse analysis using measured pressures and the ATV. Regularization has to be applied in the inverse analysis to overcome the ill-posed condition of ATV's and to reduce reconstruction error.

Step 1: Model preparation
➤ Build Boundary Mesh
➤ Apply Acoustic BC's

Step 2: ATV generation
➤ Create Field Mesh
➤ Calculate ATV's

Step 3: INA reconstruction
➤ Input measured sound pressure
➤ Inverse analysis
➤ Calculate Surface Vibration
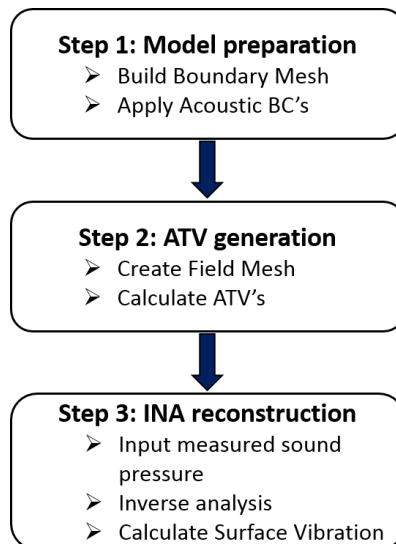
Figure 6.1: Procedure involved in INA reconstruction technique.

6.3 Results and discussion

6.3.1   Numerical models for FEM-BEM analysis

A rectangular duct of dimension 0.206 m x 0.258 m x 0.9 m with 6mm thick is considered for the analysis. The duct is made up of acrylic sheet material and has following properties: Density is $1100 \, kg/m^3$, Young's modulus is 3.2 GPa, Poisson's ratio is 0.4. A numerical model of a duct structure is shown in Fig.6.2 (a) which is meshed using SHELL-63 elements. A simply supported (SS) boundary condition is applied at both ends of the duct as shown in the Fig. 6.2(a).

An acoustic model is created by modeling the enclosed duct of dimensions 0.206 m x 0.258m x 0.9 m and meshed using SOLID-185 elements as shown in Fig.6.2 (b). Acoustic medium properties such as speed of sound-340 m/s and density-1.225 kg/m^3 are applied to the acoustic volume. A constant velocity input source is applied at one end of the duct and acoustically rigid end terminal boundary condition is applied.
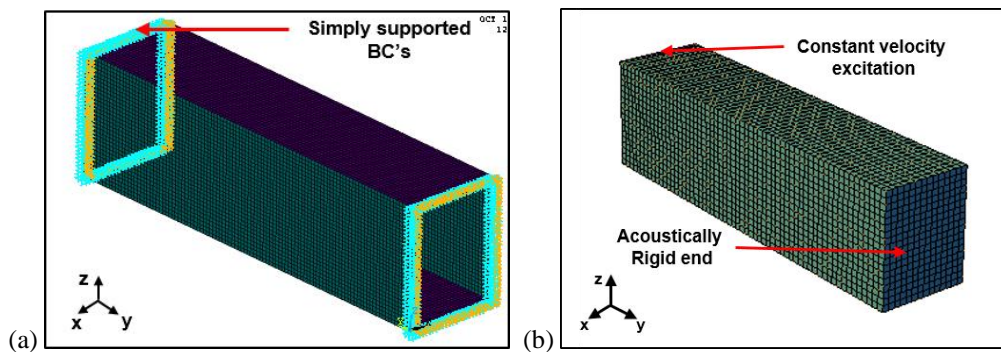
Figure 6.2: Numerical models to calculate the radiated sound power: (a) Structural model and (b) Acoustic model.

6.3.2   Radiated sound power

Sound radiated from the flexible duct wall surface is expressed in terms of sound power level. Figure 6.3 shows the radiated sound power level with respect to frequency. The peaks indicate that sound radiates efficiently at these frequencies. As discussed in earlier chapters, sound radiated from the duct walls is effective at uncoupled structural frequencies and at structural-acoustic coupled frequencies. It is observed from the graph that sound radiates efficiently at an uncoupled frequency of 100 Hz and at coupled frequencies of 235 and 257 Hz. In the present study, sound pressure is measured by virtual microphones at these frequencies to reconstruct vibration velocities.
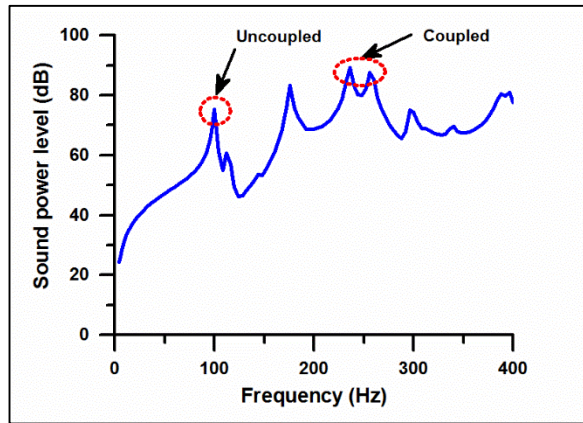
Figure 6.3: Radiated sound power level as a function of frequency for an acrylic duct.

6.3.3 Acoustic Transfer Matrix (ATM)

Acoustic transfer matrix as shown in Eq. (6.5) relates the sound pressures at different locations and structural velocities of vibrating surfaces. It plays an important role in the reconstruction of vibration velocities on the source surfaces for known sound pressures. This ATM depends on different parameters such as: (i) Geometry of source (vibrating surfaces), (ii) Measurement location, (iii) Acoustic boundary conditions like rigid surfaces, absorption surfaces (can be represented in terms of impedance or admittance), (iv) Interested frequencies and physical properties of acoustic medium. Hence, it is important to verify ATM used in INA reconstruction technique which can be done by comparing sound pressures or power in the field planes near sound radiating source.
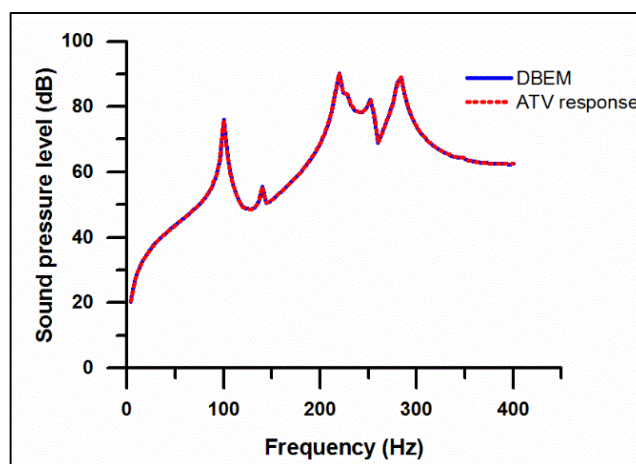
Figure 6.4: Comparison of the sound pressure level on the field plane calculated by BEM analysis and ATV response analysis.

In the present study, primarily, acoustic transfer vectors (ATVs) are calculated for considered rectangular geometry and measurement points. Then, sound pressure in field planes is calculated using acoustic transfer matrix (ATV response analysis). These results are compared to sound pressure levels obtained from FEM-BEM coupled analysis as shown in Fig. 6.4. It can be observed that both results are matching very well at complete frequency range. It is clear that the calculated ATM is correct and can be further used for reconstructing vibration velocities in INA method.

6.3.4   Selection of number of measurement points

It is important to select an appropriate number of measurement points and their distribution in order to obtain accurate reconstructed results. Measured information should be unique and complete. Here, uniqueness means individual measurement point that gives distinct information of a sound field. Generally, as a rule of thumb, the distance between two measurement points should be less than $\lambda_{min}/2$ [118]. Maximum interested frequency in the present analysis is 400 Hz, hence $\lambda_{min}/2 = 0.425$. Based upon this, number of measurement points selected in the present analysis is taken as 308, 240 and 128.

(a)   (b)

(c)
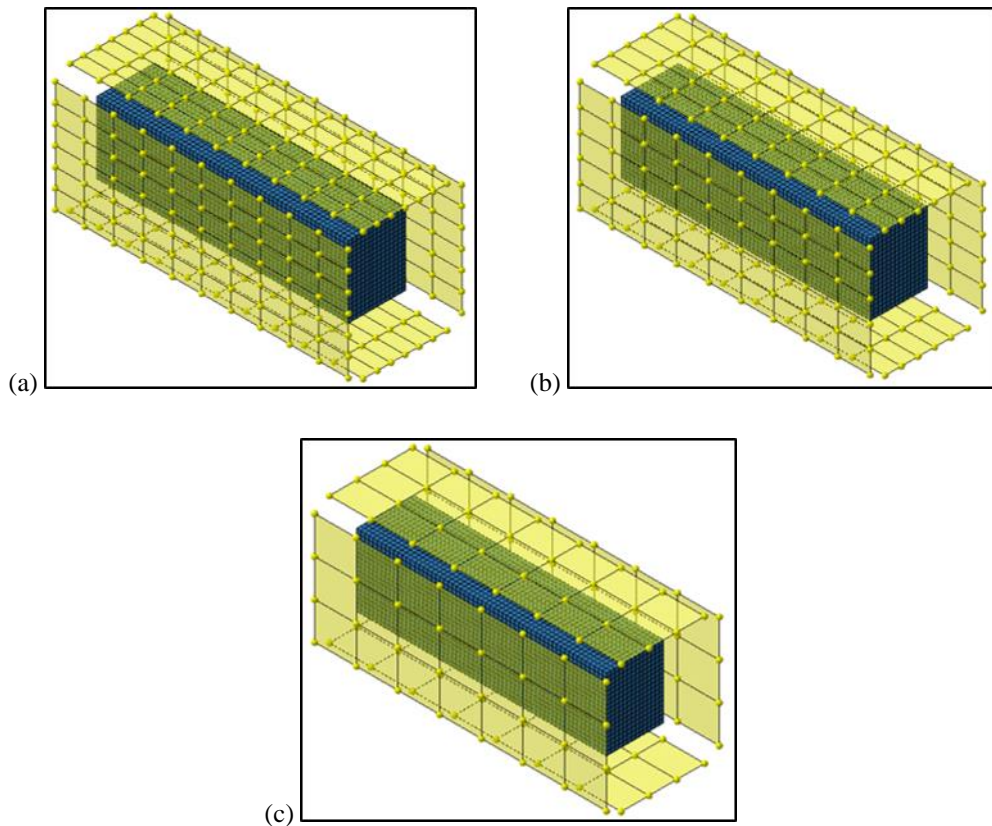
Figure 6.5: Total number of measurement points in field planes (a) 308 points (b) 240 points and (c) 128 points.

Figure 6.5 shows a set of field points on different measurement planes considered in reconstruction analysis. These measurement planes are located at a distance of 0.01m from the duct wall surfaces in all four directions. Sound pressures at all these points are calculated using numerical simulations (BEM analysis) and used for reconstruction.

Figure 6.6 shows a comparison of actual vibration velocity with reconstructed results for three different set of measurements at uncoupled frequency 100 Hz. It is observed that considering a higher number of points does not lead to good reconstruction results. This is due to a large number of measurements capturing non-unique and similar information resulting in a large number of singular values. Fig. 6.6(c) shows considerable improvement in reconstruction. However, it can be seen that 128 number of field points are sufficient to obtain good reconstruction results as shown in Fig. 6.6(d). There is a small deviation in vibration velocity pattern and magnitude.
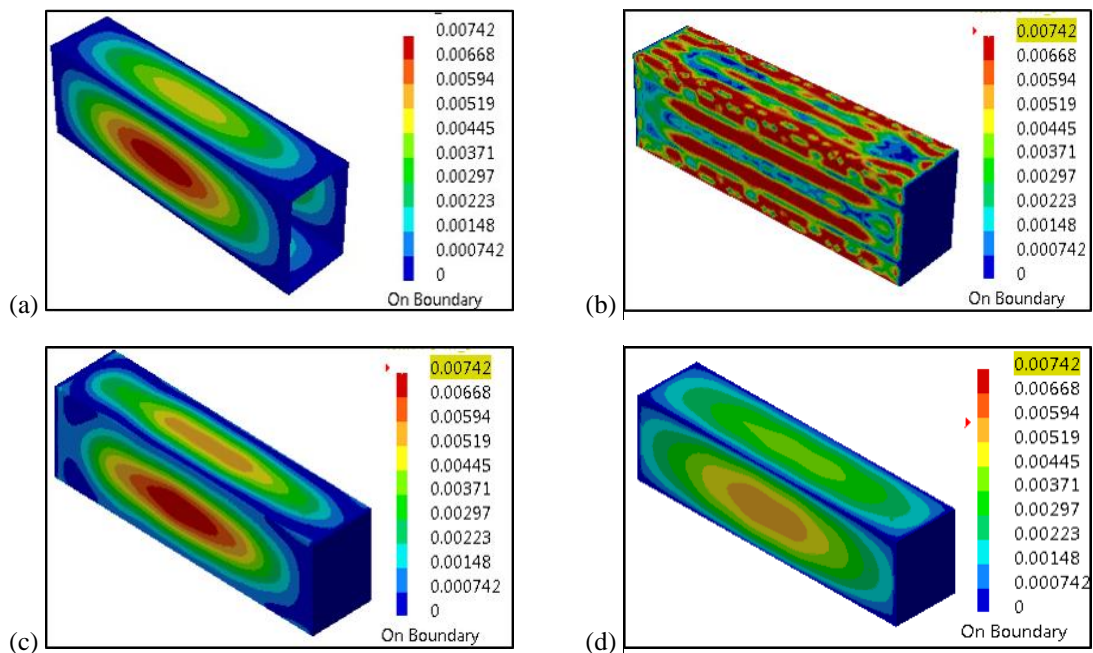
Figure 6.6: Comparison of reconstructed and actual vibration velocities at uncoupled frequency 100 Hz (a) actual (b) reconstructed using 308 field points (c) 240 field points (d) 128 field points.

Figure 6.7 shows a comparison of actual vibration velocity with reconstructed results for three different set of measurement points such as 308, 240 and 128 points at coupled frequency 257 Hz. Here too reconstruction results obtained using 128 number of field points are closer to the actual results. It is abundantly clear that total 128 number of measurement points are sufficient for the duct considered in this study. However, optimum distance for the

measurement plane from source surface needs to be determined for these 128 points. This is further discussed in the next section.
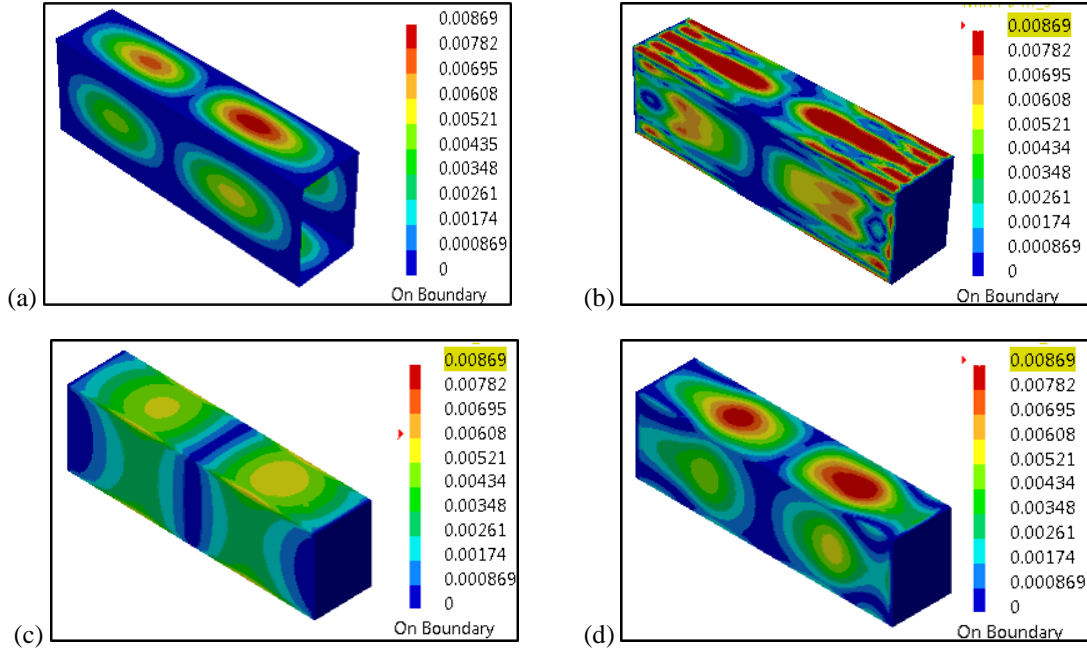
Figure 6.7: Comparison of reconstructed and actual vibration velocities at coupled frequency 257 Hz (a) actual (b) reconstructed using 308 field points (c) 240 field points (d) 128 field points.

6.3.5   Selection of measurement location

Location of measurement plane has to be selected in such a way that measuring points should capture 'enough' information of the sound field [103]. Otherwise, if measurement plane is close to source surface then information only in the localized region is captured. The other criterion to be satisfied for selecting the measurement plane is, a distance of the plane from source surface to be greater than the spacing between measurement points. However, this distance can be chosen based on reactivity and should be less than 7 dB to obtain good measurements [As discussed in Sec. 3.4. and 3.5]. Reactivity is defined as the ratio of reactive intensity (I_r) to active intensity (I_a) and can be given by the following Eq. (6.8),

$$\text{Reactivity} = 10\log_{10}\left(\frac{I_r}{I_a}\right) \tag{6.8}$$

In the current study, four different measurements planes are chosen at a distance of 0.05m interval from duct's surface. These are named as field plane (FP) 1-4, respectively. The active and reactive sound power radiated from all four flexible surfaces of a duct is calculated. Reactivity, calculated using the Eq. (6.8) near the duct walls on the different field planes is

shown in Fig. 6.8. It is shown that reactivity is maximum in FP-1 and is not suitable for measurements as reactivity is not within acceptable standard values. However, it is observed in Fig. 6.8 that maximum reactivity is less than 7 dB in FP-3 and FP-4 within the frequency range of 50 to 400 Hz.
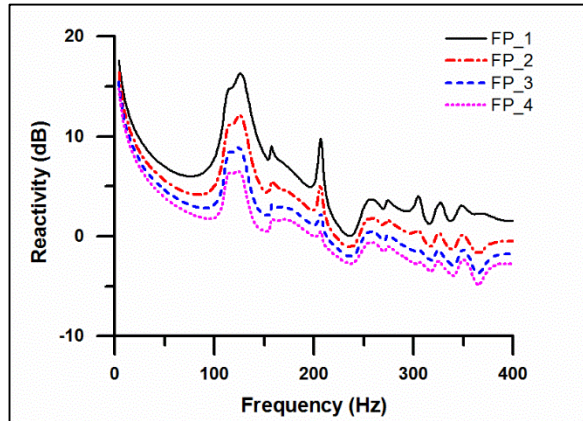
Figure 6.8: Reactivity of the four different measurement field planes.

Based on the above criteria, sound pressure is measured at a distance of 0.1m (FP2) and 0.15m (FP3) from duct's surface in the present analysis. 128 number of measurement points are used to measure the sound pressure. Figures 6.9 and 6.10 show the comparison of reconstructed results with actual vibration velocities for both uncoupled frequency of 100 Hz and coupled frequency of 257 Hz, respectively. It is observed from Fig. 6.9 that at an uncoupled frequency, vibration velocity pattern reconstructed using 0.15m measurement plane is in good agreement with actual results. However, at coupled frequency there is a small discrepancy in the reconstructed result at end and mid-surfaces of the duct and is shown in Fig. 6.10.

It can also be noticed that the reconstructed vibration velocity pattern is matching well with actual vibration velocity pattern. However, there is a deviation in the magnitude of reconstructed vibration velocity.
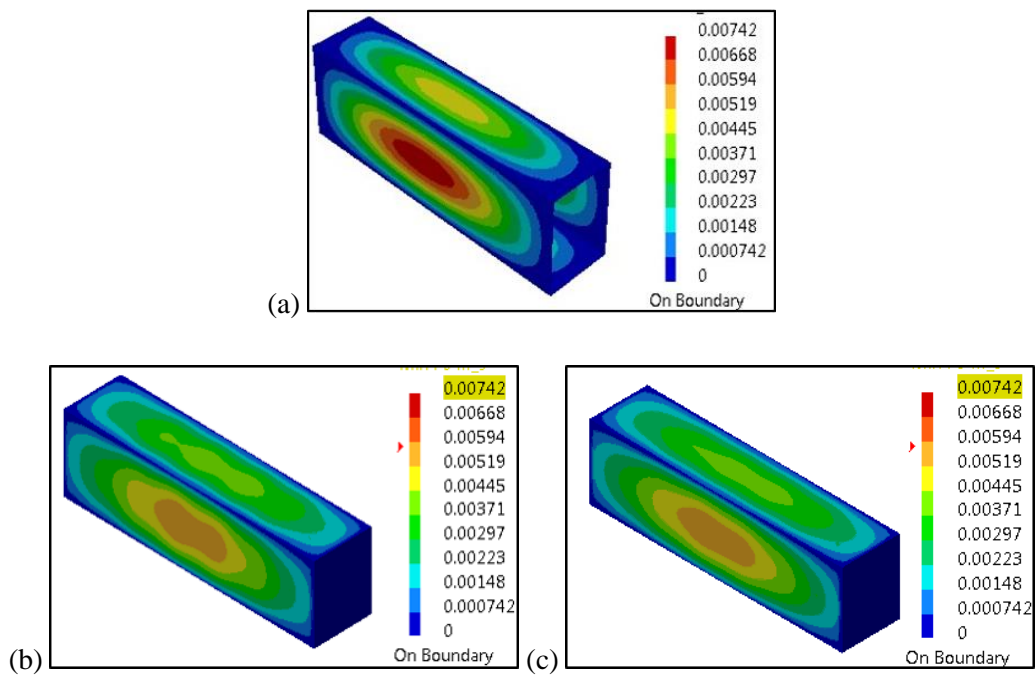
Figure 6.9: Comparison of reconstructed and actual vibration velocities at uncoupled frequency of 100 Hz for different measurement locations. (a) Actual, (b) Reconstructed by using 0.1m plane data, (c) Reconstructed by using 0.15m plane data.
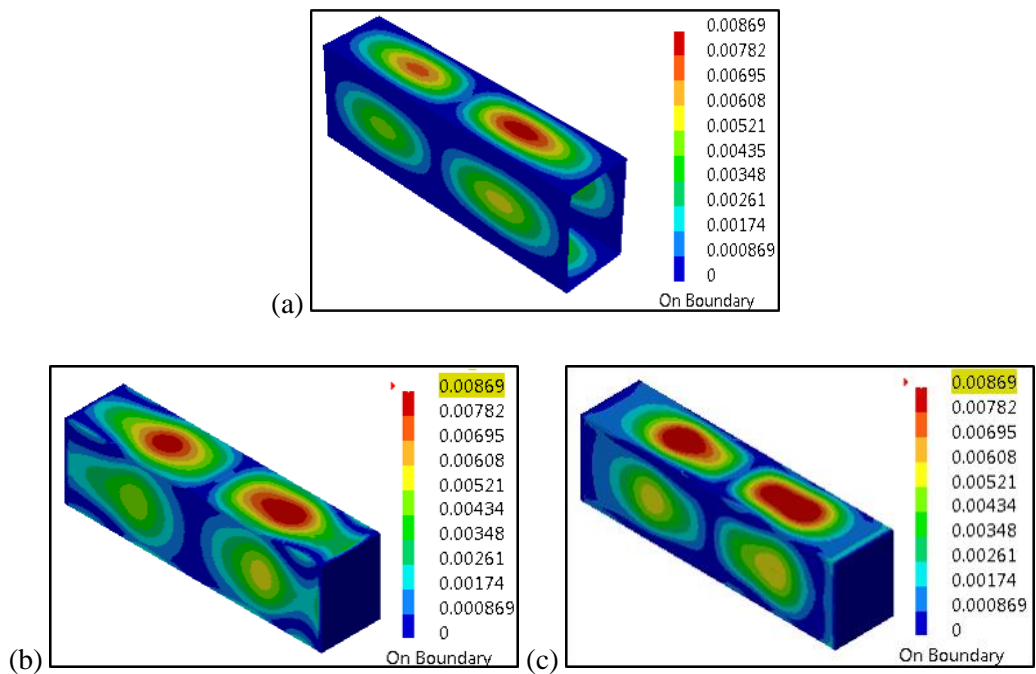
Figure 6.10: Comparison of reconstructed and actual vibration velocities at a coupled frequency of 257 Hz for different measurement locations. (a) Actual, (b) Reconstructed by using 0.1m plane data, (c) Reconstructed by using 0.15m plane data.

6.3.6 Effect of mesh density

Similar to selecting the number of sound pressure measurement points, considering number of nodes for reconstruction is also important to obtain good reconstruction results. In the present analysis, two different cases are considered. In first case, element edge length of 0.015m is used for meshing and in second case 0.01m is used. Comparison of reconstructed results for these two cases are shown in Fig. 6.11 and Fig. 6.12 for uncoupled and coupled frequencies, respectively. It is observed that vibration velocity reconstructed using finer mesh density (edge length = 0.01m) provides accurate results. It can be observed that not only the pattern of reconstructed vibration velocity but magnitude too in good agreement with actual vibration velocity. For chosen duct configuration, the magnitude of maximum actual velocity is 0.00742 m/s and reconstructed velocity is 0.00734 m/s for uncoupled frequency of 100 Hz. In case of coupled frequency, actual velocity is 0.00869 and reconstructed velocity is 0.0102 m/s. It displays a small deviation between these results.
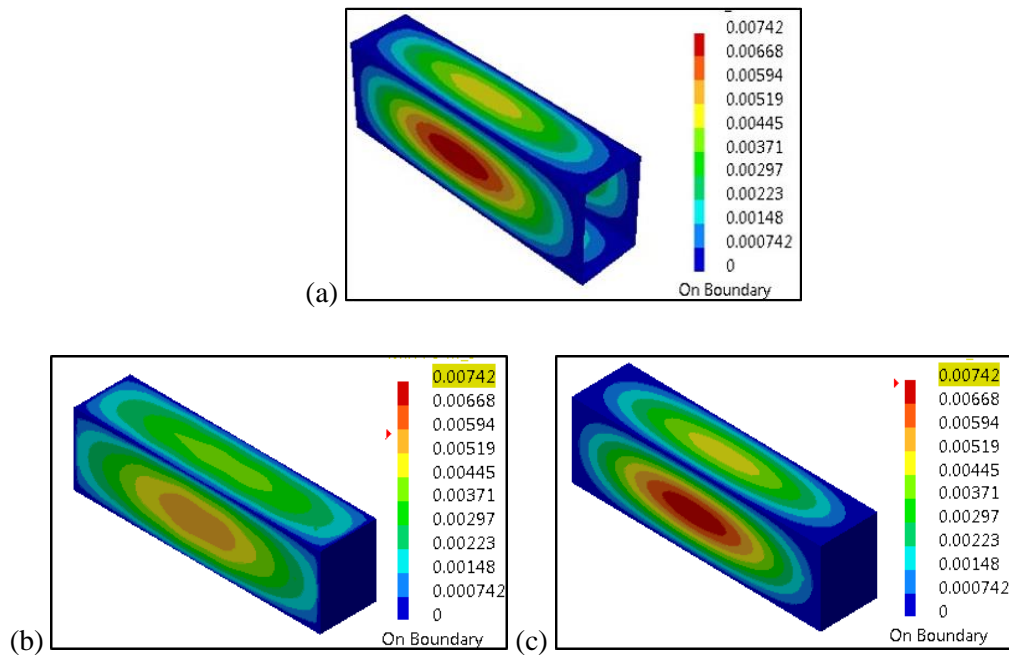
Figure 6.11: Comparison of reconstructed and actual vibration velocities at an uncoupled frequency of 100 Hz for different mesh density. (a) Actual, (b) Reconstructed by using 0.015m element edge length, (c) Reconstructed by using 0.01m element edge length.

110
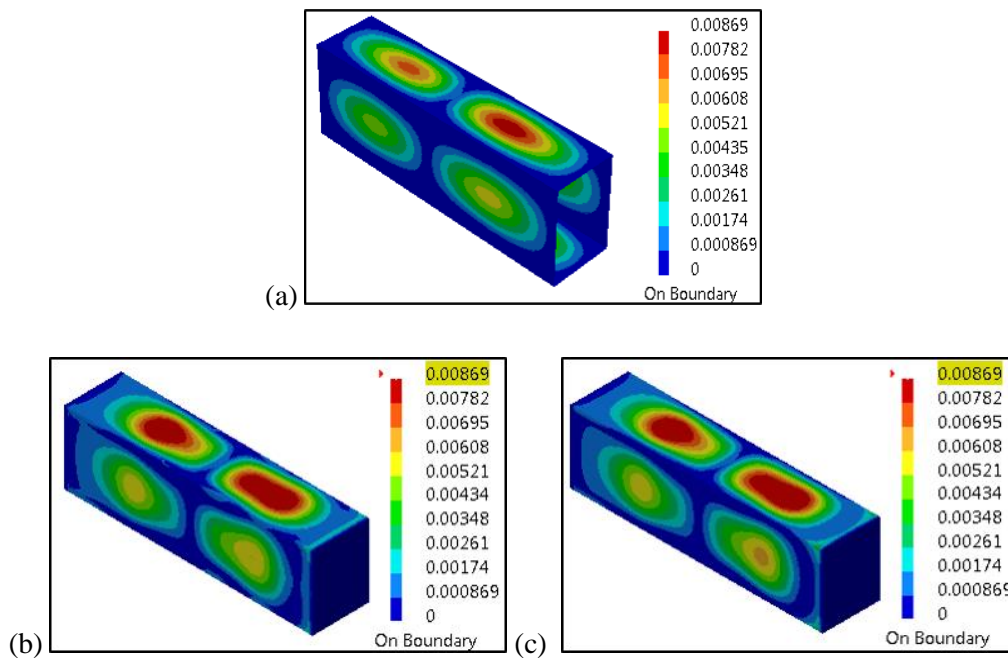
Figure 6.12: Comparison of reconstructed and actual vibration velocities at a coupled frequency of 257 Hz for different mesh density. (a) Actual, (b) Reconstructed by using 0.015m element edge length, (c) Reconstructed by using 0.01m element edge length.

From Fig. 6.6-6.12, it is observed that vibration velocity can be reconstructed accurately at uncoupled and coupled frequencies considering 128 number of measurement points located at a distance of 0.15 m from source surface with element edge length of 0.01m for given acrylic duct dimensions and boundary conditions.

6.3.7   Reconstruction of vibration velocity for a metal duct

As a part of this study, another case is studied to understand the INA methodology implemented. Similar to the acrylic duct, an INA reconstruction technique is performed on metal duct which is considered for studying sound radiation characteristics in Chapter-2. Details of the duct such as dimensions and material properties are discussed in Sec.2.3. Sound power radiated from the rectangular duct is shown in Fig. 6.13. Peaks are associated with structural uncoupled and acoustic coupled frequencies. Here, two uncoupled (First and higher order) and two coupled frequencies are indicated in the figure.
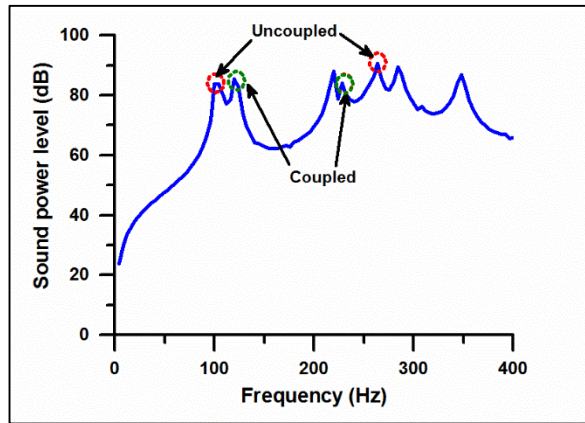
Figure 6.13: Radiated sound power level as a function of frequency for an acrylic duct.

(a)   (b)
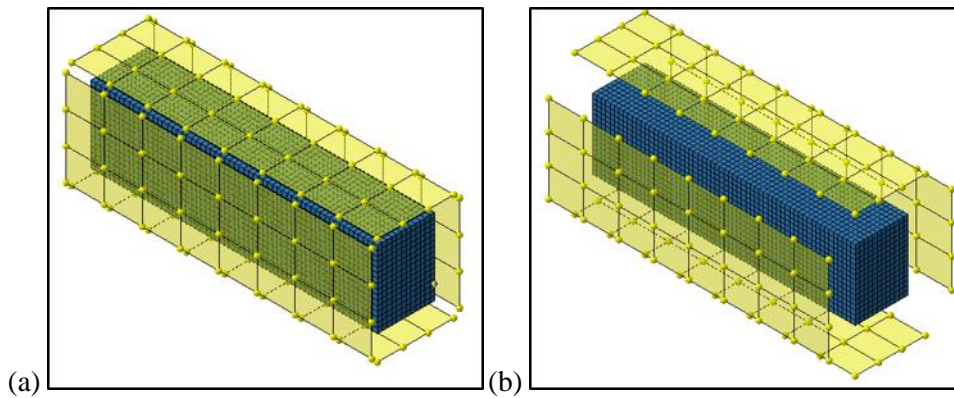
Figure 6.14: Selection of measurement points and the plane (a) 144 points at 0.08m (plane-1) and (b) 144 points at 0.2m (plane-2).

Sound pressure in two different planes is calculated using FEM-BEM (exterior) Vibro-acoustic method (with coupling). Plane-1 is located at a distance 0.08m and Plane-2 at 0.2m from the duct wall surfaces as shown in Fig. 6.14(a) and (b), respectively. Totally 144 measurement points are considered in both cases

Vibration velocity is reconstructed on the duct surfaces by INA analysis with sound pressures measured in both planes. These results are compared to translational vibration velocity which is calculated by FE-coupled analysis. Comparison of actual and reconstructed results are shown in the Fig. 6.15 and Fig. 6.16 for uncoupled frequency 100 Hz and coupled frequency 224 Hz, respectively. It is observed that reconstruction of vibration velocity by INA technique with pressure data measured in Plane-2 is better than Plane-1 pressure measurement. It can

also be noticed that the magnitude of reconstructed velocity is closer to actual vibration velocity in both the cases.

(a) (b) (c)
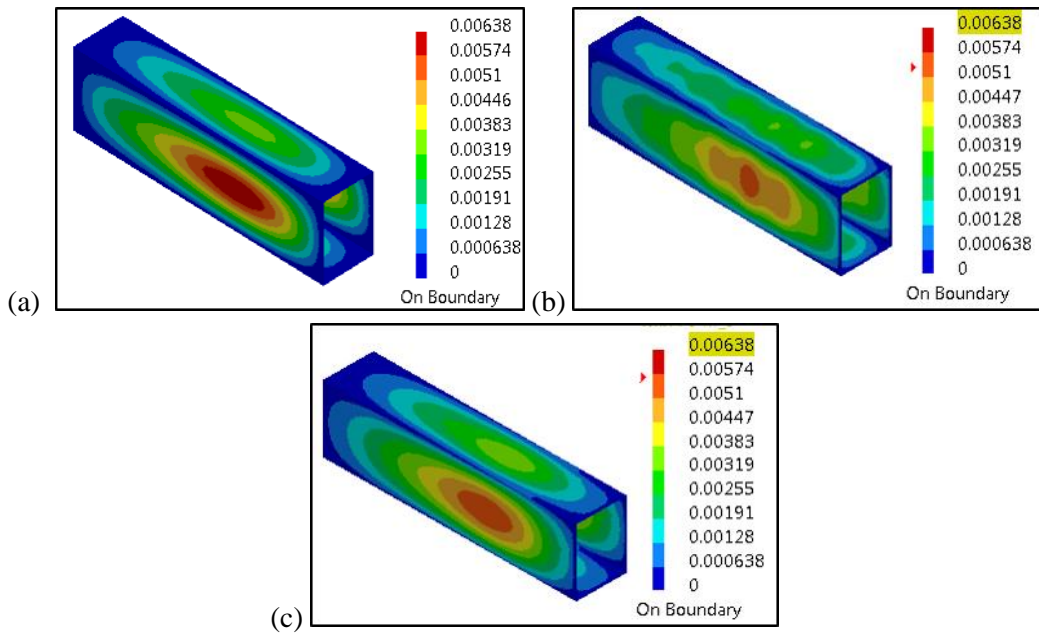
Figure 6.15: Comparison of reconstructed and actual vibration velocity pattern at uncoupled frequency 100 Hz. (a) Actual (b) Reconstructed by plane-1 data and (c) Reconstructed by plane-2 data.

(a) (b) (c)
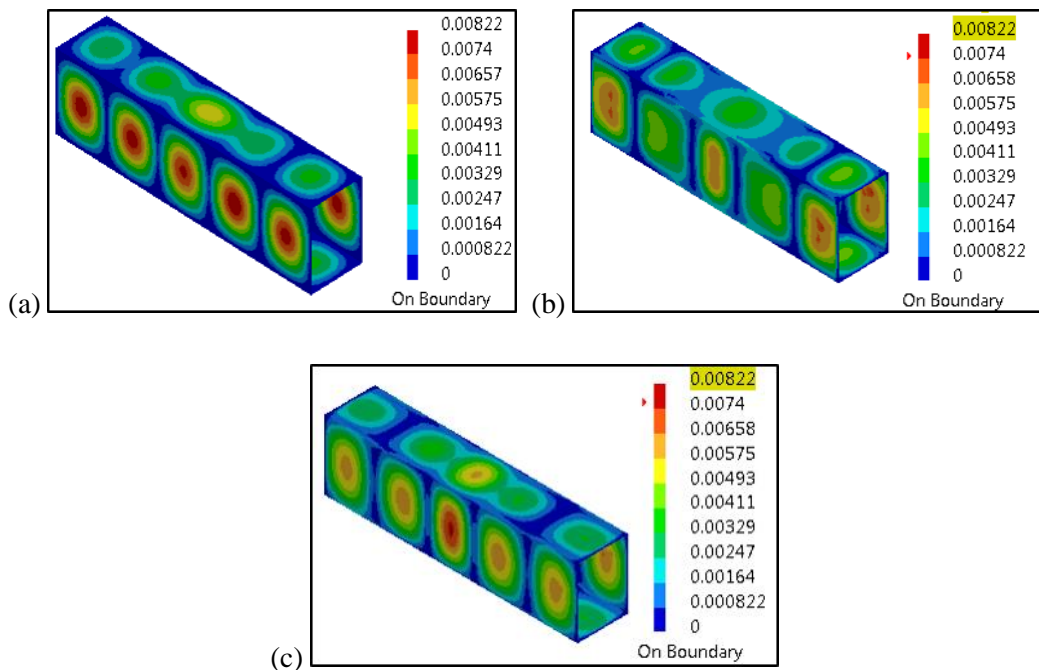
Figure 6.16: Comparison of reconstructed and actual vibration velocity pattern at coupled frequency 224 Hz. (a) Actual (b) Reconstructed by plane-1 data and (c) Reconstructed by plane-2 data.

113

Following procedure can be used for obtaining accurate reconstruction results of vibration velocity by INA technique.

(1) First, select number of sound pressure measurement points and shape of measurement planes like plane or circular, depending on the shape of the sound source. Consider 2-4 number of measurement points per wavelength based on maximum interested frequency. The selected number of points should give unique measured data.

(2) Choose the measurement plane distance from source surface in such a way that it should capture complete information of sound radiated from the source. It has to be noted that measurement plane distance from the source should be more than spacing between the measurement points. Also, reactivity in the measurement plane should be less than 7dB at interested frequency range.

(3) Number of reconstructed points are to be selected in such a manner that reconstructed vibration pattern has to be uniform. It can be obtained based on element edge length used for meshing of the boundary surfaces.

6.4 Summary

Inverse numerical acoustic technique is used to reconstruct vibration velocity on a flexible duct surface in the structure-acoustic coupled system. A rectangular duct made up of acrylic material is considered for the study. Effect of number of sound pressure measuring points, measurement plane and number of reconstruction points (mesh density) on the reconstruction results are discussed for both coupled and uncoupled frequencies. The L-curve regularization parameter selection method is used to overcome the ill-posed problem. It is noticed from reconstruction results that vibration velocity can be obtained accurately at the uncoupled frequency with less than 3% error. However, at coupled frequencies, the magnitude of vibration velocity can be reconstructed with 10 % error but there is a deviation in velocity pattern. As a part of this study, INA technique is implemented on another case also and it is observed that the results are similar.

Chapter 7

Fan Noise Source Characterization

7.1 Introduction

Characterization of sound radiation from the product is a significant task to reduce unwanted noise level during the design stage itself. Basic step while treating the noise problem is to locate source position and source ranking. There are several methods (direct & inverse) to visualize sound field and to find noise source characteristics that is acoustic pressure, particle velocity, sound intensity and sound power. NAH (Near-field Acoustic Holography) is an inverse technique to find a detailed image of the acoustical field on source surface for low frequency applications. By measuring sound pressure at a closer distance around the actual source, it is possible to reconstruct all acoustic quantities by using different inverse methods.

Fan is one of the major noise sources in the HVAC system as it produces both structure-borne sound and air-borne sound. It is necessary to study the characteristics of fan noise source. The present investigation shows the capability of four different NAH techniques to know radiation pattern of fan noise source by visualizing sound radiation from the fan mounted in free space. In this study, firstly a number of reference microphones needed to find the incoherent sources is evaluated using Singular Value Decomposition (SVD). Next, using measured sound pressure, the sound source is reconstructed by different array techniques such as: Fourier NAH, Statistically Optimized Near-field Acoustic Holography (SONAH), Equivalent Source Method (ESM) and Inverse Boundary Element Method (IBEM). As these NAH techniques are ill-posed problems, regularization techniques are used to overcome these problems and to obtain accurate reconstruction results.

7.2 Theory of NAH methods

The principle of sound source reconstruction by four different NAH methods are explained briefly in subsequent sections. The basic theory of all four NAH methods is outlined.

7.2.1 Fourier NAH

Basic principle of Fourier NAH is to reconstruct three dimensional sound field from two-dimensional pressure data measured near the source surface as shown in Fig. 7.1. As this method is applicable only for planar sources, a mathematical formulation is given in Cartesian co-ordinates.
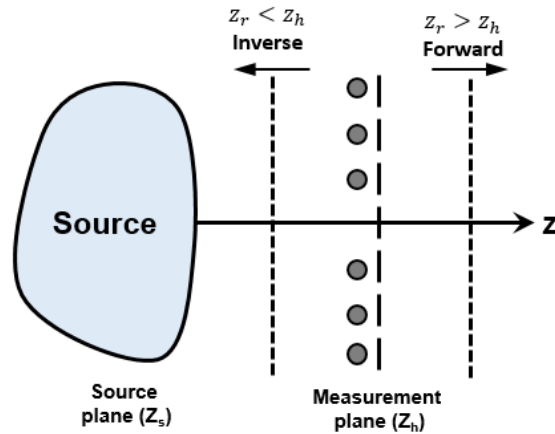
Figure 7.1: Schematic diagram of sound source and array of microphones.

Sound pressure is expressed completely and uniquely by the combination of plane (propagating) and evanescent (exponentially decaying) waves, such as [64],

$$p(x, y, z) = \sum_{k_x} \sum_{k_y} P(k_x, k_y) e^{j(k_x x + k_y y + k_z z)} \qquad (7.1)$$

In Eq. (7.1), k_x, k_y and k_z are the wavenumbers along x, y and z-directions, respectively. Exponential terms are indicated as plane or evanescent waves. The Eq. (7.1) can be written in integral form as,

$$p(x, y, 0) = \frac{1}{(2\pi)^2} \int_{-\infty}^{\infty} \int_{-\infty}^{\infty} P(k_x, k_y) e^{j(k_x x + k_y y)} \, dk_x dk_y \text{ , when } z\text{=}0 \qquad (7.2)$$

Hence, the complex amplitude pressure $P(k_x, k_y)$ is given by the corresponding 2D Fourier Transform (FT),

$$P(k_x, k_y) = \int_{-\infty}^{\infty} \int_{-\infty}^{\infty} p(x, y, 0) e^{-j(k_x x + k_y y)} \, dxdy \qquad (7.3)$$

Once the sound pressure $P(k_x, k_y)$ is known, then using Eq. (7.2) the pressure field over the 3D volume can be computed.

Case-1: $z_r \geq z_h \geq z_s$

The relation between sound field in one plane and another plane can be expressed in terms of known pressure,

$$P(k_x, k_y, z_r) = P(k_x, k_y, z_h) \, G(k_x, k_y, z_r - z_h) \tag{7.4}$$

where $P(k_x, k_y, z_r)$ represents the 2D spatial transform of the pressure field at distance z_r from the source plane and G is called as the propagator and is given by,

$$G(k_x, k_y, z_r - z_h) = e^{jk_z(z_r - z_h)} \tag{7.5}$$

Substituting the Eq. (7.5) in to Eq. (7.4) yields the following equation,

$$P(k_x, k_y, z_r) = P(k_x, k_y, z_h) \, e^{jk_z(z_r - z_h)} \tag{7.6}$$

with $k_x^2 + k_y^2 + k_z^2 = k^2$,

$$G(k_x, k_y, z_h - z_r) \equiv \begin{cases} \sqrt{k^2 - (k_x^2 + k_y^2)} & \text{for } k_x^2 + k_y^2 \leq k^2 \\ j\sqrt{(k_x^2 + k_y^2) - k^2} & \text{for } k_x^2 + k_y^2 > k^2 \end{cases} \tag{7.7}$$

The sound pressure distribution on new plane (z_r) in the space domain can be obtained by performing an Inverse Fourier Transform (IFT) on the left-hand side of Eq. (7.6),

$$p(x, y, z_r) = \mathcal{F}_x^{-1} \mathcal{F}_y^{-1} \left[P(k_x, k_y, z_h) \, e^{jk_z(z_r - z_h)} \right] \tag{7.8}$$

The expression given in Eq. (7.8) yields holographic reconstruction of the 3D sound pressure field $p(x, y, z_r)$ in terms of Fourier transform (FT) of measurement data, $p(x, y, z_h)$. This is the forward case and G is forward propagator. Here, sound pressure field is reconstructed external to the holographic (measurement) plane.

Case-2: $z_s \leq z_r \leq z_h$

If the reconstruction plane is between holographic and source plane then it becomes an inverse problem, G is inverse propagator. Reconstructed sound pressure can be obtained using following Eq. (7.9),

$$p(x, y, z_r) = \mathcal{F}_x^{-1}\mathcal{F}_y^{-1}\left[P(k_x, k_y, z_h)\frac{1}{G(k_x, k_y, z_h - z_r)}\right] \tag{7.9}$$

Once the sound pressure is obtained on the required plane then other acoustic quantities such as particle velocity and sound intensity can be calculated. The particle velocity can be obtained by Eq. (7.10), which relates velocity in wave-number domain of one plane to the components of pressure in another plane.

$$u(k_x, k_y, z_h) = \frac{k_z}{\rho_0 ck}P(k_x, k_y, z_h)\, e^{jk_z(z_r - z_h)} \tag{7.10}$$

The active intensity of sound field can be calculated by,

$$I(x, y, z_r) = \frac{1}{2}p(x, y, z_r)\, u(x, y, z_r)^* \tag{7.11}$$

The Fourier NAH is applicable only for free space, therefore pressure measurement has to be performed on an infinite surface. However, practically it is not possible and therefore it is necessary to make some assumptions on the measurement plane. Generally, larger the measurement plane (MP) more accurate the reconstructed results are but involves a tedious and lengthy process. However, limiting the size of the measuring plane causes inaccurate reconstruction results due to spectral leakage with 2D FT. Based on the different studies in available literatures, one must consider MP size to be at least two times of the actual source. This leads to low pressure values at the edges of the MP and drops to zero beyond it. This discontinuity leads to a larger error in the inverse process even for small errors in measured pressure (due to large evanescent wavenumbers). Hence, even though MP is large compared to the size of the noise source, sound pressure at edges needs to be interpret with caution. In order to reduce this discontinuity and pressures values to be at zero, at the edges, a taper window is used. This taper must be confined to the smallest size possible to avoid alteration of measured pressure. Most commonly used window in NAH technique is eight point Tukey window, given by the following equation [119],

$$f(x) = \begin{cases} \frac{1}{2} - \frac{1}{2}cos\left[\frac{\pi\left(x - \frac{L_x}{2}\right)}{x_w}\right] & \frac{L_x}{2} - x_w < x < \frac{L_x}{2} \\ 1 & x \leq \frac{L_x}{2} - x_w \\ 0 & x > \frac{L_x}{2} \end{cases}$$

$$\tag{7.12}$$

Here, x_w is width of window, L_x is length of MP along x-direction. The Tapering is applied only at each of four edges of the MP therefore only eight points are altered by the window.

118

After applying the taper to four edges, the next step is to enlarge the measuring plane by zero padding which helps to improve reconstruction results. This is typically double the size of measuring plane that is $2L_x$ and $2L_y$ along x-and y-directions, respectively.

NAH being an inverse technique is numerically unstable and as evanescent modes amplify exponentially in the reconstruction, a small error in measurement will get amplified leading to inaccuracy in reconstruction results. In order to minimize this error, a regularization is required to be applied in the inversion process.

In Fourier NAH method, to overcome this inverse problem an exponential filter is used in wavenumber space. Purpose of the filter is to reduce large wavenumber contents by trimming the spectrum at selected points. Most commonly used window function is 2D Harris cosine window which is given by following Eq. (7.13) [119],

$$
K_{window}(k_x, k_y) = \begin{cases} 1 - \frac{1}{2} e^{-\left(\frac{1 - \frac{\left| \sqrt{k_x^2 + k_y^2} \right|}{k_c}}{\alpha} \right)} & \text{for} \quad \left| \sqrt{k_x^2 + k_y^2} \right| < k_c \\ \frac{1}{2} e^{\left(\frac{1 - \frac{\left| \sqrt{k_x^2 + k_y^2} \right|}{k_c}}{\alpha} \right)} & \text{for} \quad \left| \sqrt{k_x^2 + k_y^2} \right| > k_c \end{cases}
$$

(7.13)

In Eq. (7.13), k_c is cut-off wavenumber, α is a positive constant which decides sharpness of the window cut off. If α approaches zero, then window becomes rectangular. Choice of appropriate k_c is critical in reconstruction and importantly it must prevent the significant influence of errors in measurement. However, it should allow sufficient evanescent waves for reconstruction. Hence, filter k_c should be selected such that the effect of noise effects are minimized but interested data should not be removed. These values can also be selected based on signal-to-noise ratio of the measurement along with stand-off distance between measurement and source plane.

Merits of Fourier NAH method
- ➢ It is a simple process and computationally efficient
- ➢ Resolution is good at lower frequencies.

Drawbacks of Fourier NAH method

➢ The microphone array must be at least two times larger than the source.

➢ As this method is depending on a spatial sampling of the pressure field, the resolution is low at high frequencies.

➢ Low dynamic range (signal-to-noise ratio).

➢ It is applicable only to planar, cylindrical or spherical shaped sources.

The theory described for Fourier NAH formulation is given in terms of the flowchart diagram and is shown in Fig. 7.2.
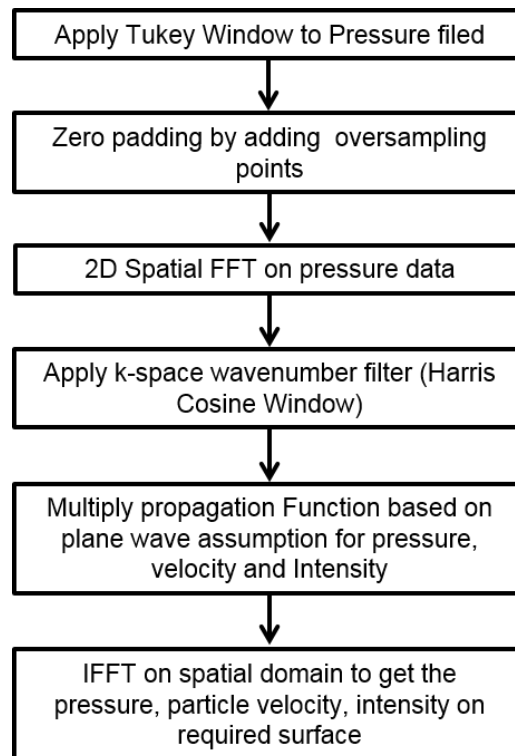
Figure 7.2: Flowchart of the Fourier Near-field Acoustic Holography method.

7.2.2   Statistically Optimized Near-field Acoustic Holography (SONAH)

SONAH is a patch holography method used to reconstruct acoustic parameters near the source surface. These parameters are obtained by projecting all propagating and weighted set of evanescent waves using the transfer matrix method. In this method, sound field is modelled in terms of elementary wave functions (plane).

Sound pressure measured in a free field is represented using a set of elementary wave functions (satisfies homogeneous wave equation) and is given by [120],

$$p(\mathbf{r}_m) = \sum_{n=1}^{N} \varrho_n \Theta_n(\mathbf{r}_m), \qquad m = 1, .. \; ... M \tag{7.14}$$

where, r is position of the measurement point, M is number of measurement points, Θ is elementary wave function, N number of elementary wave functions, ϱ_n is the complex expansion coefficients. Above Eq. (7.14) can be rewritten in the matrix form as,

$$\mathbf{B}\varrho = \mathbf{p} \tag{7.15}$$

Here, B is the matrix of wave function values at measurement positions, vector $\mathbf{p}$ is measured sound pressures and ϱ is expansion coefficients. These are represented as follows,

$$\mathbf{B} \equiv \{\Psi_n(\mathbf{r}_m)\} \equiv \begin{Bmatrix} \Theta_1(\mathbf{r}_1) & \Theta_2(\mathbf{r}_1)\,... & \Theta_N(\mathbf{r}_1) \\ \Theta_1(\mathbf{r}_2) & \Theta_2(\mathbf{r}_2)\,... & \Theta_N(\mathbf{r}_2) \\ \vdots & \ddots & \vdots \\ \Theta_1(\mathbf{r}_m) & \Theta_2(\mathbf{r}_m) & \Theta_N(\mathbf{r}_M) \end{Bmatrix} \tag{7.16}$$

$$\mathbf{p} \equiv \{p(\mathbf{r}_m)\} \equiv \begin{Bmatrix} p(\mathbf{r}_1) \\ p(\mathbf{r}_2) \\ \vdots \\ p(\mathbf{r}_M) \end{Bmatrix} \quad, \qquad \varrho \equiv \{\varrho_n\} \equiv \begin{Bmatrix} \varrho_1 \\ \varrho_2 \\ \vdots \\ \varrho_N \end{Bmatrix} \tag{7.17}$$

If, $M > N$ then, solution for expansion co-efficient can be obtained by least-squares solution (over-determined problem). In case $M < N$ then, solution can be obtained by least-norm. These solutions of elementary wave model (EWM) can be represented as LS-EWM and LN-EWM, respectively. The LS-EWM solution is given by, $\varrho = (\mathbf{B}^H\mathbf{B})^{-1}\mathbf{B}^H\mathbf{p}$ and LN-EWM solution is given by, $\varrho = \mathbf{B}^H(\mathbf{B}\mathbf{B}^H)^{-1}\mathbf{p}$. Here, symbol H represents Hermitian transpose [121].

As SONAH method is ill-posed inverse problem, regularization is applied to overcome this problem. The regularized solutions for both cases are given by,

$$\tilde{\varrho} = (\mathbf{B}^H\mathbf{B} + \varepsilon\mathbf{I})^{-1}\mathbf{B}^H\mathbf{p} \tag{7.18}$$

$$\tilde{\varrho} = \mathbf{B}^H(\mathbf{B}\mathbf{B}^H + \varepsilon\mathbf{I})^{-1}\mathbf{p} \tag{7.19}$$

Eq. (7.18) and (7.19) for LS-EWM and LN-EWM, respectively. ε is regularization parameter and $\mathbf{I}$ is identity matrix with suitable dimensions.

Sound pressure reconstructed $\tilde{\mathbf{p}}(\mathbf{r})$ in the domain Ω, at an arbitrary point $\mathbf{r}$, can be obtained by summation of wave functions and are given by,

$$\tilde{p}(\mathbf{r}) \equiv \sum_{n=1}^{N} \tilde{\varrho}_n \Theta_n(\mathbf{r}) = \tilde{\varrho}^T \boldsymbol{\alpha}(\mathbf{r}), \qquad \text{where} \quad \boldsymbol{\alpha}(r) = \begin{Bmatrix} \Theta_1(\mathbf{r}) \\ \Theta_2(\mathbf{r}) \\ \vdots \\ \Theta_N(\mathbf{r}) \end{Bmatrix} \qquad (7.20)$$

The formulation described above is applicable to spherical wave functions which are the basic version of Helmholtz' equation least-squares (HELS) method. However, by nature, cylindrical and plane waves establish continuous spectra of the sound wave. Therefore, usage of these in described formulation involves only subset of wave functions attained by sampling in wavenumber domain. To overcome this sampling issues, SONAH method is introduced and described below.

Sound pressure reconstructed at any point $\mathbf{r}$ in the domain Ω, can be obtained by a linear combination of measured sound pressures with suitable weights, $\mathbf{c}\ (\mathbf{r})$ and is given by [122],

$$\tilde{p}(\mathbf{r}) = \mathbf{p}^T \mathbf{c}(\mathbf{r}) \qquad (7.21)$$

The vector $\mathbf{c}$ comprises complex estimation weights and obtained as the least square solution of the expansion function ψ_n with reference to Eq. (7.16) and Eq. (7.20),

$$\boldsymbol{B}^T \mathbf{c}\ (\mathbf{r}) = \boldsymbol{\alpha}\ (\mathbf{r}) \qquad (7.22)$$

$$\mathbf{c}(\mathbf{r}) = (\mathbf{A}^H \mathbf{A} + \varepsilon \mathbf{I})^{-1} \mathbf{A}^H \boldsymbol{\alpha}(\mathbf{r}) \qquad (7.23)$$

Here, matrix $\mathbf{A}$ is transpose of $\mathbf{B}$, that is $\mathbf{A} \equiv \mathbf{B}^T$. Using Eq. (7.20), the elements of Eq. (7.23) can be given as follows,

$$[\mathbf{A}^H \mathbf{A}]_{ij} = \sum_n \Theta_n^*(\mathbf{r}_i) \Theta_n(\mathbf{r}_j) \qquad (7.24)$$

$$[\mathbf{A}^H \boldsymbol{\alpha}(\mathbf{r})]_i = \sum_n \Theta_n^*(\mathbf{r}_i) \Theta_n(\mathbf{r}) \qquad (7.25)$$

Here, matrix $\mathbf{A}^H \mathbf{A}$ can be identified as cross correlation of elementary wave functions between the measurement points. $\mathbf{A}^H \boldsymbol{\alpha}(\mathbf{r})$ contains cross correlation between estimation point $\mathbf{r}$ and measurement points.

Equation (7.21) can be rewritten using Eq. (7.23) as,

$$\tilde{p}(\mathbf{r}) = \boldsymbol{p}^T [\mathbf{A}^H \mathbf{A} + \varepsilon \mathbf{I}]^{-1} \mathbf{A}^H \boldsymbol{\alpha}(\mathbf{r}) \qquad (7.26)$$

Now, a special case is considered wherein elementary waves are plane propagating and evanescent waves with free field condition, as shown in Fig. 7.3. Sources present behind the source plane $z_0{}^+ < 0$ radiates into the homogeneous free space Ω with $z > z_0{}^+$.

<table>
</table>

$$Z^+ \text{ Virtual source plane} \qquad Z_0^+ \text{ Source plane}$$
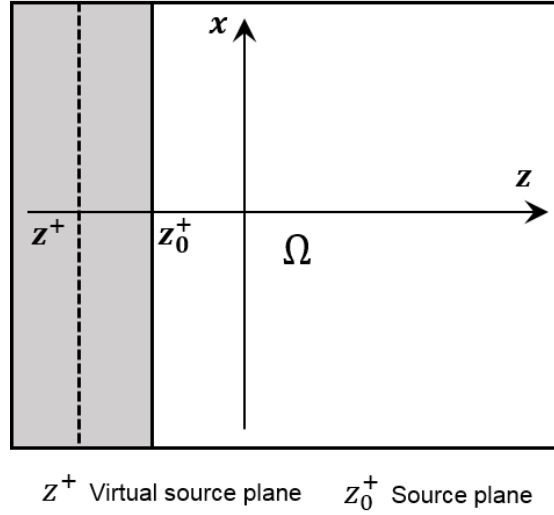
Figure 7.3: Geometry of free-field measurement and domain of the radiated sound field (Ω).

The sound field radiated into free half-space is represented by plane wave functions in form of,

$$\Phi_k(\mathbf{r}) = F(k_z)e^{-j\left(k_x x + k_y y + k_z(z - z^+)\right)} \tag{7.27}$$

Here, F is amplitude of weighting function, $z = z^+$ is virtual source plane, $\mathbf{r} = (x, y, z)$ is position vector and $\mathbf{k} = (k_x, k_y, k_z)$ is the wavenumber vector with,

$$k_z = \begin{cases} \sqrt{k^2 - \left(k_x^2 + k_y^2\right)} & for\ k_x^2 + k_y^2 \le k^2 \\ i\sqrt{\left(k_x^2 + k_y^2\right) - k^2} & for\ k_x^2 + k_y^2 > k^2 \end{cases} \tag{7.28}$$

To apply SONAH method in 2D wavenumber domain (k_x, k_y), first select a discrete subset by regular sampling intervals of $(\Delta k_x, \Delta k_y)$. Elementary wave functions are given by,

$$\Theta_n(\mathbf{r}) = \kappa\Phi_{k_n}(\mathbf{r}), \ \kappa \equiv \sqrt{\frac{\Delta k_x \Delta k_y}{2\pi k^2}} \tag{7.29}$$

In Eq. (7.29), $\mathbf{k}_n$ are sampling points in the wavenumber domain and κ is a scaling factor used to obtain a smooth transition in use of continuous wavenumber spectra.

Regularization parameter used in inversion process can be calculated from the specified dynamic range (signal-to noise ratio, SNR), by following equation [123],

$$\varepsilon = [\mathbf{A}^{\mathrm{H}}\mathbf{A}]_{ii}10^{-SNR/10} \qquad (7.30)$$

Here, $[\mathbf{A}^{\mathrm{H}}\mathbf{A}]_{ii}$ is diagonal element of the $\mathbf{A}^{\mathrm{H}}\mathbf{A}$ matrix and typical values of *SNR* are considered in the range of 15-30 dB.

Figure 7.4 shows the flow chart of SONAH formulation to calculate sound pressure on the source plane.
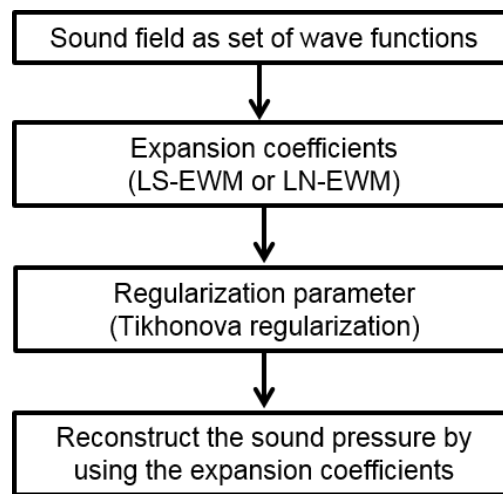
Figure 7.4: Flow chart of the Statistical Near-field Acoustic Holography method.

Merits of SONAH method
  ➢ Mathematically simple and efficient in computations.
  ➢ More number of measurements are not necessary and flexibility in applications.

Drawbacks of SONAH method
  ➢ Difficult to choose an optimum number of expansion co-efficient.
  ➢ This method is based on a wave expansion in planar, spherical, cylindrical coordinates, hence, source surface is also being a similar shape in order to map the sound field directly on the source.

7.2.3   Equivalent Source Method (ESM)

Basic principle of ESM is, radiated sound field is modelled using the distribution of simple standard sources (virtual) such as monopole, dipole or combination of both sources. Figure 7.5 shows the distribution of sources along with different planes involved in ESM technique. Here, P_v, P_s and P_h are virtual, actual source and holographic surfaces, respectively. $\mathbf{y}_n$ - is n^{th} virtual source point on virtual surface, $\mathbf{z}_i$ - i^{th} source point on actual source surface and $\mathbf{x}_m$ - is m^{th} measurement (microphone) position on the hologram surface.
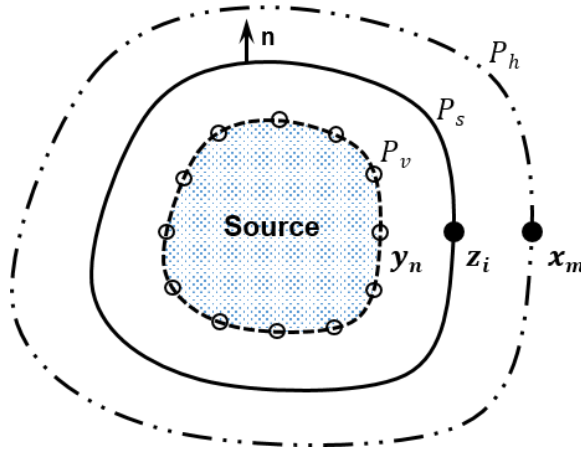
Figure 7.5: Distribution of the virtual sources and different planes used in ESM technique.

Reconstruction methodology used in ESM based NAH technique is described using two different source configurations as shown in Fig. 7.5. This practice is useful to model actual continuous sources. In first configuration, virtual source surface (P_v) is placed away from the actual source surface (P_s) with non-zero stand-off distance (SD, the distance between actual source and virtual source surfaces). In second configuration, virtual sources are distributed exactly on actual source surfaces i.e. SD is zero in second case.

7.2.3.1 Virtual source configuration-1

Acoustic pressure at field point $\mathbf{x}$, based on ESM formulation (in discretized form) is given as follows [84, 124],

$$p_h(\mathbf{x_m}) = \sum_{n=1}^{N} j\rho_0 c_0 k \, G_{hv}(\mathbf{x_m}, \mathbf{y_n}) q_v(\mathbf{y_n}), \qquad m=1, 2,..., M \qquad (7.31)$$

where, p_h is measured pressure, q_v is virtual source strength of distributed point sources. $\mathbf{x_m}$ and $\mathbf{y_n}$ are position vectors of field point (measurement) and source point, respectively. The

G_{hv} is free-space Green's function associated with source point 'n' and field point 'm' and it is given by [70],

$$G_{hv}(\mathbf{x}, \mathbf{y}) = \frac{e^{-jkr}}{4\pi r},$$ (7.32)

In Eq. (7.32), k is wavenumber $r = |\mathbf{x} - \mathbf{y}|$ and $j = \sqrt{-1}$. The Eq. (7.31) can be written in a matrix form as,

$$\mathbf{p}_h = j\rho_0\omega\mathbf{G}_{hv}\mathbf{Q}_v$$ (7.33)

Here, $\mathbf{p}_h$ represents measured sound pressure vector, $\mathbf{Q}_v$ represents virtual source strength vector, $\mathbf{G}_{hv}$ is the propagation matrix (transfer matrix), which relates holographic pressure with source volume velocity and ρ_0 is air density. The unknown source strength can be estimated by inverting Eq. (7.33) with regularization and solution is as follows,

$$\mathbf{Q}_{\text{reg}} = \frac{1}{j\rho ck}\left(\mathbf{G}_{hv}^H\mathbf{G}_{hv} + \varepsilon\mathbf{I}\right)^{-1}\mathbf{G}_{hv}^H\mathbf{p}_h$$ (7.34)

where, $\mathbf{Q}_{\text{reg}}$ is regularized estimated source strength, $\mathbf{G}_{hv}^H$ is Hermitian transpose of $\mathbf{G}_{hv}$, ε is regularization parameter and $\mathbf{I}$ is the identity matrix. Once the source strength is calculated, then acoustic parameters can be reconstructed on the surface of actual sound source. Sound pressure on source surface ($\mathbf{p}_s$) can be estimated using Eq. (7.35), here, $\mathbf{G}_{sv}$ represents propagation matrix relating actual source sound pressure to virtual source strength.

$$\mathbf{p}_s = j\rho\omega\mathbf{G}_{sv}\mathbf{Q}_{reg}$$ (7.35)

Selecting appropriate stand-off distance is very important to obtain good reconstruction results. Literature study suggested that SD varies from 0.4 to 0.5 times of microphone spacing for planar sources. However, for spherical sources, it varies from 0.8 to 1.7 times of microphone spacing [89].

7.2.3.2 Virtual source configuration-2

This type of configuration can be used for planar sources, in this case, virtual sources are distributed exactly on the actual source surface P_s. Therefore, stand-off distance is zero. Sound pressure field generated by planar sources can be expressed by Rayleigh's integral, which is given by [125],

$$p_h(\mathbf{x_m}) = 2j\rho ck \int_{P_v} G_{hv}(\mathbf{x_m}, \mathbf{y_n}) u_0(\mathbf{y_n}) dP_v(\mathbf{y}) \tag{7.36}$$

Here, u_0 is surface velocity of the source on P_s and $G_{hv}(\mathbf{x_m}, \mathbf{y_n})$ is propagation matrix between holographic pressure and source volume velocity. Eq. (7.36) can be expressed in the matrix form by using constant elements of the zeroth order discretization.

Sound pressure measured on a holographic plane and resulting velocities can be represented in matrix form as,

$$\mathbf{p}_h = 2j\rho\omega\mathbf{G}_{hv}\mathbf{Q}_v \tag{7.37}$$

Surface velocity on actual source surface (P_s) can be calculated by using the following Eq. (7.38). Here, ΔS represents average area per "*element*" on the actual source surfaces.

$$\mathbf{u}_v = \frac{1}{\Delta S}\mathbf{Q}_v = \frac{1}{j\rho\omega\Delta S}\mathbf{G}_{hv}^+\mathbf{p}_h \tag{7.38}$$

where, $\mathbf{G}_{hv}^+$ is pseudo-inverse matrix of $\mathbf{G}_{hv}$, Tikhonov regularization can be used to overcome ill-condition in the process of inversion. This is given by $\left(\mathbf{G}_{hv}^H\mathbf{G}_{hv} + \varepsilon\mathbf{I}\right)^{-1}\mathbf{G}_{hv}^H$.

Figure 7.6 shows a flowchart of ESM based NAH method for calculating unknown source strength and sound pressure on actual source plane.
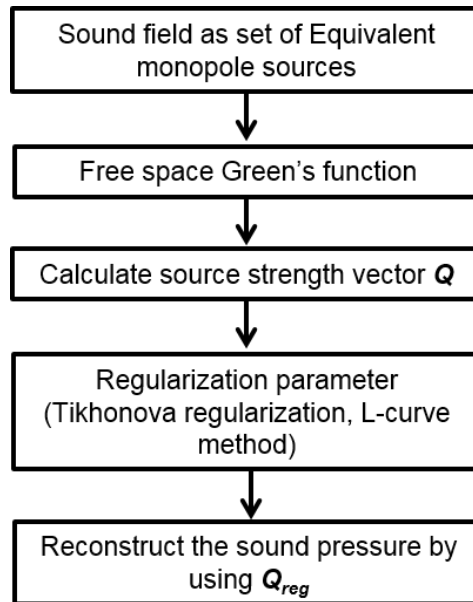
Figure 7.6: Flowchart of the equivalent source based NAH method.

Merits of ESM method

➢ It is easy to implement and computation time is low compared to other NAH methods.

➢ This method can be applied to any shape of source geometry.

Drawbacks of ESM method

➢ Difficult to select the number of equivalent sources and uncertainty of how to distribute (i.e., the distribution density).

➢ Selection of optimum stand-of-distance between the actual and virtual source surfaces is difficult.

➢ Difficult to select the suitable regularization parameter.

7.2.4 Inverse Boundary Element Method (IBEM)

Boundary Element Method (BEM) is a numerical technique that discretizes boundary of the arbitrary source geometry into a small number of elements and solves for acoustic quantities. In this technique, as source information is obtained based on the measured sound pressure or velocity, this becomes an inverse acoustic problem and its numerical implementation is called as IBEM. This technique is used to reconstruct acoustic parameters on complex source geometries. Main advantage of this method is that it discretizes only boundary of the source surfaces, which reduces computational time and storage.
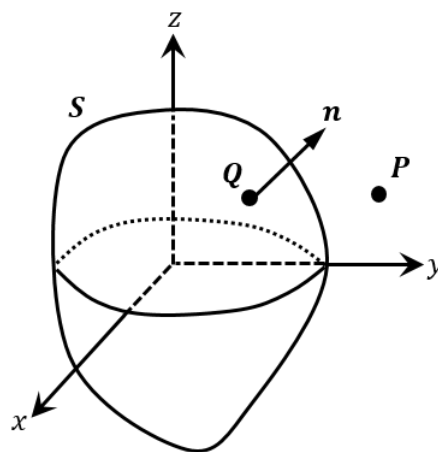
Figure 7.7: Sound radiation domain and boundary surface with the co-ordinate system

IBEM approach for sound radiation and scattering is mainly based on Helmholtz integral equation. This relates the sound pressure and normal velocity on source surface of arbitrary

shape (point Q) to sound pressure measured in the field plane (point P) as shown in Fig.7.7. This equation also considers the sound pressure of the incident wave and is given by [126],

$$Cp_h = \int_S \left(\frac{\partial G}{\partial n} p_s + jkz_0 v_n G \right) dS + 4\pi p^I \tag{7.39}$$

where, C is geometrical constant which varies depending on interest region (measurement position). "1" for inside acoustic domain, "0" for outside acoustic domain and "0.5" on boundary surface. p_h is the pressure on holographic plane, p_s and v_n are pressure and normal velocity on source surface, respectively. S is surface of source and p^I is incident sound pressure. G is Green's function for 3-D free space, which is given by,

$$G(R) = \frac{e^{-jkR}}{R} , \quad R = |P - Q| \tag{7.40}$$

Surface S is discretized into elements, resulting into a matrix equation:

$$\mathbf{C}\,\mathbf{p}_h = \mathbf{A}\,\mathbf{p}_s + jkz_0\,\mathbf{B}\,\mathbf{v}_n + 4\pi \mathbf{p}^I \tag{7.41}$$

Equation (7.41) is the result of *collocating* the point P on each nodal points of the surface mesh (discrete Q points). Here, Matrices $\mathbf{A}$ and $\mathbf{B}$ contain integrals of the kernel functions defined in Eqs. (7.39) and (7.40), which are functions of frequency and geometry only, $\mathbf{p}_s$ and $\mathbf{v}_n$ denotes pressure and normal velocities at the nodes.

If point P placed on the source surface, then left hand side of Eq. (7.41) can be subtracted by diagonal elements of the first term on right hand side. Then sound pressure on the nodal points of the source surface can be expressed in terms of normal velocity and incident pressure for radiation problem. However, for scattering problems, pressures can be expressed as a function of either normal velocity or incident pressure on the surface. Once pressures and normal velocities are obtained on the surface then sound pressures at any point of the domain can be obtained using Eq. (7.39). Therefore, in IBEM, solution over the source surface can be obtained by two steps:

(i) Solve the system of boundary element (BE) equations and obtain the pressure and normal velocities on the source surface.

(ii) Choose the points in the domain and calculate the sound pressure on these locations using previously obtained results.

Generally, solutions for BE equations vary depending on chosen boundary conditions. Eq. (7.41) can be rewritten as Eq. (7.42). Here, in matrix **A**, it is considered that the left hand side of Eq. (7.41) is subtracted in first term of right hand side.

$$\mathbf{0} = \mathbf{A}\,\mathbf{p}_s + jkz_0\,\mathbf{B}\,\mathbf{v}_n + 4\pi\mathbf{p}^I \tag{7.42}$$

Case-1: Consider a problem in which incident waves are scattered around an acoustically rigid object i.e. infinite impedance, then Eq. (7.42) becomes,

$$\mathbf{0} = \mathbf{A}\,\mathbf{p}_s + 4\pi\mathbf{p}^I$$

$$\mathbf{p}_s = \mathbf{A}^{-1}\left(-4\pi\mathbf{p}^I\right) \tag{7.43}$$

Case-2: Consider a radiation problem without external excitation and with defined normal velocities on boundary of the surface, then Eq. (7.42) becomes,

$$\mathbf{0} = \mathbf{A}\,\mathbf{p}_s + jkz_0\,\mathbf{B}\,\mathbf{v}_n$$

$$\mathbf{p}_s = \mathbf{A}^{-1}\left(-jkz_0\,\mathbf{B}\,\mathbf{v}_n\right) \tag{7.44}$$

Case-3: It is also possible to combine the known velocities ($\mathbf{v^0}$) and impedance BC's in terms of the normal velocity term, which is given by,

$$\mathbf{v}_n = \mathbf{Y}\,\mathbf{p}_s + \mathbf{v^0} \tag{7.45}$$

$$\begin{Bmatrix} v_{n_1} \\ v_{n_2} \\ \vdots \\ v_{n_M} \end{Bmatrix} = \begin{bmatrix} Y_1 & 0 & \dots & 0 \\ 0 & Y_2 & \vdots & \vdots \\ \vdots & \vdots & \ddots & 0 \\ 0 & 0 & \dots & Y_M \end{bmatrix} \begin{Bmatrix} p_1 \\ p_2 \\ \vdots \\ p_M \end{Bmatrix} + \begin{Bmatrix} v_1^0 \\ v_2^0 \\ \vdots \\ v_M^0 \end{Bmatrix} \tag{7.46}$$

Here, Y_i - are admittances at nodal points, v_i^0 - are known normal velocities on the nodes of the surface in radiation problems. Generally, only one of the right hand terms is present, but in some practical cases, both will present. This condition occurs when source surface is covered with lining material. Therefore, air normal velocity is different from normal surface velocity. Consider an example of a scattering case with known surface impedance, Eq. (7.42) becomes:

$$\mathbf{0} = \mathbf{A}\,\mathbf{p}_s + jkz_0\,\mathbf{B}\,\mathbf{v}_n + 4\pi\mathbf{p}^I$$
$$\mathbf{0} = \mathbf{A}\,\mathbf{p}_s + jkz_0\,\mathbf{B}\,\mathbf{Y}\mathbf{p}_s + 4\pi\mathbf{p}^I$$
$$\mathbf{p}_s = \left(\mathbf{A} + jkz_0\,\mathbf{B}\,\mathbf{Y}\right)^{-1}\left(-4\pi\mathbf{p}^I\right) \tag{7.47}$$

Case-4: Consider a case when both pressure and velocity conditions are presented on the boundary, then system of equation has to be rearranged to obtain the solution. Eq. (7.48) shows that one nodal point has pressure condition, so, corresponding column is exchanged.

$$
\begin{bmatrix}
a_{11} & a_{12} & \cdots & -b_{1i} & \cdots & a_{1M} \\
a_{21} & a_{22} & & -b_{2i} & & a_{2M} \\
\vdots & \vdots & & \vdots & & \vdots \\
a_{M1} & a_{M2} & \cdots & -b_{Mi} & \cdots & a_{MM}
\end{bmatrix}
\begin{Bmatrix}
p_1 \\ \vdots \\ v_i \\ p_M
\end{Bmatrix}
$$

$$
=
\begin{bmatrix}
b_{11} & b_{12} & \cdots & -a_{1i} & \cdots & b_{1M} \\
b_{21} & b_{22} & & -a_{2i} & & b_{2M} \\
\vdots & \vdots & & \vdots & & \vdots \\
b_{M1} & b_{M2} & \cdots & -a_{Mi} & \cdots & b_{MM}
\end{bmatrix}
\begin{Bmatrix}
v_1 \\ \vdots \\ p_i \\ v_M
\end{Bmatrix}
+
\begin{Bmatrix}
p_1^I \\ p_2^I \\ \vdots \\ p_M^I
\end{Bmatrix}
$$

$$\tag{7.48}$$

Figure 7.8 shows a flowchart of IBEM based NAH method for calculating sound pressure and normal velocity on the surface with known pressure values and suitable BC's. By using these values, sound pressure can be reconstructed at any point in the field plane.
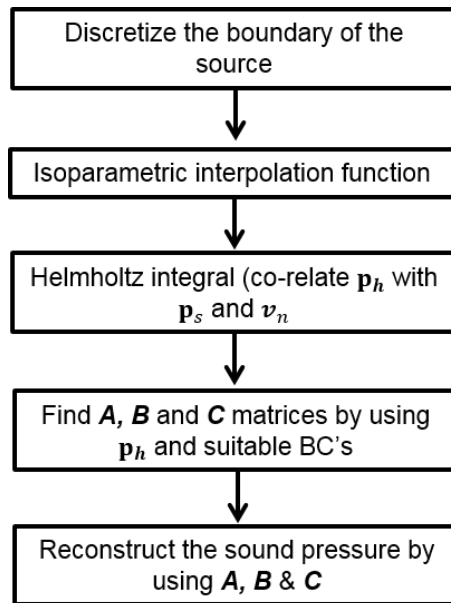
Figure 7.8: Flow chart of the Inverse boundary element method.

Merits of IBEM

> ➢ Reconstruction can be performed on an arbitrarily shaped structure and It is suitable for exterior and interior regions.
> ➢ If only a patch on the source is of interest, the measurement surface can be limited to an area (Patch IBEM)
> ➢ It has no restrictions on the locations of measurement points on a hologram surface, as long as they are in a near field.

Drawbacks of IBEM

> ➢ Computation time increases with the size of the source
> ➢ Failed to yield unique solutions if excitation frequency becomes close to certain discrete characteristic frequencies of the source.
> ➢ In the case of patch IBEM, reconstruction error increases due to partial consideration of the source modelling.

7.3   Experimental setup

The experiment has been conducted in the anechoic room to avoid reflections and background noise effects. The measurement was performed by Dr. B. Venkatesham at Ray W. Herrick Laboratories, Purdue University, USA during his stay in the overseas faculty exchange program. The signal-to-noise ratio (dynamic range) of 40 dB is maintained. A box type axial fan is used in the study. Details of the fan used in current experiment are; Box dimensions: 21 1/4" length x 4 3/4" width x 22 1/2" height, Number of blades: 5, Speed: S_1, S_2 and S_3 at 497 rpm, 638 rpm and 760 rpm, respectively.

Experiment setup for measuring sound pressure near the fan source is shown in Fig.7.9. Measurement grid size is 0.7m x 0.7m with 8x8 microphone arrangements, i.e. 64 number of microphones are used to capture pressure radiated from the source. Here, grid size and number of microphones used for recording pressure are chosen based on interested frequency. To obtain a good spatial resolution, microphone spacing should be less than half of the minimum wave length. In order to capture exponentially decaying waves, such as evanescent waves, the holographic plane should be chosen appropriately. Based on standards and from the literature, a distance of 0.63 m from the source surface is considered. Microphones are arranged with a linear spacing of 0.1 m along horizontal and vertical directions. Details of the data recorded are given in Table 7.1.
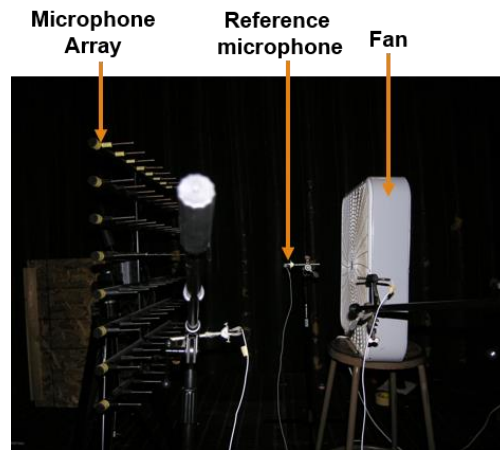
Figure 7.9: Experimental set up for measuring the sound pressure: Fan in free space

Table 7.1: Data for experimental recording

Parameters	Details	Parameters	Details
Fan Operating Speeds	3	Window	Hanning
Configurations and number of trials	3	Sampling frequency	12800 Hz
Number of reference microphones	3	Number of measurement points	64 (8x8)
Signal recording duration	20 Sec	Percent overlap	50 %

Procedure for analysis of measured data is given in terms of a flow chart as shown in Fig. 7.10. It basically involves three major steps: (i) as a first step, sound pressure has to be measured with appropriate settings such as frequency range, frequency resolution, number of microphones, arrangement of microphones, number of averages, windowing, number of averages. (ii) Number of chosen reference microphones are verified using singular value decomposition (SVD) and partial fields are calculated from the measured data. (iii) As the last step, NAH process is applied to reconstruct acoustic parameters on/ near the source surface.
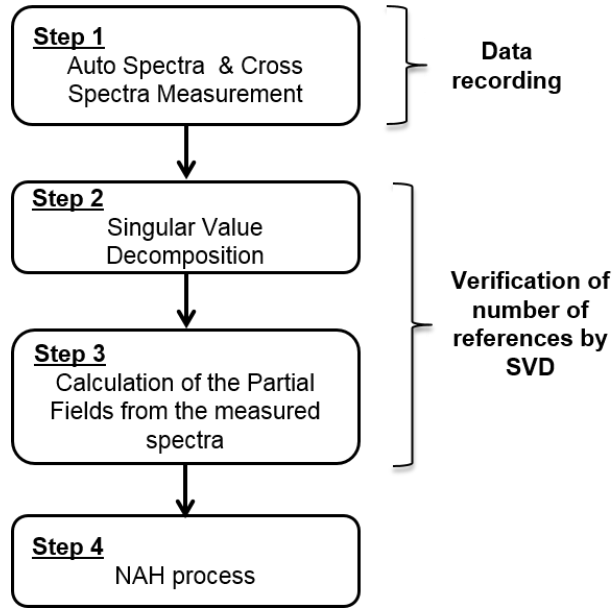
Figure 7.10: Flowchart for the measurement data analysis procedure.

7.3.1 Singular Value Decomposition (SVD)

Complex sound field needs to be decomposed into a set of partial fields which is helpful for the reconstruction process. This can be performed by cross-spectral procedure using a set of reference signals. SVD plays a critical role in decomposition of partial field. This can also be used to calculate the number of essential reference signals to define sound field and to diagonalize reference cross-spectral matrix.

Cross-spectral relations (auto-spectrum and cross-spectrum) between measured and reference signals can be given as follows [127],

$$\mathbf{C}_{rp} = \mathbf{C}_{rr}\mathbf{H}_{rp} \tag{7.47}$$

$$\mathbf{C}_{pp} = \mathbf{H}_{rp}^{H}\mathbf{C}_{rr}\mathbf{H}_{rp} \tag{7.48}$$

Here, $\mathbf{H}_{rp}$ is transfer matrix which relates measured and reference signals of measurement surface. $\mathbf{r} = [r_1 \; \cdots \; r_R]^{\mathrm{T}}$ - is Fourier transform of reference signals, $\mathbf{p} = [p_1 \; \cdots \; p_M]^{\mathrm{T}}$ - is Fourier transform of measured signals on the hologram. R is number of reference microphones, M is number of measurement points. Cross-spectral matrices can be defined as follows,

$$\mathbf{C}_{rp} = \mathrm{E}\,[\mathbf{r}^*\mathbf{p}^\mathrm{T}],$$

$$\mathbf{C}_{rr} = \mathrm{E}\,[\mathbf{r}^*\mathbf{r}^\mathrm{T}],$$

$$\mathbf{C}_{pp} = \mathrm{E}\,[\mathbf{p}^*\mathbf{p}^\mathrm{T}], \tag{7.49}$$

In Eq. (7.49), E[·] denotes expectation operator which averages the elements of **r** and **p** obtained based on time history with a limit of *Time* →∞. Superscripts T and * represents transpose operator and complex conjugate, respectively.

Reference cross-spectral matrix $\mathbf{C}_{rr}$ can be decomposed by SVD, i.e.

$$\mathbf{C}_{rr} = \mathbf{U}\,\boldsymbol{\Sigma}\,\mathbf{V}^\mathrm{H} = \mathbf{U}\,\boldsymbol{\Sigma}\,\mathbf{U}^\mathrm{H} \tag{7.50}$$

Here, $\boldsymbol{\Sigma}$ - is a diagonal matrix, comprises of singular values, **U** and **V** are unitary matrices which are collected of left and right singular vectors, respectively. In order to perform a better decomposition, total number of references must be equal to or greater than background noise level [128]. However, in practical conditions, number of references obtained by SVD may not exactly resemble number of actual independent sources generating total sound field. This is because of measured data not being precise due to the presence of bias errors.

Equation (7.50) is rearranged to obtain singular values of reference cross-spectral matrix $\mathbf{C}_{rr}$, which indicates auto-spectral amplitudes of virtual references.

$$\boldsymbol{\Sigma} = \mathbf{U}^\mathrm{H}\mathbf{C}_{rr}\mathbf{U} = \mathrm{E}\,[\mathbf{v}^*\mathbf{v}^\mathrm{T}]\; =\; \mathbf{C}_{vv} \tag{7.51}$$

In Eq. (7.51), **v** is virtual reference vector, $\mathbf{C}_{vv}$ is cross-spectral matrix between the virtual references.

7.3.2 Partial field decomposition

Partial field decomposition is performed using virtual coherence method. Here, substituting in Eq. (7.50) into Eq. (7.48) gives,

$$\mathbf{C}_{pp} = \mathbf{H}_{rp}^H\mathbf{U}\boldsymbol{\Sigma}\mathbf{U}^\mathrm{H}\mathbf{H}_{rp} = \mathbf{H}_{vp}^H\boldsymbol{\Sigma}\,\mathbf{H}_{vp} \tag{7.52}$$

Here, $\mathbf{H}_{vp}$ is transfer matrix which relates virtual reference data with measured data on the hologram surface. This can be calculated using Eq. (7.47) and Eq. (7.50),

$$\mathbf{H}_{vp} = \boldsymbol{\Sigma}^{-1}\mathbf{U}^\mathrm{H}\mathbf{C}_{rp} \tag{7.53}$$

Decomposed partial fields of the sound ($\widehat{\mathbf{P}}$), can be calculated as product of virtual transfer matrix and square root of diagonal matrix consisting singular values. This is given by,

$$\widehat{\mathbf{P}} = \mathbf{H}_{vp}^{\mathrm{T}}\mathbf{\Sigma}^{1/2} = \mathbf{H}_{rp}^{\mathrm{T}}\mathbf{U}^*\mathbf{\Sigma}^{1/2}$$

$$\widehat{\mathbf{P}} = \mathbf{C}_{rp}^{\mathrm{T}}\mathbf{U}^*\mathbf{\Sigma}^{-1/2} \tag{7.54}$$

In Eq. (7.54), i^{th} column vector of $\widehat{\mathbf{P}}$ represents i^{th} partial field. Here, it must be noted that decomposed partial fields are subject to the following condition [129],

$$\mathbf{C}_{pp} = \widehat{\mathbf{P}}^*\widehat{\mathbf{P}}^{\mathrm{T}} \tag{7.55}$$

Sufficient number of reference sets calculated by SVD technique can be verified by determining virtual coherence at each interested frequency [130]. Equation of virtual coherence is given by,

$$\gamma_{ij}^2 = \frac{\left|C_{v_j p_i}\right|^2}{C_{p_i p_i} C_{v_j v_j}} \tag{7.56}$$

where, $\mathbf{C}_{pp} = \mathbf{U}^{\mathrm{H}}\mathbf{C}_{rp}$ is cross-spectral matrix between measured and virtual reference signals. $C_{v_j p_i}$ denotes $(j,i)^{\mathrm{th}}$ element of $\mathbf{C}_{vp}$. i and j represents measurement point and partial fields, respectively.

7.4 Results and discussion

7.4.1 Singular value decomposition

In the present study, three reference microphones and 64 number of measuring points in the holographic plane are chosen for acquiring sound pressure data. By using this measured data, auto-spectral and cross-spectral matrices are calculated. Next, singular values are calculated for the measured sound pressure field. As discussed earlier, for performing an effective decomposition, a number of reference microphones must be equal to or more than the number of singular values greater than background noise level [128]. Background noise of anechoic room is also measured and corresponding singular values calculated as shown in Fig. 7.11.
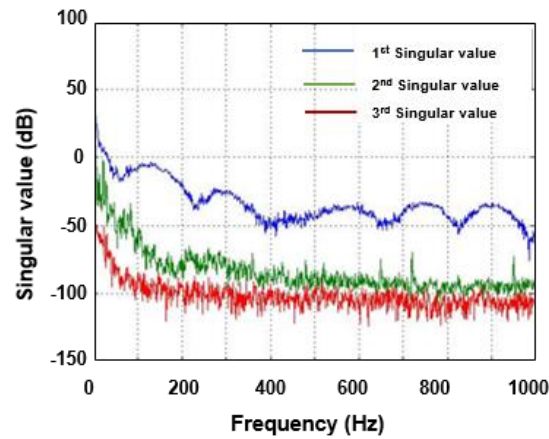
Figure 7.11: Singular values of reference cross-spectral matrices as a function of frequency for background noise measurement of anechoic room.

(a)

(b)
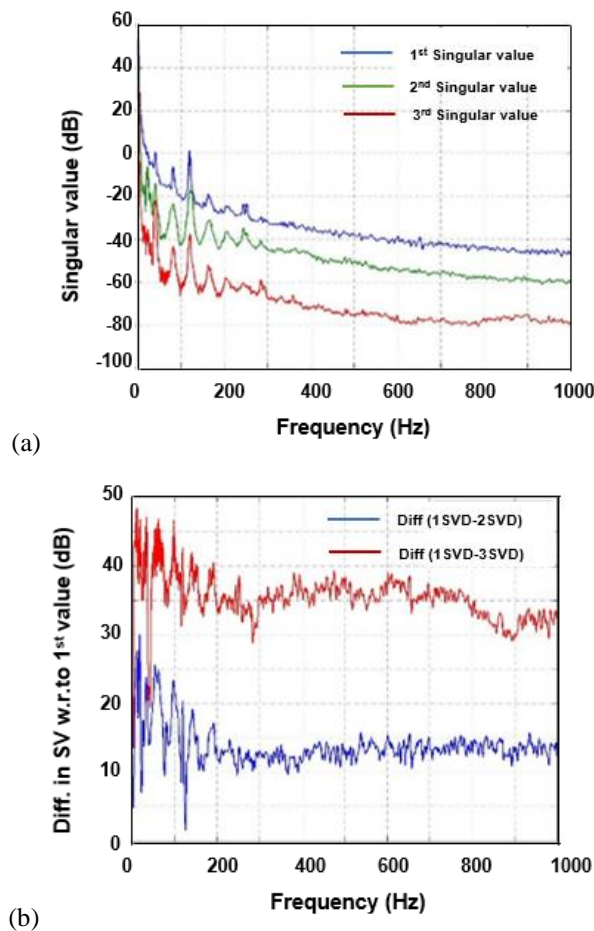
Figure 7.12: Singular values of reference cross-spectral matrices as a function of frequency at 1st BPF with Speed-1, (a) SVD for three reference microphones and (b) Difference in singular values with respect to first singular value.

The individual SVD values for three references at 1st blade passing frequency (BPF) calculated using reference cross-spectral matrix are shown in Fig. 7.12 (a). As the level of third singular value is close to background noise level three reference microphones are used

in the experiment. In principle, this indicates three references are sufficient to represent the total sound field.

Empirically, singular values which are smaller than the largest one by 30 dB may be considered as negligible [90]. As observed from Fig. 7.12(b), at the 1st BPF-41.41 Hz, the difference between SVD1-SVD2 is 14.65 dB and SVD1-SVD3 is 22.49 dB. Hence it is clear that for the 1st BPF, three reference microphones are required. Similarly, at 2nd BPF 82.02 Hz, SVD1-SVD2 is 17.29 dB and SVD1-SVD3 is 37.14 dB. At 3rd BPF the differenced values are 19.83 dB and 40.88 dB, respectively. Therefore, two references are sufficient at 2nd and 3rd blade passing frequencies.

7.4.2 Reconstructed results by NAH methods

Sound pressure data measured near the fan surface with discharge outwards for Speed-1 (approximately 500 rpm) with first three blade passing frequencies are shown in the following Fig. 7.13.
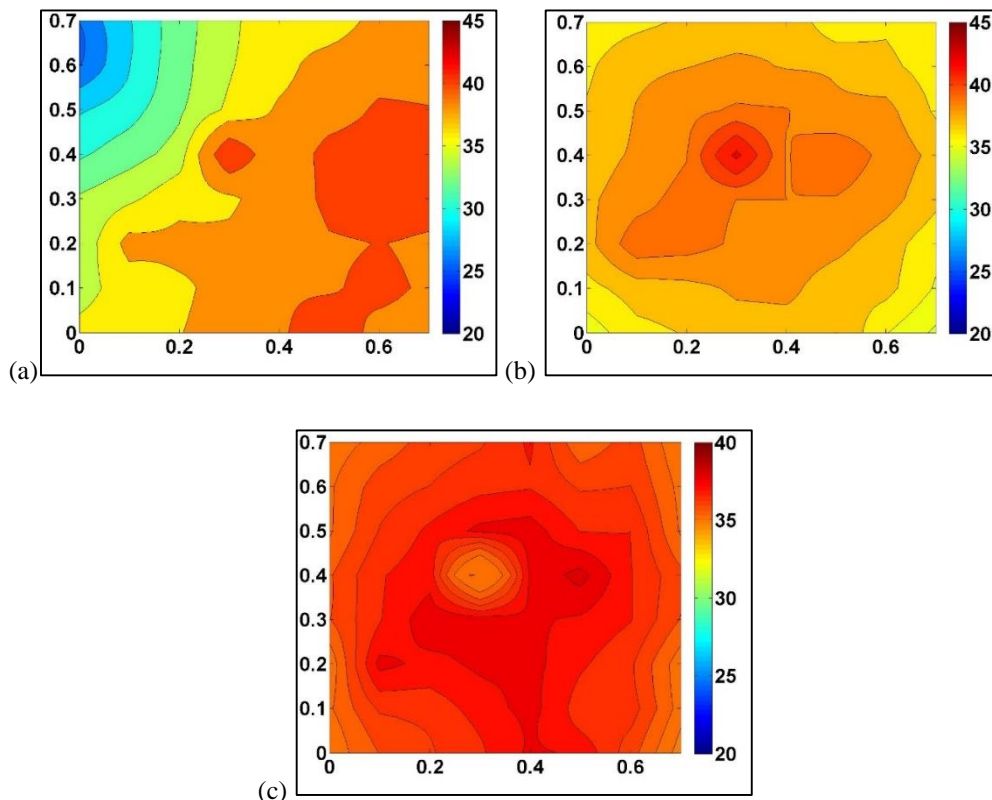
Figure 7.13: Measured sound pressure distribution on the holographic plane at different blade passing frequencies of Speed-1: (a) 1st BPF-41.41 Hz, (b) 2nd BPF-82.03 Hz, (c) 3rd BPF-120.3 Hz.

138

Sound pressure measured on a holographic plane is reconstructed using different NAH methods described in Sec. 7.2 is shown Fig.7.14. It can be observed that sound field reconstructed by ESM method is similar to measured data compared to other methods.
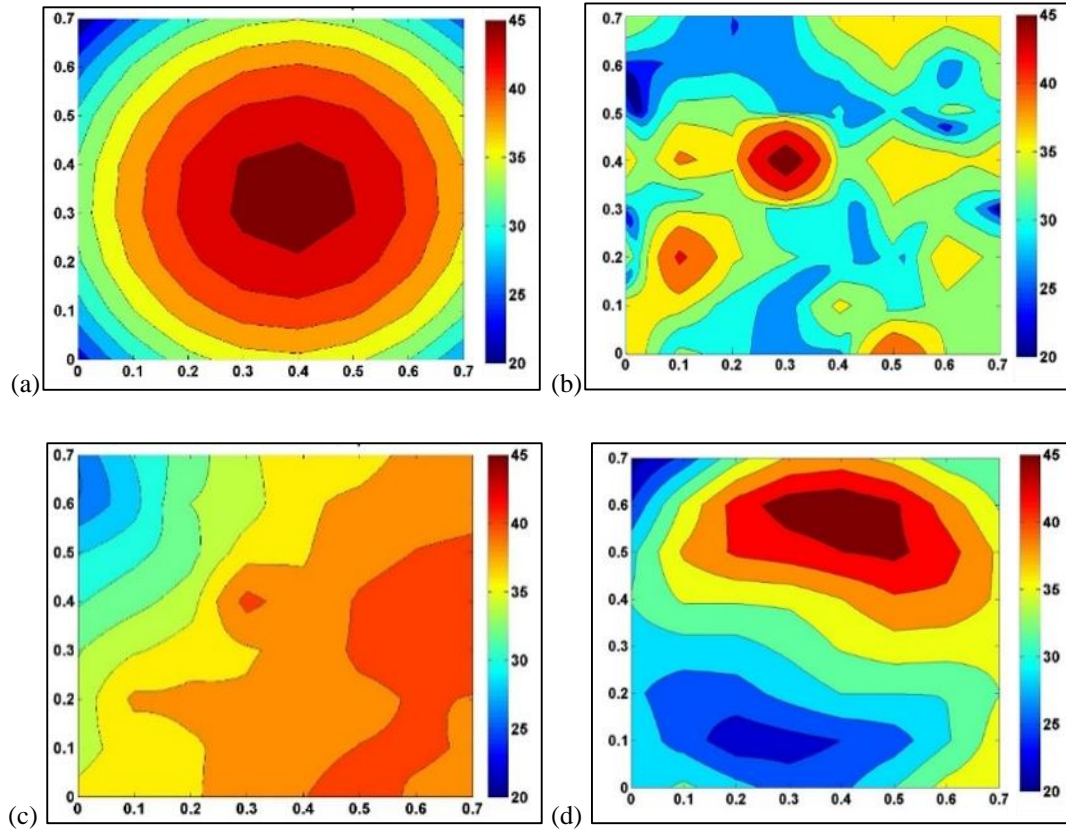
Figure 7.14: Pressure distribution reconstructed by NAH methods at 1st BPF-41.41 Hz: (a) FNAH method, (b) SONAH method, (c) ESM method and (d) IBEM method.

Sound pressure is reconstructed on a plane at distance of 0.1m from the fan's surface. In all four methods, a distance of 0.1m between the reconstructed points is considered. In case of FNAH method, following parameters are considered in the reconstruction process. Cut-off wave number, k_c - 5, positive constant, α -0.2 and oversampling-4 is considered for zero padding (to increase the size of holographic plane). In case of SONAH method, the dynamic range of 15dB is considered and size of holographic plane is considered with two times the actual measurement plane size with two layers of padding. In ESM method, a total of 64 numbers virtual monopole sources are considered which are located at 0.1m away from the actual source position (P_v=-0.1m). Regularization parameter of 0.02 is used in reconstruction which is calculated by L-curve parameter selection method. In IBEM method, co-ordinates

of the source position are chosen as 0.08 m along both *x*- and *y*-directions. Regularized parameter of 50 is chosen for the reconstruction of sound pressure near the source surface.

Reconstructed results can also be verified with measured data by comparing sound pressure level at each corresponding microphone's positions. Figure 7.15 shows the results of four different NAH methods. Figure 7.15(a) shows a comparison of measured and reconstructed results by using Fourier NAH method. It was observed that this method is unsuitable for a source having flow conditions. Results of SONAH method showed that there are a lot of variations in the sound pressure levels for measured and reconstructed. In SONAH method, as spatial resolution has dependence on dynamic range selection it requires proper selection of signal-to-noise ratio. It is observed from Fig. 7.15(c) that reconstructed results are in good agreement with measured results. ESM method is the preferred choice to reconstruct fan noise sources as compared to NAH and SONAH method. IBEM method is better to reconstruct noise sources as observed in Fig. 7.15(d). However, there are small deviations from measured data. It can be resolved by choosing proper co-efficient matrix in reconstruction calculation.
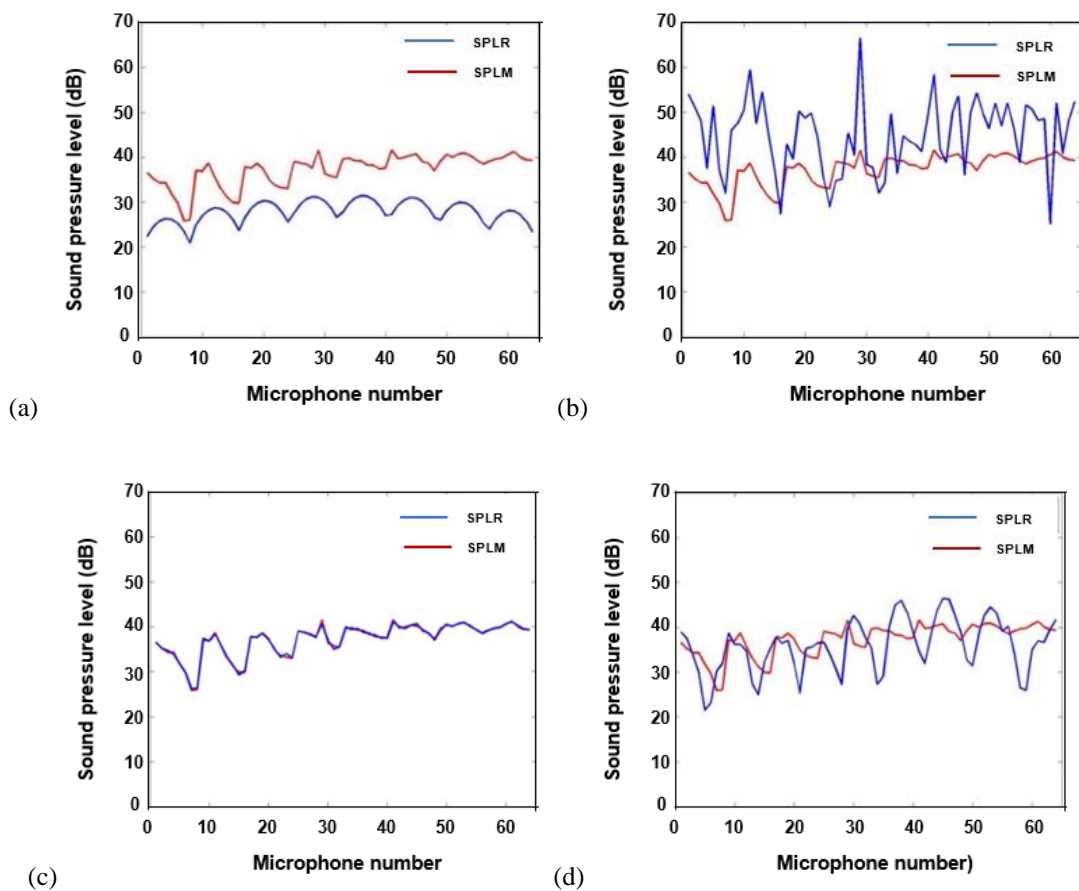
Figure 7.15: Comparison of measured and the reconstructed pressure distribution by four NAH methods at 41.41 Hz frequency.

As observed from the reconstructed results of 1st BPF, ESM is a better method for reconstruction. Therefore, using this method sound pressure is also reconstructed at 2nd and 3rd BPFs and compared to measured results as shown in Fig. 7.16 and Fig. 7.17, respectively. It can be clearly observed that there is a decent agreement between these results and radiation behaviour is like a dipole in nature.
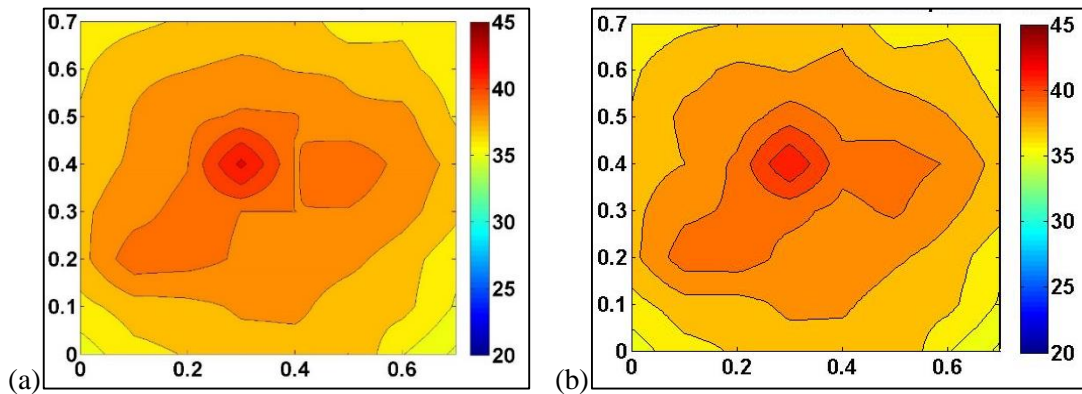
Figure 7.16: Comparison of measured (left, (a)) and the reconstructed pressure distribution (right, (b)) by ESM NAH method at 2nd BPF 82.03 Hz.
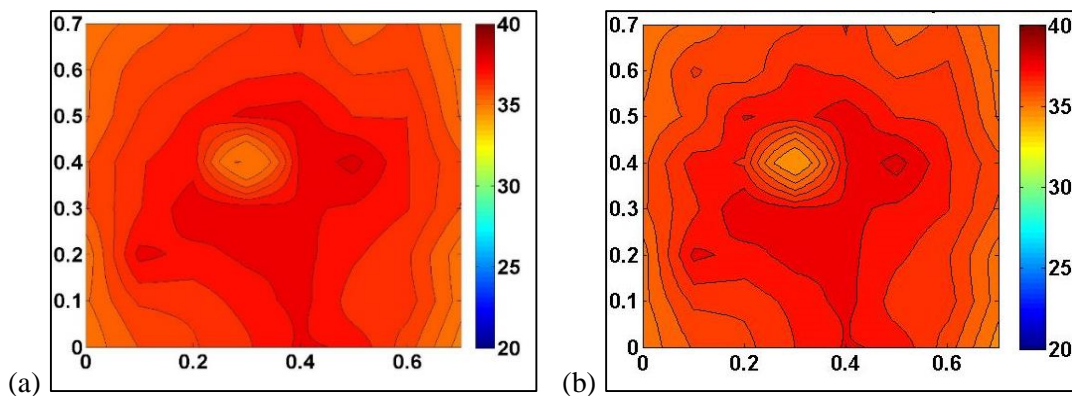
Figure 7.17: Comparison of measured (left, (a)) and the reconstructed pressure distribution (right, (b)) by ESM NAH method at 3rd BPF 120.3 Hz.

7.5   Summary

Identification of number of reference microphones is important to know the incoherent sources. In this study, essential references required for measurement are calculated using singular value decomposition. It is noticed that at 1st BPF three references, at 2nd and 3rd BPF's two reference microphones are required, respectively. Next, sound pressure is reconstructed using measured sound pressure data by four different NAH methods at three blade passing

frequencies. The reconstructed results obtained from different NAH techniques show that ESM method is best to reconstruct fan noise sources with minimal error. The behaviour of a fan at BPF is dipole in nature. A comparison of reconstructed pressures with measured values indicates that reconstructed pressure correlates very well with measured pressure.

Chapter 8

Sound Source Reconstruction on Flexible Plate backed by a Cavity using ESM Method

8.1   Introduction

Analysis of sound radiation from the flexible structures backed by an air cavity is an interesting problem in enclosure designs, heating, ventilation and air-conditioning (HVAC) problems, engine cover, transformer tank wall, etc. These types of problems involve structural-acoustic coupling phenomena between flexible structure and acoustic cavity. Sound radiates efficiently at the coupled frequencies due to structural-acoustic coupling and at uncoupled frequencies due to structural vibrations.

In this chapter, reconstruction of the sound source on a flexible plate backed by a cavity at uncoupled and coupled frequencies using ESM technique are discussed. Initially, uncoupled structural, acoustic natural frequencies and coupled frequencies are calculated from finite element analysis, and these results are corroborated with the analytical results available in the literature [12]. As next step, sound pressure radiated from a flexible surface due to acoustic excitation is calculated using FEM-BEM (finite element/boundary element method). Sound pressure (obtained from numerical simulations) data with added white noise are considered for the reconstruction. Tikhonov regularization with generalized cross-validation (GCV) and L-curve parameter selection methods are employed to overcome the ill-posedness of the problem. Effect of measurement and background noise on the accuracy of reconstruction is studied in terms of the Signal-to-Noise ratio (SNR).

8.2   Numerical modeling

Firstly, the uncoupled structural and acoustical frequencies are calculated using the finite element method. Numerical models for the flexible plate structure and acoustic cavity are shown in Fig. 8.1. For structural analysis, a rectangular plate of the dimension 0.868 m x 1.15 m with 10 gauge (2.5 mm) is modelled and meshed using shell elements. The material

properties of the structure are: 71 GPa, Elastic modulus, 2700 kg/m^3, density, and 0.3 Poison's ratio. Simply-supported boundary conditions are applied at edges of the plate and numerical modal analysis is performed using commercial software ANSYS-16. An acoustic cavity of dimensions 0.868 m x 1.15 m x 1 m is modelled and meshed using SOLID-185 elements. Air properties such as, density of 1.225 kg/m^3, speed of the sound is 340 m/s are applied and acoustic modal analysis is performed. Structural mesh mapped with acoustic mesh and coupled analysis performed using LMS virtual lab-13.
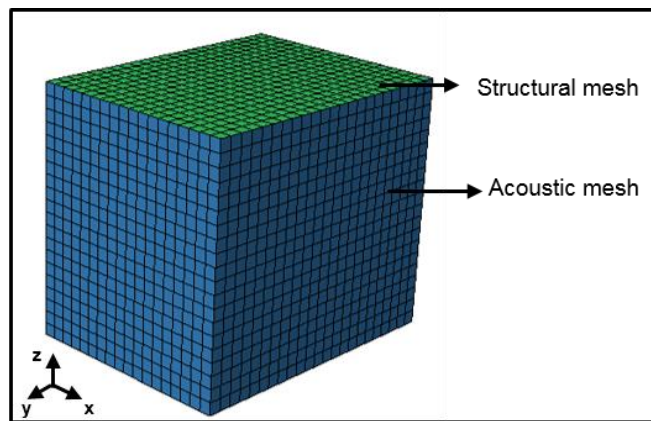
Figure 8.1: A numerical model of the structure and an acoustic cavity for coupled analysis.
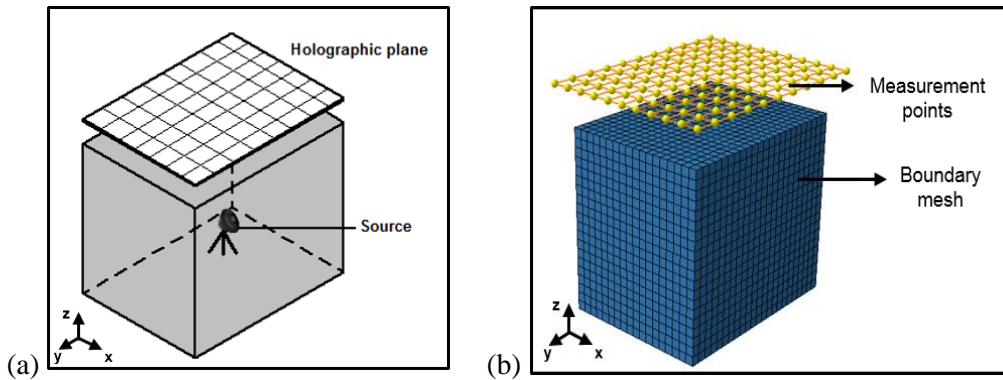
Figure 8.2: Radiated sound pressure measurements on the holographic plane: (a) Schematic (b) Numerical model

Figure 8.2 shows the schematic and numerical model for radiated sound pressure measurement. FEM-BEM analysis is performed for calculation of radiated sound pressure and power. A monopole source of the strength 0.1 kg/sec^2 is used as an acoustic source for excitation. As the first step, the vibration displacement of the flexible plate due to acoustic excitation is calculated by the FEM model. Then vibration displacement is used as input

boundary condition for BEM acoustics exterior method for calculation of radiated sound power and pressure. Dimensions of the holographic plane and spacing between measurement points are selected based on the interested frequency range.

8.3   Structural-acoustic coupled analysis

8.3.1   Uncoupled frequencies

Uncoupled structural and acoustical frequencies calculated from numerical results are compared with analytical results calculated from a mathematical model available in the literature [12]. Table 8.1 shows the comparison of numerical and analytical results till 200 Hz. Here, f_{sn} represents numerical uncoupled structural frequencies, f_{sa} represents analytical uncoupled structural frequencies. Similarly, f_{an} and f_{aa} represent numerical and analytical uncoupled acoustic frequencies, respectively. It can be observed from Table 8.1 that uncoupled structural and acoustical modes of numerical results are in good agreement with analytical results.

Table 8.1: Comparison of numerical and analytical uncoupled structural and acoustical frequencies

Uncoupled structural frequencies						Uncoupled acoustical frequencies		
Mode No.	f_{sn} (Hz)	f_{sa} (Hz)	Mode No.	f_{sn} (Hz)	f_{sa} (Hz)	Mode No.	f_{an} (Hz)	f_{aa} (Hz)
1	12.69	12.67	11	113.58	114.00	1	147.83	147.83
2	26.48	26.46	12	122.97	123.00	2	170.00	170.00
3	36.91	36.88	13	133.66	133.71	3	195.85	195.85
4	49.47	49.45	14	145.34	146.18			
5	50.65	50.67	15	146.66	147.21			
6	73.52	73.65	16	147.15	147.50			
7	77.25	77.22	17	169.62	170.49			
8	81.63	81.63	18	173.46	173.57			
9	90.88	91.02	19	186.16	187.56			
10	105.52	105.83	20	196.91	197.78			

8.3.2 Coupled frequencies

Table 8.2 shows the comparison of coupled frequencies obtained from numerical simulations with analytically calculated results. They are in good agreement. Here, f_{cn} represents numerical coupled frequencies, f_{ca} represents analytical coupled frequencies. It can be noticed that uncoupled structural frequencies 147.15 Hz, 173.46 Hz and 196.91 Hz are coupled with uncoupled acoustical frequencies 147.83 Hz, 170 Hz and 195.85 Hz, respectively. The effective coupled modes can be identified by calculating transfer factor (TF) and it varies from 0 to 1 [18]. TF values close to 1 represents the strong coupling. It can be noticed that uncoupled structural frequency 146.18 Hz is coupled with uncoupled acoustical frequency 147.83 Hz with TF value of 0.887. Similarly, 220.13 Hz structural frequency is coupled with 225.28 Hz acoustic frequency with TF value of 0.78.

Table 8.2: Comparison of numerical and analytical coupled frequencies.

Coupled frequencies					
Mode No.	f_{cn} (Hz)	f_{ca} (Hz)	Mode No.	f_{cn} (Hz)	f_{ca} (Hz)
1	21.99	21.83	13	133.40	133.43
2	26.14	26.12	14	145.03	145.78
3	36.60	36.56	15	146.58	147.12
4	49.73	49.78	16	146.99	147.33
5	50.37	50.39	17	149.34	149.40
6	73.44	73.58	18	169.56	170.42
7	77.34	77.34	19	172.48	172.43
8	81.43	81.41	20	173.50	173.61
9	90.72	90.84	21	186.21	187.61
10	105.43	105.73	22	196.78	196.98
11	113.55	113.99	23	197.01	197.63
12	122.86	122.94	24	201.01	202.61

8.4   Results and discussion

8.4.1   Data for the reconstruction

Sound radiated from the flexible surface is estimated in the near-field of the source by a set of virtual microphones. A holographic plane of dimension 1.0 m x 1.3 m with the 11x11 number of measurement points are considered, and it is located at a distance of 0.25 m from the flexible surface of the box. The spacing between measuring points along x-direction is

0.1m and along y-direction is 0.13 m. Figure 8.3 shows the sound pressure levels at 22 Hz (uncoupled) and 149 Hz (coupled) frequencies with respect to the microphones. It can be noticed that the sound pressure levels at 22 Hz frequency are more than 149 Hz frequency at all the microphone positions.
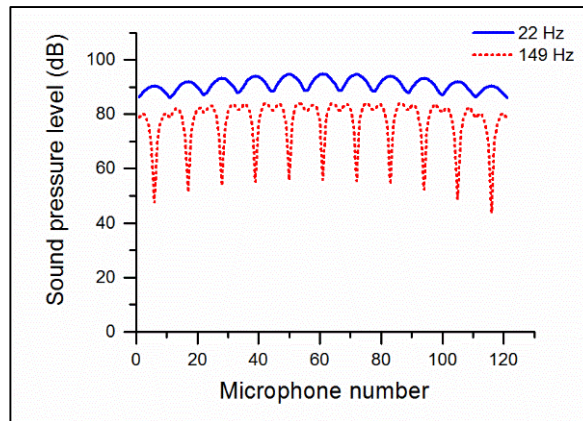
Figure 8.3: Radiated sound pressure level on the holographic plane with respect to microphone number at 22 Hz and 149 Hz frequencies.

Sound pressure estimated on the field points is used as input for ESM technique for the reconstruction. In order to create more realistic problems, the perturbation (white noise) is integrated into the pressure signal calculated by the numerical simulations. The added noise incorporates the measurement noise and background noise. Data generation from a numerical simulation with added noise is one of the alternative methods in the absence of measurement array data for testing source location NAH algorithm.

8.4.2   Radiated sound power calculation

Figure 8.4 shows the radiated sound power level measured on the holographic plane near the flexible surface of the box structure. It can be observed that sound radiates efficiently at uncoupled structural frequency 22 Hz and acoustic frequency 197 Hz. The sound power levels at these frequencies are 107.34 dB and 123.48 dB, respectively. It can be further noticed from the plot that, there are two peaks around 147 Hz. These closely spaced frequencies are due to the structural-acoustic coupling of uncoupled acoustic mode at 147.83 Hz with the uncoupled structural mode at 147.15 Hz. The split phenomenon occurs due to the energy exchange between acoustic and structural subsystems.
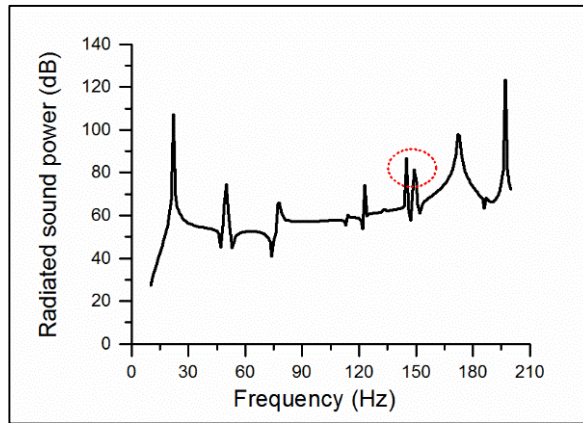
Figure 8.4: Sound power level radiated from the flexible surface of the box with respect to frequency.

8.4.3 Regularization

ESM technique is an ill-posed inverse problem. Therefore, regularization is important in order to avoid the amplification of noise presented in the measured pressure. Regularization improves the condition of the inverse matrix. In the present work, Tikhonov regularization with GCV and L-curve parameter selection methods are considered. L-curve plots for the interested frequencies of 22 Hz and 149 Hz are shown in Figs. 8.5 (a) and (b), respectively. These plots show that corner of the L-curve (regularization parameter, ε) occurs at $3.0821*10^{-6}$ for 22 Hz frequency and 0.003143 for 149 Hz frequency. Similarly, GCV curves for two interested frequencies are shown in Figs. 8.6 (a) and (b). The minimum values of the GCV curve are $2.0269*10^{-4}$ and $2.4728*10^{-4}$ for 22 Hz and 149 Hz frequencies, respectively.

(a) (b)
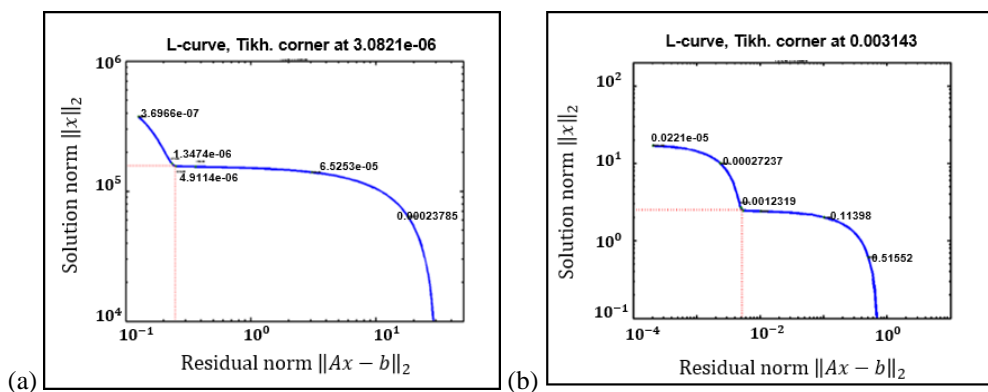
Figure 8.5: L-curves for regularization parameter selection at uncoupled and coupled frequencies: (a) 22 Hz (b) 149 Hz.

8.4.4 Reconstructed parameters

Sound pressure is reconstructed on the source plane using ESM technique with L-curve and GCV regularization parameter selection methods. Here, total 121 number of monopole sources are chosen in the virtual plane. These are arranged in the form of 11 x 11 with the spacing of 0.0868 m in the x-direction and 0.115 m in the y-direction. The retreat distance, (RD, the distance between the actual source plane to the virtual plane) varies from 0.5Δ m to 1Δ m for the planar source, where, 'Δ' is the microphone spacing [96]. In the present analysis, RD of 0.0434 m and 0.0868 m for 22 Hz and 149 Hz frequencies are used to locate the virtual sources, respectively.
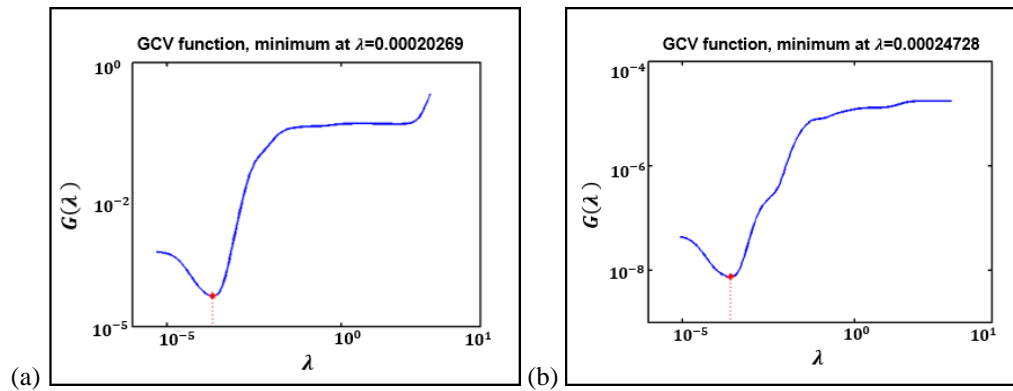
Figure 8.6: GCV-curves for regularization parameter selection at uncoupled and coupled frequencies: (a) 22 Hz (b) 149 Hz.

Figure 8.7 shows the comparison of reconstructed results with the actual results for 22 Hz and 149 Hz frequencies. It is observed from Fig. 8.7(a) that two regularization parameter selection methods provide reasonable results. However, the magnitude of the pressure obtained using L-curve method is more accurate than the GCV method. Similar behavior is also observed in Fig. 8.7(b) for 149 Hz frequency. Reconstructed results of the sound pressure on source surface can also be verified by comparing the contour plot of sound pressure distribution. Figure 8.8 shows the contour plots of the actual and reconstructed sound pressure at the frequency of 22 Hz. It can be clearly noticed that reconstructed results are in good match with the actual results.

(a)

(b)
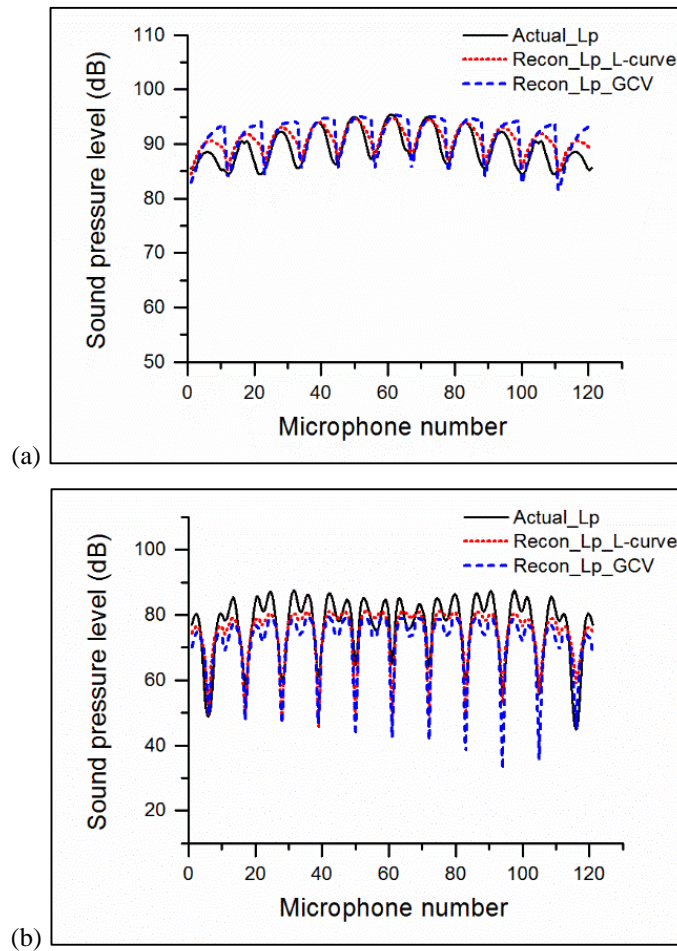
Figure 8.7: Comparison of measured and reconstructed sound pressure: (a) Uncoupled frequency 22 Hz, (b) Coupled frequency 149 Hz.

Figure 8.8 shows a comparison of actual and reconstructed sound pressure in the form of a contour plot for the coupled frequency of 149 Hz. As it is observed from the plot, both results are in good agreement. However, there is a small discrepancy between these results due to the coupling effect. Because of the existence of higher-order modes and evanescent wave, the sound radiation pattern varies as keeps moving away from the source surface. Hence, the sound pressure measured on a holographic plane may not have the information of the exponentially decaying waves and which leads to the errors in reconstruction results.
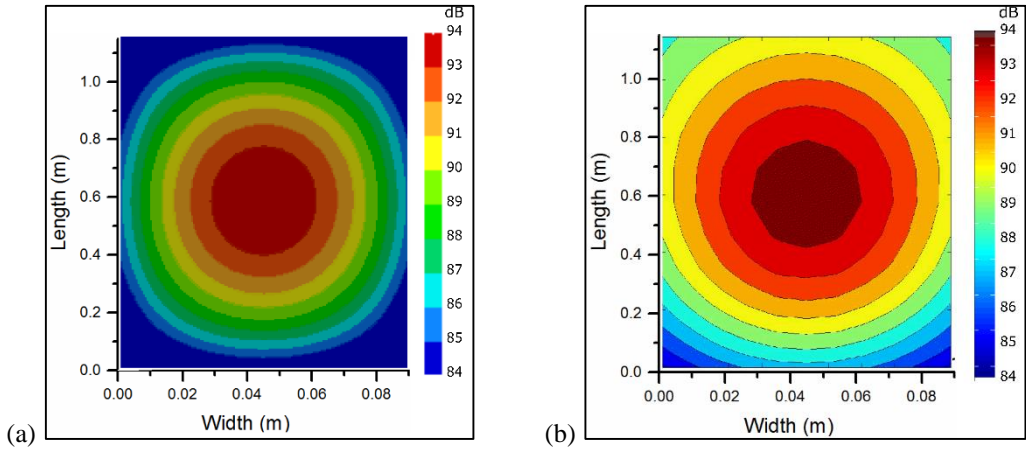
Figure 8.8: Comparison of pressure contour plots at uncoupled frequency 22 Hz: (a) Actual, (b) Reconstructed.
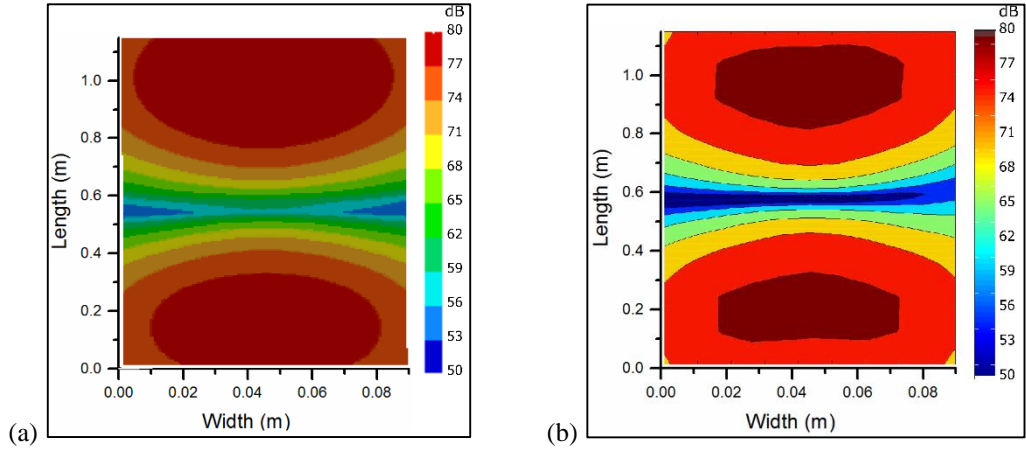
Figure 8.9: Comparison of pressure contour plots at uncoupled frequency 149 Hz: (a) Actual, (b) Reconstructed.

8.4.5 Effect of SNR on reconstruction error

Effect of noise on the accuracy of the reconstruction is studied in terms of the signal-to-noise ratio. It is defined as a ratio of signal power to the noise power. It is also called as dynamic range. It represents the arithmetical difference between the signal and noise levels, in decibels. In other words, it is the ratio of actual signal to the noisy signal, which can be given by the following expression [64],

$$SNR = 20 log_{10} \left[\frac{\|P_{signal+noise} - P_{noise}\|}{\|P_{noise}\|} \right] \tag{8.1}$$

151

In Eq. (8.1), $P_{signal+noise}$ is the measured signal with the presence of noise and P_{noise} is the noise signal. The accuracy of reconstruction of acoustic parameters can be expressed in terms of the reconstruction error. This can be written in general form as [131],

$$\frac{\|P_s - P_{s,\lambda}\|_2}{\|P_s\|_2} \times 100\% \tag{8.2}$$

where, the vectors P_s and $P_{s,\lambda}$ represents the measured and reconstructed sound pressure, respectively.

Figure 8.10 shows the reconstruction error plots as a function of SNR values at uncoupled and coupled frequencies. The different SNR values vary from 25 dB to 50 dB are considered in the intervals of 5 dB. It can be observed that at the uncoupled frequency the reconstruction error decreases uniformly as SNR values increases. However, in case of coupled frequency, the reconstruction error is not uniform. This is because of missing the information of evanescent waves in the measured signal. It is clearly evident from the reconstruction error plots that the SNR values must be high to obtain reconstruction results with less than 15% error.
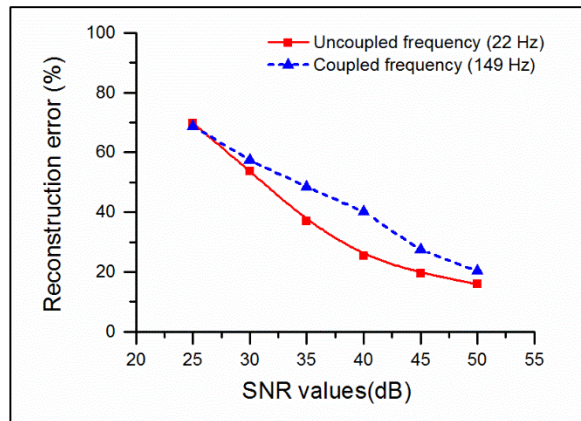
Figure 8.10: Maximum reconstruction errors for different signal-to-noise ratio at an uncoupled frequency (22 Hz) and coupled frequency (149 Hz).

8.5 Summary

Uncoupled and coupled natural frequencies are calculated by numerical simulations and corroborated with analytical results. Next, data for reconstruction is generated from predicted sound pressure levels in the near-field of the source. The sound pressure on the flexible surface of the box is reconstructed using equivalent source method. Tikhonov regularization with GCV and L-curve parameter selection methods are employed for solving ill-posed

condition. Reconstructed results are compared with actual results at both uncoupled and coupled frequencies. Effect of noise on the accuracy of the reconstruction is studied for different signal to noise ratio (SNR) values. Higher SNR values lead to good accuracy in reconstruction. Based on the regularization studies, it can be concluded that L-curve method is better as compared to GCV method for reconstruction at uncoupled and coupled frequencies.

Chapter 9

Conclusions and Scope of Future work

Aim of the present thesis is to study the vibro-acoustic behaviour of flexible rectangular ducts using direct and inverse techniques.

First part of thesis (Chapters-2 and 3), discussed sound radiation characteristics of the rectangular duct by analytical, experimental and numerical methods. An "equivalent plate" analytical model was described to calculate transverse transmission loss and radiation efficiencies of a flexible rectangular duct. These analytical results were validated with both experimental results obtained by sound intensity techniques and numerical results obtained by FEM-BEM based simulations.

As second part of thesis, modal parameters of the rectangular ducts by experimental, numerical modal analysis (Chapter-4) were studied. Three different ducts were considered and free-free boundary conditions was applied. Theoretical formulation was developed to understand the effect of duct joint condition on modal parameters and these results were validated with experimental results of rectangular duct with Pittsburgh lock joint (Chapter-5).

In third part of the thesis (Chapters- 6-8), inverse techniques such as near-field acoustic holography and inverse numerical acoustics were used to reconstruct sound field near the duct surfaces and also fan surfaces which was mounted in a free space.

Conclusions of each chapter was discussed at end of respective chapters. However, the most important conclusions drawn from the current research work is given below:

a) Sound radiation characteristics for a flexible rectangular duct has been studied using analytical, numerical and experimental methods. It has been observed that results obtained from all three methods are in good agreement. *Rectangular ducts can be modelled as an "equivalent plate model"*.

b) Breakout noise from duct walls is measured using two different sound intensity methods. It is concluded that: *Sound intensity techniques can be effectively used to measure the breakout noise*.

154

c) Effect of different duct joints on modal parameters has been studied by experimental and numerical modal analysis. An analytical model was also developed to incorporate joint condition. Based on the results it is concluded that: *Duct joints influences only mode shapes not natural frequencies.*

d) The vibration velocities were reconstructed accurately by inverse numerical acoustics method at both uncoupled and coupled frequencies of flexible rectangular ducts.

e) Fan noise source at blade pass frequency was reconstructed precisely using ESM based NAH technique.

f) Effect of signal noise on the accuracy of the reconstruction was studied for different signal to noise ratio (SNR) values. *Higher SNR values lead to good accuracy in reconstruction.*

g) L-curve method was better compared to GCV method for reconstruction at uncoupled and coupled frequencies of a rectangular duct. *Inverse techniques can be effectively used to reconstruct the sound sources in flexible ducts.*

9.1   Future work

Even though different studies are done to understand the vibro-acoustic behaviour of flexible rectangular ducts at coupled and uncoupled frequencies, further studies can be performed on the following research topics:

i) Statistical energy methods (SEA) can be applied for prediction of breakout noise at low frequencies due to the presence of higher modal density of the duct structure. A Hybrid method can be developed to predict the breakout noise for low to a high frequency range.

ii) The validated prediction models in the current study will be useful to develop design guidelines for the effective control of breakout noise from the flexible rectangular ducts.

iii) An analytical formulation for modelling of the joint can be extended for different joint conditions.

iv) A methodology can be established to reconstruct acoustic source strength inside the rectangular duct using inverse techniques.

References

[1] A. Cummings. Sound transmission through duct walls. *Journal of Sound and Vibration.* 239(4), (2001) 731-765.

[2] A. Cummings and I. J. Chang. Higher order mode and multimode acoustic transmission through the walls of flat oval ducts. *Journal of Sound and Vibration.* 108, (1986) 157-164.

[3] R. J. Astley and A. Cummings. A finite element scheme for acoustic transmission through the walls of rectangular ducts: comparison with experiment. *Journal of Sound and Vibration.* 92(3), (1984) 387-409.

[4] R. Kirby and A. Cummings. Structural/acoustic interaction in air-conditioning ducts in the presence of mean flow. *Proceedings of ISMA23*, Leuven, Belgium (1998) 677-684.

[5] H. P. Lee. Natural frequencies and mode shapes of cylindrical polygonal ducts. *Journal of Sound and Vibration.* 164, (1993) 182-187.

[6] J. D. Webb. *Noise Control in Mechanical Services.* Taylor & Francis. 1972.

[7] A. Cummings. Low frequency acoustic transmission through the walls of rectangular ducts. *Journal of Sound and Vibration.* 61, (1978) 327-345.

[8] A. Cummings. Low frequency acoustic transmission through the walls of rectangular ducts: further comments. *Journal of Sound and Vibration.* 63, (1979) 463-465.

[9] A. Cummings. Low frequency acoustic radiation from duct walls. *Journal of Sound and Vibration.* 71, (1980) 201-226.

[10] A. Cummings. Higher order mode acoustic transmission through the walls of rectangular ducts. *Journal of Sound and Vibration.* 90, (1983) 193-209.

[11] R. J. Astley and A. Cummings. A finite element scheme for attenuation in ducts lined with porous material: comparison with experiment. *Journal of Sound and Vibration.* 116(2), (1987) 239- 263.

[12] B. Venkatesham, M. Tiwari and M. L. Munjal. Analytical prediction of the breakout noise from a rectangular cavity with one compliant wall. *The Journal of the Acoustical Society of America.* 124(5), (2008) 2952-2962.

[13] B. Venkatesham, M. Tiwari and M. L. Munjal. Analytical prediction of break-out noise from a reactive rectangular plenum with four flexible walls. *The Journal of the Acoustical Society of America.* 128(4), (2010) 1789-1799.

[14] B. Venkatesham, M. Tiwari and M.L. Munjal. Prediction of brake-out noise from a rectangular duct with compliant walls. *International Journal of Acoustics and Vibration.* 16(4), (2011) 180-190.

[15] R. J. Astley, A. Cummings and N. Sormaz. A finite element scheme for acoustical propagation in flexible walled ducts with bulk reacting liners and comparison with experiment. *Journal of Sound and Vibration*. 150, (1991) 119-138.

[16] V. Martin. Perturbation of fluid-guided waves introduced by bending plates. *Journal of Sound and Vibration*. 144, (1991) 331-353.

[17] A. Cummings. Approximate asymptotic solutions for acoustic transmission through the walls of rectangular ducts. *Journal of Sound and Vibration*. 90, (1983) 211-227.

[18] W. H. Louisell. *Coupled Mode and Parametric Electronics*. John Wiley & Sons, New York, USA, 1960.

[19] A. Cabelli. The propagation of sound in a square duct with a non-rigid side wall. *Journal of Sound and Vibration.* 103(3), (1985) 379-394.

[20] E. H. Dowell, G. F. Gorman and D.A. Smith. Acoustoelasticity: General theory, acoustic modes and forced response to sinusoidal excitation, including comparisons with experiment. *Journal of Sound and Vibration.* 52, (1977) 519–542.

[21] S. M. Kim and M. J. Brennan. A compact matrix formulation using the impedance and mobility approach for the analysis of structural-acoustic systems. *Journal of Sound and Vibration.* 223, (1999) 97–113.

[22] T. R. Lin and J. Pan. Sound radiation characteristics of a box-type structure. *Journal of Sound and Vibration*. 325, (2009) 835–851.

[23] A. Cummings, I. J. Chang and R. J. Astley. Sound transmission at low frequencies through the walls of distorted circular ducts. *Journal of Sound and Vibration*. 97, (1984) 261-286.

[24] S. N. Yoursi and F. J. Fahy. Distorted cylindrical shell response to internal acoustic excitation below the cut-off frequency. *Journal of Sound and Vibration.* 52, (1977) 441-452.

[25] D. Firth. Acoustic vibration of a liquid filled distorted circular cylindrical shell. *International Journal for Numerical Methods in Engineering.* 13, (1978) 151-164.

[26] A. Cummings and I. J. Chang. A finite difference scheme for acoustic transmission through the walls of distorted circular ducts and comparison with experiment. *Journal of Sound and Vibration*. 104, (1986) 377-393.

[27] A. Guthrie. Low frequency acoustic transmission through the walls of various types of ducts. M.Sc. Dissertation, Polytechnic of the South Bank, 1979.

[28] A. Cummings and I. J. Chang. Noise breakout from flat-oval ducts. *Journal of Sound and Vibration*. 106, (1986) 17-33.

[29] A. Cummings and I. J. Chang. Sound propagation in a flat oval waveguide. *Journal of Sound and Vibration.* 106, (1986) 35-43.

[30] A. Cummings and R. J. Astley. The effects of flanking transmission on sound attenuation in lined ducts. *Journal of Sound and Vibration.* 179, (1995) 617-646.

[31] A. Cummings. The Effect of external lagging on low frequency sound transmission through the walls of rectangular ducts. *Journal of Sound and Vibration.* 67, (1979) 187-201.

[32] M. L. Munjal. Acoustic analysis and parametric studies of lagged pipes. *Noise Control Engineering Journal.* 45(3), (1997) 113-118.

[33] B. Venkatesham, M. L. Munjal and M. Tiwari. Prediction of breakout noise from acoustically lagged rectangular HVAC ducts. *Building Acoustics.* 16(4), (2009) 313-328.

[34] A. Cummings. Stiffness control of low frequency acoustic transmission through the walls of rectangular ducts. *Journal of Sound and Vibration.* 74, (1981) 351-380.

[35] C. E. Wallace. Radiation resistance of a rectangular panel. *The Journal of the Acoustical Society of America.* 51, (1972) 946–952.

[36] D. J. Ewins. *Modal testing: Theory and Practice*. Letchworth: Research studies press, Baldock, Hertfordshire, England, 2000.

[37] C. C. Kennedy and C. D. Pancu. Use of vectors in vibration measurement and analysis. *Journal of the Aeronautical Sciences.* 14, (1947) 603-625.

[38] Z. F. Fu and J. He. *Modal analysis*. Butterworth-Heinemann, Great Britain, 2001.

[39] N. M. M. Maia. Extraction of valid modal properties from measured data in structural vibrations. Doctoral dissertation, Imperial College London (University of London), 1988.

[40] B. Schwarz, M. Richardson and P. Avitabile. Locating optimal references for modal testing. *In Proceedings of the 20th International Modal Analysis Conference.* Los Angeles, 2002.

[41] D. Linehan and K. Napolitano. Accelerometer selection methods for modal pre-test analysis. *Sound and Vibration Magazine.* 6(2), (2012) 5-8.

[42] S. R. Ibrahim. Fundamentals of time domain modal identification. *Modal Analysis and Testing*. Springer, Netherlands, (1999) 241-250.

[43] C. G. Koh, B. Hong and C.Y, Liaw. Parameter identification of large structural systems in time domain. *Journal of Structural Engineering*. 126(8), (2000) 957-963.

[44] N. M. M. Maia, Modal Identification Methods in the Frequency Domain. *Modal Analysis and Testing*. Springer, Netherlands, (1999) 251-264.

[45] J. A. Brandon and A. Cowley. A weighted least squares method for circle fitting to frequency response data. *Journal of Sound and Vibration.* 89(3), (1983) 419-424.

[46] N. M. M. Maia and J. M. M. e Silva. *Theoretical and experimental modal analysis.* Research Studies Press, England, 1997.

[47] J. E. Mottershead. On the natural frequencies and antiresonances of modified structures # 294. *In Proceedings of the 17th International Modal Analysis Conference.* 3727, 1999.

[48] M. EI-Kafafy, P. Guillaume, B. Peeters, F. Marra and G. Coppotelli. Advanced frequency-domain modal analysis for dealing with measurement noise and parameter uncertainty. *In Topics in Modal Analysis I,* Springer, New York, 5, (2012) 179-199.

[49] R. J. Allemang. The Modal Assurance Criterion: twenty years of use and abuse. Sound and Vibration Magazine. 37(8), (2003) 14-23.

[50] D. J. Ewins. Model validation: Correlation for updating, *Sadhana.* 25(3), (2000) 221-234.

[51] R. D. Blevins. *Formulas for Natural Frequency and Mode Shape.* Kreiger Publ. Comp., New York, 1979.

[52] S. Azmi, W. Soedel and J. F. Hamilton. Natural frequencies and modes of cylindrical polygonal ducts using receptance methods. *Journal of Sound and Vibration.* 109, (1986) 79-88.

[53] W. Soedel. Natural frequencies and modes of cylindrical polygonal ducts using receptance methods. *Journal of Sound and Vibration.* 115, (1987) 365-366.

[54] G. Yamada and K. Kobayashi. Natural frequencies and modes of cylindrical polygonal ducts using receptance methods. *Journal of Sound and Vibration.* 115, (1987) 363-364.

[55] P. N. Chavan and B. Venkatesham. Free vibration analysis of a rectangular duct with different axial boundary conditions. *International Journal of Acoustics and Vibration.* 20(1), (2015) 10-14.

[56] S. J. Mohan and R. Pratap. A natural classification of vibration modes of polygonal ducts based on group theoretic analysis. *Journal of Sound and Vibration.* 269(3-5), (2004) 745–764.

[57] H. Xiao, J. Pan and M. Sheng. Vibration characteristics of a cylinder with asymmetries. *Proceedings of Acoustics.* Australia, 2011.

[58] K. M. Gorrepati and M. D. Rao. Analysis of modal parameters of adhesively bonded double-strap joints by the modal strain energy method. *Journal of Vibration and Acoustics.* 118(1), (1996) 28-35.

[59] S. Xu and X. Deng. An evaluation of simplified finite element models for spot-welded joint. *Finite Elements in Analysis and Design.* 40(9), (2004) 1175-1194.

[60] H. Tian, D. Zhu and H. Qin. Theoretical-experimental modeling of bolted joint interface in milling of grey cast iron HT250. *International Journal of Modeling and Optimization.* 1(1), (2011) 19-23.

[61] I. Zaman, A. Khalid, B. Manshoor, S. Araby and M. I. Ghazali. The effects of bolted joints on dynamic response of structures. *IOP Conference Series: Materials Science and Engineering.* 50(1), (2013) 12-18.

[62] S. F. Alexandre, A. F. Camarão, A. D. O. Fernandes, M. A. Bezerra, M. A. Argentino and R. R. Ripoli. A finite element approach for fatigue analysis of welded components. *SAE Tech. Paper.* No. 2001-01-4077, (2001).

[63] J. D. Maynard, E. G. Williams and Y. Lee. Near-field acoustic holography: I. Theory of generalized holography and the development of NAH. *The Journal of the Acoustical Society of America.* 78(a), (1985) 1395–1413.

[64] M. R. Bai, J. G. Ih, and J. Benesty. *Acoustic array systems: theory, implementation, and application.* John Wiley & Sons, Singapore, 2013.

[65] M. B. S. Magalhaes and R. A. Tenenbaum. Sound sources reconstruction techniques: A review of their evolution and new trends. *Acta Acustica United with Acustica.* 90(2), (2004) 199-220.

[66] K. Chelliah, G. Raman and R. T. Muehleisen. An experimental comparison of various methods of nearfield acoustic holography. *Journal of Sound and Vibration.* 403, (2017) 21-37.

[67] F. Jacobsen and Y. Liu. Near field acoustic holography with particle velocity transducers. *The Journal of the Acoustical Society of America.* 118(5), (2005) 3139-3144.

[68] F. Jacobsen and V. Jaud. Statistically optimized near field acoustic holography using an array of pressure-velocity probes. *The Journal of the Acoustical Society of America.* 121(3), (2007) 1550-1558.

[69] W. A. Veronesi and J. D. Maynard. Near-field acoustic holography: II. Holographic reconstruction algorithms and computer implementation. *The Journal of the Acoustical Society of America.* 81(5), (1987) 1307-1322.

[70] E. G. Williams. *Fourier Acoustics: Sound Radiation and Near-field Acoustical Holography.* Academic Press, 1999.

[71] J. Hald. Basic theory and properties of statistically optimized near-field acoustical holography. *The Journal of the Acoustical Society of America.* 125(4), (2009) 2105–2120.

[72] J. Gomes. Conformal Patch Holography. PhD thesis, University of Southern Denmark, 2008.

[73] C. T. Cho, J. S. Bolton, and J. Hald. Source visualization by using statistically optimized near-field acoustical holography in cylindrical coordinates. *The Journal of the Acoustical Society of America*. 118, (2005) 2355–2364.

[74] J. Hald. Patch holography in cabin environments using a two-layer handheld array and an extended SONAH algorithm. *Proceedings of Euronoise*. 2006.

[75] S. F. Wu. On reconstruction of acoustic pressure fields using the Helmholtz equation least squares method. *The Journal of the Acoustical Society of America*. 107(5), (2000) 2511-2522.

[76] T. Semenova and S. F. Wu. The Helmholtz equation least-squares method and Rayleigh hypothesis in near-field acoustical holography. *The Journal of the Acoustical Society of America*. 115(4), (2004) 1632-1640.

[77] M. S. Moondra and S. F. Wu. Visualization of vehicle interior sound field using near-field acoustical holography based on the Helmholtz-Equation Least-Squares (HELS) method. *Noise Control Engineering Journal*. 53(4), (2005) 145-154.

[78] W. A. Veronesi and J. D. Maynard. Digital holographic reconstruction of sources with arbitrarily shaped surfaces. *The Journal of the Acoustical Society of America*. 85(2), (1989) 588-598.

[79] M. R. Bai. Application of BEM (boundary element method) based acoustic holography to radiation analysis of sound sources with arbitrarily shaped geometries. *The Journal of the Acoustical Society of America*. 92(1), (1992) 533-549.

[80] Z. D. Zhang, N. Vlahopoulos, S. T. Raveendra, T. Allen, and K. Y. Zhang. A computational acoustic field reconstruction process based on an indirect boundary element formulation. *The Journal of the Acoustical Society of America*. 108(5), (2000) 2167-2178.

[81] A. Schuhmacher, K. B. Rasmussen, and P. C. Hansen. Sound source reconstruction using inverse boundary element calculations. *The Journal of the Acoustical Society of America*. 113(1), (2003).

[82] N. P. Valdivia, E. G. Williams and P. C. Herdic. Approximations of inverse boundary element methods with partial measurements of the pressure field. *The Journal of the Acoustical Society of America*. 123 (1), (2008) 109-120.

[83] A. Sarkissian. Extension of measurement surface in near-field acoustic holography. *The Journal of the Acoustical Society of America*. 115(4), (2004) 1593–1596.

[84] G. H. Koopmann, L. M. Song and J. B. Fahline. A method for computing acoustic fields based on the principle of wave superposition. *The Journal of the Acoustical Society of America*. 86(6), (1989) 2433-2438.

[85] M. Ochmann. The full-field equations for acoustic radiation and scattering. *The Journal of the Acoustical Society of America*. 105(5), (1999) 2574-2584.

[86] I. Y. Jeon and J. G. Ih. On the holographic reconstruction of vibroacoustic fields using equivalent sources and inverse boundary element method. *The Journal of the Acoustical Society of America*. 118(6), (2005) 3473-3482.

[87] N. P. Valdivia and E. G. Williams. Study of the comparison of the methods of equivalent sources and boundary element methods for near-field acoustic holography. *The Journal of the Acoustical Society of America*. 120(6), (2006) 3694-3705.

[88] N.P. Valdivia, E. G. Williams, P.C. Herdic and B. Houston. Surface decomposition method for near-field acoustic holography. *The Journal of the Acoustical Society of America.* 132 (1), (2012) 186–196.

[89] M. R. Bai, C. C. Chen and J. H. Lin. On optimal retreat distance for the equivalent source method-based nearfield acoustical holography. *The Journal of the Acoustical Society of America.* 129(3), (2011) 1407-1416.

[90] M. Lee, J. S. Bolton and L. Mongeau. Application of cylindrical near-field acoustical holography to the visualization of aeroacoustic sources. *The Journal of the Acoustical Society of America.* 114 (2), (2003) 842-858.

[91] Y. Kim and P.A. Nelson. Estimation of acoustic source strength with in a cylindrical duct by inverse methods. *Journal of Sound and Vibration.* 275, (2004) 391–413.

[92] C. R. Lowis and P. F. Joseph. Determining the strength of rotating broadband sources in ducts by inverse methods. *Journal of Sound and Vibration*. 295, (2006) 614–632.

[93] W. Zhang, S. Raveendra, M. Lee and J. Bolton. Reconstruction of noise source in a ducted fan using a generalized nearfield acoustical holography. *SAE Technical Paper*. 2010-01-0416, (2010).

[94] E.G. Williams. Regularization methods for near-field acoustical holography. *The Journal of the Acoustical Society of America*. 110(4), (2001) 1976-1988.

[95] A.N. Tikhonov and V.Y. Arsenin. *Solutions of Ill-Posed Problems.* Winston and Sons., Washington D.C., 1977.

[96] J. Gomes and P.C. Hansen. A study on regularization parameter choice in near-field acoustical holography. *The Journal of the Acoustical Society of America*. 123(5), (2008) 3385-3385.

[97] M. Hanke. *Conjugate Gradient Methods for Ill-Posed Problems*. Longman Scientific and Technical, Essex, 1995.

[98] C. R. Vogel. Solving ill-conditioned linear systems using the conjugate gradient method. *Report, Dept. of Mathematical Sciences*. Montana State University, 1987.

[99] P. C. Hansen. The L-curve and its use in the numerical treatment of inverse problems. *Advances in Computational Bioengineering*. (1999) 119-142.

[100] P. C. Hansen. Analysis of discrete ill-posed problems by means of the L-curve. *SIAM Review*. 34, (1992) 561-580.

[101] L. Elden. A note on the computation of the generalized cross-validation function for ill-conditioned least squares problems. *BIT Numerical Mathematics*. 24, (1984) 467-472.

[102] V. A. Morozov. *Methods for solving incorrectly posed problems*. Springer Verlag, New York, 1984.

[103] F. D Martinus, W. Herrin and A. F. Seybert. Surface vibration reconstruction using inverse numerical acoustics. *Journal of Engineering and Technological Sciences*. 35(1), (2003) 61-80.

[104] B. K. Gardner and R.J. Bernhard. A noise source identification technique using an inverse Helmholtz integral equation method. *Journal of Vibration, Acoustics, Stress reliability and Design*. 110, (1988) 84-90.

[105] B. K. Kim, and J. G Ih. On the reconstruction of the vibro-acoustic field over the surface enclosing an interior space using the boundary element method. *The Journal of the Acoustical Society of America*. 100, (1996) 3003-3015.

[106] M. Tournour, L. Cremers and P. Guisset. Inverse numerical acoustics based on acoustic transfer vectors. *7th International Congress on Sound and Vibration*. Germany, (2000) 2069-1076.

[107] M.L. Munjal. *Acoustics of Ducts and Mufflers*. 2nd edition., John Wiley & Sons, UK, 2014.

[108] D.A. Bies and C.H. Hansen, *Engineering Noise Control: Theory and Practice*, 4th edition, Spon Press, UK and USA, 2009.

[109] F. Jacobsen and H.E. de Bree. A comparison of two different sound intensity measurement principles. *The Journal of the Acoustical Society of America*. 118 (3), (2005) 1510–1517.

[110] Microflown technologies. *Scan & Paint V2.0, User's Manual*. 2015.

[111] F. Jacobsen. An overview of the sources of error in sound power determination using the intensity technique. *Applied Acoustics*. 50 (2), (1997) 155-166.

[112] Y. Chen, G. Jin, M. Zhu, Z. Liu, J. Du, and W. L. Li. Vibration behaviors of a box type structure built up by plates and energy transmission through the structure. *Journal of Sound and Vibration*. 331(4), (2012) 849-867.

[113] P. Vacher, B. Jacquier and A. Bucharles. Extensions of the MAC criterion to complex modes. *Proceedings of the International Conference on Noise and Vibration Engineering*. (2010) 2713-2726.

[114] M. P. Dhanesh. A study of modal testing measurement errors, sensor placement and modal complexity on the process of FE correlation. Master thesis, University of Cincinnati, (2005).

[115] Z. Ding. Natural frequencies of rectangular plates using a set of static beam functions in Rayleigh-Ritz method. *Journal of Sound and Vibration*. 189(1), (1996) 81-87.

[116] D. Zhou and Y. K. Cheung. Free vibration of line supported rectangular plates using a set of static beam functions. *Journal of Sound and Vibration*. 223(2), (1999) 231-245.

[117] S. M. Kirkup. *The Boundary Element Method in Acoustics*. 1st edition., Integrated Sound Software, 1998.

[118] A F Seybert and F. Martinus. Forward and inverse numerical acoustics for NVH applications. *In 9th International Congress on Sound and Vibration*. Orlando, Florida, 2002.

[119] D. Dhamodharan. Investigation of Holographic Reconstruction Algorithms in Near-field Acoustical Holography. Master thesis, Institute of water acoustics, University of Applied sciences, Bremen, Germany, 2006.

[120] Z. Wang and S. F. Wu. Helmholtz equation-least-squares method for reconstructing the acoustic pressure field. *The Journal of the Acoustical Society of America*. 102, (1997) 2020–2032.

[121] S. Boyd and L. Vandenberghe. *Convex Optimization*. Cambridge University Press, England, 2004.

[122] J. Hald. Patch near-field acoustical holography using a new statistically optimal method. *Bruel & Kjaer Tech. Rev.* 1, (2005) 40-50.

[123] R. Steiner and J. Hald. Near-field acoustical holography without the errors and limitations caused by the use of spatial DFT. *International Journal of Acoustics and Vibration*. 6, (2001) 83–89.

[124] J. B. Fahnline and G. H. Koopmann. A numerical solution for the general radiation problem based on the combined methods of superposition and singular-value decomposition. *The Journal of the Acoustical Society of America*. 90, (1991) 2808–2819.

[125] M. C. Unger and D. Feit. *Sound, Structures, and Their Interaction*. 2nd edition, MIT, Press, London, 1986.

[126] P. M. Juhl. The boundary element method for sound field calculations. Doctoral Thesis, Department of Acoustic Technology, Technical University of Denmark, 1993.

[127] J. S. Bendat and A. G. Piersol. *Random Data: Analysis and Measurement Procedures*, 3rd edition., Wiley, New York, 2000.

[128] S. H. Yoon and P. A. Nelson. A method for the efficient construction of acoustic pressure cross-spectral matrices. *Journal of Sound and Vibration*. 233, (2000) 897–920.

[129] H. S. Kwon and J. S. Bolton. Partial field decomposition in near-field acoustical holography by the use of singular value decomposition and partial coherence procedures. *Proceedings of NOISE-CON 98*. (1998).

[130] D. L. Hallman and J. S. Bolton. A comparison of multi-reference nearfield acoustical holography procedures. *Proceedings of NOISE-CON 94*. (1994) 929–934.

[131] J. W. Demmel. *Applied Numerical Linear Algebra*, University of California, SIAM Publishing Co., California, 1997.

[132] P. C. Hansen. Regularization tools version 4.0 for Matlab 7.3. *Numerical algorithms*. 46(2), (2007) 189-194.

Appendices

A-Simplification of quadruple integral

The simplification of the quadruple integral equation given in Eq. (18) is written for different modal indices cases as follows:

$$I_{m_1 m_2 m_1' m_2'} = \int_0^L \int_0^{L_1} \int_0^L \int_0^{L_1} sin\frac{m_1 \pi x}{L} sin\frac{m_2 \pi x_1}{L_1} sin\frac{m_1' \pi x'}{L} sin\frac{m_2' \pi x_1'}{L_1} \frac{sin\, kR}{R} \, dx_1' \, dx' \, dx_1 \, dx$$

For $m_1 = m_1'$ and $m_2 = m_2'$

$$I_{m_1 m_2 m_1' m_2'} = \frac{1}{\alpha_{m_1} \beta_{m_2}} J_1^{m_1 m_2} + J_2^{m_1 m_2} + \frac{1}{\alpha_{m_1}} J_3^{m_1 m_2} + \frac{1}{\beta_{m_2}} J_4^{m_1 m_2}$$

(A.1)

For $m_1 \neq m_1'$ and $m_2 \neq m_2'$

$$I_{m_1 m_2 m_1' m_2'} = \frac{\varepsilon(m_1' - m_1)\, \varepsilon(m_2' - m_2)}{\left(\alpha_{m_1}^2 - \alpha_{m_1'}^2\right)\left(\beta_{m_2}^2 - \beta_{m_2'}^2\right)} \left\{ \alpha_{m_1} \beta_{m_2} J_1^{m_1' m_2'} - \alpha_{m_1} \beta_{m_2'} J_1^{m_1' m_2} - \alpha_{m_1'} \beta_{m_2} J_1^{m_1 m_2'} + \right.$$

$$\left. \alpha_{m_1'} \beta_{m_2'} J_1^{m_1 m_2} \right\}$$

(A.2)

For $m_1 \neq m_1'$ and $m_2 = m_2'$

$$I_{m_1 m_2 m_1' m_2} = \frac{\varepsilon(m_1' - m_1)}{\left(\alpha_{m_1}^2 - \alpha_{m_1'}^2\right)} \left\{ \alpha_{m_1} J_3^{m_1' m_2} - \alpha_{m_1'} J_3^{m_1 m_2} + \frac{\alpha_{m_1}}{\beta_{m_2}} J_1^{m_2' m_1} - \frac{\alpha_{m_1'}}{\beta_{m_2}} J_1^{m_1 m_2} \right\}$$

(A.3)

For $m_1 = m_1'$ and $m_2 \neq m_2'$

$$I_{m_1 m_2 m_1' m_2} = \frac{\varepsilon(m_2' - m_2)}{\left(\beta_{m_2}^2 - \beta_{m_2'}^2\right)} \left\{ \beta_{m_2} J_4^{m_1 m_2'} - \beta_{m_2'} J_4^{m_1 m_2} + \frac{\beta_{m_2}}{\alpha_{m_1}} J_1^{m_2' m_1} - \frac{\beta_{m_2'}}{\alpha_{m_1}} J_1^{m_1 m_2} \right\}$$

(A.4)

Where:

166

$$\begin{Bmatrix} J_1^{m_1 m_2} \\ J_2^{m_1 m_2} \\ J_3^{m_1 m_2} \\ J_4^{m_1 m_2} \end{Bmatrix} = \int_0^{L_2} \int_0^{L_1} \begin{Bmatrix} 1 \\ (L_1 - x)(L_2 - y) \\ (L_2 - y) \\ (L_1 - x) \end{Bmatrix} x \begin{Bmatrix} \sin \alpha_{m_1} x \sin \beta_{m_2} y \\ \cos \alpha_{m_1} x \cos \beta_{m_2} y \\ \sin \alpha_{m_1} x \cos \beta_{m_2} y \\ \cos \alpha_{m_1} x \sin \beta_{m_2} y \end{Bmatrix} \frac{\sin k \sqrt{x^2 + y^2}}{\sqrt{x^2 + y^2}} dx \, dy$$

$$\text{(A.5)}$$

$$\alpha_{m_1} = \frac{m_1 \pi}{L_1}, \ \beta_{m_2} = \frac{m_2 \pi}{L_2}, \quad \varepsilon(m_1' - m_1) = \begin{cases} 1 & \text{for } m_1' = m_1 \\ 0 & \text{for } m_1' - m_1 = \pm 1, \pm 3, \pm 5 \dots \dots \\ 2 & \text{for } m_1' - m_1 = \pm 2, \pm 4, \pm 6 \dots \dots \end{cases}$$

$$\text{(A.6)}$$

The double integrals involved in Eq. (A.5) are expressed in terms of single integrals by polar coordinate transformation as follows,

$$\begin{Bmatrix} x \\ y \end{Bmatrix} = L_1 \rho \begin{Bmatrix} \cos \theta \\ \sin \theta \end{Bmatrix} \tag{A.7}$$

Double integrals can be rewritten as,

$$\mathfrak{I}_{1i}^{m_1 m_2} = \int_0^{L_2} \int_0^{L_1} \sin \alpha_{m_1} x \sin \beta_{m_2} y \frac{\cos k \sqrt{x^2 + y^2}}{\sqrt{x^2 + y^2}} dx \, dy = \mathfrak{I}_{1i}^{(1)} \left(\alpha_{m_1}, \beta_{m_2}, L_1, L_2 \right) +$$

$$\mathfrak{I}_{1i}^{(2)} \left(\alpha_{m_1}, \beta_{m_2}, L_1, L_2 \right)$$

$$\mathfrak{I}_{2i}^{m_1 m_2} = \int_0^{L_2} \int_0^{L_1} \cos \alpha_{m_1} x \cos \beta_{m_2} y \frac{\cos k \sqrt{x^2 + y^2}}{\sqrt{x^2 + y^2}} dx \, dy = \mathfrak{I}_{2i}^{(1)} \left(\alpha_{m_1}, \beta_{m_2}, L_1, L_2 \right) +$$

$$\mathfrak{I}_{2i}^{(2)} \left(\alpha_{m_1}, \beta_{m_2}, L_1, L_2 \right)$$

$$\mathfrak{I}_{3i}^{m_1 m_2} = \int_0^{L_2} \int_0^{L_1} \sin \alpha_{m_1} x \cos \beta_{m_2} y \frac{\cos k \sqrt{x^2 + y^2}}{\sqrt{x^2 + y^2}} dx \, dy = \mathfrak{I}_{3i}^{(1)} \left(\alpha_{m_1}, \beta_{m_2}, L_1, L_2 \right) +$$

$$\mathfrak{I}_{3i}^{(2)} \left(\alpha_{m_1}, \beta_{m_2}, L_1, L_2 \right)$$

$$\mathfrak{I}_{4i}^{m_1 m_2} = \int_0^{L_2} \int_0^{L_1} \cos \alpha_{m_1} x \sin \beta_{m_2} y \frac{\cos k \sqrt{x^2 + y^2}}{\sqrt{x^2 + y^2}} dx \, dy = \mathfrak{I}_{4i}^{(1)} \left(\alpha_{m_1}, \beta_{m_2}, L_1, L_2 \right) +$$

$$\mathfrak{I}_{4i}^{(2)} \left(\alpha_{m_1}, \beta_{m_2}, L_1, L_2 \right)$$

$$\text{(A.8)}$$

where,

$$\mathfrak{I}_{1i}^{(1)} = \int_0^{\tan^{-1}(\mu)} \int_0^{\sec \theta} \sin \left(L_1 \alpha_{m_1} \rho \cos \theta \right) \sin \left(L_1 \beta_{m_2} \rho \sin \theta \right) \cos(k L_1 \rho) L_1 \, d\rho \, d\theta$$

$$\text{(A.9)}$$

$$\mathfrak{I}_{1i}^{(2)} = \int_{\tan^{-1}(\mu)}^{\pi/2} \int_0^{\mu \csc \theta} \sin \left(L_1 \alpha_{m_1} \rho \cos \theta \right) \sin \left(L_1 \beta_{m_2} \rho \cos \theta \right) \cos(k L_1 \rho) L_1 \, d\rho \, d\theta$$

$$\text{(A.10)}$$

With $\mu = \frac{L_2}{L_1}$, The expressions for $\mathfrak{I}_{2i}^{(1)}, \mathfrak{I}_{2i}^{(2)}, \mathfrak{I}_{3i}^{(1)}, \mathfrak{I}_{3i}^{(2)}, \mathfrak{I}_{4i}^{(1)}, \mathfrak{I}_{4i}^{(2)}$ are similar to the $\mathfrak{I}_{1i}^{(1)}, \mathfrak{I}_{1i}^{(2)}$ as mentioned in the above Eqs. (A.9) and (A.10).

Further simplification of the Eqs. (A.9) and (A.10) gives the following expressions. These single integrals are evaluated numerically.

$\mathfrak{I}_{1i}^{(1)}$

$$= \frac{1}{4} \int_0^{\tan^{-1} \mu} \left\{ R\left(\alpha_{m_1}, -\beta_{m_2}, -k, \theta\right) + R\left(\alpha_{m_1}, -\beta_{m_2}, k, \theta\right) - R\left(\alpha_{m_1}, \beta_{m_2}, -k, \theta\right) \right.$$

$$\left. - R\left(\alpha_{m_1}, \beta_{m_2}, k, \theta\right) \right\} \, d\theta$$

$\mathfrak{I}_{2i}^{(1)}$

$$= \frac{1}{4} \int_0^{\tan^{-1} \mu} \left\{ R\left(\alpha_{m_1}, -\beta_{m_2}, -k, \theta\right) + R\left(\alpha_{m_1}, -\beta_{m_2}, k, \theta\right) + R\left(\alpha_{m_1}, \beta_{m_2}, -k, \theta\right) \right.$$

$$\left. + R\left(\alpha_{m_1}, \beta_{m_2}, k, \theta\right) \right\} \, d\theta$$

$\mathfrak{I}_{3i}^{(1)}$

$$= \frac{1}{4} \int_0^{\tan^{-1} \mu} \left\{ -S\left(\alpha_{m_1}, -\beta_{m_2}, -k, \theta\right) - S\left(\alpha_{m_1}, -\beta_{m_2}, k, \theta\right) - S\left(\alpha_{m_1}, \beta_{m_2}, -k, \theta\right) \right.$$

$$\left. - S\left(\alpha_{m_1}, \beta_{m_2}, k, \theta\right) \right\} \, d\theta$$

$\mathfrak{I}_{4i}^{(1)}$

$$= \frac{1}{4} \int_0^{\tan^{-1} \mu} \left\{ S\left(\alpha_{m_1}, -\beta_{m_2}, -k, \theta\right) + S\left(\alpha_{m_1}, -\beta_{m_2}, k, \theta\right) - S\left(\alpha_{m_1}, \beta_{m_2}, -k, \theta\right) \right.$$

$$\left. - S\left(\alpha_{m_1}, \beta_{m_2}, k, \theta\right) \right\} \, d\theta$$

$$(A.11)$$

where,

$$S\left(\alpha_{m_1}, \beta_{m_2}, k, \theta\right) = \frac{\cos(L_1(\alpha_m \cos\theta + \beta \sin\theta + k)\sec\theta)}{(\alpha_m \cos\theta + \beta \sin\theta + k)} - \frac{1}{\alpha_m \cos\theta + \beta \sin\theta + k}$$

$$R\left(\alpha_{m_1}, \beta_{m_2}, k, \theta\right) = \frac{\sin(L_1(\alpha_m \cos\theta + \beta \sin\theta + k)\sec\theta))}{(\alpha_m \cos\theta + \beta \sin\theta + k)}$$

$$(A.12)$$

The second part of the integrals in Eq. (A.8) can be calculated from Eq. (A.11)

$$\mathfrak{I}_{ji}^{(2)}\left(\alpha_{m_1}, \beta_{m_2}, L_1, L_2\right) = \mathfrak{I}_{ji}^{(1)}\left(\alpha_{m_1}, \beta_{m_2}, L_1, L_2\right) \qquad \text{for} \quad j = 1, 2$$

$$\mathfrak{I}_{3i}^{(2)}\left(\alpha_{m_1}, \beta_{m_2}, L_1, L_2\right) = \mathfrak{I}_{4i}^{(1)}\left(\alpha_{m_1}, \beta_{m_2}, L_1, L_2\right)$$

$$\mathfrak{I}_{4i}^{(2)}\left(\alpha_{m_1}, \beta_{m_2}, L_1, L_2\right) = \mathfrak{I}_{3i}^{(1)}\left(\alpha_{m_1}, \beta_{m_2}, L_1, L_2\right)$$

The integral expressions in Eq. (A.5) are expressed in terms of double integral values evaluated in Eq. (A.11)

$$J_{1i}^{m_1 m_2} = \mathfrak{I}_{1i}^{mn}$$

$$J_{2i}^{m_1 m_2} = L_1 L_2 \mathfrak{I}_{2i}^{mn} - L_1 \frac{\partial}{\partial \beta_{m_2}} \mathfrak{I}_{4i}^{mn} - L_2 \frac{\partial}{\partial \beta_{m_2}} \mathfrak{I}_{3i}^{mn} + \frac{\partial^2}{\partial \beta_{m_2} \partial \alpha_{m_1}} \mathfrak{I}_{1i}^{mn}$$

$$J_{3i}^{m_1 m_2} = L_2 \mathfrak{I}_{3i}^{mn} - \frac{\partial}{\partial \beta_{m_2}} \mathfrak{I}_{1i}^{mn} , J_{4i}^{m_1 m_2} = L_1 \mathfrak{I}_{4i}^{mn} - \frac{\partial}{\partial \alpha_{m_2}} \mathfrak{I}_{1i}^{mn}$$

B- Eigen frequency equation

Minimize the total energy (kinetic and strain) by substituting the Eq. (5.6) in Eq. (5.1) to (5.33), which is given as follows,

$$\frac{\partial}{\partial A_{mn}}(U_{max} - T_{max}) = 0 \tag{B1}$$

Here, for simplicity circumferential and axial length are represented as 'a' and 'b', respectively.

$$\frac{\partial}{\partial A_{mn}}\left\{\left[\frac{1}{2}e^{2i\omega t}\sum_{m=1}^{\infty}\sum_{n=1}^{\infty}A_{mn}^2\int_0^1\int_0^1\left\{\frac{D_x}{a^4}\left(\frac{\partial^2\Phi_m}{\partial x_1^2}\Psi_n\right)^2 + \frac{2H}{a^2b^2}\left(\frac{\partial^2\Phi_m}{\partial x_1^2}\Psi_n\right)\left(\Phi_m\frac{\partial^2\Psi_n}{\partial y^2}\right) + \right.\right.\right.$$
$$\frac{D_y}{b^4}\left(\Phi_m\frac{\partial^2\Psi_n}{\partial y^2}\right)^2 - \frac{4D_{xy}}{a^2b^2}\left[\left(\frac{\partial^2\Phi_m}{\partial x_1^2}\Psi_n\right)\left(\Phi_m\frac{\partial^2\Psi_n}{\partial y^2}\right) - \left(\frac{\partial\Phi_m}{\partial x_1}\frac{\partial\Psi_n}{\partial y}\right)^2\right] -$$
$$\left.\left.\rho h(i\omega\,\Phi_m\Psi_n)^2\right\}a\,d\alpha\,b\,d\beta\right] + U_{rs}\right\} = 0 \tag{B2}$$

$$\sum_{m=1}^{\infty}\sum_{n=1}^{\infty}\frac{b^4}{H}A_{mn}\int_0^1\int_0^1\left\{\frac{D_x}{a^4}\left(\frac{\partial^2\Phi_m}{\partial x_1^2}\Psi_n\right)^2 + \frac{2H}{a^2b^2}\left(\frac{\partial^2\Phi_m}{\partial x_1^2}\Psi_n\right)\left(\Phi_m\frac{\partial^2\Psi_n}{\partial y^2}\right) + \frac{D_y}{b^4}\left(\Phi_m\frac{\partial^2\Psi_n}{\partial y^2}\right)^2 - \right.$$
$$\frac{4D_{xy}}{a^2b^2}\left[\left(\frac{\partial^2\Phi_m}{\partial x_1^2}\Psi_n\right)\left(\Phi_m\frac{\partial^2\Psi_n}{\partial y^2}\right) - \left(\frac{\partial\Phi_m}{\partial x_1}\frac{\partial\Psi_n}{\partial y}\right)^2\right] - \rho h\,\omega^2(\Phi_m\Psi_n)^2\right\}d\alpha\,d\beta +$$
$$\frac{1}{a\,b\,e^{2i\omega t}}\frac{b^4}{H}\frac{\partial}{\partial A_{mn}}(U_{rs}) = 0 \tag{B3}$$

Let $\gamma = \frac{a}{b}$, $\quad E_{mi}^{(r,s)} = \int_0^1\left(\frac{d^r\Phi_m}{d\alpha^r}\right)\left(\frac{d^s\Phi_i}{d\alpha^s}\right)d\alpha$ and $\quad F_{nj}^{(r,s)} = \int_0^1\left(\frac{d^r\Psi_n}{d\beta^r}\right)\left(\frac{d^s\Psi_j}{d\beta^s}\right)d\beta$

Let $\overline{k_r} = \frac{k_r\,b}{D}$ and $Dx = Dy = H = D, Dxy = (1-\mu)D/2$ \tag{B4}

$$\sum_{m=1}^{\infty}\sum_{n=1}^{\infty}A_{mn}\int_0^1\int_0^1\left\{\frac{D_x}{H\gamma^4}\left(\frac{\partial^2\Phi_m}{\partial x_1^2}\Psi_n\right)^2 + \frac{2}{\gamma^2}\left(\frac{\partial^2\Phi_m}{\partial x_1^2}\Psi_n\right)\left(\Phi_m\frac{\partial^2\Psi_n}{\partial y^2}\right) + \frac{D_y}{H}\left(\Phi_m\frac{\partial^2\Psi_n}{\partial y^2}\right)^2 - \right.$$
$$\frac{4D_{xy}}{H\gamma^2}\left[\left(\frac{\partial^2\Phi_m}{\partial x_1^2}\Psi_n\right)\left(\Phi_m\frac{\partial^2\Psi_n}{\partial y^2}\right) - \left(\frac{\partial\Phi_m}{\partial x_1}\frac{\partial\Psi_n}{\partial y}\right)^2\right] - \frac{\rho h\,\omega^2 b^4}{H}(\Phi_m\Psi_n)^2\right\}d\alpha\,d\beta +$$
$$\frac{1}{a\,b\,e^{2i\omega t}}\frac{b^4}{H}\frac{\partial}{\partial A_{mn}}(U_{rs}) = 0 \tag{B5}$$

$$\sum_{m=1}^{\infty}\sum_{n=1}^{\infty} A_{mn}\left\{\frac{1}{\gamma^4}E_{mi}^{(2,2)}F_{nj}^{(0,0)} + \frac{2}{\gamma^2}E_{mi}^{(0,2)}F_{nj}^{(2,0)} + E_{mi}^{(0,0)}F_{nj}^{(2,2)} - \frac{2\,(1-\mu)}{\gamma^2}\left[E_{mi}^{(2,0)}F_{nj}^{(0,2)} - \right.\right.$$

$$\left.E_{mi}^{(1,1)}F_{nj}^{(1,1)}\right] - \frac{\rho h\,\omega^2 b^4}{D}E_{mi}^{(0,0)}F_{nj}^{(0,0)} + \frac{b^3}{a\,D}\left(\frac{b}{a^2}\,k_r\int_0^1\left(\left(\frac{\partial\Phi_m}{\partial x_1}\Psi_n\right)_{\alpha=0,\beta} - \right.\right.$$

$$\left.\left.\left.\left(\frac{\partial\Phi_m}{\partial x_1}\Psi_n\right)_{\alpha=1,\beta}\right)d\beta\right)\right\} = 0$$

(B6)

$$\sum_{m=1}^{\infty}\sum_{n=1}^{\infty} A_{mn}\left\{\frac{1}{\gamma^4}E_{mi}^{(2,2)}F_{nj}^{(0,0)} + \frac{2}{\gamma^2}E_{mi}^{(0,2)}F_{nj}^{(2,0)} + E_{mi}^{(0,0)}F_{nj}^{(2,2)} - \frac{2\,(1-\mu)}{\gamma^2}\left[E_{mi}^{(2,0)}F_{nj}^{(0,2)} - \right.\right.$$

$$\left.E_{mi}^{(1,1)}F_{nj}^{(1,1)}\right] - \frac{\rho h\,\omega^2 b^4}{D}E_{mi}^{(0,0)}F_{nj}^{(0,0)} + \frac{1}{\gamma^3}\ \overline{k_r}\int_0^1\left(\left(\frac{\partial\Phi_m}{\partial x_1}\Psi_n\right)_{\alpha=0,\beta} - \left(\frac{\partial\Phi_m}{\partial x_1}\Psi_n\right)_{\alpha=1,\beta}\right)d\beta\right\} =$$

$$0$$

(B7)

Equation (A7) can be written as,

$$\sum_{m=1}^{\infty}\sum_{n=1}^{\infty}\left[C_{mnij} - \lambda^2 E_{mi}^{(0,0)}F_{nj}^{(0,0)}\right]A_{mn} = 0$$

Here, the stiffness matrix C_{mnij} is given by:

$$C_{mnij} = C_{plate} + C_{bc} + C_{ts} + C_{rs}$$

(B8)

where,

$$C_{plate} + C_{bc} + C_{ts} = \frac{1}{\gamma^4}E_{mi}^{(2,2)}F_{nj}^{(0,0)} + \frac{2}{\gamma^2}E_{mi}^{(0,2)}F_{nj}^{(2,0)} + E_{mi}^{(0,0)}F_{nj}^{(2,2)} - $$

$$\frac{2\,(1-\mu)}{\gamma^2}\left[E_{mi}^{(2,0)}F_{nj}^{(0,2)} - E_{mi}^{(1,1)}F_{nj}^{(1,1)}\right]$$

(B9)

$$C_{rs} = \frac{1}{\gamma^3}\ \overline{k_r}\int_0^1\left(\left(\frac{\partial\Phi_m}{\partial x_1}\Psi_n\right)_{\alpha=0,\beta} - \left(\frac{\partial\Phi_m}{\partial x_1}\Psi_n\right)_{\alpha=1,\beta}\right)d\beta$$

(B10)

$$\lambda^2 = \frac{\rho h\,\omega^2 b^4}{D}$$

(B11)

List of Publications Constituting the Thesis

Published Journals:

[1] **Nagaraja, Jade** and Venkatesham. B., Experimental Study of Breakout Noise Characteristics of a Flexible Rectangular Duct, *Mechanical Systems and Signal Processing*, 108, 156–172, 2018.

[2] **Nagaraja, Jade** and Venkatesham. B., Sound Source Reconstruction on Flexible Plate backed by a Cavity using Equivalent Source Method, *NOISE Theory and Practice*, 4(1), 5-17, 2018.

[3] Praveena, R., **Nagaraja, Jade** and Venkatesham, B., Sound Radiation Characteristics of a Rectangular Duct with Flexible Walls, *Advances in Acoustics and Vibration*. Article ID 6053704, 1-15, 2016.

[4] **Nagaraja, Jade** and Venkatesham. B., Study on Effect of Joints on the Modal Parameters of Rectangular Duct, *International Journal of Acoustics and Vibration*, [*Accepted*].

[5] **Nagaraja, Jade** and Venkatesham, B., Free Vibration Analysis of Rectangular Ducts with Different Joint Conditions, *Journal of Theoretical and Applied Mechanics* [*Accepted*].

Manuscripts submitted / under preparation:

[6] **Nagaraja, Jade** and Venkatesham. B., Effect of Pittsburgh Joint on Breakout Noise of Rectangular Duct, Archives of Acoustics, [**Communicated**].

[7] **Nagaraja, Jade**, Nidheesh, V. and Venkatesham. B., Influence of Duct Joint on Modal Parameters of Rectangular Duct, [**Communicated**].

[8] **Nagaraja, Jade**, and Venkatesham. B., Reconstruction of Surface Vibration on a Flexible Rectangular Duct using Inverse Numerical Acoustics, [**Under preparation**].

Conferences:

[1] **Nagaraja, Jade** and Venkatesham. B., Fan noise Source Characterization using NAH Methods", National Symposium on Acoustics: Mysore 2014, November 12-14, 2014.

[2] **Nagaraja, Jade** and Venkatesham. B., Experimental Measurement of Breakout Noise from the Rectangular Duct, National Symposium on Acoustics: Donapaula, Goa, October 07-09, 2015.

[3] **Nagaraja, Jade** and Venkatesham. B., Application of NAH Method for the Prediction of Sound Radiation from a Flexible Box Structure, INTER-NOISE and NOISE-CON Congress and Conference Proceedings, 253 (4), 3993-3999. Institute of Noise Control Engineering, 2016.

[4] **Nagaraja, Jade**, Nidheesh, V., and Venkatesham. B., Reconstruction of Vibration Velocity on a Flexible Rectangular Duct by Using Inverse Numerical Acoustic Technique, International Symposium on Acoustics for Engineering Applications, KIIT Gurgaon, India, 17-19 November, 2016.